IAEA TECDOC SERIES

IAEA-TECDOC-2045

Advancing the State of the Practice in Uncertainty and Sensitivity Methodologies for Severe Accident Analysis in Water Cooled Reactors in the QUENCH-06 Experiment

Final Report of a Coordinated Research Project

IAEA
International Atomic Energy Agency

ADVANCING THE STATE OF THE PRACTICE IN UNCERTAINTY AND SENSITIVITY METHODOLOGIES FOR SEVERE ACCIDENT ANALYSIS IN WATER COOLED REACTORS IN THE QUENCH-06 EXPERIMENT

The following States are Members of the International Atomic Energy Agency:

AFGHANISTAN
ALBANIA
ALGERIA
ANGOLA
ANTIGUA AND BARBUDA
ARGENTINA
ARMENIA
AUSTRALIA
AUSTRIA
AZERBAIJAN
BAHAMAS
BAHRAIN
BANGLADESH
BARBADOS
BELARUS
BELGIUM
BELIZE
BENIN
BOLIVIA, PLURINATIONAL STATE OF
BOSNIA AND HERZEGOVINA
BOTSWANA
BRAZIL
BRUNEI DARUSSALAM
BULGARIA
BURKINA FASO
BURUNDI
CABO VERDE
CAMBODIA
CAMEROON
CANADA
CENTRAL AFRICAN REPUBLIC
CHAD
CHILE
CHINA
COLOMBIA
COMOROS
CONGO
COSTA RICA
CÔTE D'IVOIRE
CROATIA
CUBA
CYPRUS
CZECH REPUBLIC
DEMOCRATIC REPUBLIC OF THE CONGO
DENMARK
DJIBOUTI
DOMINICA
DOMINICAN REPUBLIC
ECUADOR
EGYPT
EL SALVADOR
ERITREA
ESTONIA
ESWATINI
ETHIOPIA
FIJI
FINLAND
FRANCE
GABON
GAMBIA
GEORGIA
GERMANY
GHANA
GREECE
GRENADA
GUATEMALA
GUINEA
GUYANA
HAITI
HOLY SEE
HONDURAS
HUNGARY
ICELAND
INDIA
INDONESIA
IRAN, ISLAMIC REPUBLIC OF
IRAQ
IRELAND
ISRAEL
ITALY
JAMAICA
JAPAN
JORDAN
KAZAKHSTAN
KENYA
KOREA, REPUBLIC OF
KUWAIT
KYRGYZSTAN
LAO PEOPLE'S DEMOCRATIC REPUBLIC
LATVIA
LEBANON
LESOTHO
LIBERIA
LIBYA
LIECHTENSTEIN
LITHUANIA
LUXEMBOURG
MADAGASCAR
MALAWI
MALAYSIA
MALI
MALTA
MARSHALL ISLANDS
MAURITANIA
MAURITIUS
MEXICO
MONACO
MONGOLIA
MONTENEGRO
MOROCCO
MOZAMBIQUE
MYANMAR
NAMIBIA
NEPAL
NETHERLANDS
NEW ZEALAND
NICARAGUA
NIGER
NIGERIA
NORTH MACEDONIA
NORWAY
OMAN
PAKISTAN
PALAU
PANAMA
PAPUA NEW GUINEA
PARAGUAY
PERU
PHILIPPINES
POLAND
PORTUGAL
QATAR
REPUBLIC OF MOLDOVA
ROMANIA
RUSSIAN FEDERATION
RWANDA
SAINT KITTS AND NEVIS
SAINT LUCIA
SAINT VINCENT AND THE GRENADINES
SAMOA
SAN MARINO
SAUDI ARABIA
SENEGAL
SERBIA
SEYCHELLES
SIERRA LEONE
SINGAPORE
SLOVAKIA
SLOVENIA
SOUTH AFRICA
SPAIN
SRI LANKA
SUDAN
SWEDEN
SWITZERLAND
SYRIAN ARAB REPUBLIC
TAJIKISTAN
THAILAND
TOGO
TONGA
TRINIDAD AND TOBAGO
TUNISIA
TÜRKİYE
TURKMENISTAN
UGANDA
UKRAINE
UNITED ARAB EMIRATES
UNITED KINGDOM OF GREAT BRITAIN AND NORTHERN IRELAND
UNITED REPUBLIC OF TANZANIA
UNITED STATES OF AMERICA
URUGUAY
UZBEKISTAN
VANUATU
VENEZUELA, BOLIVARIAN REPUBLIC OF
VIET NAM
YEMEN
ZAMBIA
ZIMBABWE

The Agency's Statute was approved on 23 October 1956 by the Conference on the Statute of the IAEA held at United Nations Headquarters, New York; it entered into force on 29 July 1957. The Headquarters of the Agency are situated in Vienna. Its principal objective is "to accelerate and enlarge the contribution of atomic energy to peace, health and prosperity throughout the world''.

IAEA-TECDOC-2045

ADVANCING THE STATE OF THE PRACTICE IN UNCERTAINTY AND SENSITIVITY METHODOLOGIES FOR SEVERE ACCIDENT ANALYSIS IN WATER COOLED REACTORS IN THE QUENCH-06 EXPERIMENT

FINAL REPORT OF A COORDINATED RESEARCH PROJECT

INTERNATIONAL ATOMIC ENERGY AGENCY
VIENNA, 2024

COPYRIGHT NOTICE

For further information on this publication, please contact:

Nuclear Power Technology Development Section
International Atomic Energy Agency
Vienna International Centre
PO Box 100
1400 Vienna, Austria
Email: Official.Mail@iaea.org

Printed by the IAEA in Austria
February 2024

IAEA Library Cataloguing in Publication Data

Names: International Atomic Energy Agency.
Title: Advancing the state of the practice in uncertainty and sensitivity methodologies for severe accident analysis in water cooled reactors in the QUENCH-06 experiment / International Atomic Energy Agency.
Description: Vienna : International Atomic Energy Agency, 2024. | Series: IAEA TECDOC series, ISSN 1011–4289 ; no. 2045 | Includes bibliographical references.
Identifiers: IAEAL 24-01662 | ISBN 978-92-0-108524-5 (paperback : alk. paper) | ISBN 978-92-0-108624-2 (pdf)
Subjects: LCSH: Nuclear accidents. | Water cooled reactors. | Nuclear facilities — Safety measures. | Nuclear facilities — Experiments.

FOREWORD

The IAEA launched the coordinated research project entitled Advancing the State-of-Practice in Uncertainty and Sensitivity Methodologies for Severe Accident Analysis in Water Cooled Reactors in 2019, bringing together experts from Member States with relevant technologies. The primary objectives were to advance the understanding and characterization of sources of uncertainty and their effect on the key figure of merit for predictions of severe accident progression in water cooled reactors; to improve capabilities and expertise in Member States to perform state of the art uncertainty and sensitivity analysis with severe accident codes; and to support relevant research by graduate students. The participating Member State organizations contributed to two major exercises: a QUENCH-06 test application uncertainty exercise and a nuclear power plant application uncertainty exercise that was divided into subtasks addressing boiling water reactors, pressurized water reactors (including small modular reactor designs), pressurized heavy water reactors and water cooled, water moderated power reactors.

This publication compiles contributions from four organizations from four Member States, each detailing their respective approaches to the uncertainty and sensitivity assessment methods applied in simulating the QUENCH-06 experiment conducted at the Karlsruhe Institute of Technology (Germany) in December 2000. The QUENCH-06 experiment was designed to explore the behaviour of nuclear fuel under oxidizing and quenching conditions during severe accident scenarios in light water reactors. The experiment was characterized by three primary phenomenological phases: the pre-oxidation phase, the heat-up phase and the quenching phase. Because of its comprehensive nature, this experiment was chosen as the benchmark for evaluating the performance of the severe accident codes employed by participants in this coordinated research project.

The IAEA acknowledges the efforts and assistance of the contributors listed at the end of this publication. The IAEA officer responsible for this publication was T. Jevremovic of the Division of Nuclear Power.

EDITORIAL NOTE

This publication has been prepared from the original material as submitted by the contributors and has not been edited by the editorial staff of the IAEA. The views expressed remain the responsibility of the contributors and do not necessarily represent the views of the IAEA or its Member States.

Guidance and recommendations provided here in relation to identified good practices represent expert opinion but are not made on the basis of a consensus of all Member States.

Neither the IAEA nor its Member States assume any responsibility for consequences which may arise from the use of this publication. This publication does not address questions of responsibility, legal or otherwise, for acts or omissions on the part of any person.

The use of particular designations of countries or territories does not imply any judgement by the publisher, the IAEA, as to the legal status of such countries or territories, of their authorities and institutions or of the delimitation of their boundaries.

The mention of names of specific companies or products (whether or not indicated as registered) does not imply any intention to infringe proprietary rights, nor should it be construed as an endorsement or recommendation on the part of the IAEA.

The authors are responsible for having obtained the necessary permission for the IAEA to reproduce, translate or use material from sources already protected by copyrights.

The IAEA has no responsibility for the persistence or accuracy of URLs for external or third party Internet web sites referred to in this publication and does not guarantee that any content on such web sites is, or will remain, accurate or appropriate.

CONTENTS

1. INTRODUCTION

1.1.BACKGROUND

On 28 March 1979 a cooling malfunction at Three Mile Island Unit 2 (TMI-2) reactor caused part of the core to melt, the conditions being more severe than design basis accidents; it was the most serious accident in the USA commercial power plant operating history. Regardless of the accident not causing any detectable health effects on plant workers or the public, it brought changes in many areas of nuclear power plant (NPP) operation. This also included the development of severe accident codes to address significant lack of understanding of what happened during that accident. The accident at the Fukushima NPP in 2011 in Japan, reinforced the necessity to extend the focus of international research and development efforts to containment phenomena impacting the source term to the environment (including aerosol and core melt behaviour in the containment, risk of combustible gas mixtures, and other associated phenomena).

After the Fukushima Daiichi accident, the IAEA held, in cooperation with the OECD/NEA, the International Experts' Meeting (IEM) on Strengthening Research and Development Effectiveness in the Light of the Accident at the Fukushima Daiichi Nuclear Power Plant at IAEA Headquarters in Vienna, Austria, 16–20 February 2015. The objective of this IEM was to facilitate the exchange of information on R&D activities and to further strengthen international collaboration among Member States and international organizations. One of the main conclusions of the IEM was that the Fukushima Daiichi accident had not identified completely new phenomena to be addressed but the accident highlighted some areas where the knowledge and understanding of issues associated with severe accidents and other related topics needed to be strengthened. As one of the follow-up meetings for the IEM, the IAEA held a Technical Meeting on Post-Fukushima Research and Development Strategies and Priorities at its Headquarters, Vienna, Austria, 15–18 December 2015. The objective of that workshop was to provide a platform for experts from Member States and international organizations to exchange perspectives and information on strategies and priorities for R&D regarding the Fukushima Daiichi accident and severe accidents in general. The experts agreed that for better understanding of the progression of the Fukushima Daiichi accident one of the most prioritized areas is to better understand the phenomenology of severe accidents and to develop, improve and benchmark severe accident analysis codes.

As a response to Member States interests in information exchange on the current status of severe accident simulation and modelling codes and tools for water cooled reactors (WCRs) and as a response to the request from the Technical Working Groups on Advanced Technologies for light water cooled reactors (LWRs) and heavy water cooled reactors (HWRs), the IAEA Technical Meeting on the Status and Evaluation of Severe Accident Simulation Codes for Water Cooled Reactors was held in Vienna Austria, 9–12 October 2017. At the meeting, the code developers and severe accident analysis practitioners met to share experiences and demonstrate state of art practices. In this technical meeting it was observed that often severe accident analysts did not know the accuracy of their analyses or lack confidence in the results of their calculation and did not have good appreciation of the sources of uncertainty or variability in their analyses and therefore could not quantify the uncertainties in their predicted results. These codes allow the uncertainties in an analysis to be expressed in terms of variability in the code input and boundary conditions that could be propagated through the severe accident analysis producing an ensemble of answers from which probability distributions instead of single realization point values. In this way a likelihood distribution of accident figures of merit (FOM) is obtained that give indications of mean values, central tendencies and dispersion in the answers. In the present era, codes have undergone substantial enhancements, and computational platforms have

experienced remarkable speed improvements. These platforms now possess greatly accelerated execution capabilities, leveraging massively parallel computational resources equipped with thousands of individually accessible processors. As a result, sampling-based methods for addressing uncertainty in selected accident sequences have become more accessible, providing valuable assistance to the endeavours of severe accident analysis.

The International Atomic Energy Agency (IAEA) Coordinated Research Project (CRP) on Advancing the State-Of-Practice in Uncertainty and Sensitivity Methodologies for Severe Accident Analysis in Water Cooled Reactors (WCRs) was launched in 2019. By bringing together the experts from the IAEA Member States with relevant technologies, the primary objectives of this CRP were to advance the understanding and characterization of sources of uncertainties and their effects on the key figure-of-merit predictions in severe accident codes for water cooled reactors, improve capabilities and expertise in Member States to perform state-of-the-art uncertainty and sensitivity analysis with severe accidents codes, and support graduate students relevant research.

The IAEA organizes CRP to facilitate the co-operation on research and development, including the development and validation of computer codes for design and safety analysis of NPPs, to bring together the experts from the Member States with WCRs technologies experienced in developing and using the severe accident codes to further advance the state-of-knowledge on uncertainty propagation in severe accident simulation and modelling analyses. The newly developed knowledge is shared with developing Member States through various activities: support of their graduate students, participation in training workshops, and participation in the exercises. The CRP is specifically aimed at improving the state of practice in severe accident analyses by examining and characterizing the impact of uncertainty and variability on severe accident simulation and modelling.

1.2.OBJECTIVE

The objective of this publication is to highlight the state-of-knowledge on uncertainty propagation in severe accident analyses that has been accumulated by experienced analysts with the aim of increasing the sophistication and competency of the practitioners in this field addressing the uncertainty and sensitivity assessment methods for the QUENCH-06 experiment that has been performed at the Karlsruhe Institute of Technology (Germany) in December 2000. The test application exercise was aimed at consolidating existing experience in the development of a strong technical basis for establishing uncertainty and sensitivity methodologies in severe accident analyses. The insights gained from the test application exercise lead towards newly generated knowledge to be referred on the uncertainty and sensitivity analysis and methods for severe accident codes with the intent of capturing the best practices and lessons learned.

Besides the QUENCH-06 test application uncertainty exercise, the plant application uncertainty exercises addressed boiling water reactors (BWRs), pressurized water reactors (PWRs) inclusive of small modular reactor (SMRs) designs, pressurized heavy water reactors (PHWRs), and water-water energetic reactors (VVERs); the results from these analyses are presented in corresponding separate publications.

1.3. SCOPE

The scope of this publication is the QUENCH-06 test [1] exercise performed by the CRP participants in support of addressing improvement in sophistication and quality of severe accident analyses with

various codes that generated new knowledge relevant to evaluation of uncertainties and sensitivity analysis of severe accident simulation and modelling. The CRP exercises were developed as per flow diagram shown in Fig. 1 indicating the five publications, each addressing a specific plant application exercise and outlining relevant research technical results with lessons learned and best practices [2].

Participating organizations in this exercise and contributors to this publication were:

— National Agency for New Technologies, Energy and Sustainable Economic Development (ENEA, Italy);
— Nuclear Safety Institute of the Russian Academy of Sciences (IBRAE RAN, Russian Federation);
— Karlsruhe Institute of Technology (KIT, Germany);
— Lithuanian Energy Institute (LEI, Lithuania).

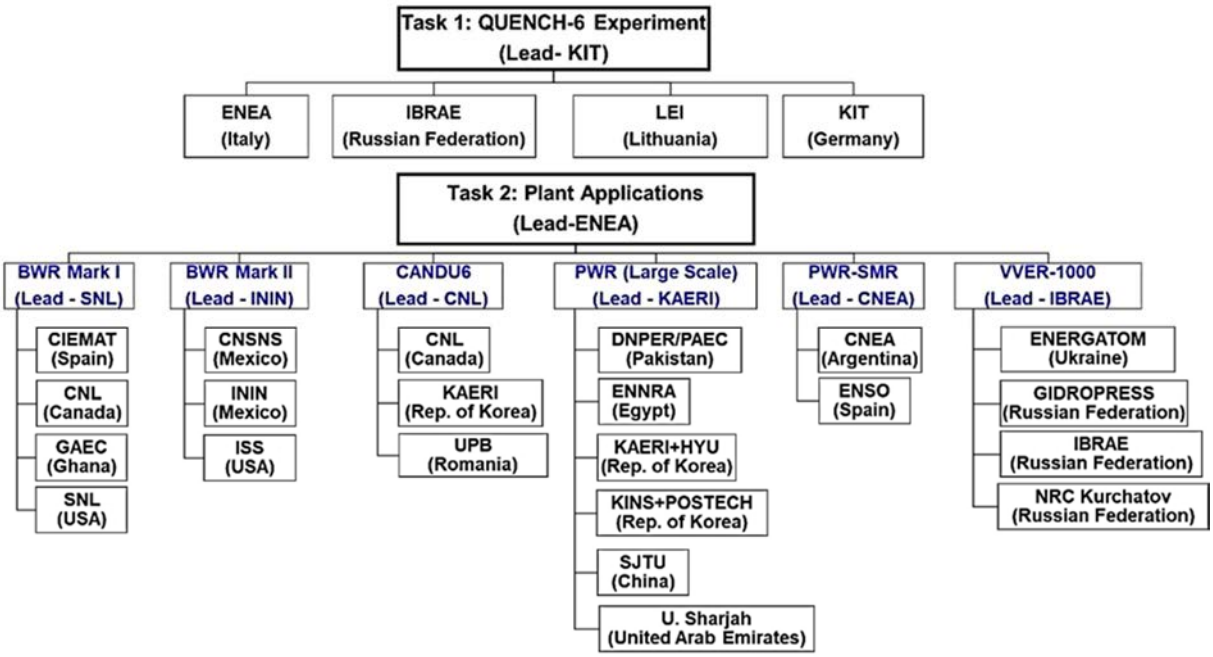

FIG. 1. CRP tasks and participants (refer to list of acronyms for the organizations full names).

1.4. STRUCTURE

This publication is structured such to provide the readers with a logical progression from the general background and detailed information regarding calculations and results to summary and main conclusions. The participating organizations employed their own calculation framework for the uncertainty and sensitivity analyses and three different severe accident analysis codes applied to the analysis of the QUENCH-06 experiment.

Following this introductory section, Section 2 provides an overview of the QUENCH-06 test and the assessment of the uncertainty and sensitivity exercise. Section 3, Section, 4, Section 5, and Section 6 provide the details of the QUENCH-06 models of the integral codes used by the participating organizations as well as the description of the methodologies employed for performing the uncertainty and sensitivity analyses and the corresponding results, the analysis performed by the participating

organizations, scope of the analysis, codes used, and results obtained. Finally, the main outcomes of the activity and lessons learned are provided in the conclusion section.

2. QUENCH-06 UNCERTAINTY AND SENSITIVITY EXCERSICE

The analysis of the QUENCH-06 experiment that has been conducted at the Karlsruhe Institute of Technology on December 2000 (KIT, Germany) [1, 3] is widely used exercise to test the uncertainty and sensitivity analysis methodologies applied to the results of the simulations using relevant severe accident codes.

The exercise consisted of two phases. Firstly, different participants assessed the inputs of the severe accident codes for analysing the QUENCH-06 test and the simulations with best estimate inputs to be compared with the experimental data as provided by KIT. Such set of results are labelled in this publication as nominal case. Secondly, the participants applied uncertainty and sensitivity analysis tools and methodologies of their choice. This publication provides details on the specifications of these uncertainty and sensitivity analysis methods, including lists of uncertain parameters and the FOMs used in the analyses.

2.1. DESCRIPTION OF QUENCH FACILITY

The most important accident management measure to terminate a severe accident transient in LWRs is the injection of water to cool the uncovered core. The QUENCH experimental programme exists since 1996 (following-up the CORA bundle tests) at KIT in order to perform detailed investigations of the effect of reflooding on fuel bundle degradation [4, 5]. More than 20 integral bundle tests were carried out. The main objective of the QUENCH programme is the analysis of the H_2 production resulting from the steam interaction with overheated elements of an assembly loaded with 21–31 electrically heated fuel rod simulators. The programme, supported by separate effect tests and code analyses, also aims at identifying the limits such as but not limited to temperature and injection rate for which a successful reflood and quench can be achieved, investigating the performance of different kinds of cladding materials.

The QUENCH programme therefore provides experimental and analytical data for the development of quench related models of integral code systems such as, i.e., ASTEC [6] and MELCOR [7]. Since 2005, the QUENCH test facility operates in two modes: the forced convection and the boil-off mode. The pressure in the test section is usually ~0.2MPa. In the forced convection mode (Fig. 2, [8]), superheated steam and argon (carrier gas) enter the test bundle at the bottom. Argon, steam, and H_2 produced in the zirconium–steam reaction flow upward inside the bundle. Once reached the top, the mixture flows through a water cooled off-gas pipe to the condenser, where the not condensed steam is separated from the non-condensable gases (usually argon and H_2). The quenching water or the superheated steam are injected through a separate line (bottom quenching in Fig. 2). In the boil-off mode the steam inlet is closed, so that the test bundle can be filled with water, which can be boiled off by applying electric bundle power and additional electric power by an auxiliary heater located in the lower plenum of the bundle. In that case, the carrier gas argon is injected at the bundle head.

The QUENCH experiments can be terminated either by quenching with water from the bottom (in both operating modes) or by the injection of cold steam from the bottom (in the forced convection mode only). The main component of the QUENCH test facility is the test section with the test bundle (Fig. 3, [1]).

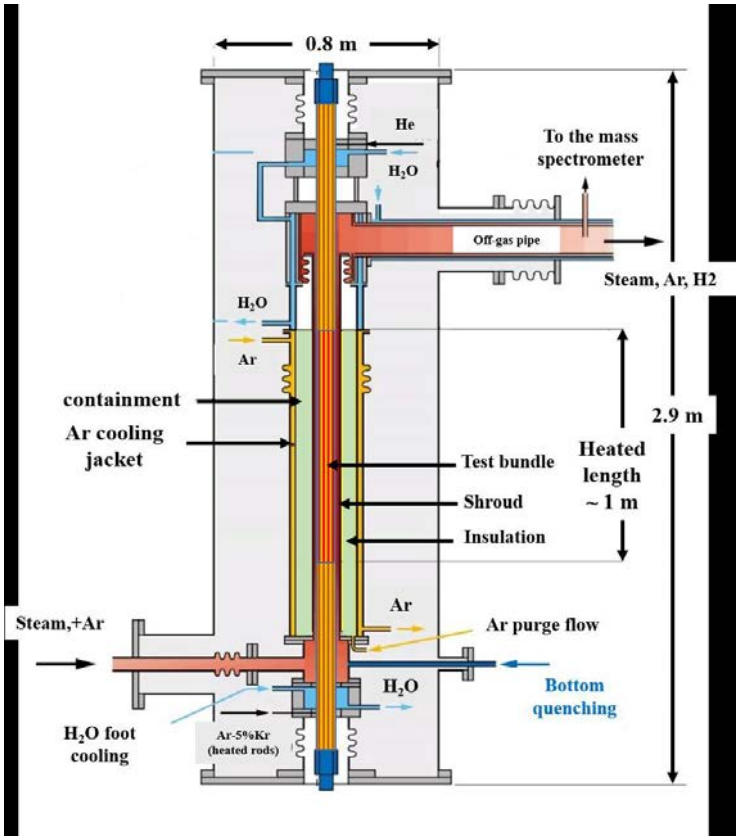

FIG. 2. Test section with test bundle and fluid lines.

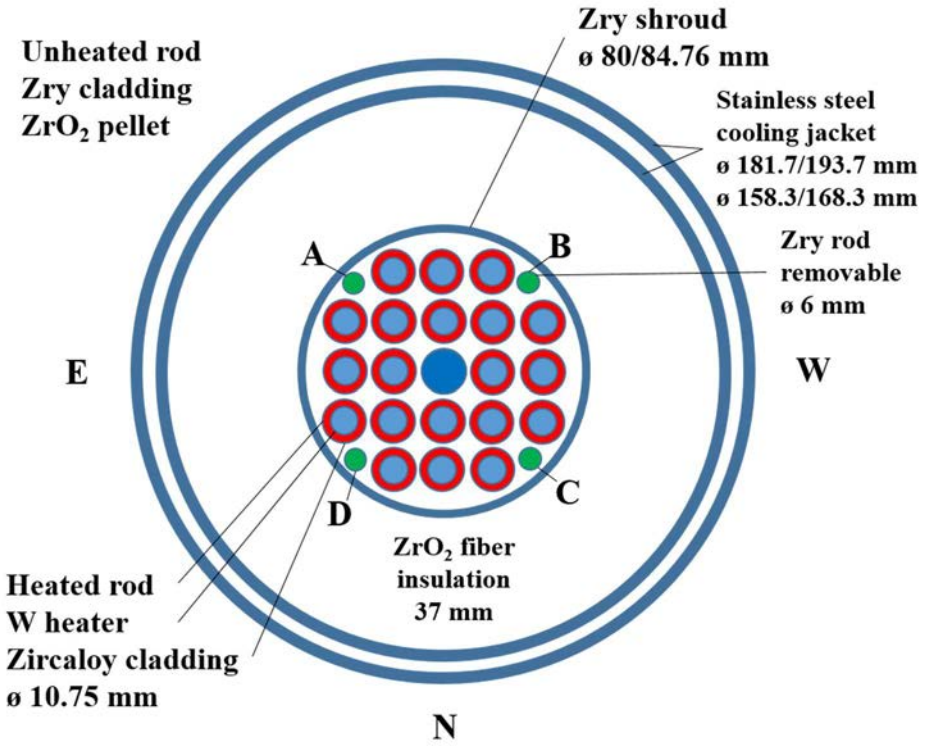

FIG. 3. Cross section of QUENCH-06 test bundle, shroud, insulation, and cooling jacket (Zry is zircoloy) [1]

The PWR type test bundle consists of 21 fuel rod simulators (total axial length ~2.5m). The rod cladding and grid spacers are identical to those used in LWRs with respect to materials and dimensions. Twenty fuel rod simulators are heated over a length of 1024 mm by means of 6mm diameter tungsten heaters installed in the centre of the rod and surrounded by annular ZrO_2 pellets. The heaters are connected to the cable leading to the DC (direct current) electric power supply (70 kW) by means of molybdenum and copper electrodes. The central fuel rod simulator is unheated and it is used as instrumented or as absorber rod. The fuel rod simulators are held in position by five grid spacers (four made of Zircaloy and one of Inconel).

The heated rods are filled with Ar–5%Kr or He (optional) at a pressure of ~0.22 MPa. The krypton additive as well as helium allow the detection of a first test rod failure with the help of a mass spectrometer. Four Zircaloy corner rods are installed in the bundle. Three of them are used for thermocouple instrumentation, while the fourth rod can be withdrawn from the bundle anytime during the test, to check the axial oxidation scale at that time.

The test bundle is surrounded by 2.38 mm thick shroud of Zircaloy, by a 37 mm thick ZrO_2 fibre insulation that extends to the upper end of the heated zone, and by double-walled cooling jacket of stainless steel that extends up to the upper end of the test section. The H_2 produced during the tests is analysed by using: (1) state-of-the-art mass spectrometer "BALZERS GAM 300" located at the off-gas pipe and (2) commercial type H_2 detection system "Caldos 7G", located behind the off-gas pipe and condenser. The mass spectrometer allows analysing all off-gas species including steam, while the Caldos system works for binary Ar/H_2 mixtures only. The temperature of the test bundle, of the shroud, and of the cooling jackets are monitored by several thermocouples located at different elevations.

2.2. DESCRIPTION OF QUENCH-06 EXPERIMENT

The QUENCH-06 bundle test (Fig. 3) was successfully performed at KIT in December 2000. The sequence of events and phases is shown in Table 1. The test is shown in Fig. 4 (electrical power history) and Fig. 5 (inlet flow rates) [1, 3].

TABLE 1. SEQUENCE OF EVENTS AND PHASES OF THE QUENCH-06 TEST BASED ON [1, 3]

Time (s)	Event	Phase
0	Start of data recording	
30	Heat up to about 1500 K	Pre-oxidation
1965	Pre-oxidation at about 1500 K	
6010	Start of the power transient	Transient
6620	Withdrawal of the corner rod B	
7179	Shut down of the steam supply, fast water injection, switch of the argon supply	Reflooding
7181	Steam mass flow rate at zero	
7205	Start of the electrical power reduction to 4 kW	
7221	Decay heat level reached	
7431	Shut down of the quench water injection, electrical power shut off	
11,420	End of data acquisition	

The bundle is heated by a series of stepwise increase of the electrical power up to 4 kW from room temperature to 873 K in an atmosphere of flowing Argon (3 g/s) and steam (3 g/s).

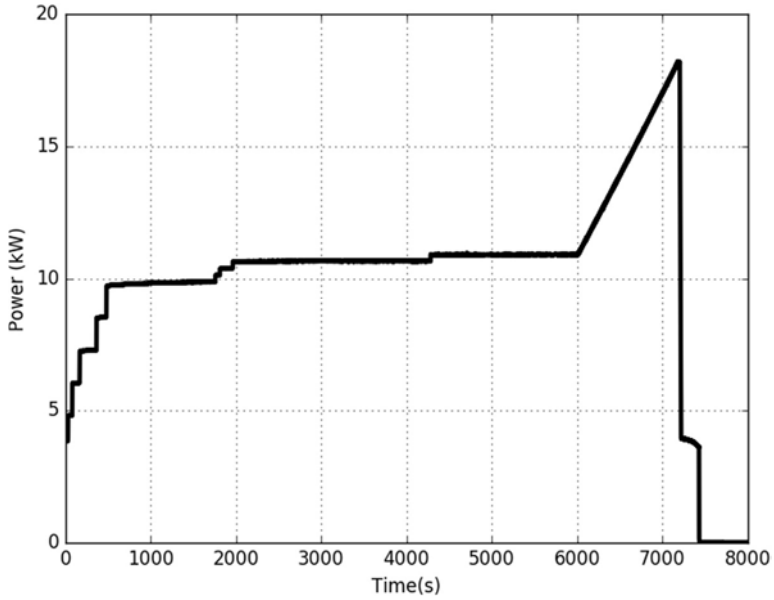

FIG. 4. Power history of the QUENCH-06 test.

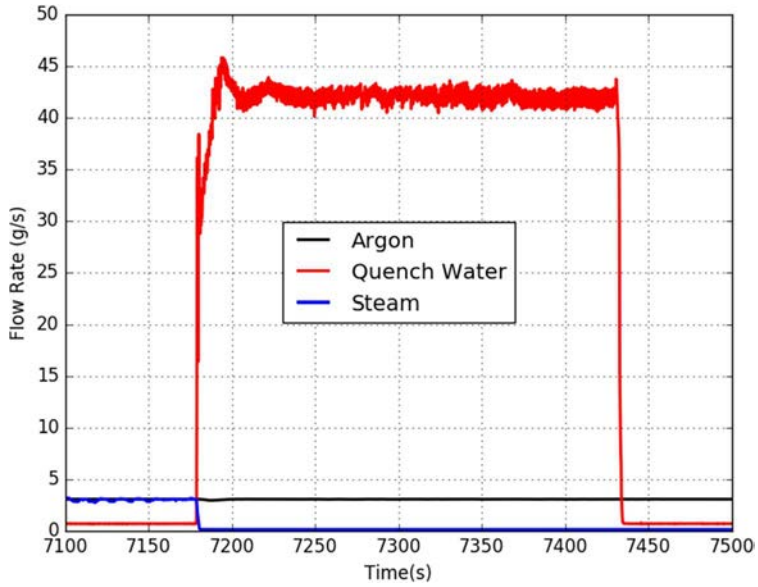

FIG. 5. Argon, steam, and quench water flow rates.

At the end of such stabilization period, the pre-oxidation phase begins: the power is increased up to 11 kW and the maximum axial temperature is maintained constant at 1473 K for 4046 s. The transient phase beings at 6000 s and it is triggered by ramping the electrical power of the bundle at 0.3 W/s/rod between 1450 K and 1750 K, based on the thermocouple signal at 950 mm elevation. During the transient phase and before any temperature excursion the corner rod B (Fig. 3) is withdrawn at 6620 s to evaluate the oxidation at that time. The quench phase begins when the temperature of the central rod has reached ~1873 K and the temperature of at least three rods exceeds 1973 K. The quenching sequence starts at 7179 s: the superheated steam flow is turned off, the argon flow is switched over to the bundle head, and a rapid water pre-injection (4 kg in 5 seconds) from the bottom of the test section occurs. At the same time, the quench pump starts to inject water (1.4 g/s/rod) from the bottom of the test section for about 250 s. A detailed examination of available experimental data [9] revealed a delay of the quench water injection into the test section ranging from 34 s to 41 s. About 20 s after the injection, the electrical

power is reduced to about 4 kW within 15 s, to simulate the decay heat levels. The flooding of the bundle is terminated when the shroud temperature at 1150 mm height indicates a local wetting. The cooling of the test section to about 400 K is completed at about 250 s after the beginning of the flooding. Few seconds later, the quench water injection and the electrical power are shut off, the experiment being terminated.

2.3. FIGURES OF MERIT AND UNCERTAINTY PARAMETERS

The FOMs were selected according to the main findings of the QUENCH-06 experiment. As discussed in Section 2.1, the evaluation of hydrogen production following the reflooding of a pre-oxide bundle was one of the main goals of the QUENCH-06 experiment. Other than hydrogen production, the attention was focused on phenomena triggering the hydrogen release following the cladding oxidation, namely the cladding temperature and the oxide scale. The FOMs of the QUENCH-06 exercise are shown in Table 2. Such quantities are employed to demonstrate the uncertainty and sensitivity analysis methodologies applications by the CRP participants.

TABLE 2. FIGURE OF MERITS

Time (s)	Parameter
1	Total mass of accumulated H_2
2	Temperature of the central fuel rod simulator at elevation 950 mm
3	H_2 generation rate
4	Axial profile of the oxide scale of the corner rod at 6620 s
5	Axial profile of the average oxide scale of the heated rods at the end of the scenario

The selection of the uncertainty in input parameters and the assessment of the corresponding probability distribution functions (PDFs) are based on previous uncertainty and sensitivity analysis performed for the CORA-W2 [10] and the QUENCH-08 experiments [11, 12], the QUENCH-06 experiment report [1, 3], and the ASTEC code documentation. The uncertainty geometry parameters and the corresponding uncertainties are shown in Table 3. The uniform PDFs are based on engineering judgments[1].

TABLE 3. UNCERTAINTY PARAMETERS RELATED TO GEOMETRY

#	Parameter	Uncertainty Range (mm)	Probability Distribution
1	Rod pitch	14.3 ± 0.15	Uniform
2	Fuel pellet simulator (ZrO_2) external diameter	9.15 ± 0.02	Uniform
3	Cladding thickness	0.725 ± 0.00725	Uniform
4	Internal diameter Shroud	80 ± 0.8	Uniform
5	Thickness of the Shroud	2.38 ± 0.023	Uniform
6	Thickness of the Insulator	37.0 ± 0.37	Uniform

The input parameters concerning the boundary conditions of the experiment are shown in Table 4. The PDFs are assumed normal, the standard deviation being set equal to the measurement standard uncertainty 2% [1, 3]. The model parameters concerning the integrity criteria of the oxide layer of the cladding are shown in Table 5. The parameters are chosen based on the analysis of the results of the

[1] The uncertainty parameters were identified based on validation analyses of different integral codes against the experiments. Engineering judgement was applied to evaluate the uncertainty range of the uncertainty parameters for which no information were provided. Furthermore, the mean values employed for each PDF were selected based on data used in the datasets of the integral codes, mainly ASTEC.

Phébus experiments concerning the early degradation phase of the fuel rods [12]. Based on the ASTEC documentation, the fuel rod failure may occur either when the ZrO_2 temperature exceeds 2300 K or the oxide layer thickness is lower than 250 μm. The failure temperature and the oxide threshold thickness are estimated to be affected by 5% (T=2248 K is the ZrO_2 solidus temperature) and 10% uncertainty, respectively.

TABLE 4. UNCERTAINTY PARAMETERS RELATED TO BOUNDARY CONDITIONS

#	Parameter	Mean Value	STD[2]
7	Instant of the quench water injection (s)	7215	± 0.5%
8	Quench water mass flow rate at the bundle inlet (kg/s)	Experiment	± 2%
9	Argon mass flow rate at the bundle inlet (kg/s)	Experiment	± 2%
10	Steam mass flow rate at the bundle inlet (kg/s)	Experiment	± 2%
11	Pressure at the bundle outlet (bar)	2.0	± 2%
12	Electrical power	Experiment	± 2%
13	Quenching water temperature (K)	Experiment	± 2%
14	Fuel/clad internal pressure (bar)	2.2	± 2%

TABLE 5. UNCERTAINTY PARAMETERS RELATED TO INTEGRITY OF CLADDING

#	Parameter	Uncertainty Range	Probability Distribution
15	Threshold thickness (μm)	Reference Value ± 10%	Uniform
16	Failure temperature of the ZrO_2 layer (K)	Reference Value ± 5%	Uniform

The parameters related to the radiative and convective heat transfer phenomena are shown in Table 6 and Table 7, respectively. Engineering judgments are employed to evaluate the uncertainty ranges. The rod and the shroud anisotropic factors (Table 6) are affected by 5% uncertainty. The parameters for the convective heat transfer modelling are assumed to be affected by 5% uncertainty also. The parameters related to the material movement modelling are shown in Table 8. As in [9–12], uniform PDFs are assessed, the uncertainty being set equal to 5%.

TABLE 6. UNCERTAINTY PARAMETERS RELATED TO RADIATIVE HEAT TRANSFER MODELLING

#	Parameter	Uncertainty Range	Probability Distribution
17	Rod anisotropic factor	Reference Value ± 10%	Uniform
18	Shroud anisotropic factor	Reference Value ± 10%	Uniform

TABLE 7. UNCERTAINTY PARAMETERS RELATED TO CONVECTIVE HEAT TRANSFER MODELLING

#	Parameter	Uncertainty Range	Probability Distribution
19	Heat transfer coefficient due to droplet projection	Reference Value ± 5%	Uniform
20	Height above the quench front concerned by droplet projection	Reference Value ± 5%	Uniform
21	Threshold void fraction to allow exchange with liquid droplets	0.99–0.999	Uniform

[2] STD: standard deviation

TABLE 8. UNCERTAINTY PARAMETERS RELATED TO MATERIAL MOVEMENT MODELLING

#	Parameter	Uncertainty Range	Probability Distribution
22	Max. value of the ratio permeability/viscosity	Reference Value ± 5%	Uniform
23	Min. liquid fraction allowing the material relocation (%)	0.0, 5	Uniform

3. SPECIFICATIONS OF A NUMERICAL TEST PROBLEM

The exercise on the QUENCH-06 performed at the QUENCH facility adopting the ASTEC code (V2.2 beta) [14] has the objective to validate the code models for early degradation phenomena and hot core quenching. The comparison of the reference calculation against the experimental data and the accuracy evaluation are aimed at assessing, both qualitatively and quantitatively, the accuracy of the code predictions. The uncertainty quantification aims at studying the uncertainty of the code results and identifying the main sources of uncertainty of the selected FOMs.

3.1. DESCRIPTION OF SEVERE ACCIDENT CODE

The ASTEC code [6] was developed by the French Institut de Radioprotection et de Sûreté Nucléaire (IRSN); it aims at simulating a complete severe accident sequence in WCRs. The code is composed of different modules, each featuring different physical models and suitable to simulate a specific zone of the reactor. An ASTEC module can be used as stand-alone code or can be coupled with other modules, depending on the user's needs. The main applications of the code are the source term evaluation, probabilistic safety assessment Level 2, accident management studies, to mention just a few [1]. In this exercise, the ICARE module is employed to model the test bundle components of the QUENCH facility. The thermal hydraulics of the system is calculated by coupling ICARE to CESAR module. The ASTEC V2.2 beta code version is used. CESAR [15] is the ASTEC module designed to simulate the thermal hydraulics of WCRs, inside the reactor pressure vessel, the primary and the secondary systems. It is one dimensional integral code, characterized by a two phase flow model. The chosen five equations approach considers two equations for the mass balances, two for the energy balances and one averaged momentum balance equation.

The set of equations is closed by a phase slip model. A six equations two phase flow model is also available in CESAR, starting from ASTEC V2.2 beta. CESAR is based on a finite volumes' discretization approach, solving the energy and mass balance equations on the control volumes, while the momentum equations are calculated on the junctions between volumes. The Newton's method is adopted for the time integration, using a fully implicit scheme. An optimized lower upper algorithm is implemented for the Jacobian matrix inversion. Up to five non-condensable gases can be used in the simulation. ICARE [16] is the module dedicated to core structures modelling and the simulation of in-vessel core degradation phenomena. It includes mechanical models, support for chemical reactions typical of the core degradation, it can model the release of fission products and represent the core degradation and relocation in the lower plenum, until failure of the lower head. ICARE adopts basic two dimensional cylindrical axially symmetric objects to reproduce most of the internal core components and the related heat exchange with the coolant fluid. The core fluid patterns for the coolant are represented by CHANNEL objects, completing the core meshing and allowing the CESAR module to compute the thermal hydraulics inside the core and the lower plenum.

3.2.DESCRIPTION OF QUENCH-06 MODEL

This section describes the QUENCH-06 geometry and modelling assumptions, physical phenomena and initial boundary conditions used in modelling.

3.2.1. Geometry and modelling assumptions

The ASTEC model of the test section is radially composed by two main coaxial channels. The unheated fuel rod and eight inner electrically heated fuel rods constitute the inner ring and are inserted in the inner fluid channel (channel-1). The external 12 electrically heated rods and four Zr corner rods define the outer ring and are inserted in the outer fluid channel (channel 2), as shown in Fig. 6 [17].

The two concentric fluid channels are embedded in the structure of the internal shroud, which is included in the fibre insulation, along the active zone (heated by tungsten heaters), and in the argon gap in the unheated length. Externally, the inner tube of the annular cooling jacket has been modelled as depicted in Fig. 6and it embeds all of the structures [17]. Additionally, the model includes the grid spacers and the plates.

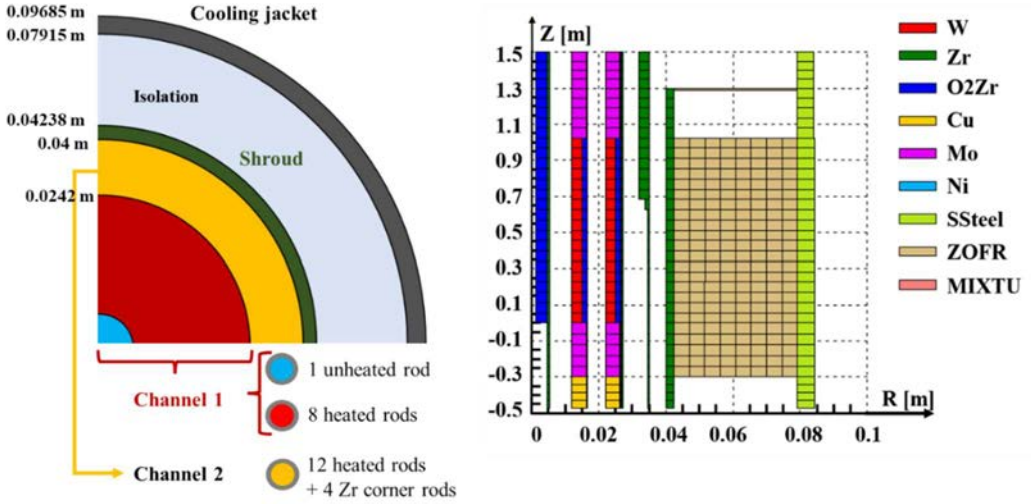

(a) *(b)*

FIG. 6. (a) ASTEC model radial view of the QUENCH test section, (b) Conversion of the QUENCH model in the ASTEC computation together with the materials distribution (MIXTU refers to a mixture of several pure materials or a dislocated solid material).

The ICARE geometry considers azimuthal symmetry for all the elements. Concerning the axial discretization, the bundle is subdivided into equal slices, each 55 mm in height. This discretization and the materials distribution throughout the core are also shown in Fig. 6. Therein, the “O2Zr” material corresponds to the ZrO_2 and “ZOFR” to the specific ZrO2 alloy composing the fibre insulation. In addition, the following assumptions were made:

— Tungsten heater is in contact with the fuel pellets to avoid the radiation from heater with unknown surface properties (e.g. roughness);

— Since it is not possible to remove physical elements from ICARE during the calculation, the four corner rods are present in the bundle during the whole transient (in the experiment the corner rod B was extracted after the pre-oxidation phase);
— Several time dependent boundary conditions have been introduced according to the experimental measurements [3]:
    - Electrical power generated in the inner and outer rings; pressure, temperature and mass flow rate of the inlet fluids (Ar, steam, water);
    - Axial temperature distribution of the bundle components (central rod, heated and corner rods, shroud, grids, plates, etc.) at the start of transient provided as an initial condition.

3.2.2. Physical phenomena modelling

The following relevant physical phenomena, related to the in-vessel early degradation phase, have been taken into account in the ICARE model of the bundle.

— Heat transfer:
    - Conduction within each element and between the elements in contact;
    - Convection for the elements facing the fluid channels (i.e. fuel and corner rods, shroud, grids, plates), by using "DRACCAR" convection model [15, 16];
    - Radiation among fuel rods simulators claddings, corner rods and the shroud.
— Chemical interactions:
    - Zr components oxidation (corner rods, rods cladding, grids, shroud);
    - Steam entrainment into the fiber or the argon gap after shroud failure was not modelled.
— Mechanical processes:
    - Cladding, corner rod, shroud and grid components failure if their temperature is > 2375 K and ZrO_2 thickness is <300 μm;
    - Cladding, corner rod, shroud and grid components failure if their temperature is > 2500 K;
    - Relocation of molten material along the rods and molten material oxidation.

3.2.3. Initial and boundary conditions

At the start of the sequence, the initial temperature distribution of the components (central rod, heated and corner rods, shroud, grids, plates, etc.) is provided as a function of the axial level. The initial axial temperature distributions are taken from the experimental data of the available thermocouples and interpolated for the components in which no thermocouple is located. The time evolution matrix of the applied thermodynamic quantities (mass flow rate, temperature, pressure) of the coolant fluids injections (argon, steam and main water) is taken from the experimental data (FM 401, F 205, Fm 104). The injections is defined as fluid source boundary conditions to the two CESAR fluid channels. Without detailed flow rate measurements available, the 4 L of pre-injection water (at 370 K and 6 bar) is assumed to take place at the constant rate of about 0.769 kg/s, for the 5 s of injection. The mass flow rate of the considered fluids injection is shown in Fig. 7 At the channel outlet, a constant pressure boundary condition of 0.2 MPa is applied. The time evolution of the electric power applied to the outer and inner heated rods is adopted from the experimental data (E 505, E 506), and its distributions between the two rings is shown in Fig. 8.

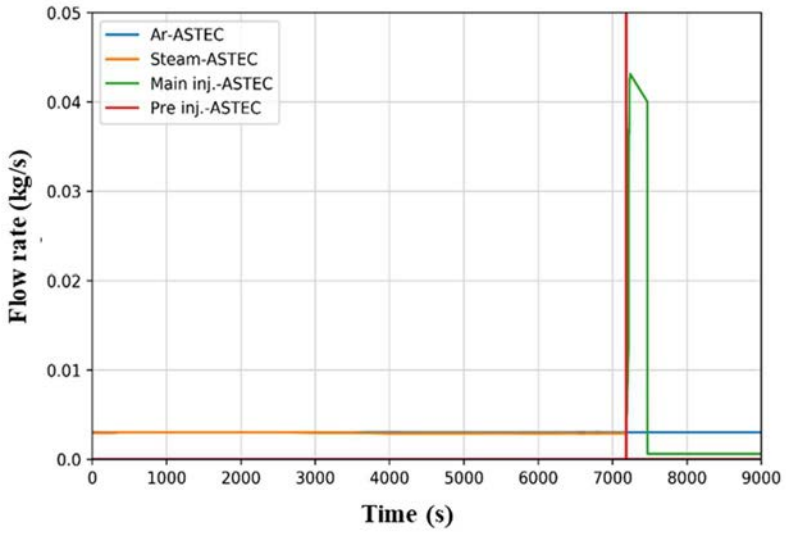

FIG. 7. Argon (FM 401), steam (F 205), main water (FM 104) and pre-injection (estimated) mass flow rate, used as boundary conditions for the ASTEC input.

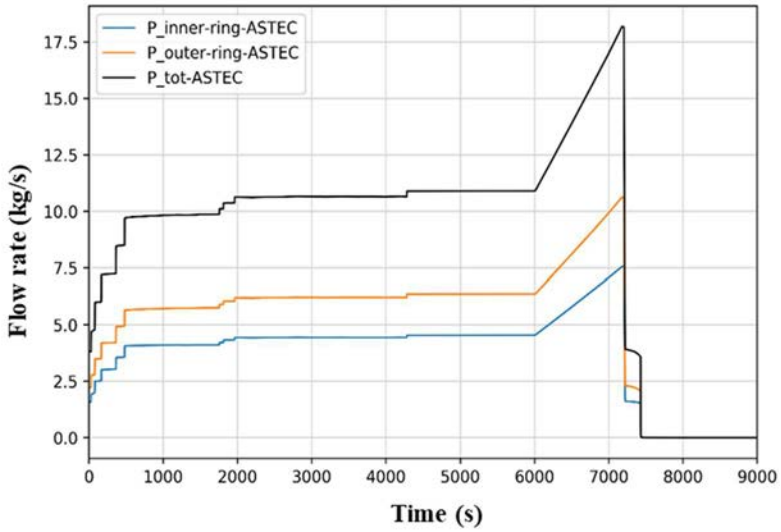

FIG. 8. Electric power generated in the inner ring heated rods (E 505), in the outer ring heated rods (E 506) and total electric power, considered as boundary conditions for the ASTEC input.

3.3.DESCRIPTION OF UNCERTAINTY AND SENSITIVITY METHODOLOGY

To conduct uncertainty quantification on the outcomes of deterministic codes, various methodologies have been developed. The selected one here is the probabilistic propagation method of input uncertainties [18, 19]. This method involves identifying input parameters subject to uncertainty, each defined by a reference value, a range of variation, and a PDF type. A random sampling of these uncertain input parameters is carried out to generate a set of input values, which are then used to perform multiple code calculations within the same sequence. Consequently, every code run corresponds to a unique result in terms of FOMs, as all uncertain input parameters assume different values. The number of simulations can be determined based on guidelines provided in [20, 21], which link the minimum number of code runs to the desired probability content, confidence level, and the number of FOMs.

Moreover, the number of runs is influenced by the number of limit sides (both upper and lower limits, or only one limit) associated with each FOM [22].

The calculation results are subjected to statistical analysis to extract information about the FOMs. Additionally, this analysis can encompass characterizing the relationship between the input uncertain parameters and the FOMs. This characterization can be achieved through the computation of correlation coefficients or regression coefficients, such as the Pearson and the Spearman correlation coefficients, respectively, which describe the linear and monotonic relationships between an input parameter and a chosen output FOM. In this analysis, absolute values of the correlation coefficient exceeding 0.5 are deemed significant, values between 0.2 and 0.5 indicate a moderate correlation, and values lower than 0.2 indicate a low correlation [19].

One notable advantage of this method is that the number of calculations required for uncertainty quantification is independent of the number of input uncertain parameters. Nevertheless, challenges may arise if the code encounters simulation failures, disrupting the link between the number of simulations and confidence intervals. Moreover, when dealing with many calculations, the use of a multicore computer or a cluster platform becomes crucial to complete the analysis within a reasonable timeframe.

3.3.1. Description of the uncertainty and sensitivity tool and coupling with the severe accident code

The uncertainty tool RAVEN (Risk Analysis and Virtual ENviroment) is used [24, 25]. It is a multi-purpose code for parametric and probabilistic analysis, developed by Idaho National Laboratory, USA. Its development started in 2012 aiming at a risk assessment studies in the framework of the LWRs sustainability programme, focusing the effort on coupling it to the RELAP codes. RAVEN is an open source code based on Python [26] that uses an object oriented approach. Parallel simulations, for both standard and high performance computing systems, are supported. RAVEN can perform:

- Classical and advanced statistical analyses;
- Parametric studies;
- Limit surfaces determination;
- Machine learning with artificial intelligence algorithms;
- Data mining with clustering techniques;
- Phase space optimization;
- Sampling with dynamic event trees.

Leveraging its artificial intelligence capabilities, RAVEN has the capacity to create reduced-order models, serving as surrogates for intricate physical codes. These reduced-order models are designed to efficiently mimic the behaviour of the more complex code. The input file structure in RAVEN employs an XML format, organizing the operations into modular blocks, with a straightforward main block outlining the sequence of steps to be executed and their respective order. This structured approach simplifies the process of defining and executing tasks, enhancing the efficiency and effectiveness of RAVEN's artificial intelligence-driven operations.

RAVEN features specific interfaces to exchange information with a number of widely used codes (e.g. MAAP, MELCOR, MODELICA, RELAP); the codes that do not have a dedicated interface yet can also be used through a generic interface. As an alternative, following the open source approach, users can

develop their own specific interfaces that, after thorough tests, can be integrated in the RAVEN package. RAVEN – ASTEC coupling is described as follows:

— Starting from the generic interface of RAVEN, a dedicated interface for the RAVEN-ASTEC coupling was developed and the Python file included in the RAVEN source code. A dedicated ASTEC input-deck has also to be prepared for the codes coupling, and to allow RAVEN to retrieve the information needed to modify the ASTEC input-deck and to run the calculations on the cluster high performance computing platform. The main input information on the uncertainty quantification analysis has also to be specified in the RAVEN input XML file. In particular, it contains:
  - The list of uncertain input parameters with their ranges and PDFs type;
  - Information on the sampling of input parameters (e.g. sampling strategy; number of calculations; number of calculations to be run in parallel);
  - The list of FOMs selected and the statistical analyses to be performed;
  - In case of implementation on a cluster, all the instruction for the communication with the high performance computing infrastructure.

— With this information, RAVEN drives the uncertainty quantification process. The ASTEC-RAVEN coupling workflow for uncertainty quantification is summarized in Fig. 9, according to [27]:
  - RAVEN samples the values of the selected input uncertain parameters;
  - It generates a set of input decks by using the sampled values;
  - It runs the code calculations communicating with the computer infrastructure;
  - It collects the results and performs the statistical analysis.

In addition, to expand the statistical analysis, the post-processing of the data results collected by RAVEN is performed by directly using Python statistics libraries [26].

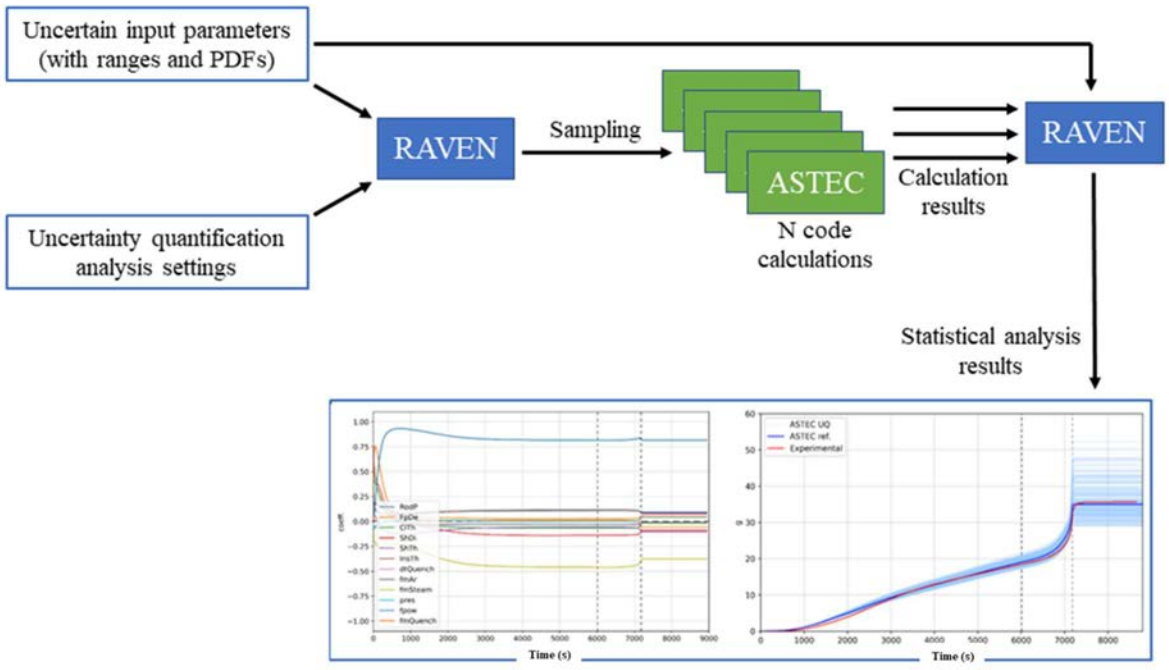

FIG. 9. ASTEC–RAVEN coupling workflow for uncertainty and sensitivity analysis.

3.3.2. Selection of the uncertainty input parameters and assessment of the related probability distributions

The uncertain input parameters to be used in the uncertainty quantification analysis have been provided to the ENEA team by KIT, along with their corresponding ranges of variations, PDFs type and reference values. The 23 input uncertain parameters described in Section 2.3 have been employed. Table 9 shows the ASTEC reference values of the integrity criteria and heat exchange models' parameters.

TABLE 9. ASTEC REFERENCE VALUES

#	Parameter	Reference value
15	Threshold thickness (μm)	300
16	Failure temperature of ZrO_2 layer (K)	2374
17	Rod anisotropic factor	0.5
18	Shroud anisotropic factor	0.15
19	Heat transfer coefficient due to droplet projection	100
20	Height above the quench front concerned by droplet projection	0.8
21	Threshold void fraction to allow exchange with liquid droplets	0.999
22	Max. ratio of permeability/viscosity	0.1
23	Min. liquid fraction allowing material relocation	0.0

The FOMs selected for the uncertainty quantification are the ones proposed by KIT (Section 2.3), except for FOM5, where the internal ring heated rod has been considered instead of the average:

1) Total mass of accumulated H_2 (kg);
2) Temperature of the central fuel rod simulator at elevation 950 mm (K);
3) H_2 generation rate (kg/s);
4) Axial profile of the oxide scale of the corner rod at 6620 s (μm);
5) Axial profile of the oxide scale of the internal ring heated rod at the end of the scenario (μm).

3.4.RESULTS OF NOMINAL CASE

The analysis and description of the code results against the experimental data have been carried out by considering three main phases:

- Pre-oxidation phase: from the start of the transient (0 s) to 6011 s, when the electric power applied to the heated-up rods begins to be ramped;
- Heating up phase: from the beginning of electric power increase (6011 s) to the first injection of water (7179 s);
- Quenching phase: from the pre-injection of water (7179 s) to the end of the test (9000 s).

Relevant parameters are considered to evaluate the reference calculation results:

- H_2 total mass produced;
- H_2 production rate;
- Cladding temperature of heated rods (inner and outer rings) at the most heated elevation;
- Temperature of corner rods at the most heated elevation;
- Temperature of shroud at the most heated elevation;
- ZrO_2 thickness axial profile of extracted corner rod, at the extraction time;
- ZrO_2 thickness axial profile of heated rods cladding, at the end of test;

— ZrO_2 thickness axial profile of corner rods, at the end of test;
— ZrO_2 thickness axial profile of shroud, at the end of test

3.4.1. Pre-oxidation phase

At the start of the transient (t = 0 s) the argon and steam sources (around 3 g/s) are activated as well as the stepwise increase of power in the heated rods. In the experiment the power is calibrated to reach a maximum cladding temperature of 1474 K; and then to keep it for 4046 s. In the ASTEC calculation the power is imposed by using the experimental data as reference. Figures 10–13 show the temperatures evolution of the corner rod, the inner and the outer heated rods cladding and the shroud temperature, respectively. The ASTEC calculated temperatures are compared to the temperatures of the thermocouple's measurements (inner heated rods: TFS 2/13, TFS 3/13; outer heated rods: TFS 4/13, TFS 5/13; corner rod: TIT A/13, shroud: TSH 13/270, TSH 13/90), at the elevation of 950 mm, expected to be the most heated-up level along the transient. In the figures, the three phases are highlighted with vertical dashed line, 6011 s and 7179 s. Since the bundle components are modelled as azimuthal symmetric objects by ICARE, only one temperature is reported at each different elevation. In the experiments there are often two thermocouples per component at the same elevation at different azimuthal angles. In this case both the experimental temperatures are compared to code results.

During the electrical steps heating-up of the bundle (0–2000 s), heat is transferred from heated rods to all system components, and all internal structures are brought up to temperature close to 1500 K (at the 950 mm elevation. In around 3000 s, quasi-steady conditions are reached and maintained until the end of the pre-oxidation phase. For the corner road temperatures, as shown in Fig. 10, a discrepancy of maximum 100 K between the experimental measurements and the code results are observed at the beginning of plateau (at ~3000 s). A similar but smaller difference is obtained for the temperature of the inner ring rod cladding (maximum of 80 K, with the south-east thermocouple), as seen in Fig. 11. For the outer heated rods cladding shown in Fig. 12, and shroud temperatures shown in Fig. 13 a quantitative agreement between the experimental and calculated values is observed. The calculated temperatures seem to take more time to reach the higher temperatures needed to give the steady conditions.

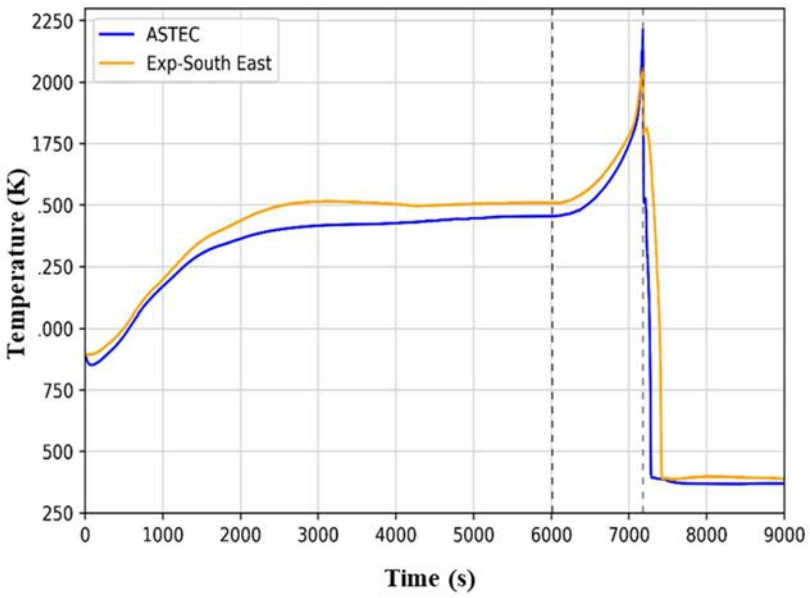

FIG. 10. Corner rod temperature from experimental data (TIT A/13) and code calculation, at 950 mm of elevation.

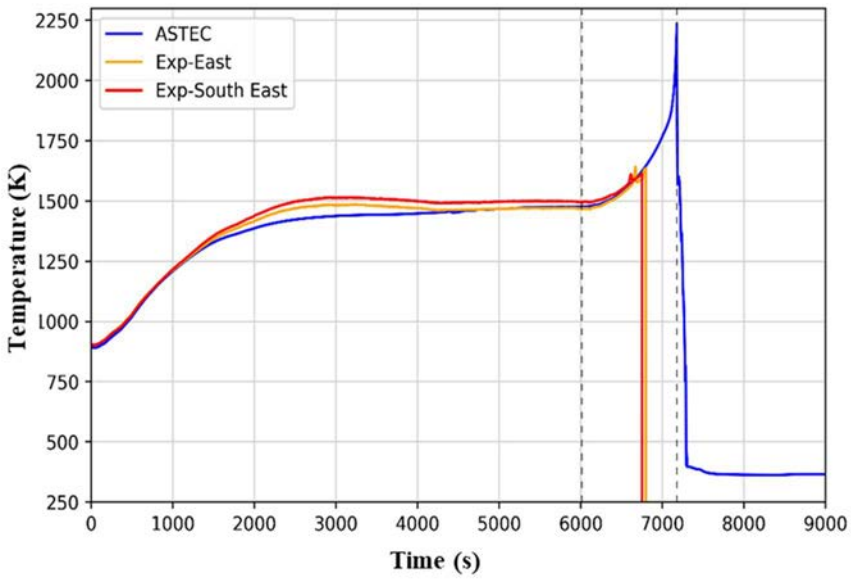

FIG. 11. Inner ring heated rod cladding temperature from experimental data (TFS 2/13, TFS 3/13) and code calculation, at 950 mm of elevation.

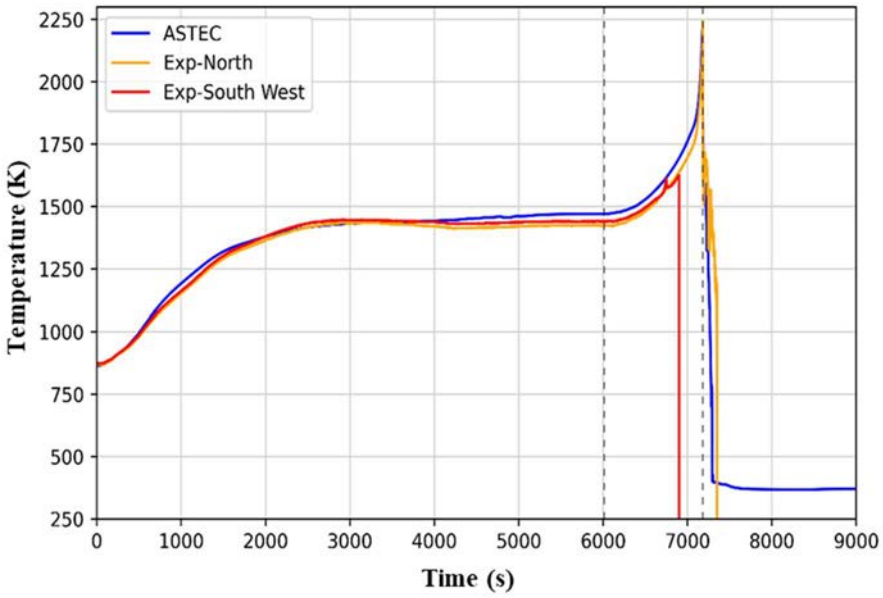

FIG. 12. Outer ring heated rod cladding temperature from experimental data (TFS 4/13, TFS 5/13) and code calculation, at 950 mm of elevation.

Figure 14 shows total H_2 mass produced along the transient and Fig. 15 shows H_2 production rate (g/s). The experimental data are obtained by the mass spectrometer located downstream the test bundle.

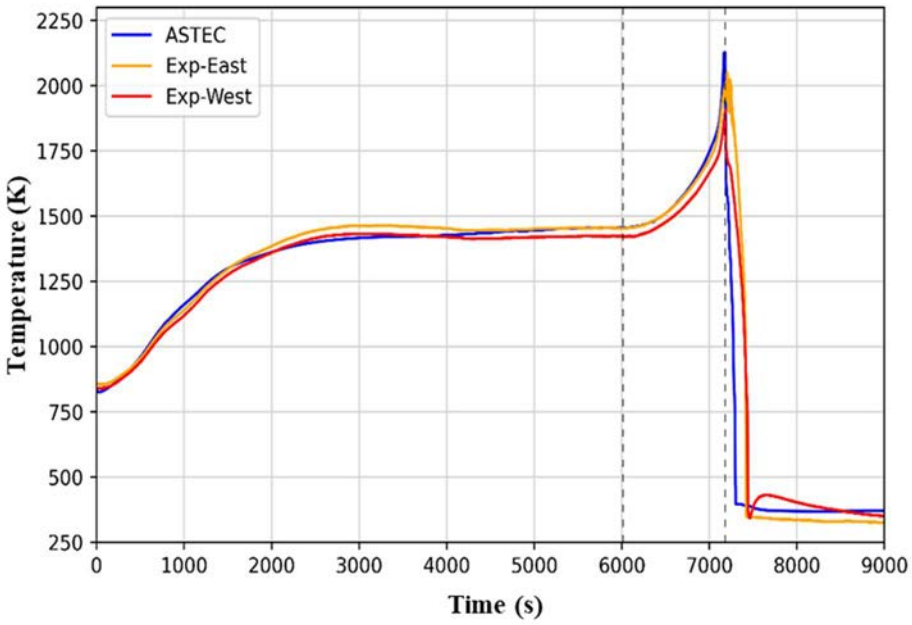

FIG. 13. Shroud temperature from experimental data (TSH 13/270, TSH 13/90) and from calculation, at 950 mm of elevation.

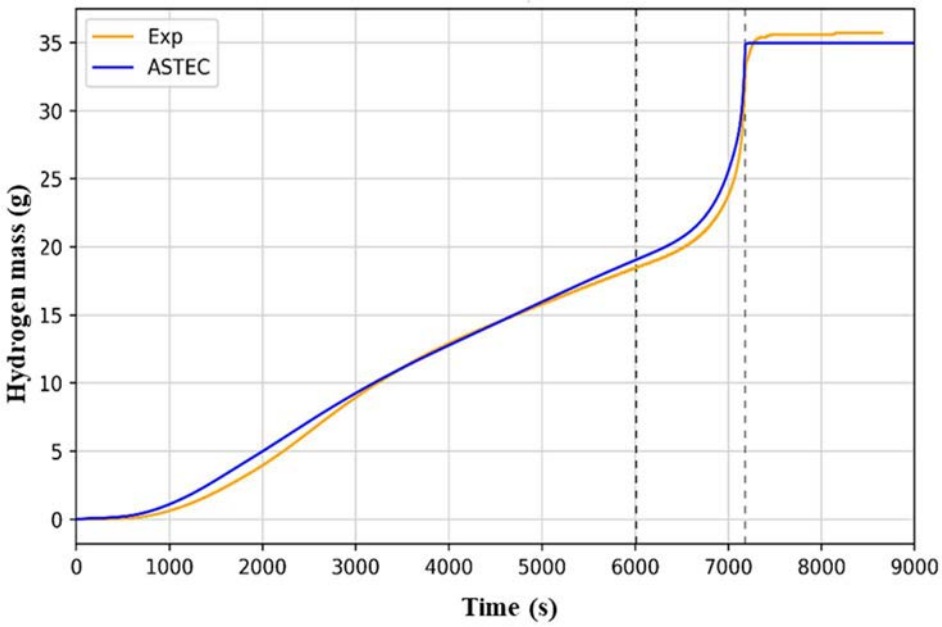

FIG. 14. H_2 cumulated production from experimental data and code calculation.

During the pre-oxidation phase the production rate of H_2 (Fig. 15), and thus the Zircaloy oxidation processes, features a first quasi linear increase which follows the temperature increment in the heat-up of the bundle. After about 2500 s, the production rate reaches a local maximum and then decreases during the constant temperature phase. The H_2 production rate decreasing at constant temperature (constant oxidation conditions) is caused by the Zr oxidation kinetics. The oxidation is driven by the O_2 diffusion in the ZrO_2 layer, whose thickness increases during the oxidation phase. The ASTEC simulation shows a qualitative prediction of this phenomenon. The H_2 production maximum in the code results occurs around 200 s earlier and is 0.001 g/s lower (Fig. 15).

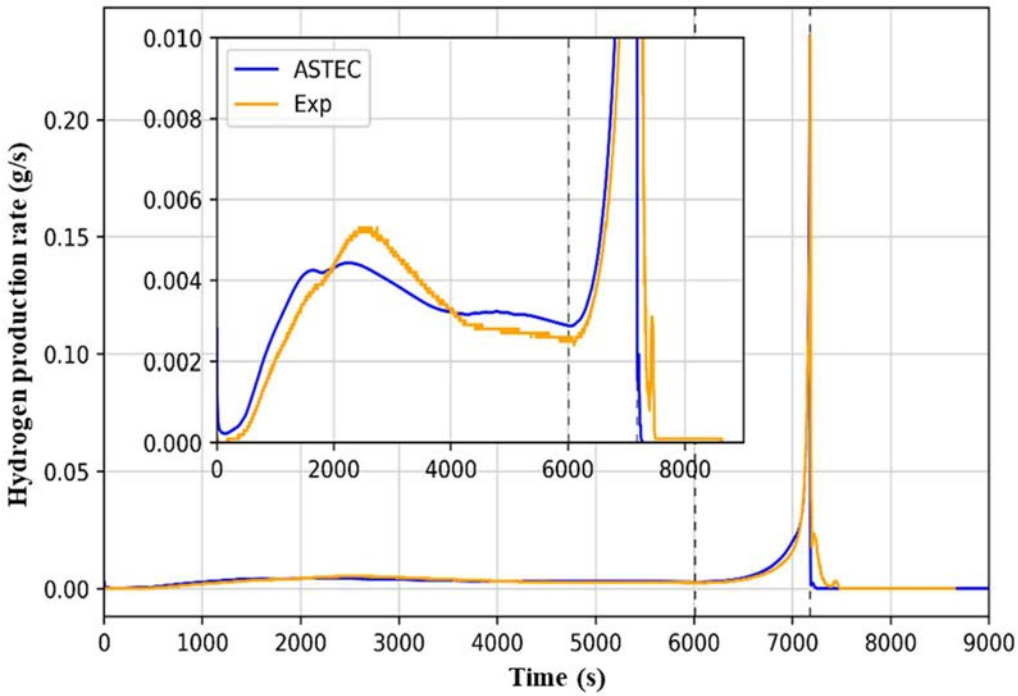

FIG. 15. H_2 production rate from experimental data and code calculation.

The accumulated H_2 mass produced at 6010 s, at the end of the pre-oxidation phase, is 18.5 g obtained in the experiments and 19.0 g obtained in the simulation. In Fig. 16 the ASTEC graphical representation of temperature distribution in the bundle components is shown, at the start of the transient and at the end of the pre-oxidation phase. A general heat up is present between the two timings and the maximum temperatures axial level is at approximately 950 mm as expected from the experiment.

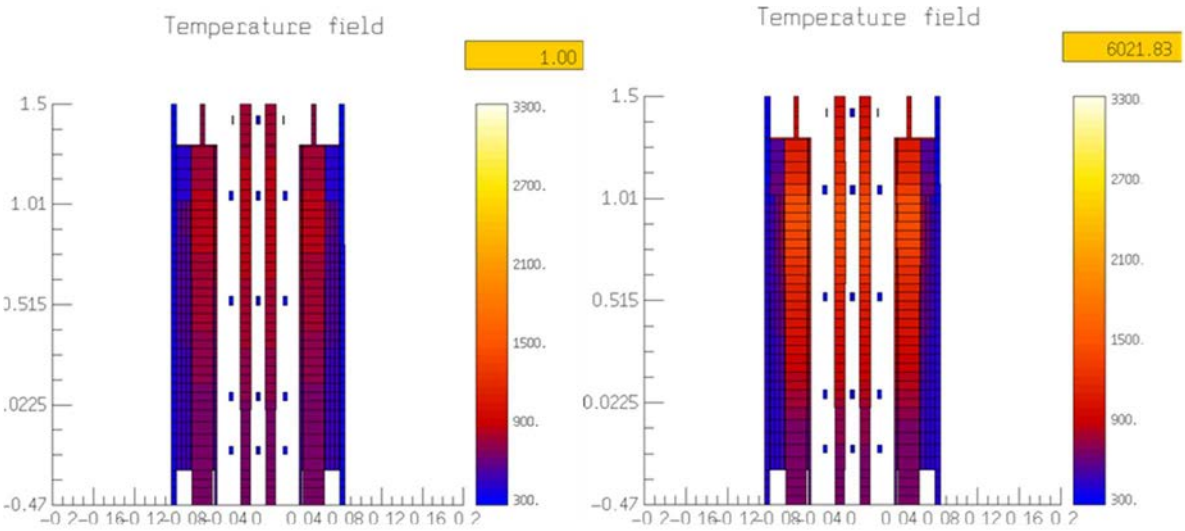

FIG. 16. ASTEC masks of temperature distribution, for t = 1 s and t = 6021 s.

3.4.2. Heating-up phase

The heating-up phase is considered to start at 6011 s, once the electric power applied to the heated rods is ramped with an increase rate of 0.3 W/s per rod (Fig. 8). The temperatures evolution of the inner and the outer heated rods cladding, the corner rod and the shroud, at 950 mm of elevation, from 6011 s (onset of heating up phase) to 7600 s are shown in Figs. 17–20. Unfortunately, some thermocouples failed during the heating up [1].

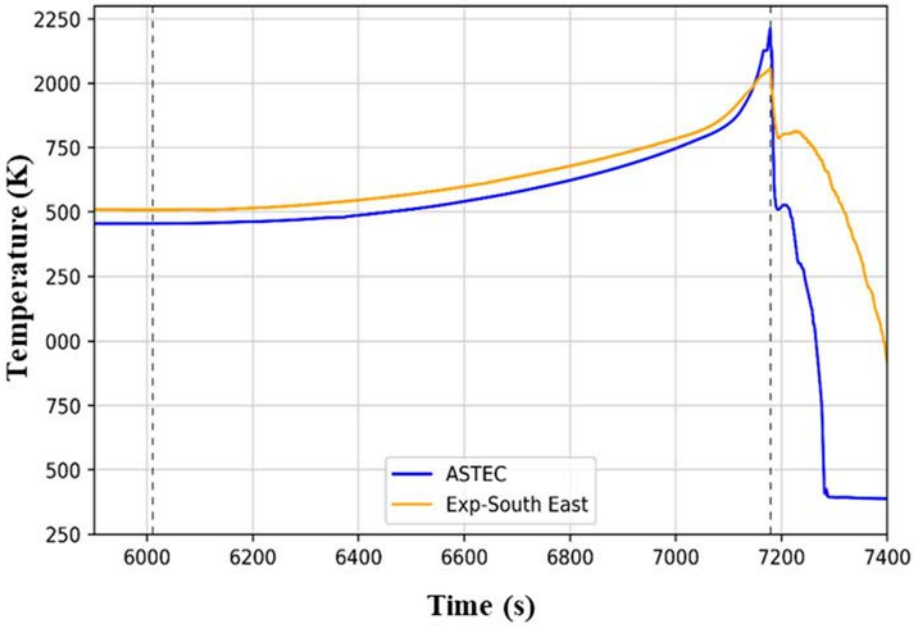

FIG. 17. Corner rod temperature from experimental data (TIT A/13) and code calculation at 950 mm elevation (heating up phase).

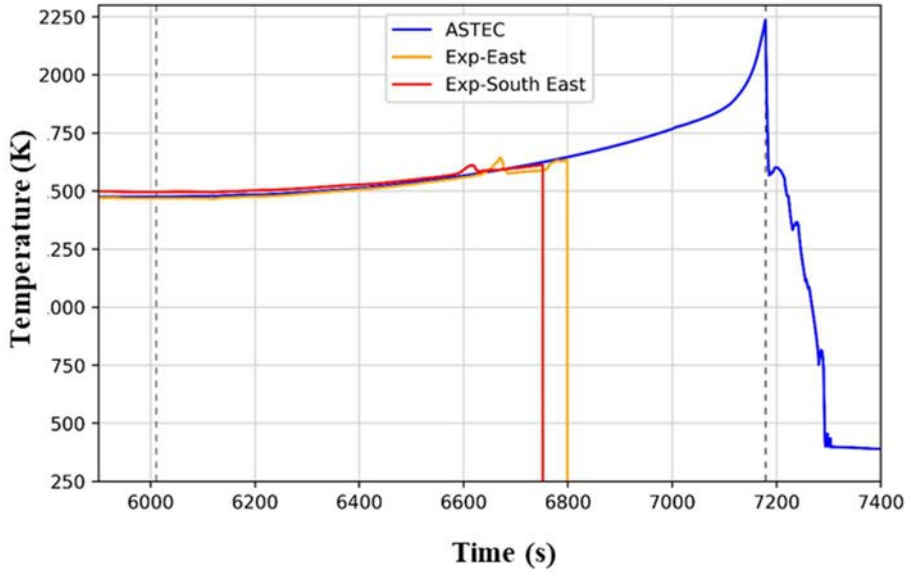

FIG. 18. Inner ring heated rod cladding temperature from experimental data (TFS 2/13, TFS 3/13) and code calculation at 950 mm elevation (heating up phase).

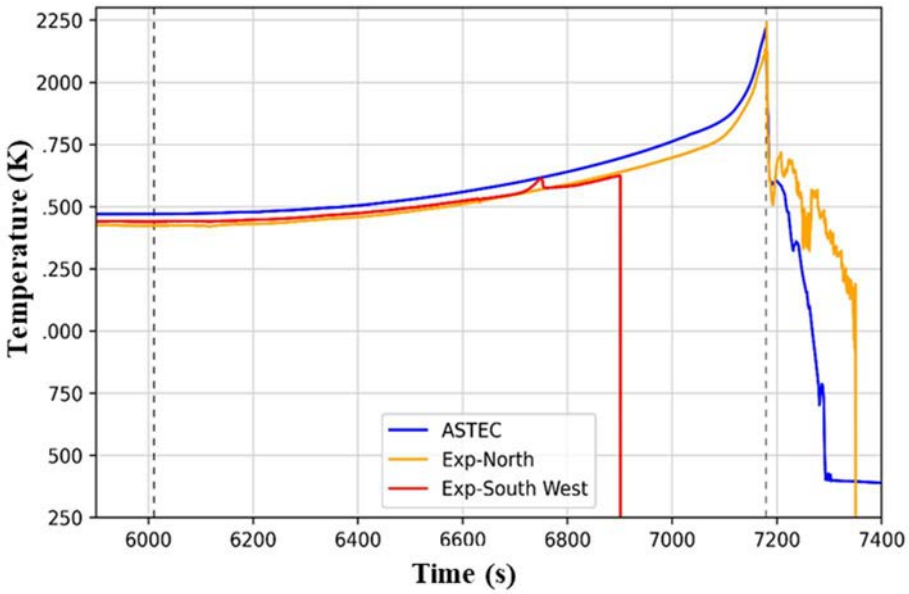

FIG. 19. Outer ring heated rod cladding temperature from experimental data (TFS 4/13, TFS 5/13) and code calculation, at 950 mm of elevation (heating up phase).

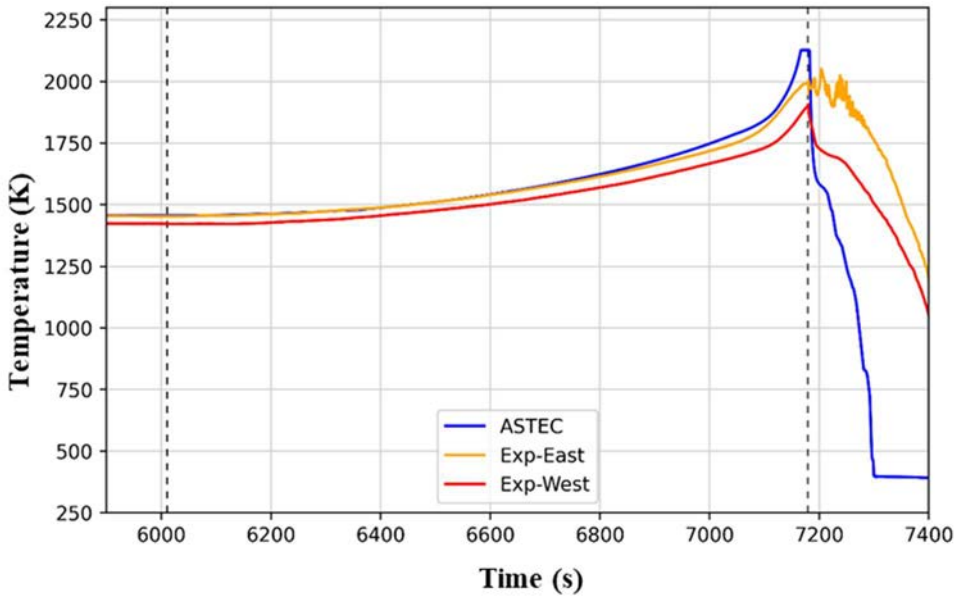

FIG. 20. Shroud temperature from experimental data (TSH 13/270, TSH 13/90) and code calculation, at 950 mm of elevation (heating up phase).

In both experimental data and the ASTEC simulation, the structures temperature starts to increase after around 200 s from the onset of the heating up. At this point the rods temperatures increase at a rate close to 0.32 K/s, which is kept between 1450 K and 1750 K, in calculation as well as in the experiment. Once temperature reaches 1770 K, the oxidation processes accelerate due to reaction runaway; the steep escalation of the component temperature then takes place.

The temperature escalation is best fitted by the code calculation in the outer ring fuel rods as can be seen in Fig. 19, where the temperature peaks at 7179 s are very close (about 2250 K). The corner rod experimental temperature (Fig. 17) and the shroud experimental temperature (Fig. 20) feature a slower

acceleration than the one calculated by ASTEC, ending up to a final lower temperature peak. The H_2 production rate and the total mass produced are shown in Figs. 21 and 22, respectively.

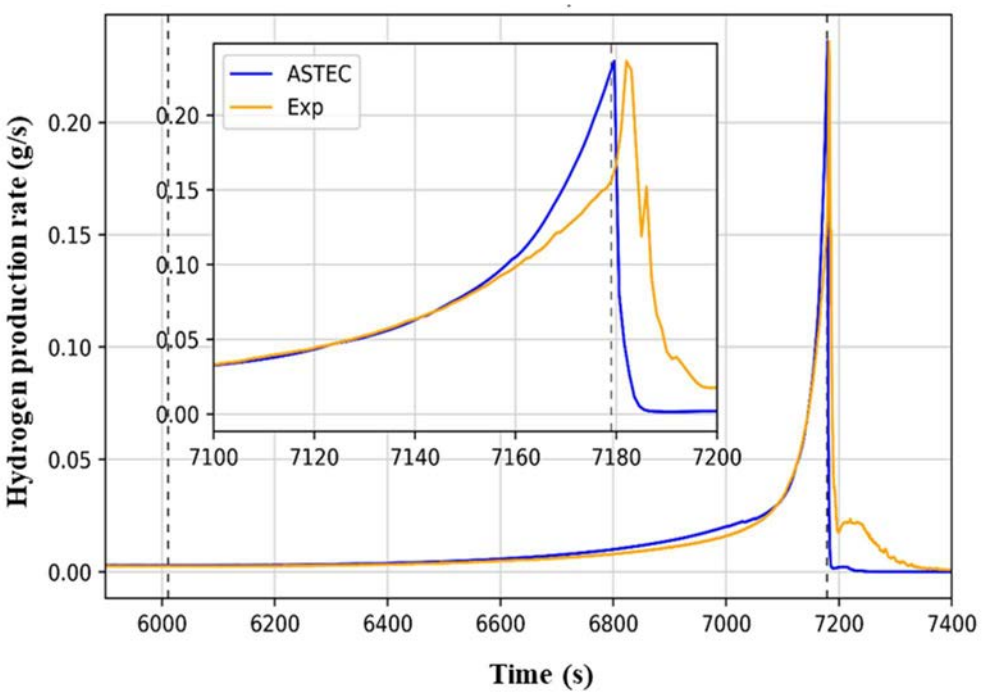

FIG. 21. H_2 production rate from experimental data and code calculation (heating up phase).

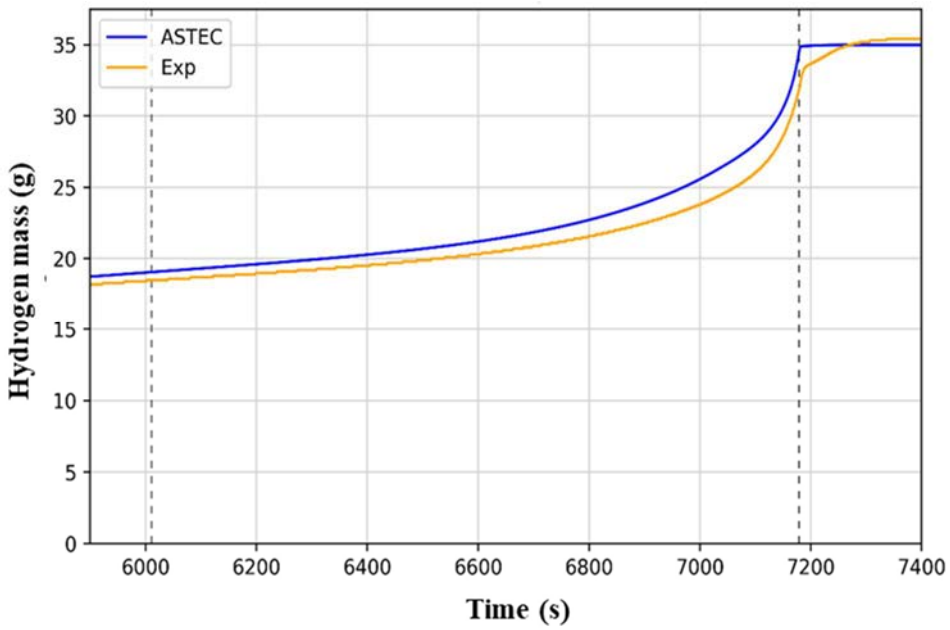

FIG. 22. H_2 cumulated mass produced from experimental data and code calculation (heating up phase).

It can be seen from Fig. 21 that the H_2 production rate is well predicted by the code until the acceleration of the oxidation rate (at about 7100 s). However, in the last 20 s of oxidation before the quenching time, the code predicts larger reaction acceleration, in agreement with the temperature behaviour, giving a higher H_2 production at the end of the heat-up phase. The calculated production rate peak is 0.23 g/s,

almost at the quenching time (0.5 s later). The experimental H_2 production rate at quenching time is 0.17 g/s, while the production peak of 0.23 g/s is obtained 3 s later. It is important to note that the H_2 generation rate predicted by the code is obtained at the exact instant of production, while the experimental detection of this parameter may have some seconds of delay with respect to the real production in the bundle. Indeed, due to its location, the mass spectrometer "GAM 300" could have a delay of 5 s [1].

The accumulated H_2 mass calculated at the end of the heating-up phase (7179 s) remains slightly higher with total value of 35 g, compared to the experimental value of 33 g. Figure 23 shows the ASTEC graphical representation of the temperature distribution along the bundle components, at the onset and at the end of the heating up phase. A general heat up can be observed between the two timings and the temperatures reaching the highest values at approximately 950 mm of elevation, as in the experiment.

During the heating-up phase, at 6620 s, one of the four corner rods is removed in the experiment to study the rod oxidation state at the beginning of the heating-up phase. In Fig. 24 the ZrO_2 thickness profile along the extracted corner rod elevation is plotted against the simulation result. From the experimental ZrO_2 profile comparison with the ASTEC results, in Fig. 24, the same qualitative profile is observed. The maximum oxidation level is at about 950 mm of elevation for both the experimental and the calculation values, showing the agreement on the most heated up and therefore oxidized elevation along the bundle. The ZrO_2 thickness at 950 mm is close to 200 µm for the experimental data and about 180 µm in the code calculation. At lower elevations (between 200 mm and 800 mm) the code predicts a thicker oxidation layer than the experimental results. Figures 25 and 26 show the calculated material composition of the bundle components at 6620 s (control rod extraction) and the oxidation of all Zr components peak at around 950 mm, respectively.

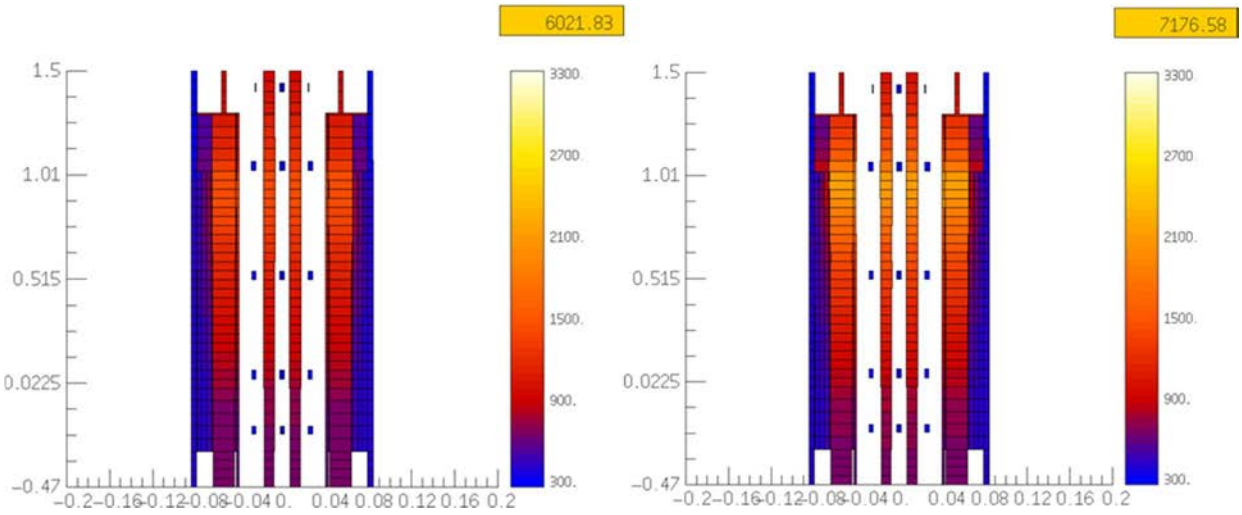

FIG. 23. ASTEC masks of temperature distribution, for t = 6021 s and t = 7176 s.

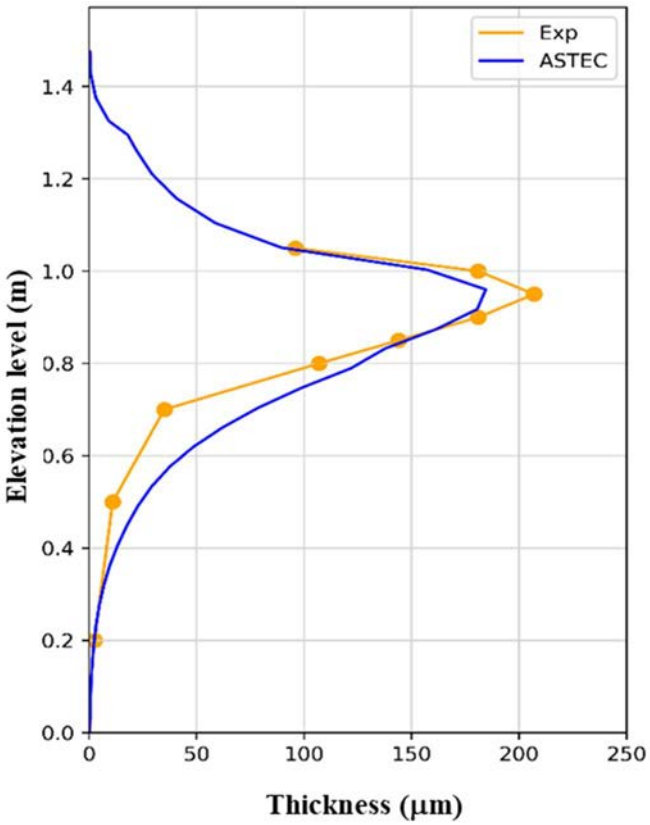

FIG. 24. ZrO_2 thickness profile of the corner rod extracted (control road B) at 6620 s.

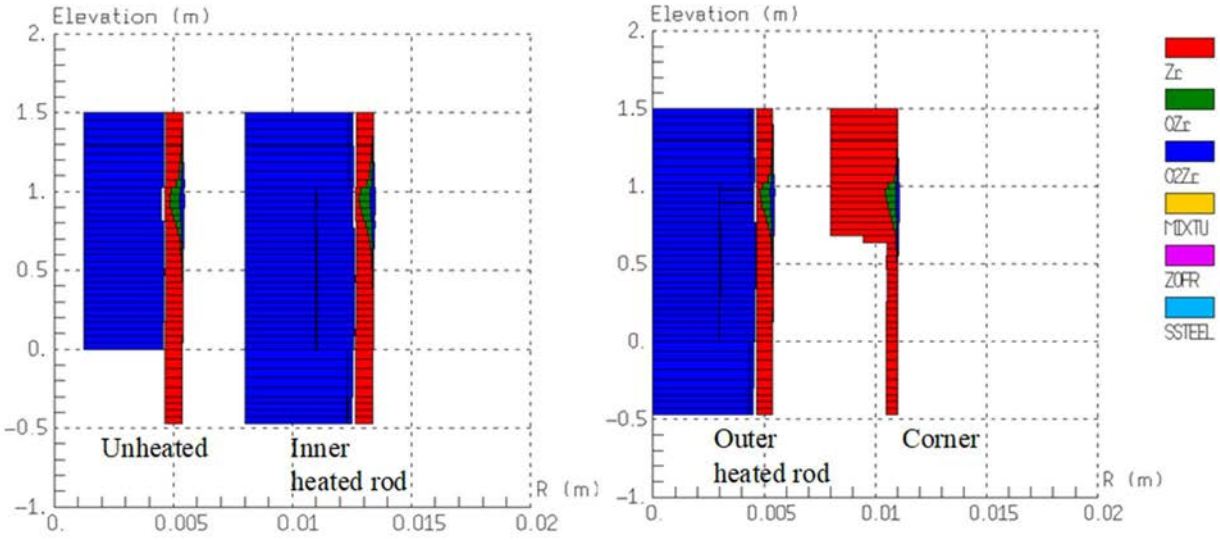

FIG. 25. ASTEC results materials of unheated and inner-ring heated rods (left); materials of outer-ring heated rod and corned-rod (right), at 6620 s.

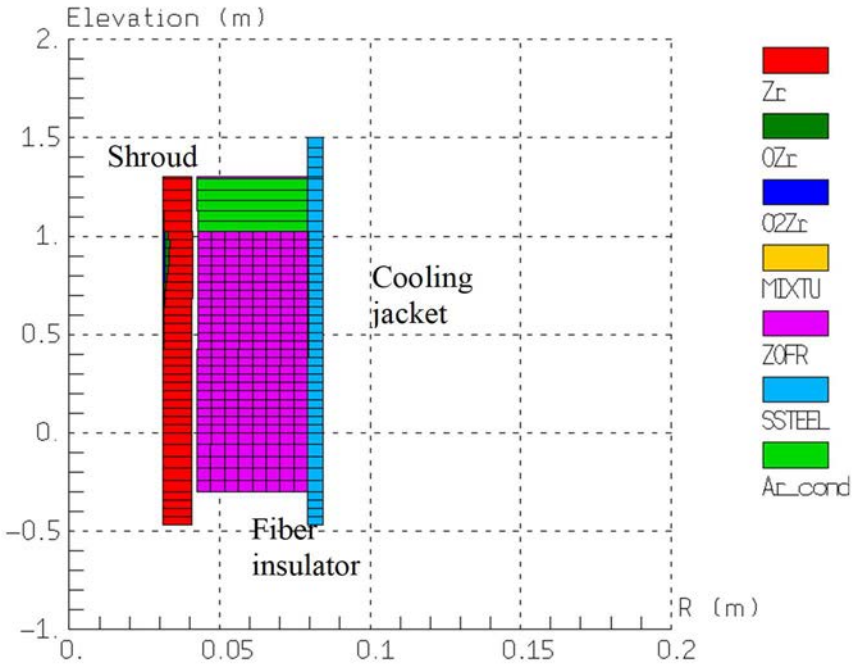

FIG. 26. ASTEC results materials of shroud at 6620 s.

3.4.3. Quenching phase

At the onset of the quenching phase (7179 s) the argon source is moved to the top of the channels, the steam source is turned off and the pre-injection system is activated for water injection to the bottom inlet; 26 s later, the electric power is reduced from 18.2 kW to 4 kW, within a ramp of 16 s. At 7215 s the main injection system begins to pump water in the bundle from the bottom end (see Fig. 5). Based on the experiment the shroud and some of the heated rods fail at the quenching time. As it is confirmed in post-test direct observation of components, the localized melting of both the shrouds and of some of the heated rods occurs at the elevation of ~950 mm and determines the relocation of a limited mass of melted material [1].

Figures 27 and 28 show the compositions of the bundle components at the quenching time (which is the same at the simulation end) as predicted by ASTEC. It can be observed that the code predicts the local melting of Zr in the shroud and in the corner rods at around 950 mm of elevation. Yet, the presence of solid ZrO_2 and ZrO layers make that the loss of integrity conditions set in the input (Section 2.3) are never reached during the test, and this prevents any relocation of material. Based on the post-experiment analysis of the components, it is observed that the failure takes place without considerable core damages (no considerable core geometry modification and mass relocation) and, consequently, only a negligible internal cladding oxidation takes place. Therefore, neglecting the limited relocation of melt and few internal cladding oxidations, the ASTEC calculation is not in disagreement with the experiment.

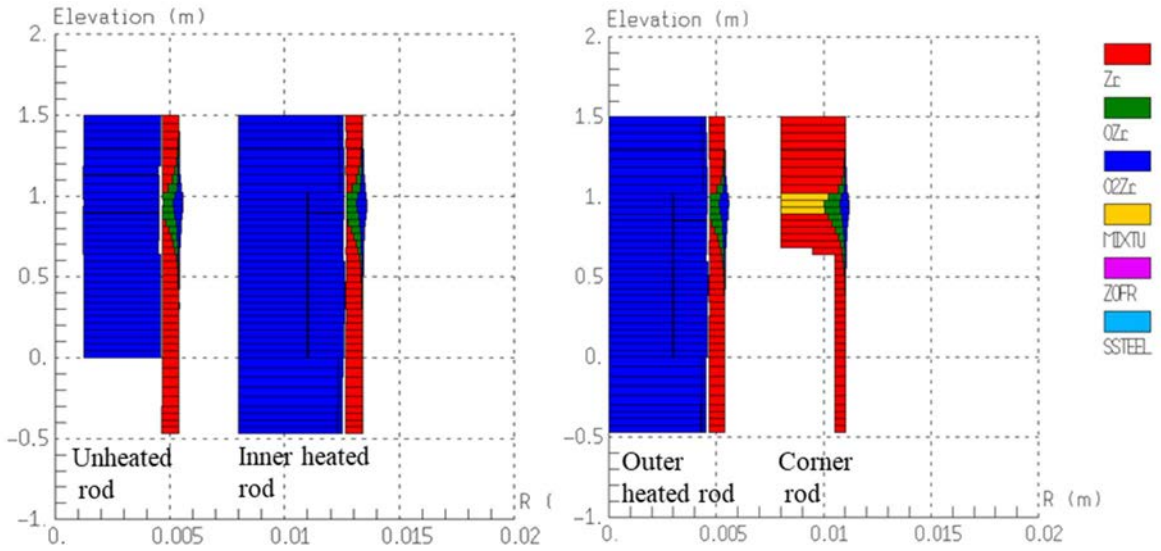

FIG. 27. ASTEC results materials of unheated and inner-ring heated rods (left); materials of outer-ring heated rod and corned-rods (right), at 7179 s.

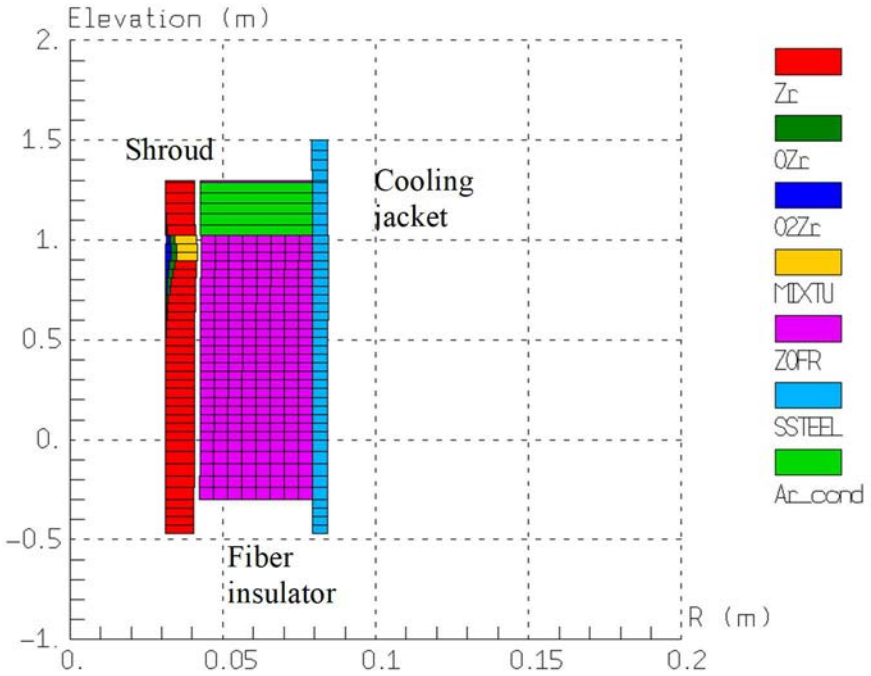

FIG. 28. ASTEC results materials of shroud at 7179 s.

The ASTEC calculated temperatures of the inner and the outer heated rods cladding, the corner rod and the shrouds, at 950 mm of elevation in comparison with the experimental data are shown in Figs. 29–32. The selected time is 7100 s–7500 s allowing to focus on the quenching phenomena. In each figure the quenching time (pre-injection time), the power reduction time and the main injection onset time are indicated within vertical lines.

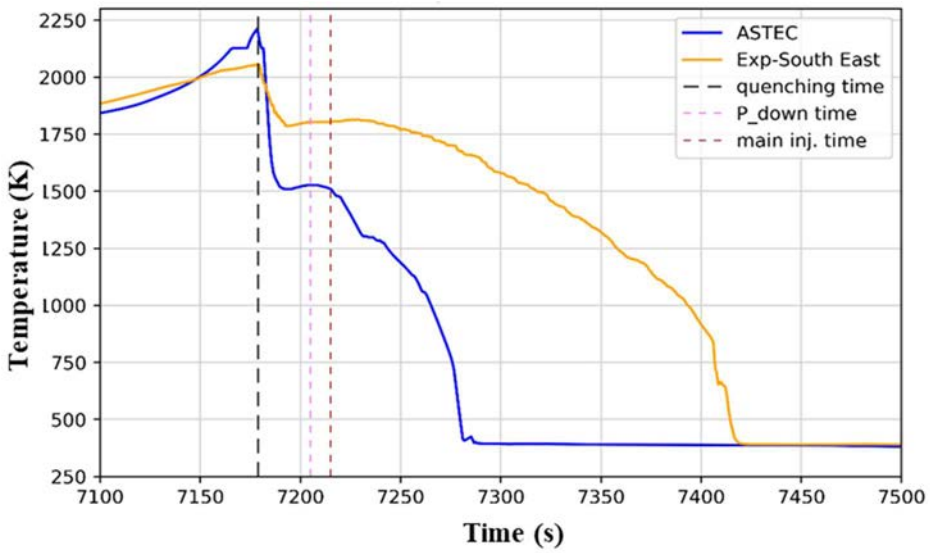

FIG. 29. Experimental (TIT A/13) and calculated corner rod temperature at 950 mm of elevation (quenching phase).

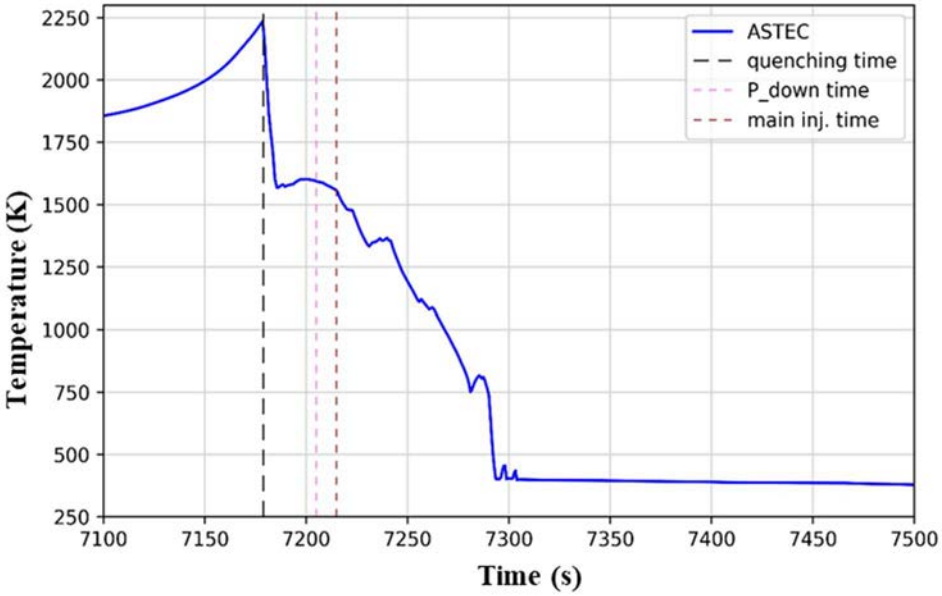

FIG. 30. Experimental (TFS 2/13, TFS 3/13) and calculated inner ring heated rod cladding at 950 mm of elevation (quenching phase).

For the corner rod and the heated rods cladding, a qualitative agreement in the temperature evolution can be observed between the code and the experimental values; the first fast quench cooling takes place right after the pre-injection, leading to temperatures to decrease by several hundred degrees in ~ 15 s. The fast drop in temperature (quenching) due to the pre-injected water, is followed by a slight increment of the cladding temperature between the end of the pre-injection and the beginning of the main injection. The second cooling phase is caused by the main cooling water injection; being slower moderate cooling it ends with nearly the saturation temperature of the coolant at the system pressure. The code predicts higher quenching for the corner rods temperatures (Fig. 29), while the agreement is better for the heated rods (Figs. 30 and 31). However, in both cases, the code predicts faster second cooling, leading to the final temperature at120 s earlier than observed in the experiment. Also, for shroud temperature at 950

mm (Fig. 32), ASTEC predicts faster cooling, reaching the final temperature almost 150 s earlier. No experimental data are available for the inner ring heated rods temperature at 950 mm of elevation.

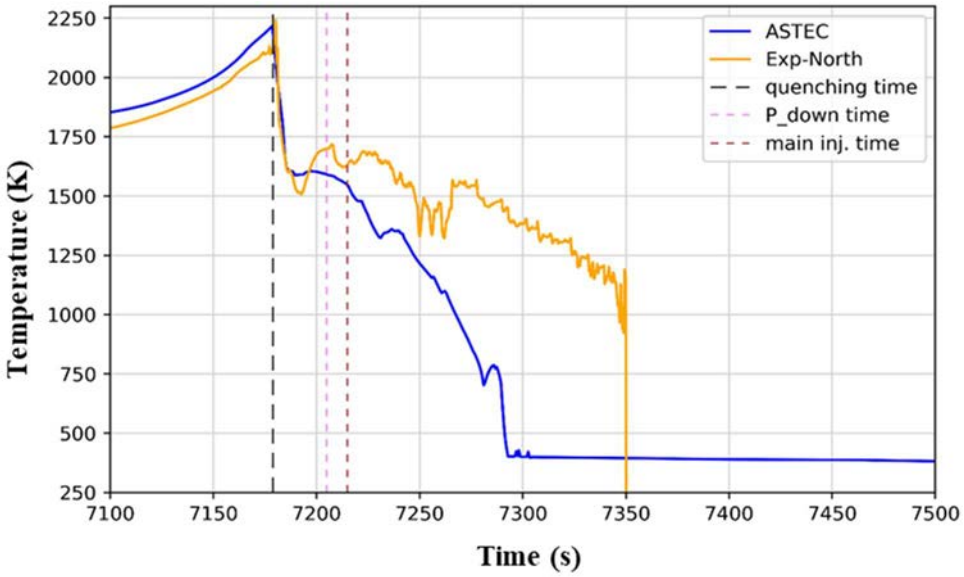

FIG. 31. Experimental (TFS 4/13, TFS 5/13) and calculated outer ring heated rod cladding temperature at 950 mm of elevation (quenching phase).

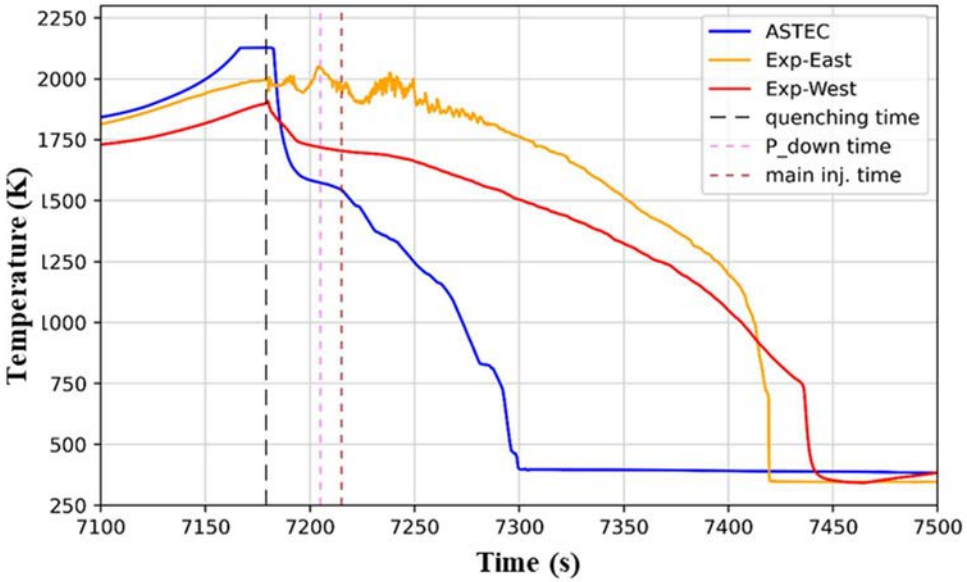

FIG. 32. Experimental (TSH 13/270, TSH 13/90) and calculated shroud temperature at 950 mm of elevation (quenching phase).

The H_2 production rate in the range 7100–7500 s (quenching phase) is shown in Fig. 33. The code predicts rapid decrease in H_2 production after the quenching onset, reaching almost zero net production in a few seconds. Considering a delay of 5 s in the experiment on detecting the H_2, the drop in the production rate due to the quenching is close to the calculated value. However, in agreement with the temperatures behaviour, the experiment shows an average production rate of 0.02 g/s which is kept for around 140 s. The total amount of H_2 mass produced, shown in Fig. 22, indicates that at the end of the test an overall mass is slightly higher, around 1 g.

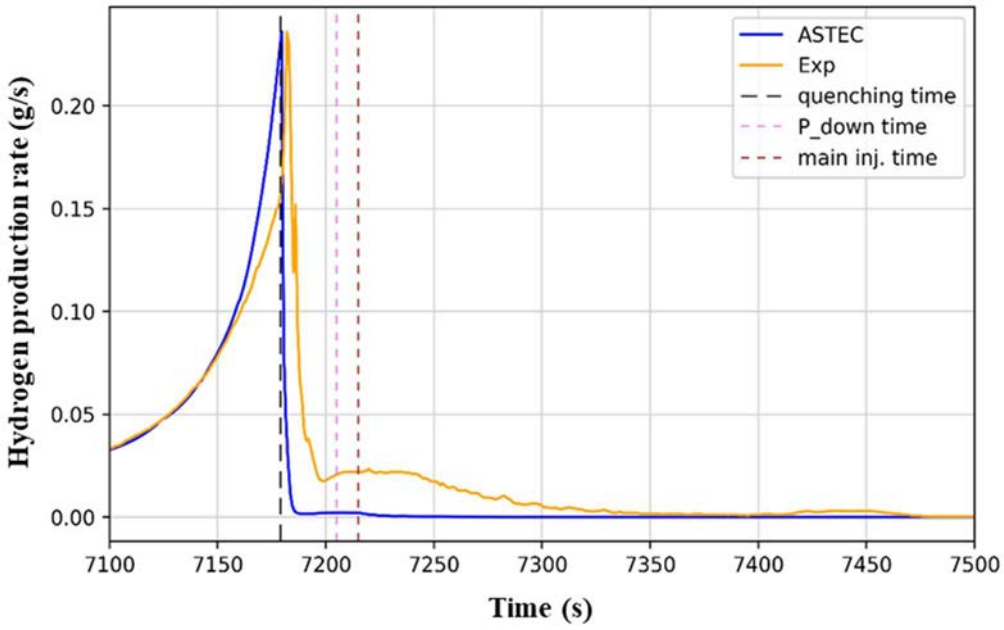

FIG. 33. Experimental and calculated H_2 production rate (quenching phase).

The liquid level measured in the experiment (Lm 501: differential pressure measurement between bottom and top of the bundle) and the calculated collapsed level in two fluid channels are shown in Fig. 34. Both results show that the first water level peak due to the pre-injection, and a water level increase following the onset of the main water injection. The results show good prediction of the liquid mass evaporation during the transient.

The ASTEC temperature distribution in the bundle components, and the void fraction along the fluid channels at different instants are shown in Figs. 35–41. The timings are:7176 s at the end of heating up phase, 7181 s (during the pre-injection and quenching,7187 s at the end of pre-injection,7215 s at the onset of main injection,7240 s for power reduced to 3.9 kW, 7280 s main injection at zero.

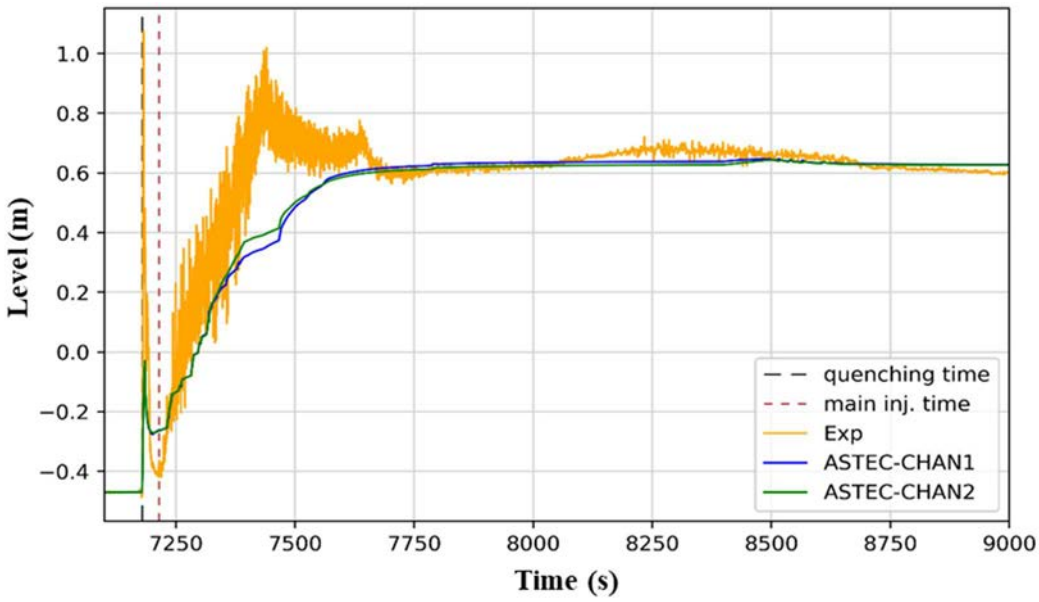

FIG. 34. Liquid level measured in the experiment (Lm 501) and calculated collapsed level in channels 1 and 2.

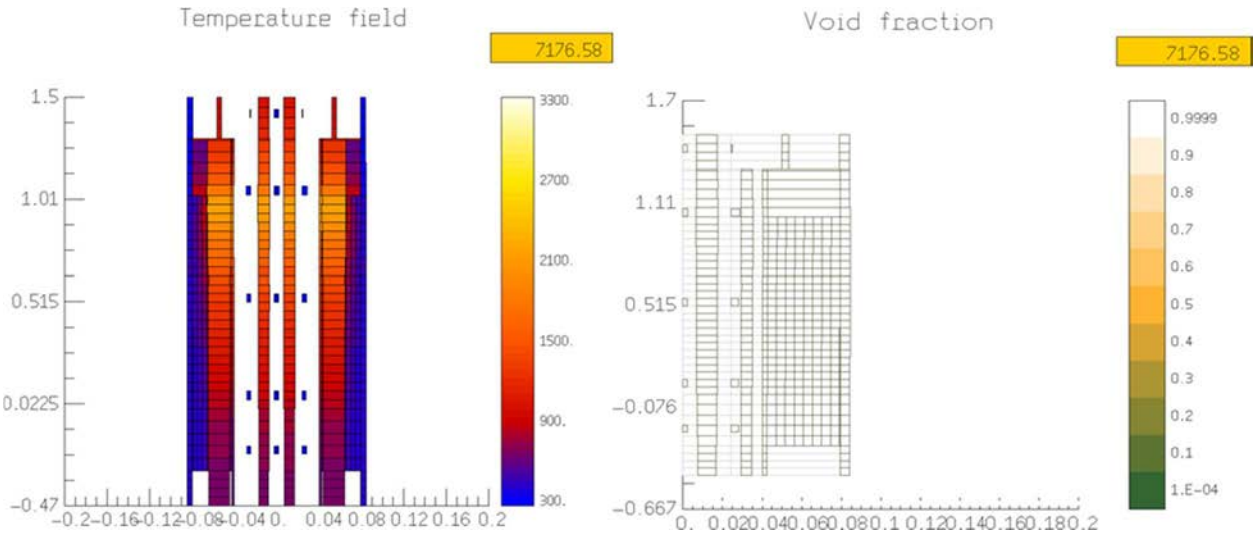

FIG. 35. ASTEC temperature distribution and void fraction in the bundle at 7176 s.

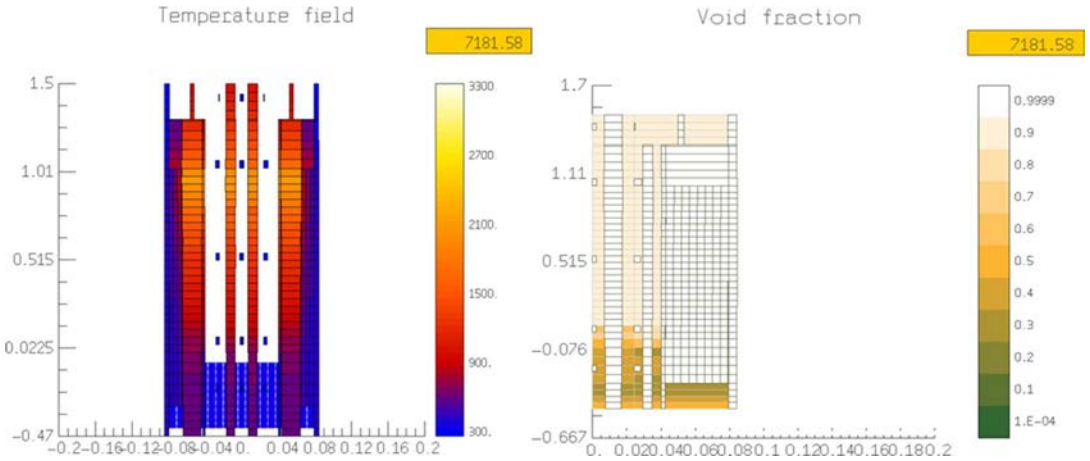

FIG. 36. ASTEC temperature distribution and void fraction in the bundle at7181 s.

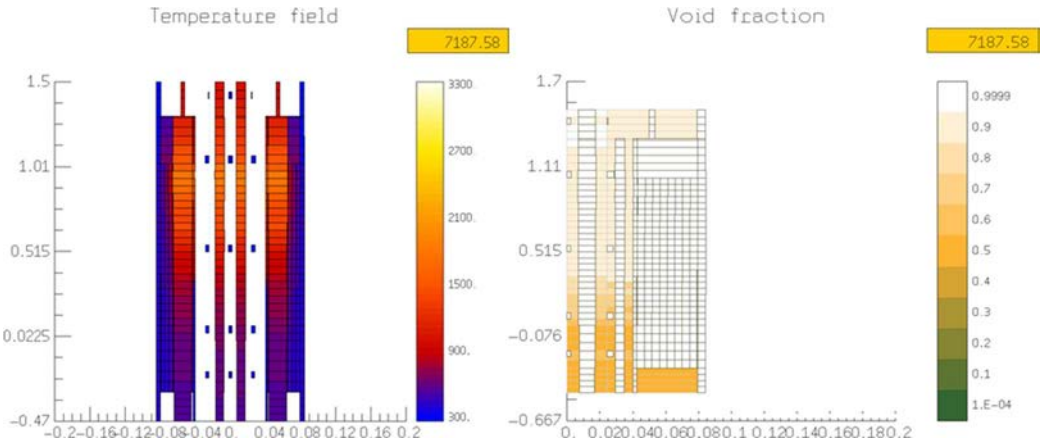

FIG. 37. ASTEC temperature distribution and oid fraction in the bundle at7187 s.

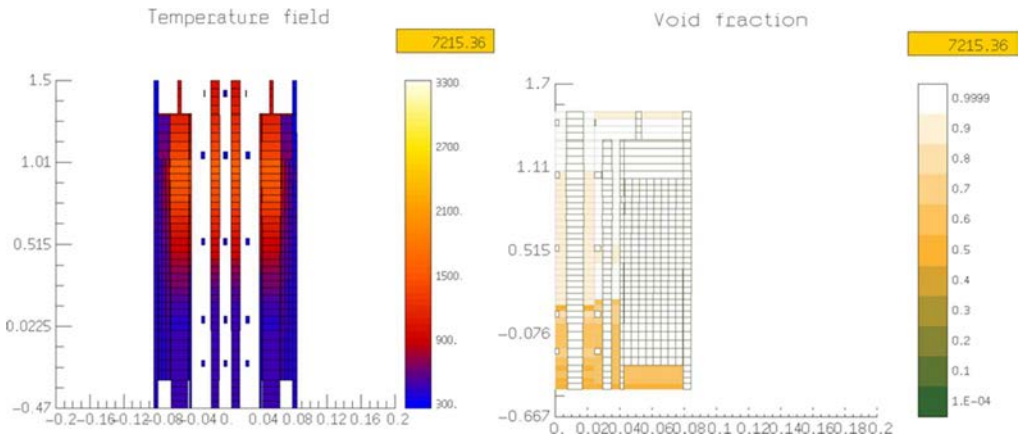

FIG. 38. ASTEC temperature distribution and void fraction in the bundle at7215 s.

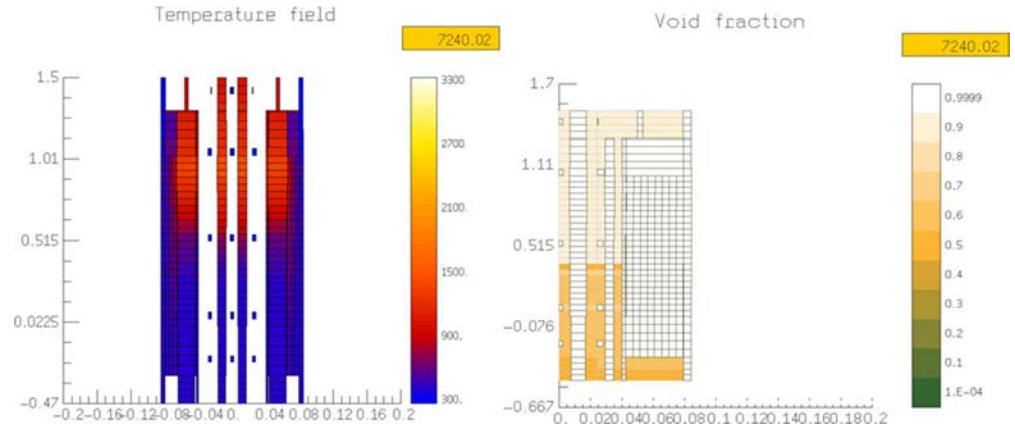

FIG. 39. ASTEC temperature distribution and void fraction in the bundle at7240 s.

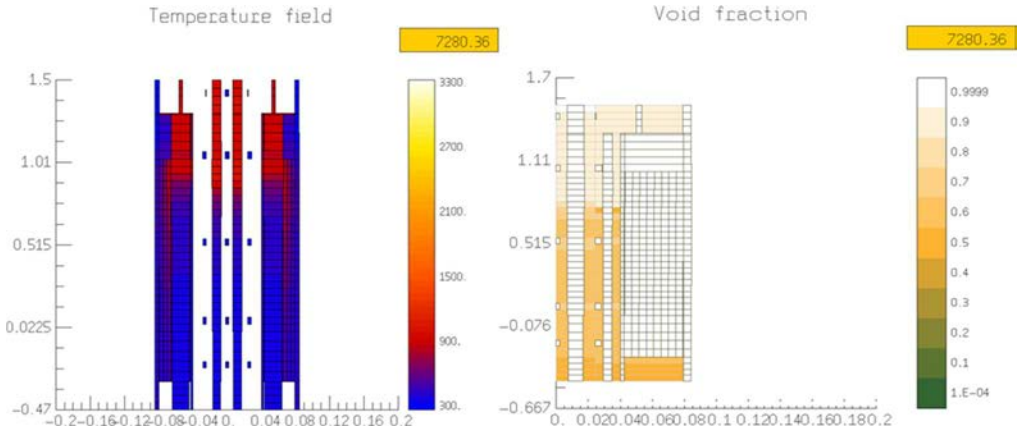

FIG. 40. ASTEC temperature distribution and void fraction in the bundle at7280 s.

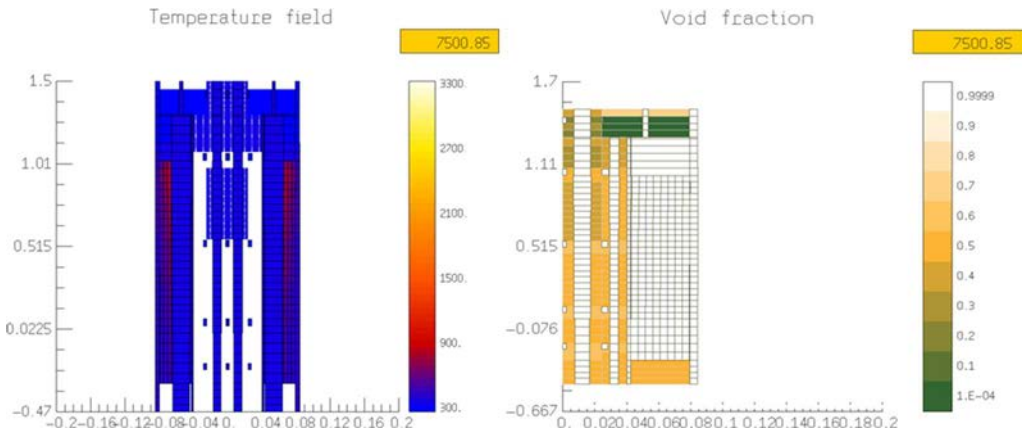

FIG. 41. ASTEC temperature distribution and void fraction in the bundle at 7500 s.

The axial profiles of the ZrO_2 thickness for the corner rods, the heated rods and the shroud at the end of the test (9000 s) are shown in Fig. 42. Fig. 43 and Fig. 44, respectively. The axial profile of the heated rods considered in the experiment as shown in Fig. 43 is calculated by averaging the ZrO_2 thickness for all heated rods. The same approach is adopted for the corner rods (not extracted) based on the experimental data shown in Fig. 42. The calculated ZrO_2 thickness for the two representative heated rods (inner and outer) are shown in Fig. 43 while the ZrO_2 thickness of the corner rod is shown in Fig. 42. A good agreement is obtained for the corner rods oxidation profiles as shown in Fig. 42. The maximum ZrO2 thickness, at 950 mm of elevation, is 460 µm. The heated rods profile shown in Fig. 43 indicates an underestimation of Zr oxidation (at 950 mm elevation for both the inner and outer rods. The qualitative shape of the oxidation profile is well predicted by the code.

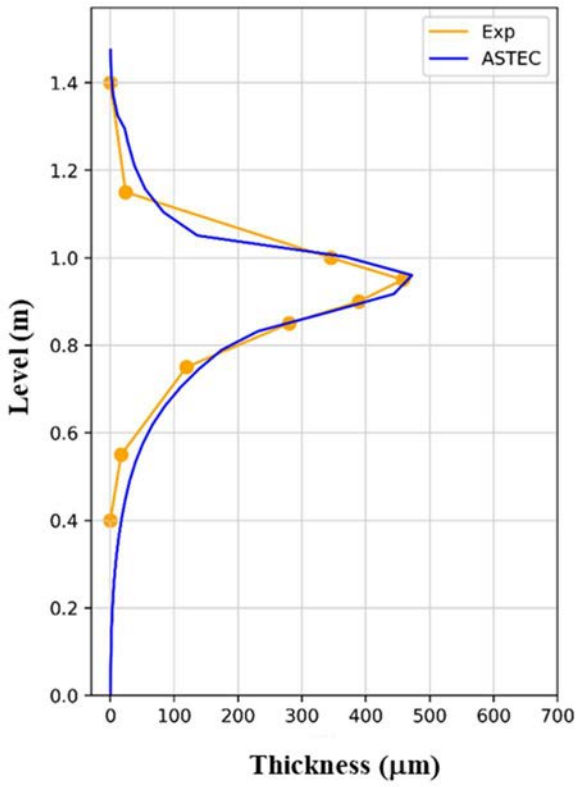

FIG. 42. Averaged corner rod ZrO_2 thickness profile at 9000 s.

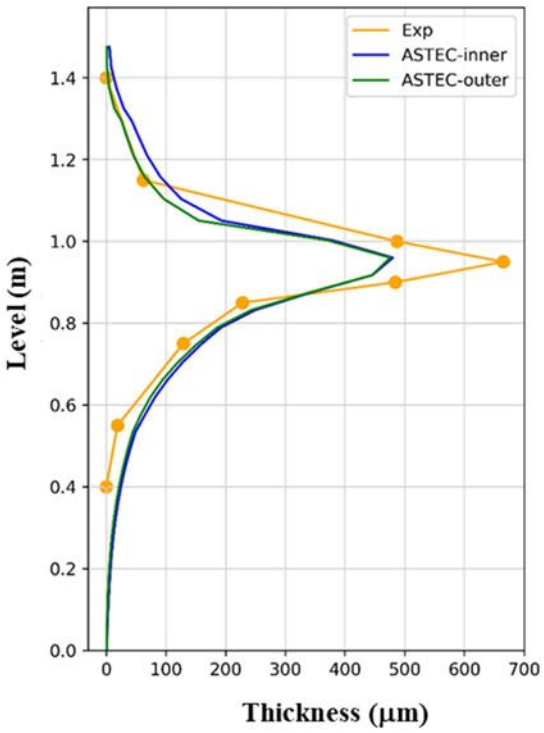

FIG. 43. Averaged heated rod ZrO_2 thickness profile at 9000 s.

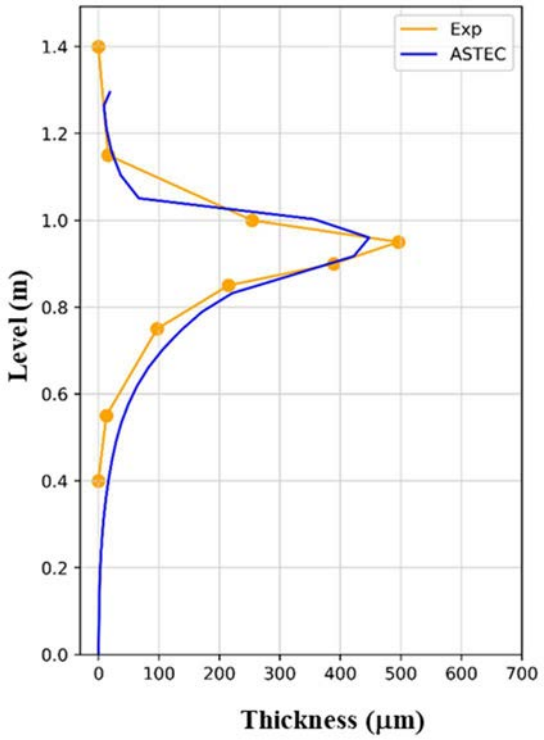

FIG. 44. Averaged shroud ZrO_2 thickness profile at 9000 s.

The experimental value for the oxidation thickness at 950 mm is about 680 µm, while the calculated thickness is 200 µm lower. The code prediction of the shroud's oxidation profile is shown in Fig. 44 indicating slight underestimation of the thickness peak at 950 mm; the experimental value is 500 µm

while the code predicts value of about 450 μm. The final material composition in the component of the bundle is the same as the one reported for the quenching timings as shown in Figs. 27 and 28.

3.4.4. Fast Fourier transform based method analysis of the QUENCH-06 ASTEC simulations

The quantitative accuracy evaluation of the ASTEC code results are conducted through the Fast Fourier Transform Based Method (FFTBM) [19, 28]. In the FFTBM, the difference between the calculated and the experimental data is passed from the time domain to the frequency domain using the Fast Fourier Transform. Then, the accuracy evaluation is performed on two parameters: the average amplitude and the weighted frequency [29]. The accuracy evaluation is mainly based on the average amplitude; the lower the average amplitude, the more accurate is the result. The weighted frequency is an additional qualitative information that may be considered for the accuracy evaluation [28]; it gives information about the frequencies that more significantly contribute to the discrepancies between the calculated and the experimental data. The tool adopted to perform the FFTBM analysis is the JSI FFTBM Add-In 2007, developed at Jožef Stefan Institute (Slovenia) [29, 31]. The default cut-off frequency of 0.4 Hz is used. Usually, several parameters are considered for the accuracy evaluation and the total average amplitude is computed through proper weighting factors [32]. However, the selection of weighting factors for the total accuracy may be subjective and it requires several experiments [33]. Therefore, no widely recognized weighting factors are derived for severe accident specific quantities (such as H2 mass production). Thus, as described in [19], the weighting factors are then set equal to one and the total average amplitude reduces to the average of the average amplitude of the various parameters. The FFTBM is applied considering the three vs previously identified ten parameters: the H2 mass cumulative production, two collapsed levels and seven wall temperatures at different locations. The reference threshold values for the average amplitude for the accuracy evaluation are [19, 34]:

- AA≤0.3: very good code prediction;
- 0.3<AA≤0.5: good code prediction;
- 0.5<AA≤0.7: poor code prediction;
- AA≥0.7: very poor code prediction.

The FFTBM analysis results are shown in Table 10. The failed experimental values are excluded from the accuracy evaluation, and are marked with "*". In the pre-oxidation phase (0 s–6011 s), the code prediction can be classified as very good for all the considered parameters. The total average amplitude is 0.06 and the code prediction is very good according to the previous thresholds. In the heat up phase (6011 s–7179 s), three thermocouples failed, and they are not considered in the accuracy evaluation. The code prediction of all the other parameters can be classified as very good with the total average amplitude of 0.10. Finally, in the quenching phase (7179 s–9000 s) the failure of a fourth thermocouple occurred and is not included. The code prediction for the remaining temperature measurements can be classified as good, with a general anticipation of the temperature reduction as seen in Figs. 29–32. The collapsed levels average amplitude is slightly higher than 0.5, mainly due to a slight calculated underestimation when compared to the experiment[3]. The result for the H_2 mass production shows an

[3] The presence of oscillations in the experimental and/or calculated data could give relatively high values of average amplitude even if the curves, from a visual observation, seem to be in reasonable agreement. These oscillations can introduce higher frequencies that in principle could not be physical but add spurious contribution in the average amplitude computation, increasing its value. Therefore, in a validation process for safety review purpose, more detailed analysis are necessary to analyze the nature of the oscillations both in the experimental and/or calculated signals and by investigating the average amplitude

average amplitude of 0.15 and could be classified as very good. The total average amplitude is equal to 0.44 in this last phase.

TABLE 10. FFTBM RESULTS

VARIABLES	PRE-OXIDATION PHASE		HEAT UP PHASE		QUENCHING PHASE	
	Average Amplitude	Weighted Frequency	Average Amplitude	Weighted Frequency	Average Amplitude	Weighted Frequency
M_H2_g	0.04	0.04	0.11	0.06	0.15	0.07
W_Lev_1	0.13	0.10	0.06	0.11	0.61	0.12
W_Lev_2	0.13	0.10	0.06	0.11	0.59	0.12
T_CRod	0.07	0.03	0.14	0.07	0.41	0.02
T_HR_inner_1	0.03	0.02	*	*	*	*
T_HR_inner_2	0.04	0.02	*	*	*	*
T_HR_outer_1	0.05	0.04	0.05	0.06	*	*
T_HR_outer_2	0.04	0.04	*	*	*	*
T_Shro_1	0.04	0.03	0.18	0.06	0.40	0.02
T_Shro_2	0.04	0.02	0.10	0.07	0.46	0.03
Total	0.06		0.10		0.44	
M_H2_g	0.04	0.04	0.11	0.06	0.15	0.07
W_Lev_1	0.13	0.10	0.06	0.11	0.61	0.12
W_Lev_2	0.13	0.10	0.06	0.11	0.59	0.12
T_CRod	0.07	0.03	0.14	0.07	0.41	0.02
T_HR_inner_1	0.03	0.02	*	*	*	*
T_HR_inner_2	0.04	0.02	*	*	*	*
T_HR_outer_1	0.05	0.04	0.05	0.06	*	*
T_HR_outer_2	0.04	0.04	*	*	*	*

3.5.RESULTS OF THE UNCERTAINTY AND SENSITIVITY ANALYSIS

The uncertainty quantification of the ASTEC results is carried out applying the probabilistic propagation of input uncertainties method (Section 3.3). The RAVEN tool is used to set up the ASTEC calculations by sampling the input uncertain parameters according to their ranges and PDFs, as specified in Section 2.3. Following the methodology described in Section 3.3, the one-sided statistical tolerance limit is considered to evaluate the minimum number of code runs, considering five FOMs. Accordingly, by imposing a probability content and a confidence level of 95%, a minimum number of 181 calculations is required.

The computational power available based on the RAVEN-ASTEC implementation on a high-performance computing platform provides the resources needed to run such number of calculations. In addition, accounting for possible code failures, the final number of code runs is raised to 200. In addition, despite that the number of input parameters does not affect the minimum number of calculations required, for the sensitivity analysis the sampling size need to be much larger than the number of uncertain input parameters [35]. All 200 ASTEC calculations are completed successfully, and the analysis of the results is described according to the selected FOMs. The first FOM analysed for the uncertainty quantification analysis is the total mass of accumulated H2. The ASTEC dispersion band is

values as a function of the cut-off frequency. It is also important to notice the role of the weight of each parameter for the calculation of the total; this weight determines the contribution of each parameter in computing the total accuracy.

shown in Fig. 45 in comparison to the experimental data and the reference calculation result. Figure 46 shows the cumulative H2 mean value and the STD in comparison to the experimental data.

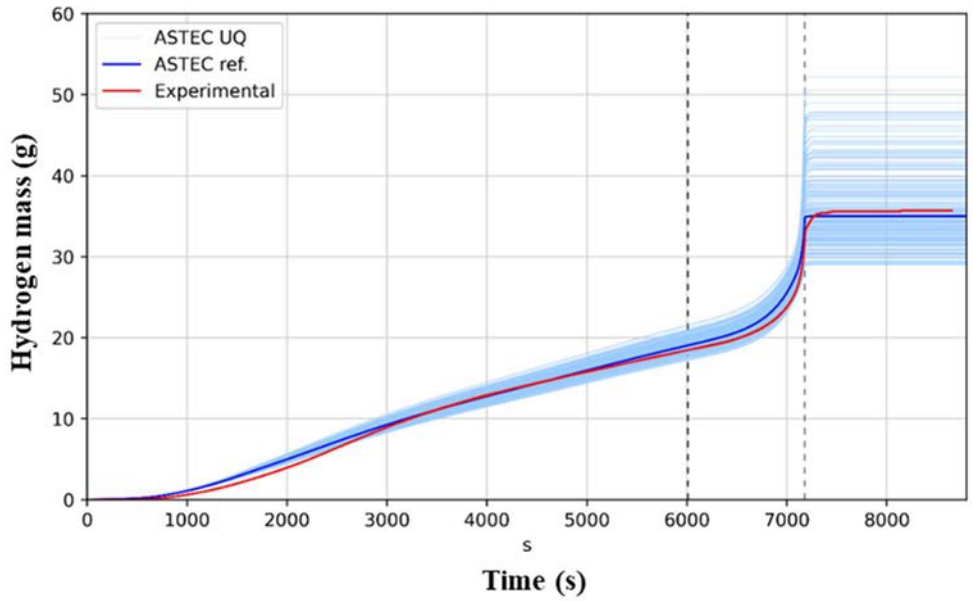

FIG. 45. ASTEC dispersion of total mass of accumulated H_2 in comparison to experimental data.

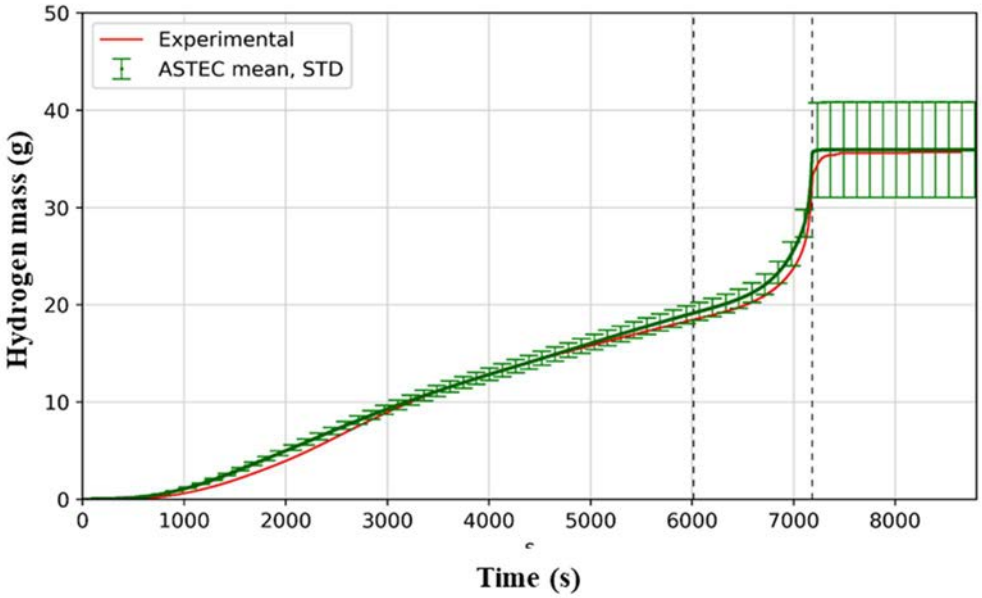

FIG. 46. Mean value and STD of total mass of accumulated H_2, against experimental data.

During the pre-oxidation phase the calculated dispersion band width increases as can be seen in, Fig. 45, and, consequently the STD as well, as seen in Fig. 46. After around 2200 s of simulation the experimental data is included in the results dispersion band. The heat-up phase is characterized by constant increase of dispersion of the total accumulated H2mass until around 7050 s. At this point (onset of oxidation acceleration), the dispersion of the results (band width and STD) shows a very fast increase. In order to underline this behaviour, Fig. 47 shows the time derivative of STD of total accumulated H_2 mass.

The STD derivative shows the spread of results from around 7050 s and rapidly reduces around 50 s after the quenching injection takes place (at around 7230 s). The results dispersion band presents a width of 23 g at the end of the transient. Additional conclusions can be drawn from Fig. 48 showing the final rods material composition for two calculations of the 200, taken at the extremes of the total accumulated H_2 mass (lowest oxidation on the left and highest oxidation on the right).

One scenario shows no melting of materials (see Fig. 48 (a)) and the other one shows localized material melting and relocation in the meshes around 950 mm of elevation. The reference scenario shown in Fig. 25 is between the two (localized melting without relocation), similarly to the experimental data. The values of Pearson and Spearman correlation coefficients, related to total accumulated H_2 mass and computed for the 22 input uncertain parameters, are depicted in Fig. 49, Fig. 50, Fig. 51, and Fig. 52, respectively.

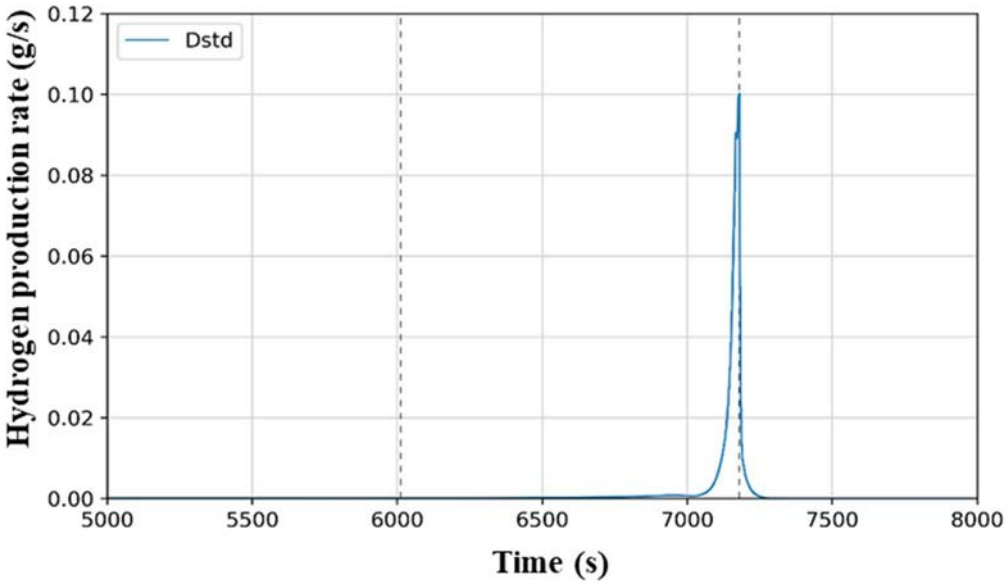

FIG. 47. Time derivative of ASTEC results STD of total mass of accumulated H_2.

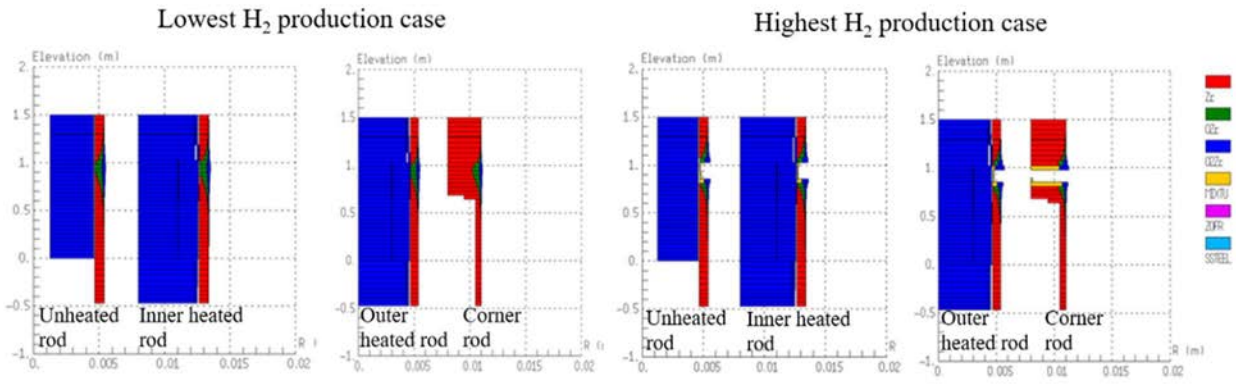

(a) *(b)*

FIG. 48. (a) Final components materials in the lowest and (b) highest H_2 production cases.

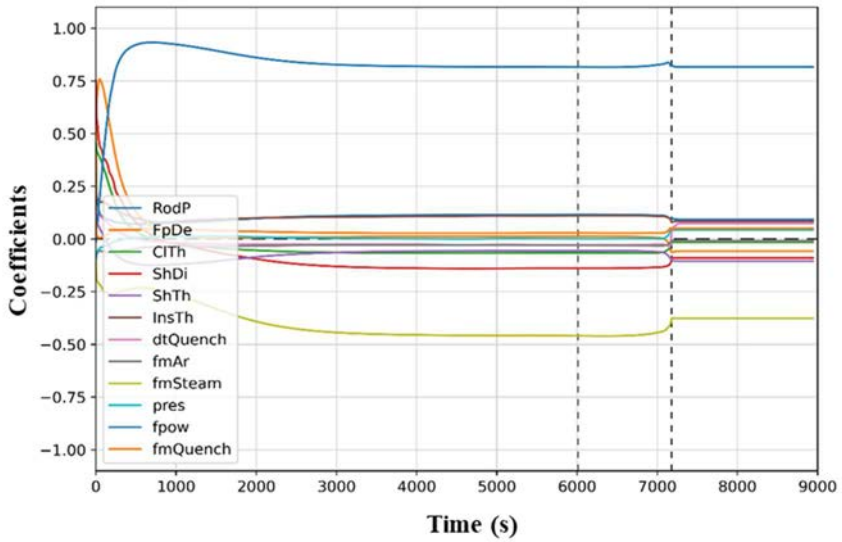

FIG. 49. Pearson correlation coefficient related to total accumulated H_2 mass (geometric and boundary conditions input parameters).[4]

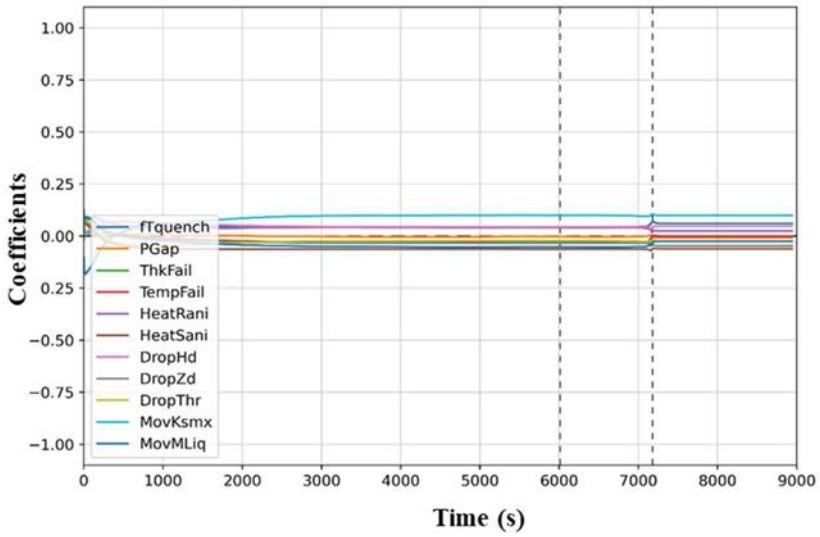

FIG. 50. Pearson correlation coefficient related to total accumulated H_2 mass (cladding integrity criteria and physical models).

From Figs. 49–52, showing the Pearson and the Spearman coefficients for the geometrical parameters and for the initial and boundary conditions, it can be concluded that along the sequence (after 1000 s) the only two uncertain input parameters showing a moderate or significant linear (Pearson) and a

[4] RodP , FpDe, ClTh, ShDi, ShTh, InsTh refer to the parameters 1 to 6 in Table 3, respectively;
dtQuench, fmQuench, fmAr, fmSteam, pres, fpow, ftquench, and PGap refer to the parameters 7 to 14 in Table 4, respectively;
ThkFail and TempFail refer to the parameters 15 and 16 in Table 5, respectively;
HeatRani and HeatSani refer to the parameters 17 and 18 in Table 6, respectively;
DropHd, DropZd and DropThr refer to the parameters 19 and 21 in Table 7, respectively;
MocKsmx and MovMliq refer to the parameters 22 and 23 in Table 9, respectively.

monotonic (Spearman) correlation with the FOM are the argon mass flow rate (moderate negative correlation) and the power in the bundle (significant positive correlation).

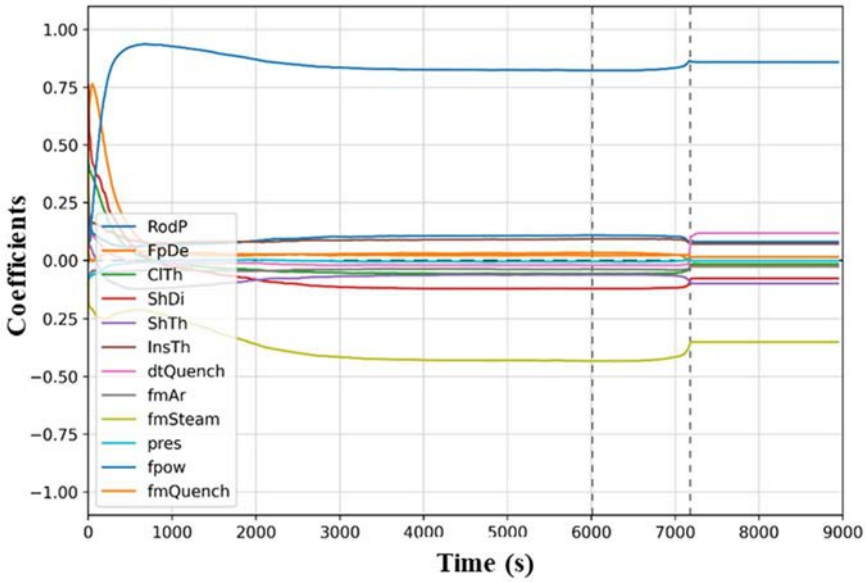

FIG. 51. Spearman correlation coefficient related to total accumulated H_2 mass (geometric and boundary conditions input parameters).

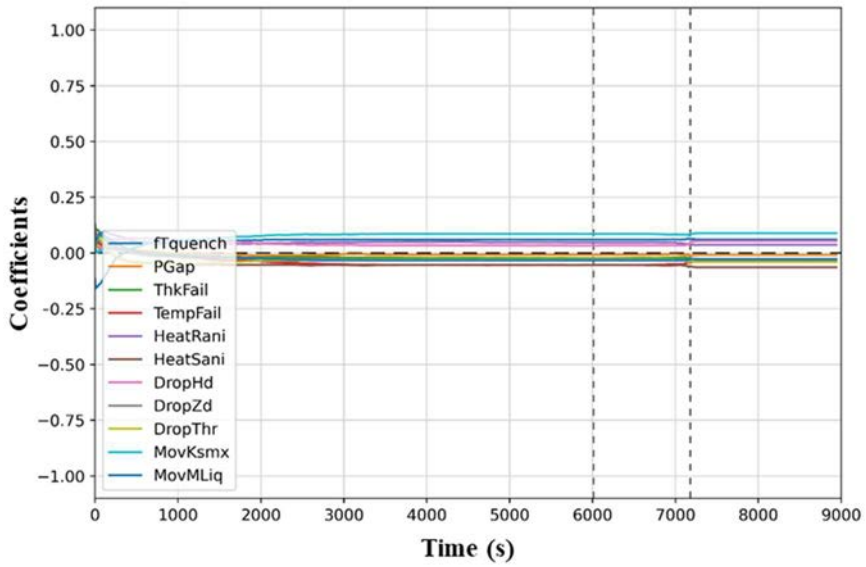

FIG. 52. Spearman correlation coefficient related to total accumulated H_2 mass (cladding integrity criteria and physical models).

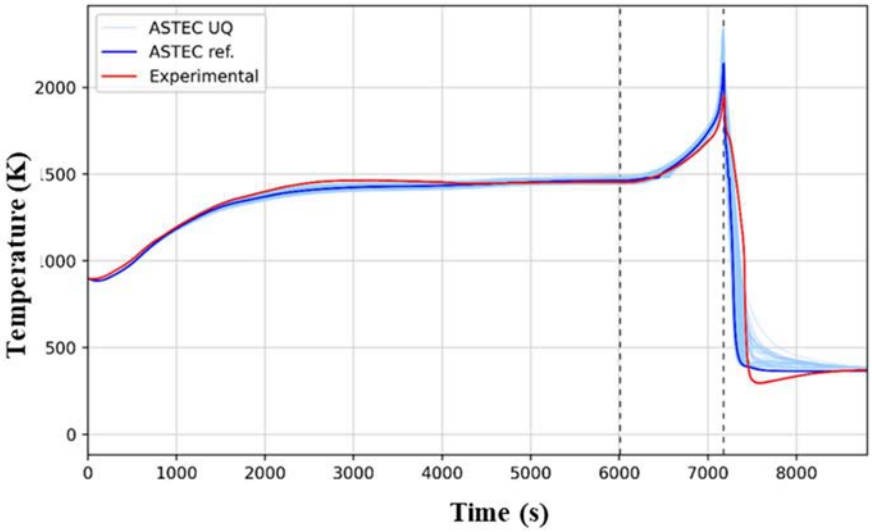

FIG. 53. Results dispersion of internal temperature inf the central fuel rod simulator at the elevation of 950 mm, against experimental data.

The first 500 s of transient shows different correlations, but it needs to be considered the low H_2 mass produced in this time interval and therefore the low value of the absolute uncertainty (Fig. 46). None of the uncertain input parameters related to integrity cladding criteria and physical models show linear or monotonic correlation with the selected FOM. The second considered FOM is the internal temperature of the central (unheated) fuel rod simulator at elevation of 950 mm. The results dispersion band of this FOM against the experimental data and the reference calculation result is shown in Fig. 53. In this case the results spreading in the transient is lower than for the previous FOM. Some observations on the results spread can be analysed considering the mean value and the STD between 6500 s and 8500 s as shown in Fig. 54.

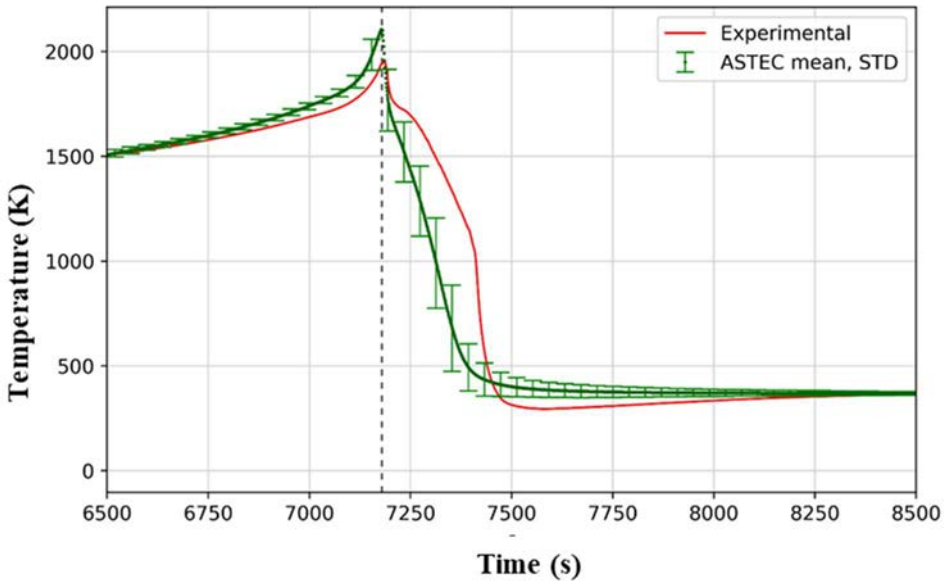

FIG. 54. Mean value and STD of internal temperature in the central fuel rod simulator at the elevation of 950 mm, against experimental data.

The results spreading (in terms of STD and results dispersion band width) of the central fuel rod simulator temperature behaves differently when compared to total accumulated H_2 mass FOM. Indeed, it shows a first minor increase in the reaction acceleration and heat-up of the bundle, while the main widening of STD (and results dispersion band width) occurs after the onset of quenching, and its maximum value is reached at around 7350 s during the cooling of the bundle. Figure 53 shows that the temperature is not always enveloped by the results dispersion band. In particular, the major discrepancies are observed during the temperature decreasing. This discrepancy confirms what was observed for the components cooling after the quenching injection. The discrepancies between the code results and the experimental data in the temperatures decrease during water injection could be attributed to the thermal hydraulic models of the code or to the adopted nodalization approach. Further studies need to be done to investigate it further.

The Spearman and Pearson correlation coefficients for the temperature in the central fuel rod simulator at 950 mm are shown in Fig. 55–58. The correlation coefficients capture significant positive correlation of the FOM with the core power, and the moderate negative correlation with the steam mass flow rate, during the pre-oxidation and the heat-up phases. After the onset of quenching, quite different correlations are captured by the two coefficients and during the temperature decreasing the higher correlations are: the instant of quenching injection, which shows significant positive correlation with a peak at 100 s after the experimental quenching time; the threshold void fraction to allow exchange with liquid droplets, with a significant negative value, about 150 s after the reference quenching time; the electric power whose value decreases to a moderate correlation. The shroud internal diameter shows a significant moderate correlation only at the beginning of the transient before the bundle heat-up. The results dispersion band of the H_2 generation rate is shown in Fig. 59 against the experimental data, highlighting the last part of the heat-up phase and the quenching (7000 s–7300 s).

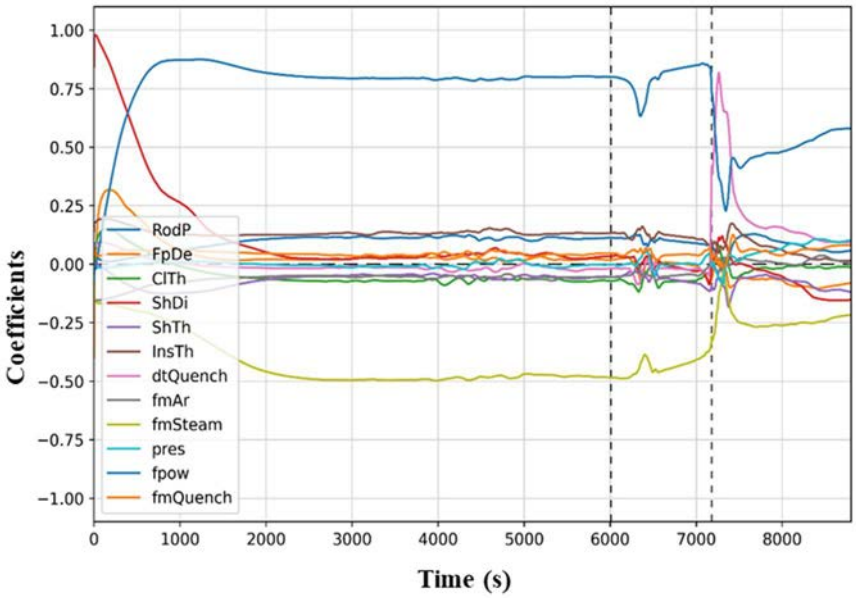

FIG. 55. Pearson correlation coefficient related to the internal temperature of the central fuel rod simulator at the elevation of 950 mm (geometric and boundary conditions input parameters).

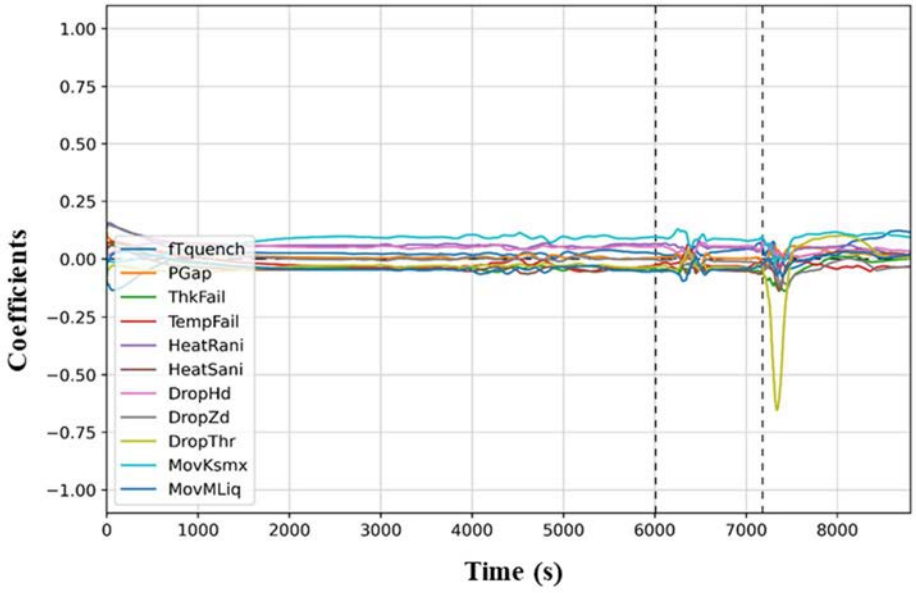

FIG. 56. Pearson correlation coefficient related to the internal temperature of the central fuel rod simulator at the elevation of 950 mm (cladding integrity criteria and physical models).

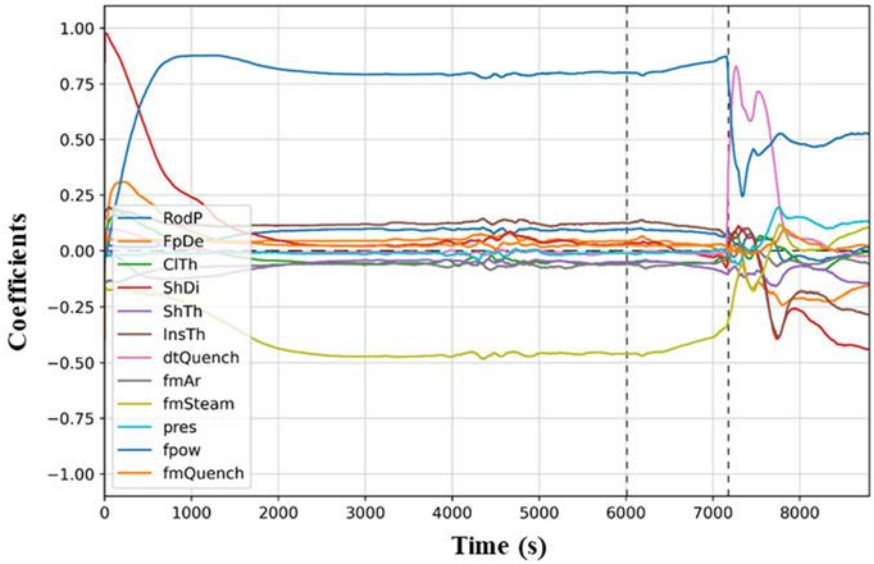

FIG. 57. Spearman correlation coefficient related to the internal temperature of the central fuel rod simulator at the elevation of 950 mm (geometric and boundary conditions input parameters).

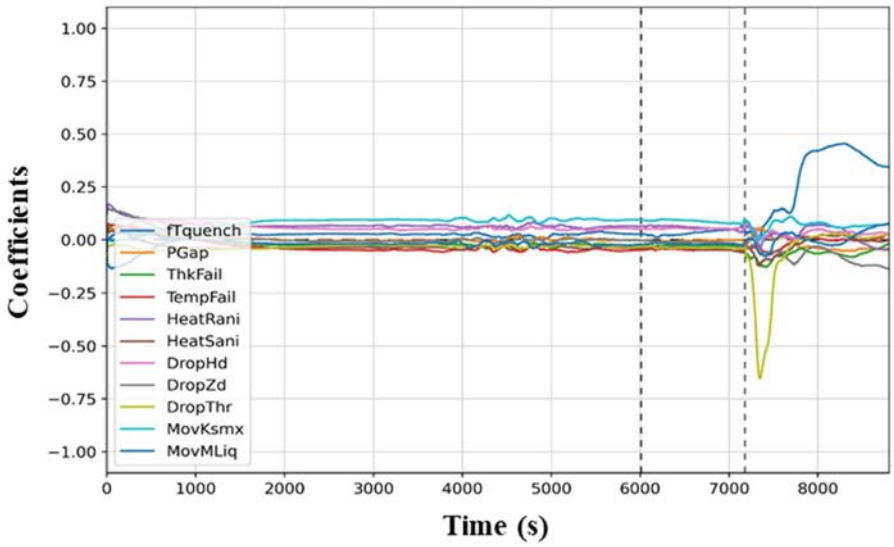

FIG. 58. Spearman correlation coefficient related to the internal temperature of the central fuel rod simulator at the elevation of 950 mm (cladding integrity criteria and physical models).

As shown in Fig. 59, the results dispersion band width increases considerably after the acceleration of the oxidation processes (at about 7050 s). After the quenching takes place the width of the results dispersion band reduces again. Considering ~5 s delay for the detection of H_2 in the experiment, the experimental data is always enveloped within the calculated dispersion band, except for the 150 s after the quenching, when none of the calculations capture the remaining oxidation and H_2 production. Despite the H_2 generation rate reaching peaks four times the magnitude of the experimental value, only few calculations (around 10 over 200) show these peaks, which are far from the experimental value.

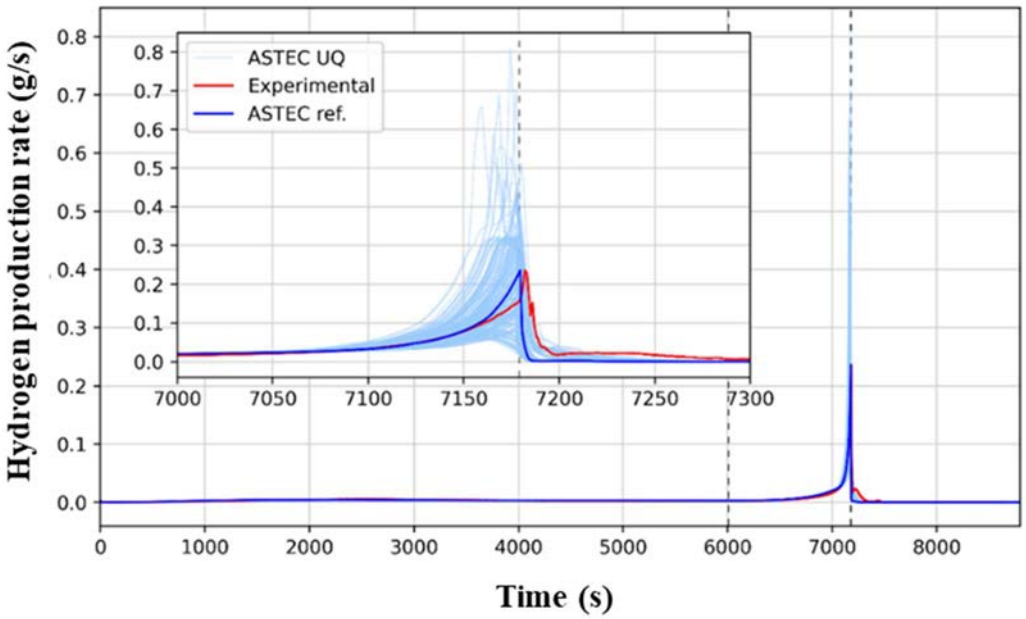

FIG. 59. Results dispersion of H_2 generation rate, against experimental data.

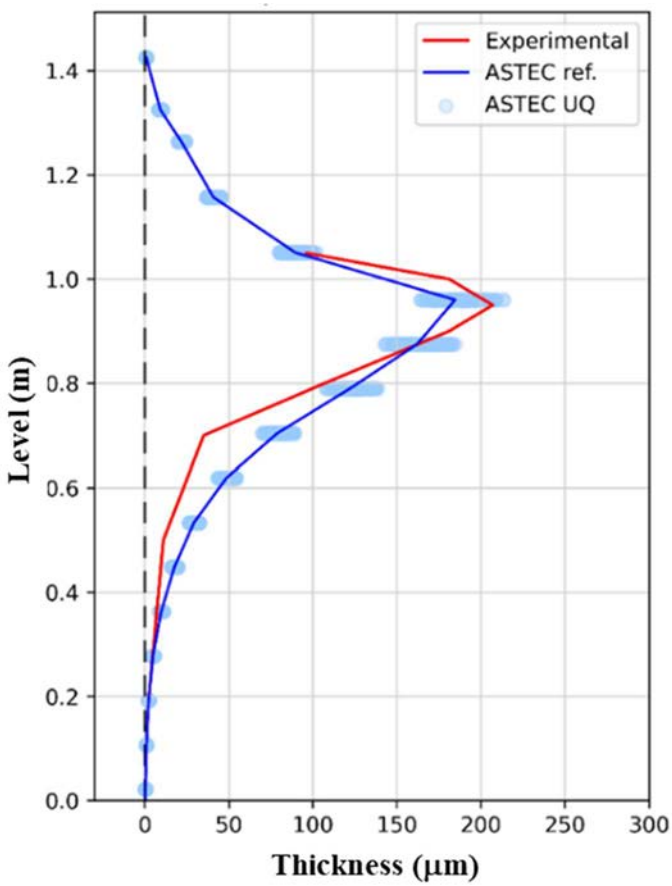

FIG. 60. Results dispersion of the axial profile of corner rod oxide at 6620 s against experimental data.

The results spreading of the axial profile of the oxide scale of the corner rod at 6620 s against the reference calculated value are shown in Fig. 60. It also shows the experimental oxidation profile of the corner rod extracted at the same time. The width of the results dispersion band increases with the reference calculation thickness. The maximum results spreading of around 55 µm is reached at the level of 950 mm. The experimental data is not enveloped within the results dispersion band for levels lower than 800 mm.

Figure 61 shows Pearson coefficients related to this FOM at different elevations, while Fig. 62 shows Spearman coefficients related to the same FOM. From the correlation coefficients related to the axial profile of the oxide scale of the corner rod at 6620 s, it can be inferred that the input variation of electrical power has a significant positive correlation along the rod elevation, the steam mass flow rate has a moderate negative correlation along the elevations lower than 1300 mm, and the shroud internal diameter has a moderate negative correlation at elevations presenting low oxidation thickness (above 1300 mm and below 500 mm). The results dispersion band of the axial profile of the oxide scale of the internal-ring heated-rod at the end of the scenario (9000 s) are shown in Fig. 63. The results dispersion band is shown against the experimental data (averaged on the rods of the same ring) and the ASTEC calculated reference value.

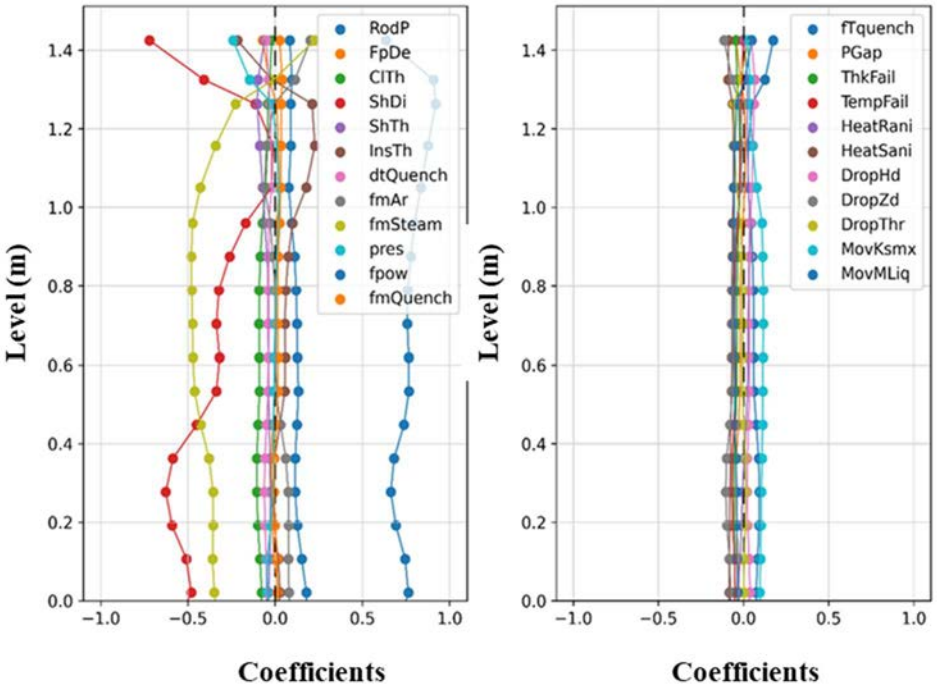

(a) *(b)*

FIG. 61. Pearson correlation coefficient related to the axial profile of the oxide scale of the corner rod at 6620 s, for geometric and boundary conditions parameters (a), and for cladding integrity criteria and physical models' parameters (b).

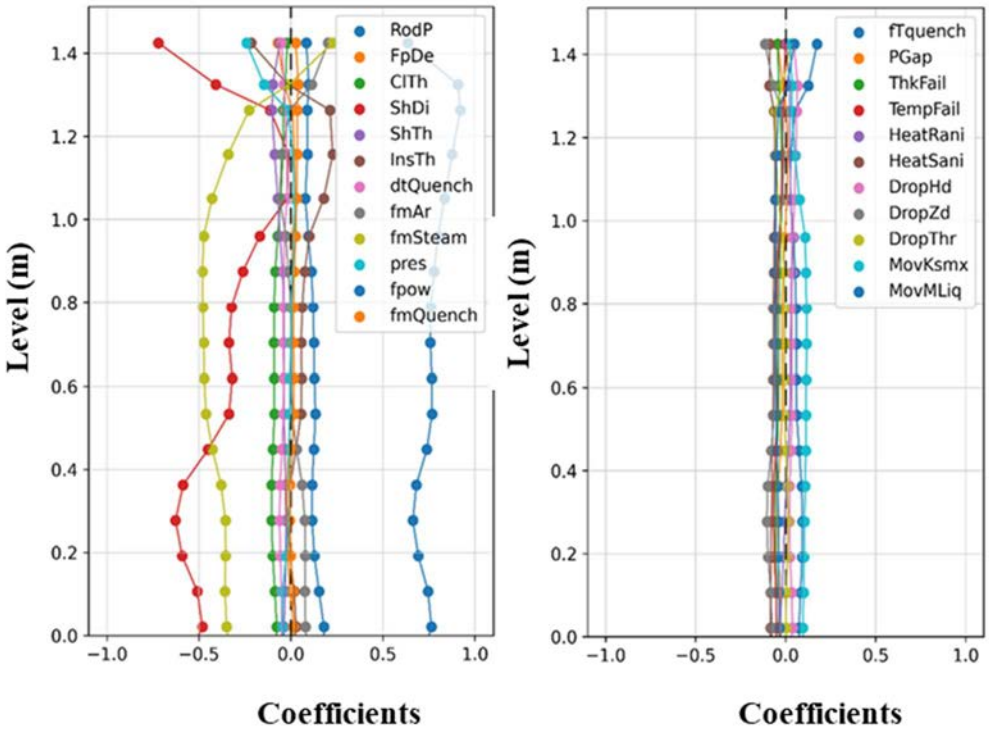

(a) *(b)*

FIG. 62. Spearman correlation coefficient related to the axial profile of the oxide scale of the corner rod at 6620 s, for geometric and boundary conditions parameters (a), and for cladding integrity criteria and physical models parameters (b).

From Fig. 63, it can be noted that at the most oxidized elevations (from around 800 mm to 1150 mm) the ZrO_2 thickness shows a spread of the results larger than the other portion of the rod. In addition, as previously explained (refer to Fig. 48), in some of the uncertainty analysis simulations the degradation advances until the failure and relocation of material in the meshes located around 950 mm of elevation. In case of cladding relocation, the ZrO_2 thickness is 0 as can be seen in Fig. 63. This can be considered as a bifurcation of the output domain of the FOM due to the edge effect of the changing in the core degradation phenomenology (relocation of melted material) between the different simulations. This behaviour is not unexpected considering that the reference simulation (and the experimental observation) shows a situation which can be already on the edge within the relocation phenomenology.

The Pearson correlation coefficients related to the axial profile of the oxide scale of the internal-ring heated-rod at the end of the scenario are shown in Fig. 64. The same data is shown in Fig. 65 for the Spearman coefficients. The coefficients are calculated only for the ZrO_2 thickness of the non-relocated material (non-zero results in Fig. 63). Pearson and Spearman coefficients for this FOM show significant correlation with the power in the bundle, in agreement with the previous FOMs. A significant correlation for this FOM is also present for the shroud internal diameter, increasing within the extremes of the rod elevations. Differently from the previous result (Fig. 62), this correlation is positive at the bottom of the bundle elevation and negative at the top elevations. Also, in this case the correlation is absent at the elevations (around 950 mm) with the highest results spreading.

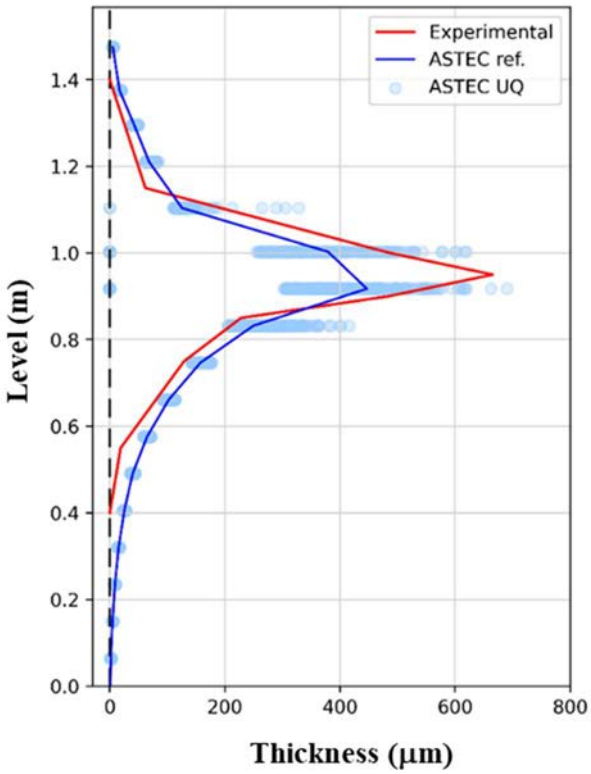

FIG. 63. Results dispersion of the axial profile of the oxide scale of the internal-ring heated-rod at the end of the scenario, against experimental averaged profile.

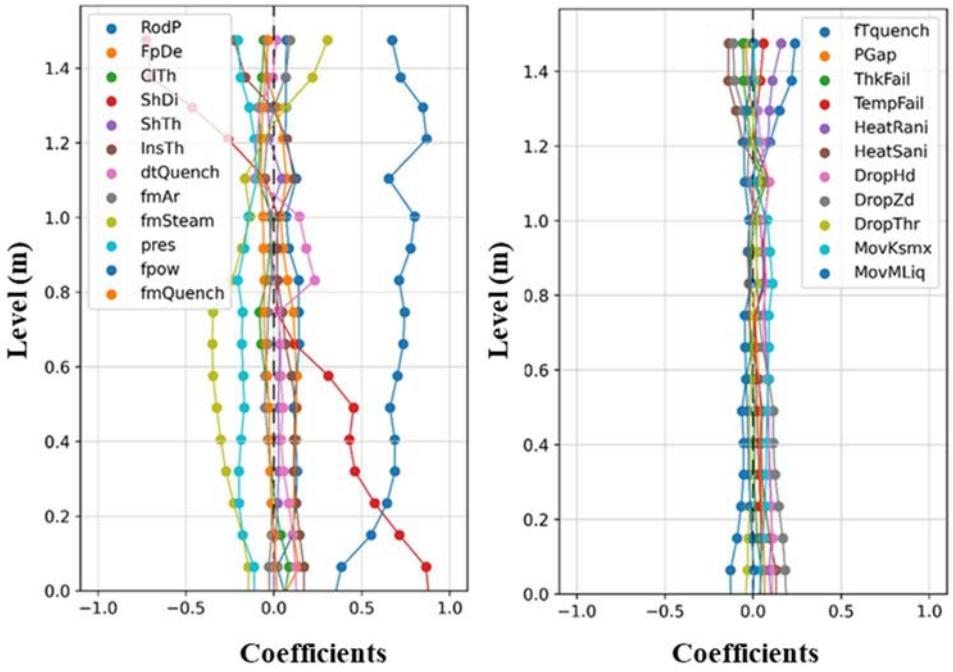

(a) *(b)*

FIG. 64. Pearson correlation coefficient related to the axial profile of the oxide scale of the internal-ring heated-rod at the end of the scenario, for the geometric and boundary conditions parameters (a), and for the cladding integrity criteria and physical models parameters (b).

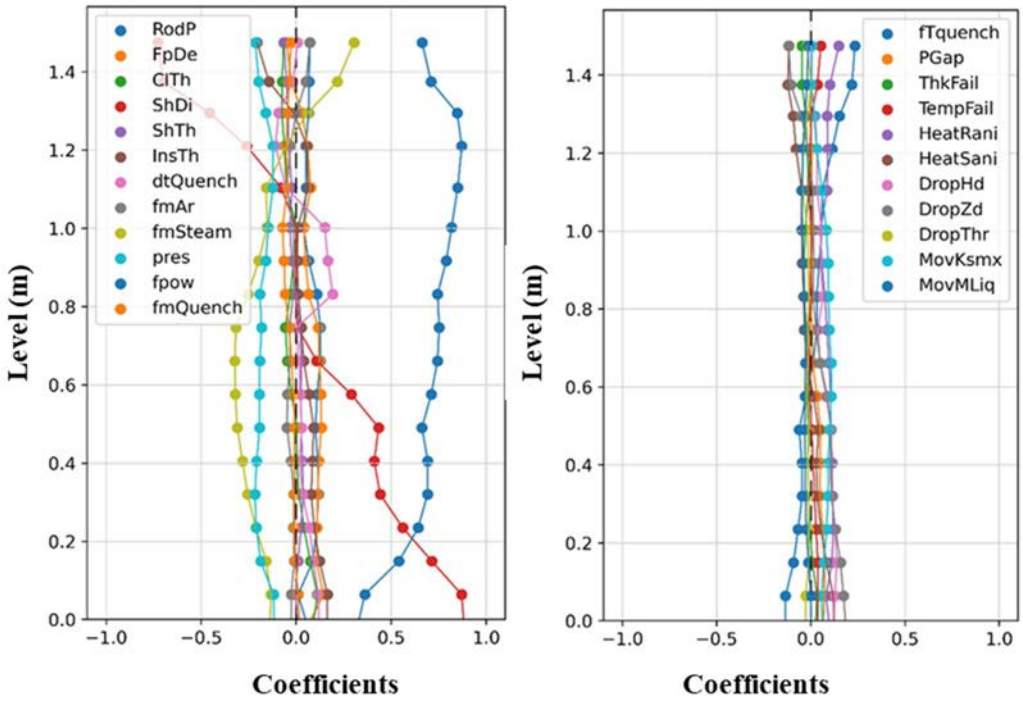

(a) *(b)*

FIG. 65. Spearman correlation coefficient related to the axial profile of the oxide scale of the internal-ring heated-rod at the end of the scenario, for the geometric and boundary conditions parameters (a), and for the cladding integrity criteria and physical models parameters (b).

3.6.CONCLUSIONS, LESSONS LEARNED, AND BEST PRACTISES

The ASTEC code proves the effectiveness of the methodology applied to accuracy evaluation and uncertainty quantification against experimental data.

The visual comparison of the reference calculation against the experimental data provides qualitative evaluation of the code prediction capabilities, by considering selected relevant parameters. It is used to identify the main physical phenomena defining the transient, to investigate the code qualitative prediction of each phenomenon, and to select the phenomena which are not well predicted in the simulation and that need further improvement. Since several phenomena occurring during the transient can characterize some temporal windows, it is a best practice to define the main phase in which the transient can be divided, and then to separately analyse the code phenomena prediction in each identified phase.

The quantitative accuracy evaluation supports the code accuracy evaluation by providing a quantitative assessment of the code prediction. The FFTBM method provides a quantitative accuracy evaluation of selected calculated parameters against the experimental data. Some care needs to be taken regarding the selection of the experimental and the calculated data to be compared.

The choice of probabilistic propagation of input uncertainties using the Wilks formula guarantees that the statistical confidence in the results is not affected by the input uncertain parameters number, and it is an advantage when this number is large as presented in this exercise. Moreover, with a correlation analysis it is possible to characterize the relationship of each uncertain input parameter with the FOM and eventually to find the main sources of uncertainty.

The FOMs provided by KIT are related to main phenomena governing the sequence: fuel rods heat-up and oxidation in super-heated steam environment, early core degradation phenomena, and quenching of hot core within intact geometry.

From direct comparison of the reference simulation against the experimental data and from the FFTBM results, it can be concluded that the code simulation provides a very good prediction of the phenomena governing the pre-oxidation phase. This involves the oxidation kinetics of Zr components in super-heated steam environment and the heat exchange in the test section. During the heating-up phase, the ASTEC prediction of the selected relevant parameters can be classified as very good by the FFTBM analysis. The only discrepancy with the experimental results is related to the prediction of a faster heat-up of some components (e.g. corner rod, shroud) during the runaway of Zr oxidation. The quenching phase shows certain discrepancy in the code prediction of the selected relevant parameters behaviour, but in general the accuracy is evaluated as good by the FFTBM. In particular, the second quenching injection leads to a faster cooling and temperatures drop of some components and to a following anticipated stop of the oxidation processes. This may be caused by a slight overestimation of convection heat transfer simulated by the code during quenching, but also to the assumptions adopted in nodalization. Additional studies and a sensitivity analysis may be conducted. The profiles of ZrO_2 thickness at the end of the simulation are predicted by the code from both a qualitative and a quantitative point of view. ASTEC predicts the local melting of materials at the most heated-up level without loss of the integrity conditions, in a similar way to what is observed in the post-experiment analysis of the bundle (local material melting without structures loss of geometry). The water level evolution in the test section and the final level is predicted. The code prediction of the total H_2 mass production is 1 g lower

than the experimental value, with 36 g in total. This proves the capability of the code to predict the overall Zr oxidation process.

The uncertainty quantification allows to characterize the results spreading of the selected FOMs due to the input uncertain parameters variation. The uncertainty of the total mass of accumulated H_2 (in terms of results spreading band width and STD) increases as the sequence progresses. The maximum increase (in terms of derivative of results spreading band width and STD) is observed during the phenomenon of oxidation acceleration, over the last seconds of heating-up phase. The spread in the total mass of accumulated H_2 within this phenomenology can be expected also by considering the non-linear behaviour of the oxidation reaction for temperatures higher than around 1770 K.

A different behaviour is observed in the time evolution of results spreading affecting the temperature of the central fuel rod simulator at elevation 950 mm. This FOM shows results spread mainly along the quenching phase of the transient. In addition, it is to underline that different behaviour of this FOM during the cooling with respect to the experimental data underlines the challenges in the prediction of the heat exchange and cooling of the bundle components during the quenching phenomena.

The results spreading bands of the ZrO_2 thickness profile is lower at 6620 s and becomes larger at the end of the transient. In all cases the width of the results spreading band is larger nearby the most heated up elevation of 950 mm, and narrower in the less oxidized zones.

A reason for the general results spreading in this sequence can be attributed to the fact that the reference calculation (as well as the experiment) is close to a core degradation phenomenology. In the reference calculation the conditions for the component's loss of integrity and material relocation are not reached, however, at the onset of quenching, these conditions are very close to be met by several components. Therefore, many of the uncertainty simulations show different phenomenology than the one observed in the reference calculation (and in most of the uncertainty analysis calculations); structures failure and material relocation that lead to further oxidation and H_2 production since the internal surfaces become available for steam oxidation.

Several severe accident codes models and phenomenology have often to deal with non-linear phenomena (e.g. oxidation runaway) and cliff-edge effects (e.g. components failures and relocation) which, in several cases, may determine a spread in the uncertainty of the calculated values. For this reason, it becomes crucial to investigate the phenomena mainly affected by a spread of the uncertainty and to find related sources.

3.6.1. Best practices

Performing uncertainty quantification studies using the current methodology presents certain challenges. Special challenge is the determination of suitable ranges and PDFs for the chosen uncertain input parameters. It is crucial to exercise caution in this selection process. Furthermore, the approach used to calculate the minimum number of code runs is valid only under specific assumptions, which may not always hold true. When code failures occur, the guarantee of probability content within the confidence interval becomes uncertain. The statistical framework might not be applicable in cases where the function between the input and output phase spaces is not continuous, such as when there is a bifurcation in the output domain of a FOM, for instance, the ZrO_2 thickness at the most heated-up level. Although the chosen approach does not impose a limit on the number of uncertain input parameters, the number of code calculations must significantly exceed the number of input uncertain parameters [35]. In the

selection of FOMs, it is essential to consider that integral parameters provide information that encompasses the entire domain of integration. To conduct a more comprehensive analysis, it is advisable to select multiple integral FOMs across various domains of integration, such as time and volume, as well as local parameters. This approach ensures a more thorough exploration of uncertainty.

3.6.2. Main sources of uncertainty resulting from the analysis

In pursuit of identifying the primary sources of uncertainty concerning the FOMs and their evolution over time, a comprehensive correlation analysis is conducted, employing both Spearman and Pearson coefficients. These coefficients served to capture the correlation between each input parameter and each FOM in terms of both linear and monotonic relationships.

During the pre-oxidation phase, two key observations emerged. There is a significant positive correlation between the total mass of accumulated H_2 and the temperature of the central fuel rod simulator at elevation 950 mm with the power in the bundle, coupled with a negative moderate correlation with the steam mass flow rate. This outcome is quite rational, as an increase in power leads to higher temperatures, subsequently accelerating oxidation in the test section, while steam flow serves as a coolant, dissipating heat from the bundle. Furthermore, the correlation coefficients revealed a positive correlation between the FOMs and the shroud's internal diameter, as well as with the fuel pellets' external diameter at the sequence's outset. However, it is worth noting that, initially, there was a dispersion of results with a minimal effect on the FOMs.

The heating-up phase exhibits similar correlations for the investigated FOMs, with the exception of a gradual reduction in the correlation between the temperature of the central fuel rod simulator at elevation 950 mm and the steam flow rate input parameter. Notably, the axial profile of the oxide scale on the corner rod at 6620 seconds reflects the same correlations with the parameters discussed previously. Additionally, a negative correlation is evident with the shroud's internal diameter at less oxidized elevations.

In the quenching phase, distinct correlations emerge, especially for the temperature of the central fuel rod simulator at elevation 950 mm, compared to the preceding phases. Following the quenching injection, there is a reduction in the correlation with the electric power and steam flow rate, transitioning to moderate and low correlations.

A significant positive correlation peaks with the instant of quenching injection parameter. Moreover, a notable negative correlation is observed with the coefficient of the threshold void fraction for exchange with liquid droplets. This may be attributed to its influence on convection heat exchange during quenching. When considering the axial profile of the oxide scale on the internal-ring heated-rod at the end of the scenario, it primarily correlates with the electric power at all elevations, with the shroud's internal diameter demonstrating a moderate correlation only at less oxidized elevations.

4. INDIVIDUAL REPORT: IBRAE (RUSSIAN FEDERATION)

This section details main characteristics of the SOCRAT code used to analyse the QUENCH-06 experimental data, describes the QUENCH-06 model and discusses the results.

4.1. DESCRIPTION OF SEVERE ACCIDENT CODE

The SOCRAT code [36, 37] is suitable for coupled modelling of a wide range of thermohydraulic, physicochemical, thermomechanical and aerosol processes at all stages of accident progression, starting from initial event to corium release following the reactor vessel failure and consequent ex-vessel processes in a containment. The following SOCRAT modules are used for numerical simulation of severe accident:

- RATEG, simulating two fluid thermal hydraulics in circuits;
- SVECHA, simulating physical-chemical processes in the core;
- HEFEST, modelling the materials behaviour in the lower plenum and reactor pressure vessel degradation;
- BONUS calculates the accumulation of fission products in the fuel during the irradiation period, and decay heat in fuel after SCRAM.
- RELEASE calculates the formation of fission products compounds and gases (radioactive materials) in the fuel and their release from the fuel to the gas gap of the fuel rod.
- GAPREL calculates release of radioactive materials from the gas gap to the primary circuit.
- PROFIT simulates behaviour of radioactive materials in the primary circuit.
- MFPR_MELT simulates release of radioactive materials from the molten corium pool in the lower plenum.
- RACHIM calculates the activity, mass, and power of isotopes from the masses of chemical compounds of fission products.
- HEFEST-EVA is intended for core catcher modelling;
- TOCHKA is a module for calculation of neutron power in the core in point kinetics approximation with account for thermal hydraulic feedbacks including the reactivity insertion, and calculation of decay heat power immediately after SCRAM.

The SOCRAT code provides special interface for coupling with a stand-alone NOSTRADAMUS code that is used for realistic modelling of the atmospheric spread and deposition of radioactive substances, and dose rates to population. The SOCRAT is applied to licensing support of VVER units; it supports safety systems design, planning of the experiments, PSA Level 2 deterministic analysis, SAMG development and verification, crisis centres support, and education.

4.2.DESCRIPTION OF QUENCH-06 MODEL

The model of the QUENCH-06 experiment was developed based on the description of the QUENCH facility [1]. The nodalization scheme of the model is shown in Fig. 66. The hydraulic flow part of the rod bundle is modelled in one dimensional approximation. At the entrance to the rod bundle, two boundary conditions for the flow rate are set, which simulate the supply of a vapor-argon mixture and water. At the outlet of the bundle, a pressure boundary condition is set. The flow rates and pressure specified in the boundary conditions are time dependent and equal to the respective experimental measurements. Additionally, the lower and upper cooling of the assembly with water is simulated. The model includes an argon cooling jacket located at the periphery of the test section. In the flow part of the rod bundle, heat exchange is considered between the coolant and the elements simulating the central rod, fuel rod imitators, corner rods, spacer grids, and the shroud. All heated fuel rod imitators are modelled by one average rod. In the flow part of the cooling jacket, the heat exchange of argon with the inner and outer walls is considered. Convective heat transfer with air is set on the outer surface of the cooling jacket (not indicated in the scheme). Radiative heat transfer in the bundle and in the cooling,

jacket is also modelled. Special attention is paid to thermal conductivity of thermal insulation. According to [38] the thermal conductivity of thermal insulation in an argon atmosphere at a pressure of 1 bar is known only for five temperature values. As shown in Fig. 67, the working region that covers the temperatures that are measured in the QUENCH-06 experiment is quite wider. To simulate the thermal insulation conductivity in the whole working region, a cubic polynomial is used to approximate the data found in [34]. The approximating function is defined as follows:

$$\lambda = 2.18 \cdot 10^{-11} \cdot T^3 - 1.38 \cdot 10^{-8} \cdot T^2 + 4.52 \cdot 10^{-5} \cdot T + 0.0495 \qquad (1)$$

where λ is thermal conductivity in $W \cdot m^{-1} \cdot K^{-1}$, and T is temperature in K.

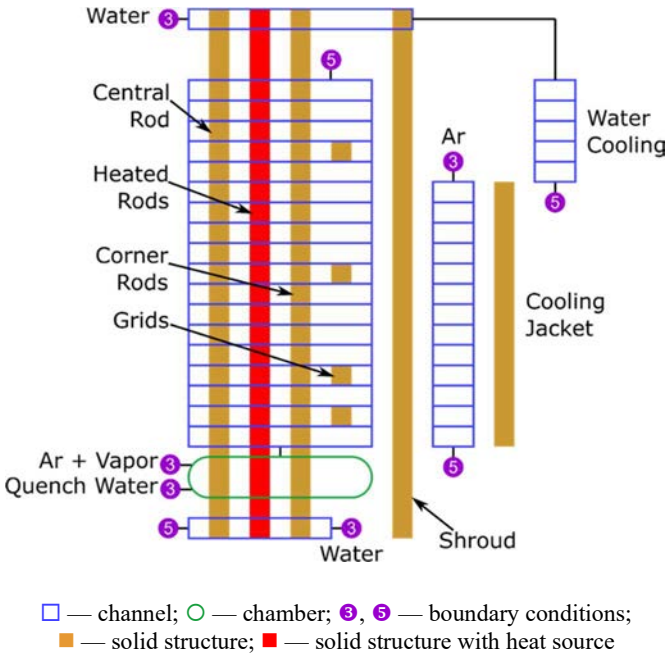

FIG. 66. SOCRAT code nodalization scheme of the QUENCH-06 experiment.

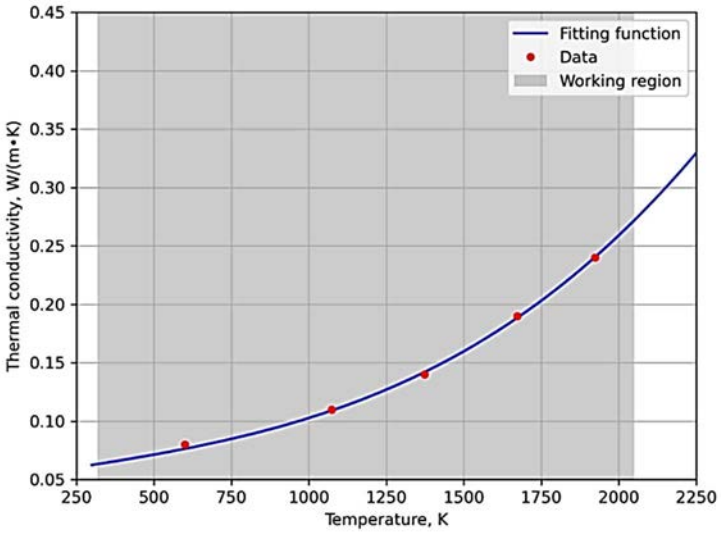

FIG. 67. ZYFB-3 thermal conductivity.

The SOCRAT code lacks the capability to simulate the axial thermal expansion of solid elements. Consequently, it becomes essential to consider this aspect when incorporating the temperature dependence of specific electrical resistance. The temperature dependence provided in Table 11 accounts for the sample's elongation during the heating process, particularly when employing a fixed mesh for simulations [39].

TABLE 11. SPECIFIC ELECTICAL RESISTANCE OF TUNGSTEN

***T*, K**	**300**	**400**	**500**	**600**	**700**	**800**	**900**	**1000**
ρ, μΩ/cm	5.45	7.84	10.3	12.9	15.6	18.5	21.4	24.4
T, K	1100	1200	1300	1400	1500	1600	1700	1800
ρ, μΩ/cm	27.4	30.5	33.7	36.9	40.2	43.5	46.8	50.2
T, K	1900	2000	2100	2200	2300	2400	2500	2600
ρ, μΩ/cm	53.6	57.1	60.5	64.0	67.5	71.0	74.6	78.1

The electrical resistance of the circuit outside the modelled region is set constant in calculation, and equal to 3.0 mΩ per rod. The total electrical power supplied by the generator is set as a boundary condition. The fast water injection system, which consists of a pressurized water tank and a supply pipeline, is modelled in calculation by a boundary condition. It is known from the experimental data that 4 L of water were supplied from the tank in about 5 s. The volume of the supply pipe is estimated to be 2.1 L. Thus, 1.9 L of the supplied 4 L can reach the simulated lower part of the assembly. The flow rate of the supplied water is not known and need to be estimated. Based on the analysis of the measured water level dynamics in the bundle, it can be concluded that the water flow could be approximated by the exponent function and injection duration is longer than 5 s. It is assumed in calculation that 1.9 kg of water entered the lower part of the assembly according to the exponential law. The flow rate of the supplied water is calculated formulas follows:

$$\dot{m} = \begin{cases} 0, & t \le t_1 \; or \; t > t_1 + \Delta t \\ m \cdot \dfrac{e^{\frac{\Delta t-(t-t_1)}{A}}-1}{A \cdot e^{\frac{\Delta t}{A}}-(\Delta t-1)}, & t > t_1 \end{cases} \quad (2)$$

where:
$\dot{m}$: mass flow rate kg/s;
$m = 1.9$: mass of supplied water, kg;
$t_1 = 7179$: time of quenching initiation, s;
$\Delta t = 19$: duration of water supply, s;
$A = 8$: adjustable parameter characterizing the steepness of the curve, s.

Figure 68 shows the time dependence of the mass flow rate of the supplied water from the tank. The description of the experiment indicates that an unexpected leakage of coolant with an unknown flow rate occurred in the pipeline between the flow meter location and the bundle inlet. The readings of the water level indicate a significant delay in the supply of water to the bundle. Preliminary calculations shows that the delay could be ~18 s and about 17 g/s of the coolant did not reach the assembly. The boundary condition that is used in SOCRAT model is shown in Fig. 69.

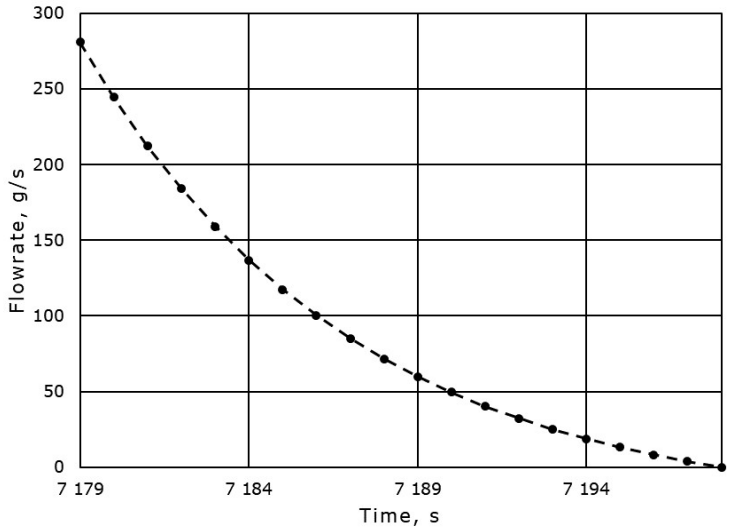

FIG. 68. Fast water injection flow rate.

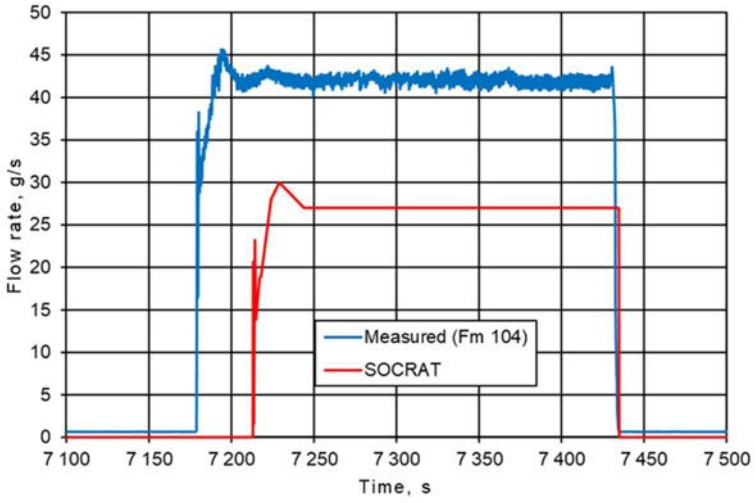

FIG. 69. Quenching flow rate.

4.3.RESULTS OF NOMINAL CASE

A comparison of the electric parameters of heated fuel rod imitators in the experiment and the calculation is shown in Fig. 70. The calculated value of the electric current per rod lies between the values measured in the inner and outer rings of the imitators. The obtained value of the resistivity per rod is in good agreement with the experimental data. Since the resistivity of the imitators is a function of temperature, a good agreement with the measurements suggests that the evolution of the average temperature of the imitators is correctly reproduced in the calculation. The calculation shows that only 60% of the total electrical power is released in tungsten heaters, the rest of the power is released in the current leads.

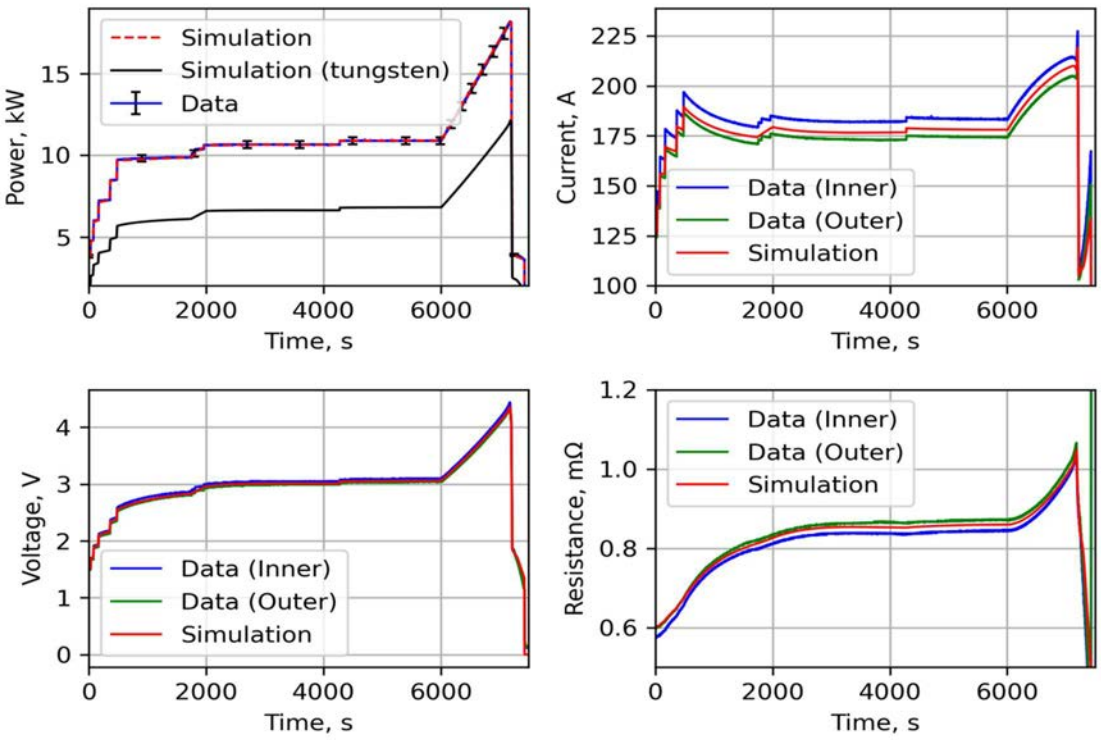

FIG. 70. Electric behavior of a rod bundle.

A comparison of the calculated and measured temperature dynamics in the assembly at the 950 mm level at the beginning of the pre-oxidation phase is shown in Fig. 71. This elevation corresponds to a hot spot of the bundle in the transient stage. It can be seen that in the first heating stage, the calculated value of the shroud inner temperature underestimates the measured values by ~25 K, and when entering the pre-oxidation stage, it fits into the standard measurement uncertainty. The measured azimuthal temperature profile at the shroud is about 30 K at the pre-oxidation phase, therefore, an underestimation of the calculated temperature value by 10 K is in a good agreement with the measurements.

The calculated temperature of heated fuel rod imitators (average for all heated rods) lies within the spread of the locally measured values over the entire considered time interval. The temperature of the central unheated rod is underestimated by ~50 K in the calculation. This is most likely because in the model, the gas flow in the bundle is modelled in a one dimensional approximation without radial profile. In the experiment, the gas temperature in the central part of the assembly could be significantly higher than that on the periphery.

The axial profiles of temperature along the heated fuel rod imitators and inner shroud surface at the end of the pre-oxidation phase are shown in Fig. 72. The model correctly reproduces the influence of grid spacers located at 50, 550, and 1050 mm on the profile shape, and the predicted profile is in good agreement with the measured one along the heated part of the rods. One can notice a radial non-uniformity at the unheated upper part of the imitators. In that region, the model results lie close to the higher temperature values.

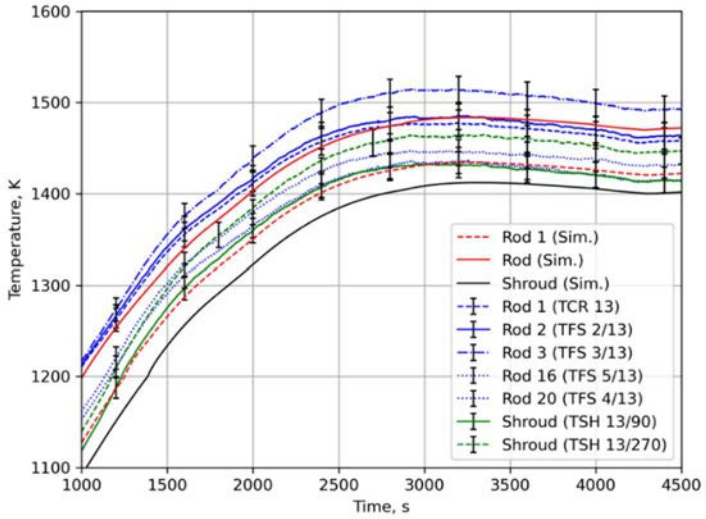

FIG. 71. Temperatures at elevation 950 mm at the beginning of pre-oxidation phase.

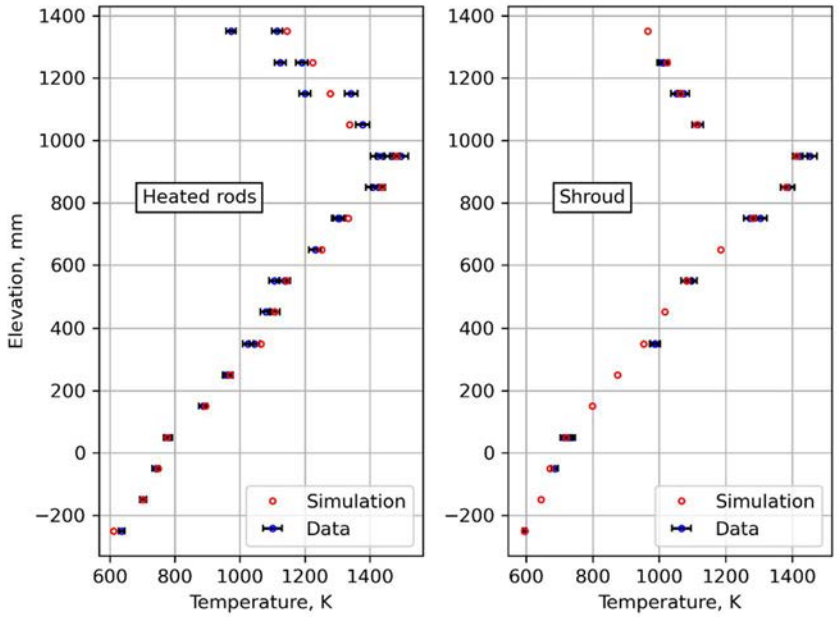

FIG. 72. In-bundle axial profiles of temperature before the transient phase (at 6000 s).

A comparison of calculated and measured temperatures of the bundle in the transient and quenching phases is shown in Fig. 73 indicating that at the beginning of the power increase, the dynamics of the temperature increase in the rods are in good agreement with the measurement data. After reaching ~ 1650 K, all thermocouples located on the fuel rods fail, except for only one (TFS 4/13). A comparison of the average calculated temperature of the fuel rods with the locally measured temperature in the fuel rod #20 shows underestimation of the heating rate in the calculation. However, when water is supplied from the fast injection system, the heating rate in the calculation increases sharply and corresponds to that observed in the experiment. The underestimation of the temperature of the shroud reaches ~ 40 K in the calculation by the time of quenching initiation, however, a sharper increase in temperature is observed when water is supplied which compensates this underestimation.

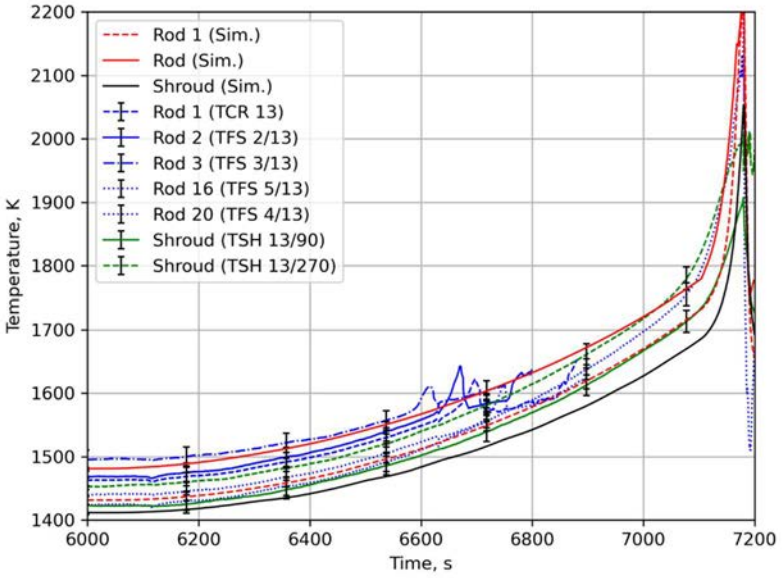

FIG. 73. Temperatures at elevation 950 mm elevation during the transient and quenching phases.

A comparison of temperatures in the assembly at the 950 mm elevation during the quenching phase is shown in Fig. 74. It can be seen that the predicted maximum temperature of the fuel rod imitators is in good agreement with the measured value. On the inner surface of the shroud, the calculation shows a slight overestimation of the maximum temperature. When quenching by the fast water injection system, a sharp decrease in bundle temperatures is observed both in the calculation and experiment. This is probably due to the arrival of relatively cold steam. Then, when the pump is running, the assembly is slowly cooled in the film boiling heat transfer mode. The calculation demonstrates a slightly later wetting of the surfaces than that in the experiment.

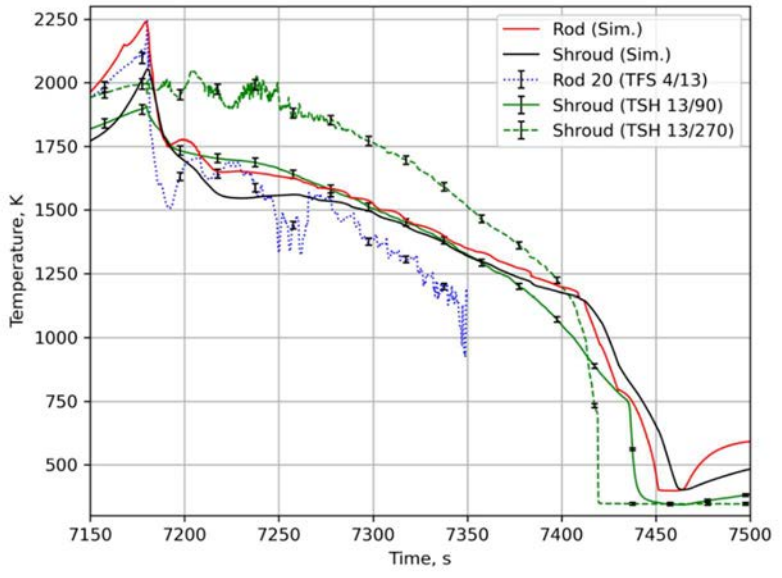

FIG. 74. Temperatures at 950 mm elevation at the quenching phase.

A comparison of the calculated and measured values of the collapsed coolant levels in the bundle is shown in Fig. 75. The calculation results are presented by two curves. The actual mass water level was

calculated based on the void fraction in the hydraulic cells along the test section. The level estimation is based on the total pressure drop between the inlet and outlet of the bundle, with account for the pressure drop due to two phase friction. The sharp spike of the level that occurred in gauge readings when water was supplied by the fast injection system is explained by the pressure drop due to the two-phase flow friction of the gas-liquid mixture in the bundle.

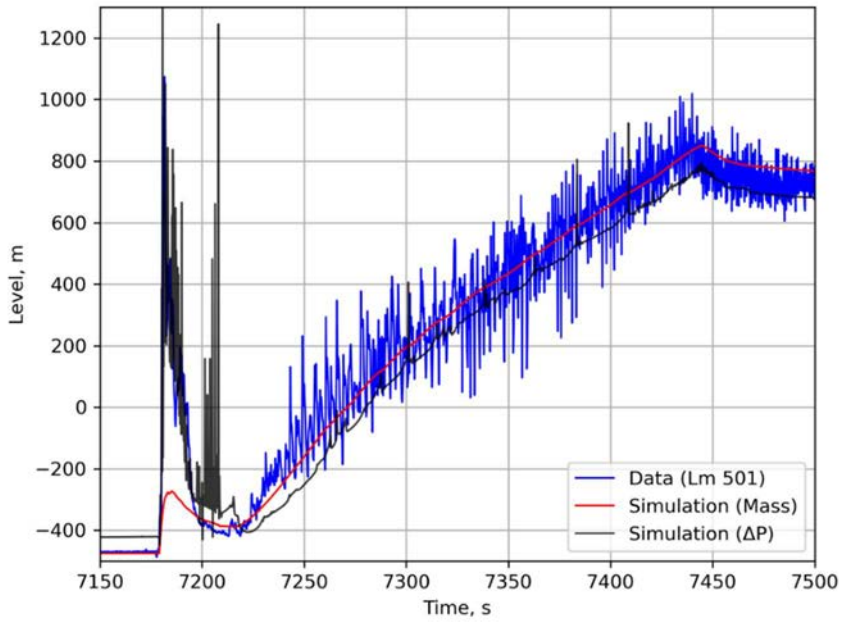

FIG. 75. Collapsed water level.

A comparison of the calculated and measured thicknesses of the ZrO_2 layer on the surface of fuel rod imitators and the angular rod B is shown in Figs. 76 (a) and (b), respectively.

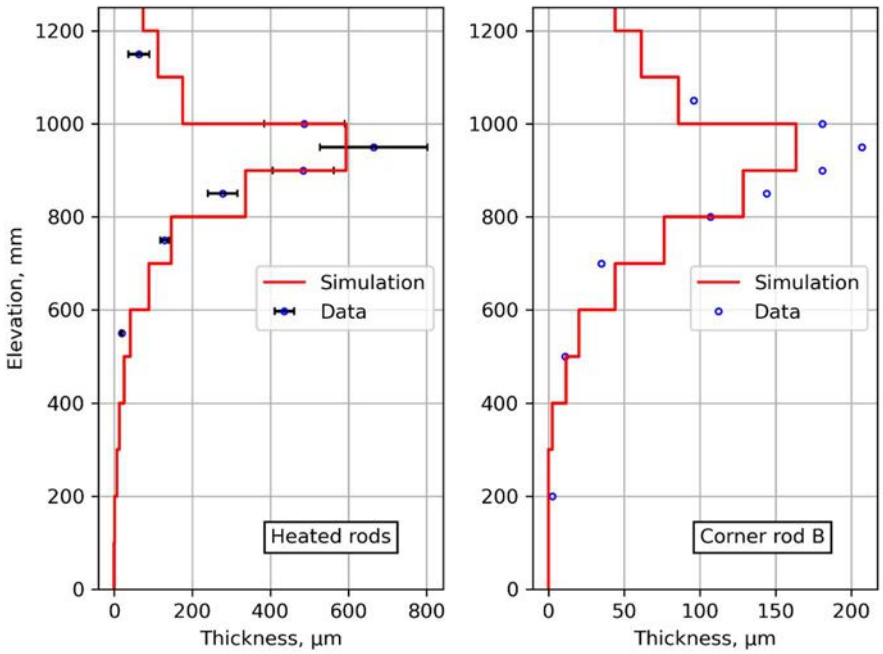

FIG. 76. ZrO_2 layer thickness in (a) heated rod and (b) corner rod B.

For fuel rod simulators, the oxide thicknesses are presented at the end of the experiment. For angular rod B they correspond to the time 6620 s when the rod was removed from the bundle. For comparison with the calculation results, the measurements for fuel rod imitators were averaged over all rods. Measurements are represented by mean values and standard uncertainties. One can see an underestimation of the layer thickness in the upper unheated part of the rods and overestimation in the middle-heated part. In general, the calculated profile is in good agreement with the measurements.

The accumulated mass of H_2 represents an integral flow of H_2 through bundle outlet. A comparison of the calculated and measured values of the total mass of accumulated H_2 and the H_2 flow rate is shown in Fig. 77. Calculated values correspond to the rod bundle outlet, and they account for a time lag between H_2 release to the channel and its appearance at the bundle outlet. Reference case results are summarized in Table 12. The discrepancy between calculations and data is calculated with:

$$E = \frac{S - D}{D} \cdot 100\% \tag{3}$$

where S is a calculation result and D is a measured value.

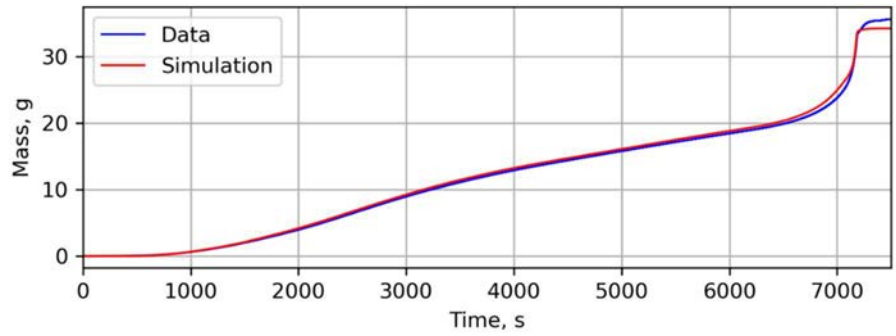

(a)

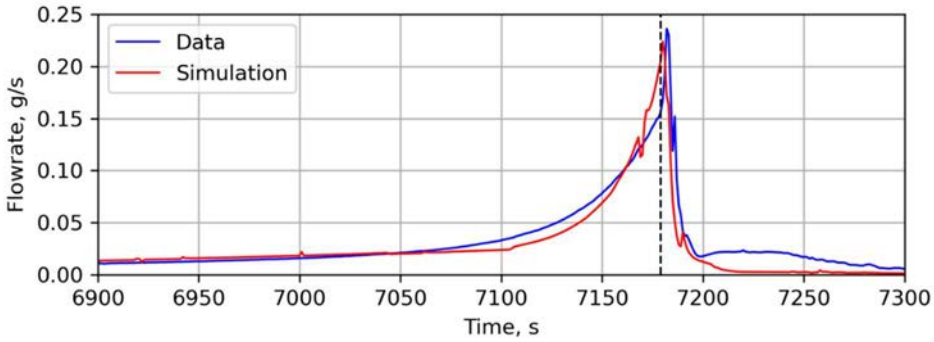

(b)

FIG. 77. (a) Hydrogen mass and (b) hydrogen flowrate.

The SOCRAT overestimates the mass of H_2 accumulated by quenching (FOM #2) by 2%. The calculation result demonstrates that 95% of total mass of H_2 is released at that phase of the experiment, which is in good agreement with measured value 89%. At quenching phase, the calculation shows 57% lower H_2 production (FOM #3). Nevertheless, at that phase a small amount of H_2 was produced, therefore an estimation of total mass of H_2 is only 4% smaller than the measured value (FOM #1). The main data acquisition frequency at QUENCH facility at the beginning of transient phase is changed from

1 to 5Hz. The same value was set in SOCRAT code. The mass spectrometer results have a lower frequency of 1Hz. This means that calculated H_2 production rate needs to be corrected to the mass spectrometer data time scale for proper comparison. The correction is made by linear interpolation of accumulated mass followed by its differentiation. The corrected H_2 production rate is showed on Fig. 77 (b). Uncorrected calculated peak H_2 production rate (FOM #4) was equal to 331 mg/s, while the corrected one is 223 mg/s. Thus, the model underestimates the peak value of H_2 production rate by 5 %.

TABLE 12. REFERENCE CASE RESULTS

FOM #	***S***	***D***	***E***
1	34.2 g	35.7 g	–4 %
2	32.6 g	31.9 g	+2 %
3	1.6 g	3.8 g	–58 %
4	224 mg/s	236 mg/s	–5 %

Comparison of reference case results with measurements shows that the developed model correctly reproduces the rod bundle behaviour observed in the QUENCH-06 experiment.

4.4.DESCRIPTION OF UNCERTAINTY AND SENSITIVITY METHODOLOGY

The uncertainty analysis of experimental results is an integral part of the validation process. The uncertainty is inherent to both the experimental measurements and the numerical predictions. The uncertainty analysis methodology, graphically shown in Fig. 78, is based on the ASME V&V20 standard [40] for computational fluid dynamics and heat transfer as follows [41]:

$$\delta_S = S - T \tag{4}$$

$$\delta_D = D - T \tag{5}$$

where:
D: value of the measured parameter in the experiment that is used to validate the code;
S: calculated value of the measured parameter;
T: true (unknown) value of the parameter;
δ_S: error of the calculated value S;
δ_D: error of the measured value D.

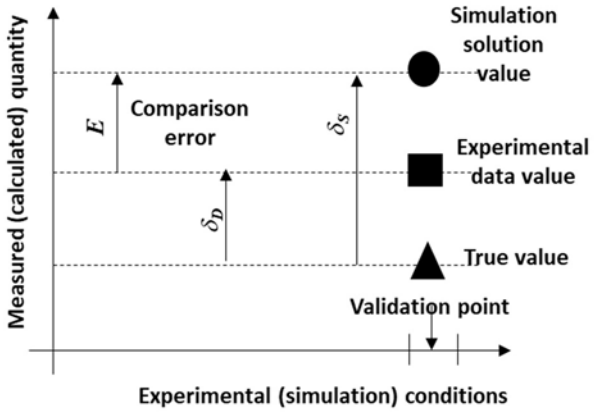

FIG. 78. Schematic nomenclature for uncertainty analysis.

The error E of the calculation result in relation to the measurement, or comparison error in short, is defined by the difference between the calculation S and measurement D. It can be expressed through errors δ_S and δ_D, considering their definitions:

$$E = S - D = (S - T) - (D - T) = \delta_S - \delta_D. \quad (6)$$

The error δ_S of the calculated value has three components:

— δ_{model}, which is due to simplifications and assumptions made in the model (hereafter called "model error" for brevity);
— δ_{num}, resulting from discretization of the system of equations ("numerical error");
— δ_{input}, accounting for lack of knowledge for input data required for calculation ("input data error").

Thus:

$$\delta_S = \delta_{model} + \delta_{input} + \delta_{num}. \quad (7)$$

In a broad context, the term model typically refers to a physical and mathematical representation of a process or phenomenon within a code. However, in specific instances, the concept of a model can be expanded to encompass unalterable elements. For example, when dealing with intricate multiscale and multiphysical processes, the term "model" can include a fixed (immutable) computational submesh. In such cases, the user of a code is restricted to modifying only the initial and boundary conditions for this model.

The purpose of code validation in the proposed approach is to estimate the model error δ_{model}, and for this purpose the following algorithm is considered [40]. The combination of the above expressions gives an expression to determine the comparison error E:

$$E = \delta_S - \delta_D = \delta_{model} + \delta_{input} + \delta_{num} - \delta_D \quad (8)$$

to obtain:

$$\delta_{model} = E - (\delta_{input} + \delta_{num} - \delta_D). \quad (9)$$

The model error δ_{model} is determined not only by the comparison error E, but also by the input data error, numerical error and measurement error. In the case when the errors δ_D, δ_{num} and δ_{input} can be neglected, the δ_{model} error coincides with the comparison error E. On the right side of the equation for δ_{model} the sign and modulus are known only for the comparison error E. Assuming randomness and independence of all quantities in the method [40] the validation uncertainty $u_{val}$is introduced as follows:

$$u_{val} = \sqrt{u_{input}^2 + u_{num}^2 + u_D^2} \quad (10)$$

where u_{input}, u_{num}, u_D are standard uncertainties corresponding to errors δ_{input}, δ_{num}, δ_D. In case when the measured quantity is calculated by reduction equation and shares input parameters with

simulation model, errors δ_{input} and δ_D cannot be considered as independent. In this case validation uncertainty can be expressed as:

$$u_{val} = \sqrt{u_{input+D}^2 + u_{num}^2} \tag{11}$$

The method of transforming the probability distributions of input parameters into a probability distribution of the output is used to estimate the uncertainties u_{input} and $u_{input+D}$. Here it is assumed that any input parameter with a fixed value corresponds to a group of model parameters (relate to model error δ_{model}). While any varied parameter is attributed to a group of input parameters (relates to input data error δ_{input}) and is addressed in uncertainty analysis.

Schematic algorithm of Monte Carlo approach in case of common input parameters for data and calculation is shown in Fig. 79. Here $I_1, \dots I_M$ is a set of input parameters for data calculated by data reduction equation. Its element can be a directly measured value, a reference data or a result of other data reduction equation. The set $I_1, \dots I_K$ contains the input parameters for simulation. In the considered case these two sets have an intersection area. For each input parameter a PDF need to be prescribed. An uncertainty range can be estimated based on experimental data, characteristics of the measuring device and measuring procedure or expert judgement. A type of PDF is selected based on the distribution of repeated measurements or the principle of maximum of the Shannon entropy [42]. To propagate input uncertainties for data reduction equation and calculation, several N Monte Carlo simulations need to be performed with randomly chosen inputs. For each pair (data and calculation result) a comparison error E_i is estimated. An absolute value of comparison error is calculated as follows:

$$E_i = S_i - D_i \tag{12}$$

Alternatively, the relative value of E_i is calculated with:

$$E_i = \frac{S_i - D_i}{\bar{D}} \tag{13}$$

where S_i and D_i are random values of calculation and measurement results and $\bar{D}$ is an average measurement result. Average value of comparison error $\bar{E}$ is calculated with:

$$\bar{E} = \frac{1}{N}\sum_{i=1}^{N} E_i \tag{14}$$

Validation uncertainty $u_{input+D}$ for case of dependent data and calculation is estimated by unbiased estimator for the population variance:

$$u_{input+D}^2 = \frac{1}{N-1}\sum_{i=1}^{N} (E_i - \bar{E})^2 \tag{15}$$

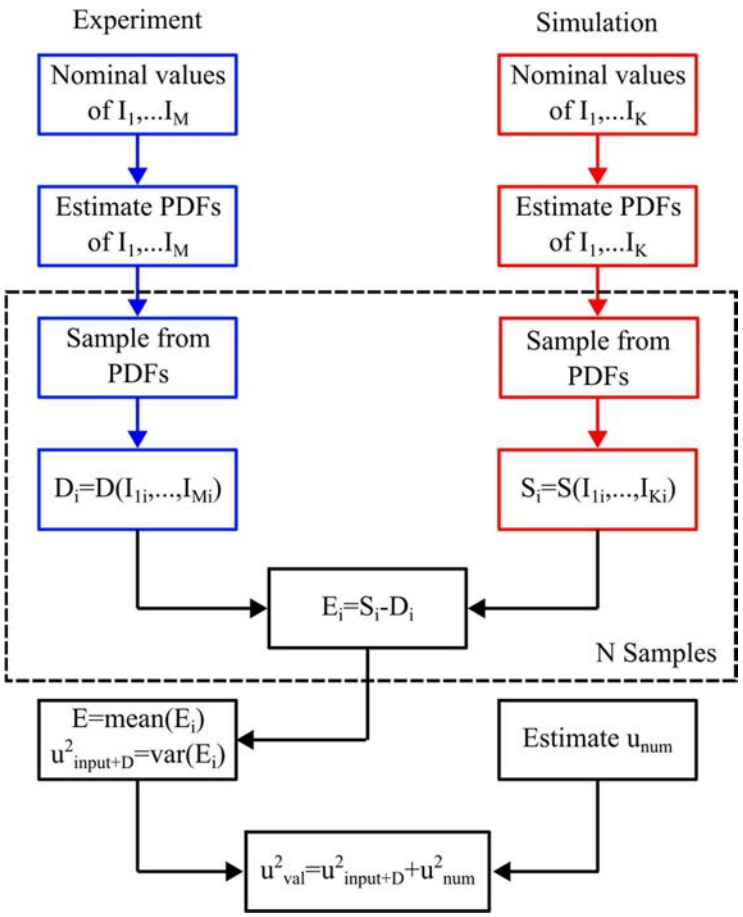

FIG. 79. Monte Carlo approach when data and calculation have common parameters.

The estimation of u_{num} is based on the Richardson extrapolation [40]. The advantage of using Richardson extrapolation is that it can be applied to non-uniform grids and can be used to estimate the uncertainty u_{num} for any calculated parameter (local and integral) [43]. A standard numerical uncertainty u_{num} is estimated according to ASME V&V20 procedure based on grid convergence index (GCI):

$$u_{num} = GCI/k \tag{16}$$

$$GCI = \frac{F_s \cdot e_a}{r^p - 1} \tag{17}$$

$$e_a = \left|\frac{S_{coarse} - S_{fine}}{S_{fine}}\right| \tag{18}$$

where expansion factor $k = 1.15$ and safety factor $F_s = 3$ are provided for two grid studies, r is a grid refinement factor, p is order of numerical method, S_{coarse} and S_{fine} are simulation results on coarse and fine grids respectively.

Uncertainty analysis is supplemented by sensitivity analysis [44]. The purpose of sensitivity analysis is to detect a monotonic correlation between the input parameters and the calculation results. Sensitivity analysis is performed based on Spearman's rank correlation coefficient. Using this correlation coefficient provides an advantage of the independence between the analysis result and the PDFs of the parameters, and the non-sensitivity to outliers in a series of random values. The determination of the

presence of correlation is formulated via statistical testing of the null hypothesis H_0 for the independence of two parameters. The *J*-statistics and ρ-statistics are used to test the null hypothesis:

$$J = \frac{\rho}{2} \cdot \left(\sqrt{N-1} + \sqrt{\frac{N-2}{1-\rho^2}} \right) \tag{19}$$

$$\rho = \frac{\sum_{i=1}^{N} (R_i - \bar{R}) \cdot (S_i - \bar{S})}{\sqrt{\sum_{i=1}^{N} (R_i - \bar{R})^2 \cdot \sum_{i=1}^{N} (S_i - \bar{S})^2}} \tag{20}$$

where N is the number of observations, ρ is Spearman's rank correlation coefficient, R_i and S_i are the ranks of observations, $\bar{R} = \bar{S} = (N+1)/2$. Critical values of *J*-statistics and ρ-statistics are estimated:

$$J_{cr}(\alpha) = \frac{1}{2} \cdot u_\alpha + \frac{1}{2} t_\alpha (N-2) \tag{21}$$

$$\rho_{cr}(\alpha) = \frac{u_\alpha}{\sqrt{N-1}} \tag{22}$$

where u_α–α-quantile of standard normal distribution, $t_\alpha(N-2)$–α-quantile of Student's t-distribution with $N-2$ degrees of freedom. Null hypotheses is rejected at α confidence level, if

$$J_{cr}\left(\frac{1+\alpha}{2}\right) \leq |J| \tag{23}$$

$$\rho_{cr}\left(\frac{1+\alpha}{2}\right) \leq |\rho| \tag{24}$$

The methodology described above is implemented in the ELENA module of SOCRAT code [37]. The calculation process for uncertainty and sensitivity analysis is presented in Fig. 80. The process can be described by following steps:

1) Preparation of template input deck for SOCRAT code with marked places for insertion of random values of input parameters;
2) Preparation of input deck for ELENA module with description of PDFs, random sample size, description of results to be analysed;
3) Generation of random matrix and set of input decks for SOCRAT code;
4) Execution of *N* simulations;
5) Collecting results of prescribed FOM;
6) Uncertainty and sensitivity analysis of FOMs.

Generation of random matrix is one of the most critical stages of uncertainty analysis. Each vector of random values needs to meet certain criteria: fitting the desired PDF and independency from other random vectors. Algorithm of random vector generation is schematically shown on Fig. 81.

The process begins with the initiation of the random value generator using a random seed value. The random vector generated with this seed is then subjected to the Kolmogorov-Smirnov test to assess its goodness of fit. If the test does not meet the specified confidence level, a new seed needs to be chosen. For those vectors that successfully pass the test, pair correlations with existing random vectors are computed using Spearman's rank correlation. If the null hypothesis of independence is rejected at the designated confidence level, a new random seed is selected. Conversely, if the null hypothesis is not

rejected, the current random vector is accepted for further use. This method ensures that the generated random values conform to the required statistical properties and relationships.

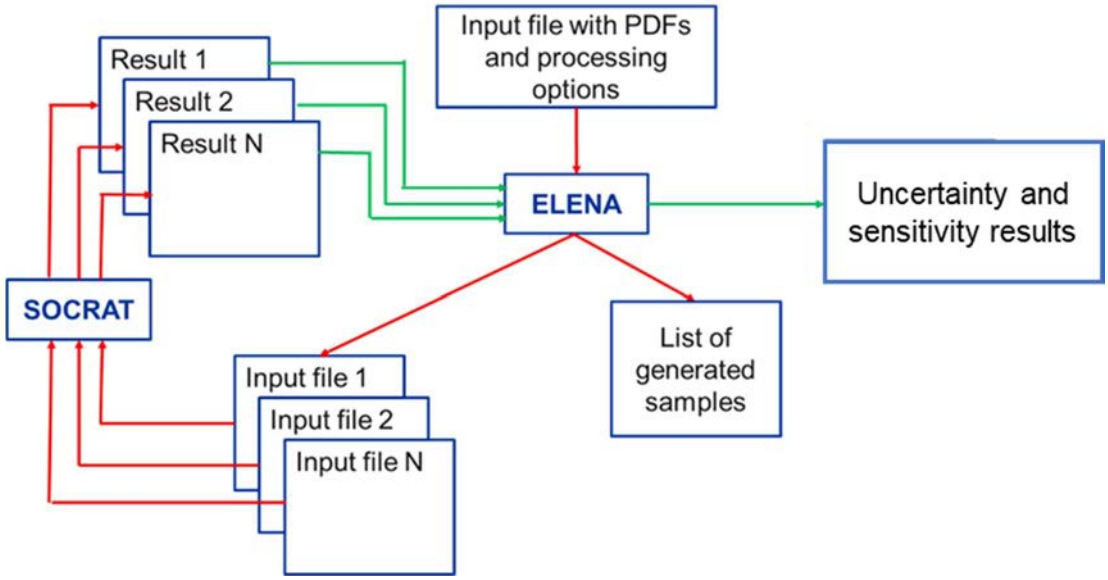

FIG. 80. Calculation scheme of ELENA module.

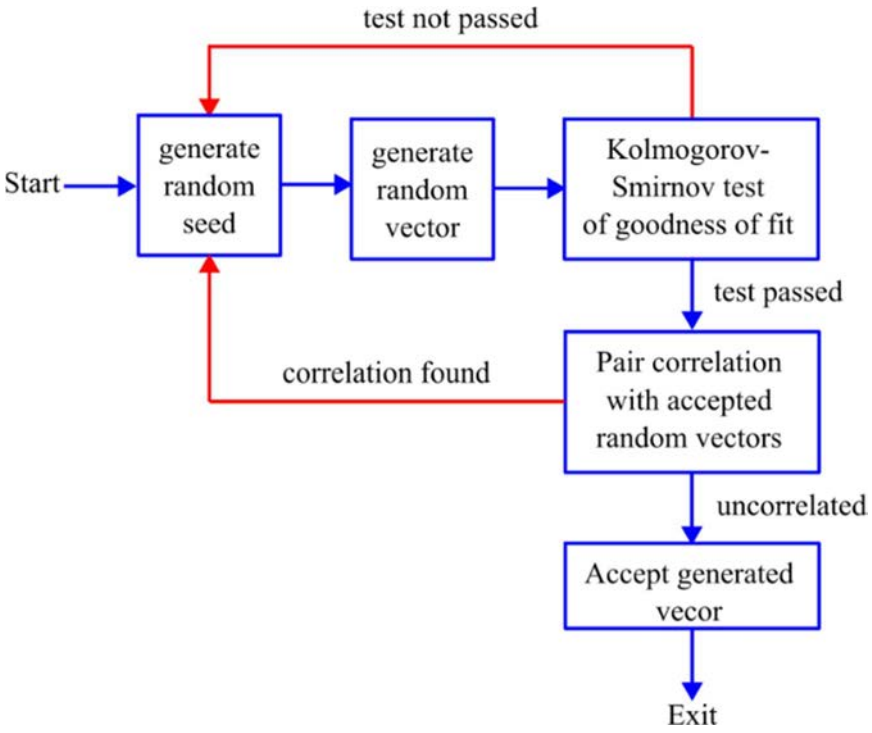

FIG. 81. Generation of single random vector.

4.5.RESULTS OF THE UNCERTAINTY AND SENSITIVITY ANALYSIS

For uncertainty and sensitivity analysis the mass of H_2 accumulated at different stages and the peak H_2 production rate was selected as shown in Table 13.

TABLE 13. FIGURES OF MERIT

#	Parameter
1	Total mass of accumulated H_2
2	Mass of H_2 accumulated by quenching
3	Mass of H_2 accumulated at quenching
4	Peak H_2 production rate

The geometrical parameters considered in the uncertainty analysis correspond to the list as provided by KIT. The time of the main water injection start is excluded from the list. The reason is that this time is not known from the flow meter readings and represents a fitting parameter in calculation. Also, the uncertainty of gas flow rate measurement at the QUENCH facility is reported by experimenters to be 0.5%. Therefore, the standard deviations for parameters 9 and 10 are reduced from 2% to 0.5%. The temperature of the gases and water supplied was measured by NiCr/Ni thermocouples. According to information from the experiment, the uncertainty of temperature measurement by thermocouples is 2K. Therefore, the standard deviation for parameter 13 is changed from 2 % to 2 K. The temperature of the vapor-argon mixture is also added to the list of uncertain input parameters, the standard deviation for it is set to 2K. Parameters 15–23 relate to code models and are not addressed in the uncertainty analysis. Table 14summarizes input uncertain parameters addressed in uncertainty and sensitivity analysis.

TABLE 14. INPUT PARAMETERS FOR UNCERTAINTY AND SENSITIVITY ANALYSIS

#	Parameter	Uncertainty Range	Probability Distribution
1	Rod pitch (mm)	14.3 ± 0.15	Uniform
2	Fuel pellet simulator (ZrO_2) external diameter (mm)	9.15 ± 0.02	Uniform
3	Cladding thickness (mm)	0.725 ± 0.00725	Uniform
4	Internal diameter shroud (mm)	80 ± 0.8	Uniform
5	Thickness of the shroud (mm)	2.38 ± 0.023	Uniform
6	Thickness of the Insulator (mm)	37.0 ± 0.37	Uniform
7	Gas inlet temperature (K)	± 2K	Gauss
8	Argon mass flow rate at the bundle inlet (kg/s)	± 0.5%	Uniform
9	Steam mass flow rate at the bundle inlet (kg/s)	± 0.5%	Uniform
10	Pressure at the bundle outlet (bar)	± 2%	Uniform
11	Electrical power (kW)	± 2%	Uniform
12	Quench water mass flow rate at the bundle inlet (kg/s)	± 0.2%	Uniform
13	Quenching water temperature (K)	± 2K	Gauss
14	Fuel/cladding internal pressure (bar)	± 2%	Uniform

To analyse the dependence of the calculation results on grid (nodalization scheme) refinement, an additional calculation was made with a nodalization that has twice as many cells. A comparison of the measured and calculated axial temperature profiles along the fuel rod imitators and the inner surface of the shroud at the end of pre-oxidation phase for two nodalizations is shown in Figs. 82 (a) and (b), respectively. The good agreement of the temperature profiles for two nodalization schemes demonstrates that the simulation results converge, and the number of cells used in reference case is sufficient. There is a good agreement of both calculations with the experimental values. The largest deviation is observed in the upper part of the assembly (above 1000 mm) probably due to significant radial assembly temperature profile, while in the calculation all heaters have the same (average) temperature. The measured H_2 accumulated during the experiment and H_2 production rate with calculated values using two nodalizations are shown in Fig. 83.

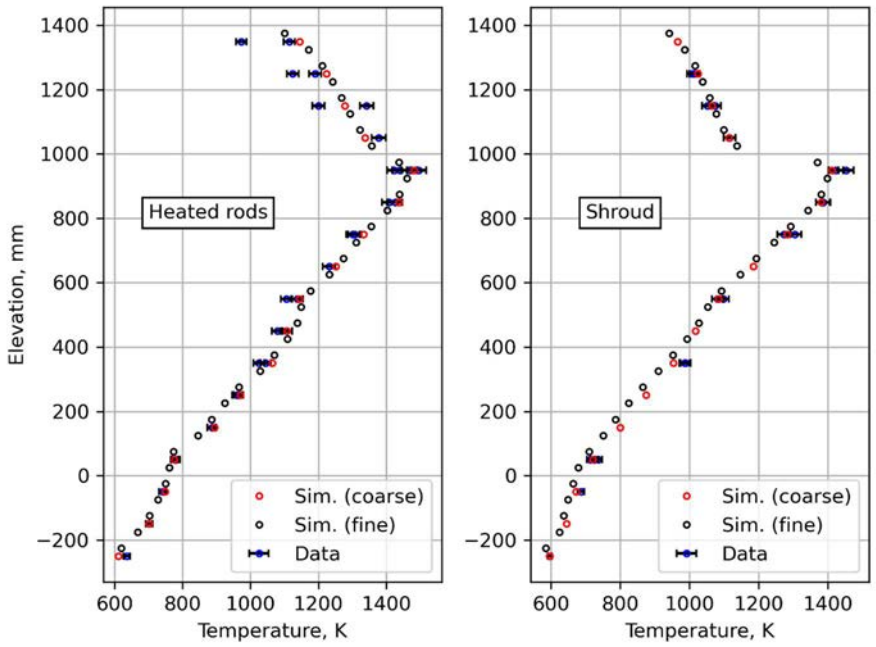

(a) *(b)*

FIG. 82. In-bundle axial temperature profiles before the transient phase (at 6000 s): (a) heated rods and (b) shroud.

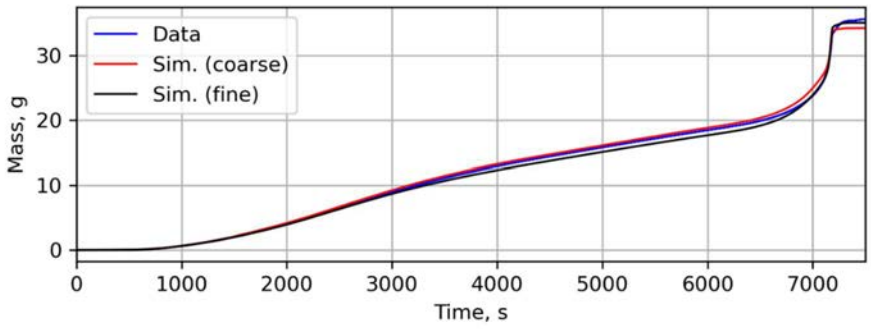

(a)

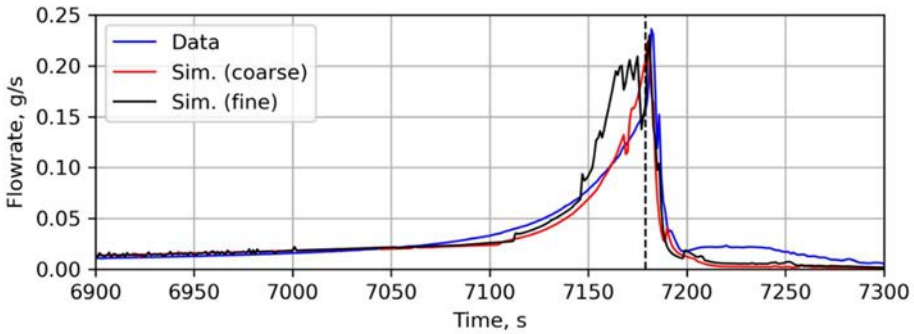

(b)

FIG. 83. (a) Hydrogen mass and (b) hydrogen flowrate.

The fine nodalization shows higher production rate at transient phase. This could be explained by a less sharp temperature profile at hot spot (900 mm–1000 mm in Fig. 82) produced by fine nodalization. Using the fine nodalization in additional 0.5 g of H_2 produced before the quenching phase and additional 0.4 g at quenching phase. Peak H_2 production rates corrected to mass spectrometry acquisition frequency are quite close: 224 mg/s for coarse nodalization and 230 mg/s for fine nodalization. Table 14 summarizes the grid refinement results (grid refinement factor $r = 2$, order of method $p = 1$). Numerical uncertainty for H_2 mass produced during bundle oxidation in steam is quite low and comparable with measurement uncertainty. On the other hand, a high numerical uncertainty at the quenching phase is found. Quite a small amount of H_2 is released, and a small deviation at the bundle cooling rate can result in a noticeably different H_2 production. This change is negligibly small compared to total H_2 mass.

TABLE 14. NUMERICAL UNCERTAINTY ESTIMATION.

FOM #	S_{coarse}	S_{fine}	e_a, %	GCI, %	u_{num}, %
1	34.2 g	35.1 g	2.6	7.8	6.8
2	32.6 g	33.1 g	1.5	4.5	3.9
3	1.6 g	2.0 g	20.0	60.0	52.2
4	224 mg/s	230 mg/s	2.6	7.8	6.8

To perform an uncertainty analysis, a sample size of 1000 is generated for each input parameter. When generating samples, seed numbers for the pseudo random number generator are selected randomly, and each resulting sample is qualified. The qualification consisted of performing the Kolmogorov-Smirnov agreement test making sure that the obtained sample corresponds to the required distribution function and checking the paired correlation between the newly generated sample and the ready samples of input parameters. The pair correlation is tested based on the Spearman's nonparametric criterion. A comparison of empirical and analytical cases for each input parameter is shown in Fig. 84. Qualification ensures that uncertainty and sensitivity analysis results will not suffer from incorrect input parameters.

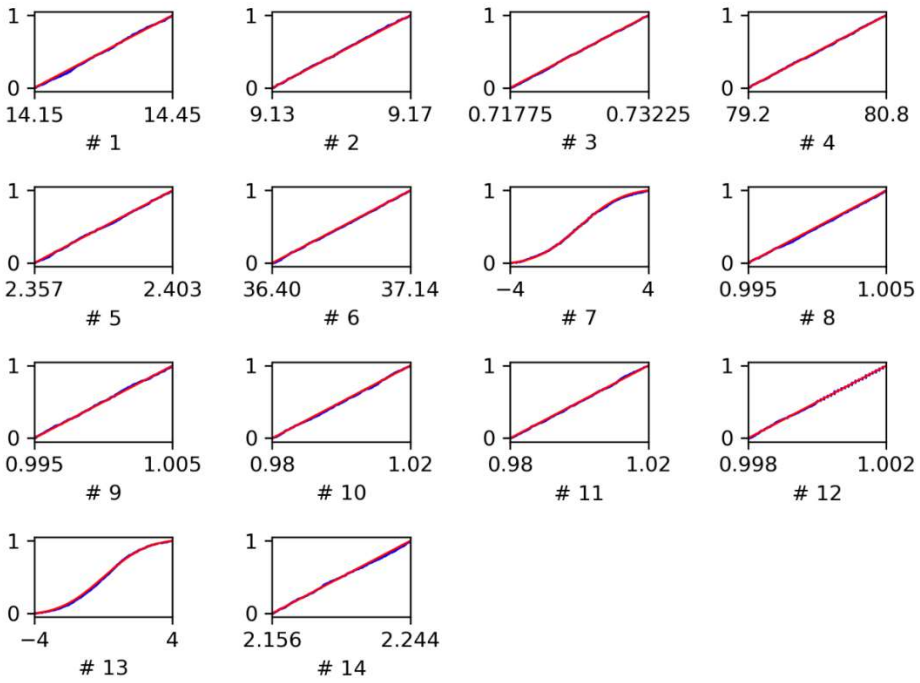

FIG. 84. Empirical (▪) and analytical (▪) CDFs for input parameters.

Monte Carlo calculations are performed using the obtained matrix of random values of input parameters. Although the experiment itself is performed under conditions when the temperatures of the claddings are close to melt release, the results of calculations shows that two variants are likely. One group of calculations shows melt release at least at one axial cell, and in the other group, the bundle stayed intact till the end of the test.

The results of the numerical analysis of the H_2 production and the accumulated mass have a common input uncertain parameter with data. In [1], it is stated that the hydrogen mass flow rate $\dot{m}_{H_2}$ at the assembly outlet is an indirectly measurable parameter and is determined by the following data reduction equation:

$$\dot{m}_{H_2} = \frac{M_{H_2}}{M_{Ar}} \cdot \frac{C_{H_2}}{C_{Ar}} \cdot \dot{m}_{Ar} \tag{25}$$

where $\dot{m}_{Ar}$ – inlet argon flow rate kg/s; M_{H_2} и M_{Ar} – H_2 and argon molar mases, kg/mole; C_{H_2} и C_{Ar} – molar concentrations measured by mass spectrometer. The mass flow rate of argon is a common input uncertain parameter for the experimentally measured flow rate of H_2 and the calculation.

The H_2 mass accumulated by the end of the experiment is obtained by numerical integration of the time dependence of H_2 production; therefore, this consideration is valid to the mass as well. To perform the uncertainty analysis according to the proposed methodology, a vector of random values is generated for the experimentally measured H_2 flow rate and H_2 mass according to:

$$D_i = \overline{D} \cdot \frac{I_{8,i}}{\bar{I}_8} \tag{26}$$

where D_i и $\overline{D}$ – random and best estimate of the measurement, $I_{8,i}$ и $\bar{I}_8$ – random and best estimate of the argon mass flow rate.

Convergence of Monte Carlo calculations is demonstrated by comparing mean value of a comparison error $\bar{E}$ for the first half of series with $\bar{E}$ obtained from all calculations. Table 15 shows that $N = 1000$ calculations are enough to estimate average comparison error because difference between estimations Δ is one order of magnitude smaller than estimated values of $\bar{E}$.

TABLE 15. CONVERGENCE OF MONTE CARLO RESULTS

FOM #	$\bar{E}(N = 500)$	$\bar{E}(N = 1000)$	Δ
1	+4.2 %	+4.0 %	–0.2 %
2	+7.9 %	+8.2 %	+0.3 %
3	–27.8 %	–31.2 %	–2.4 %
4	+4.4 %	+4.5 %	+0.1 %

Table 16 summarizes uncertainty analysis results considering all calculation results, and Table 17 summarizes results for the intact bundle.

A comparison of values of $u_{\text{input}+D}$ in both tables shows that melt release increases the calculation results uncertainty. Limiting the analysis by results with intact geometry gives a biased estimation of the mean value $\bar{S}$.

TABLE 16. UNCERTAINTY ANALYSIS RESULTS

FOM #	$\bar{S}$	$\bar{D}$	$\bar{E}$, %	$u_{\text{input+D}}$, %	u_{num}, %	u_{val}, %
1	37.1 g	35.7 g	4.0	22.3	6.8	23.3
2	34.5 g	31.9 g	8.2	17.6	3.9	18.0
3	2.6 g	3.8 g	–31.2	71.7	52.2	88.7
4	247 mg/s	236 mg/s	4.5	52.8	6.8	53.2

TABLE 17. UNCERTAINTY ANALYSIS RESULTS (INTACT ONLY).

FOM #	$\bar{S}$	$\bar{D}$	$\bar{E}$, %	$u_{\text{input+D}}$, %	u_{num}, %	u_{val}, %
1	31.0 g	35.6 g	–13.2	6.7	6.8	9.5
2	29.9 g	31.9 g	–6.2	6.0	3.9	7.2
3	1.1 g	3.8 g	–72.0	14.4	52.2	54.1
4	149.9 mg/s	236 mg/s	–36.5	24.4	6.8	25.3

For clarity and convenience of physical interpretation of the results, it is easier to examine two groups of results separately. For $\alpha = 0.95$ confidence level and $N = 502$ number of observations $J_{cr} = 1.962$ and $\rho_{cr} = 0{,}088$. Both sensitivity coefficients J and ρ are presented in Tables 18 and 19 respectively. Coefficients that have absolute values higher than critical ones are highlighted in bold.

TABLE 18. SENSITIVITY COEFFICIENTS (INTACT)

Par#	FOM #1		FOM #2		FOM #3		FOM #4	
	ρ	J	ρ	J	ρ	J	ρ	J
1	-0.082	-1.848	-0.078	-1.754	**-0.102**	**-2.290**	**-0.091**	**-2.043**
2	-0.021	-0.466	-0.051	-1.133	**0.095**	**2.127**	**0.119**	**2.661**
3	-0.047	-1.063	-0.072	-1.622	0.026	0.578	0.047	1.053
4	-0.038	-0.860	-0.039	-0.880	-0.053	-1.178	-0.057	-1.282
5	0.002	0.050	0.004	0.086	-0.002	-0.043	-0.007	-0.159
6	0.011	0.241	0.010	0.234	-0.001	-0.011	-0.011	-0.253
7	0.037	0.835	0.042	0.929	0.015	0.342	0.022	0.485
8	0.051	1.147	0.053	1.182	0.051	1.152	0.044	0.982
9	**-0.113**	**-2.527**	**-0.115**	**-2.573**	**-0.098**	**-2.206**	**-0.090**	**-2.026**
10	0.004	0.090	-0.001	-0.018	0.021	0.466	0.012	0.260
11	**0.886**	**31.327**	**0.903**	**33.537**	**0.818**	**25.030**	**0.797**	**23.666**
12	-0.056	-1.251	-0.052	-1.166	-0.071	-1.596	-0.060	-1.343
13	0.008	0.181	0.006	0.139	0.013	0.293	0.005	0.101
14	0.015	0.337	0.013	0.300	0.028	0.636	0.011	0.251

It can be seen from Table 18 that the total mass of H_2 (FOM #1) in the calculations without melting is positively correlated to the electrical power (parameter 11), and negatively correlated to the steam flow rate at the assembly inlet (parameter 9). The positive correlation with the electrical power may be because increasing the supplied power results in respective increase of the power generated in the tungsten heater and, consequently, increase of the temperature of zirconium claddings in the bundle. Due to the positive exponential dependence of the zirconium oxidation rate on temperature, the mass of released H_2 increases at a fixed time.

TABLE 19. SENSITIVITY COEFFICIENTS (MELTED)

Par#	FOM #1		FOM #2		FOM #3		FOM #4	
	ρ	J	ρ	J	ρ	J	ρ	J
1	-0.044	-0.976	-0.021	-0.447	-0.069	-1.535	-0.050	-1.107
2	**0.215**	**4.857**	**0.184**	**4.131**	**0.202**	**4.546**	**0.215**	**4.851**
3	**0.114**	**2.559**	**0.105**	**2.346**	**0.113**	**2.532**	**0.104**	**2.324**
4	-0.034	-0.747	-0.030	-0.664	-0.067	-1.498	-0.031	-0.697
5	-0.069	-1.548	-0.075	-1.680	-0.070	-1.552	**-0.093**	**-2.070**
6	0.006	0.139	0.032	0.716	-0.024	-0.554	0.036	0.806
7	**0.138**	**3.085**	**0.166**	**3.719**	0.062	1.374	**0.120**	**2.685**
8	-0.002	-0.046	-0.002	-0.053	0.039	0.875	-0.039	-0.869
9	-0.043	-0.948	-0.032	-0.711	-0.041	-0.921	0.009	0.206
10	-0.024	-0.535	-0.064	-1.436	0.035	0.777	0.025	0.563
11	**0.666**	**17.361**	**0.703**	**18.842**	**0.441**	**10.383**	**0.433**	**10.169**
12	0.015	0.339	0.029	0.646	0.014	0.316	0.001	0.029
13	0.049	1.102	0.051	1.133	0.045	0.995	0.004	0.098
14	0.026	0.583	0.036	0.798	0.026	0.568	0.045	1.006

The negative correlation with the flow rate of the supplied steam is probably due to the fact that a higher flow rate of steam provides a better heat sink from the fuel rods, that results in lower temperatures of the claddings. The same correlations were obtained for mass of H_2 accumulated by quenching (FOM #2). As it follows from Table 19, the mass of H_2 accumulated at quenching (FOM #3) has a positive correlation with the electrical power (parameter 11) and the pellet diameter (parameter 2), and a negative correlation with rod pitch (parameter 1) and the steam flow rate (parameter 9). The explanation for its correlations with electrical power and steam flow rate is the same as that was provided above for the correlation of total mass of H_2.

In SOCRAT, the rod pitch value is used to determine a free volume in the bundle that can be filled with the melt, and it is also used for calculation of view factors in the radiative heat transfer model. Since the considered calculation results are where melt release did not occur, the first mentioned role of rod pitch is not applicable. When the rod pitch increases, larger surface of the rods is exposed to the inner surface of the shroud. This leads to an increase of the heat sink from the bundle and decrease of the bundle temperatures. At the quenching phase the radiative heat transfer dominates and determines the evolution of bundle temperatures, which means that higher heat sink leads to smaller H_2 production. The variation of the pellet diameter is implemented in calculations in such a way that its increase is accounted for in the decrease of gap thickness between the pellet and the cladding. All other inputs being equal, setting a larger pellet size provide smaller thermal resistance between the heater and the cladding. During an intense vapor-zirconium reaction in such calculation, stronger positive feedback between the oxidation intensity and the local electrical power will be observed. As a result, this can lead to a faster increase in the total power in the oxidizing cell (electrical and chemical) and faster increase of the cladding temperature, which will provide a higher value of the H_2 produced. The same results were obtained for peak H_2 production rate (FOM #4) in calculations without melting.

The scatter plots for FOMs with total electric power (parameter 11) are shown in Figs. 103–106. One can see a strong positive correlation between FOMs and input uncertain parameter. An increase in total electric power leads to an increase in the mass of H_2 and its peak production rate in both groups of

calculations, with intact geometry by the end of the test and with melt release. These scatter plots confirm the conclusion made from the correlation analysis. The mass of H_2 in calculations without melting varies from ~25 g to ~40 g. The observed boundary between calculations series without melting and a series in which at least one cell got molten is not clear. It is impossible to draw an unambiguous conclusion that a decrease of electrical power would prevent the assembly melting, even if other parameters are left uncertain.

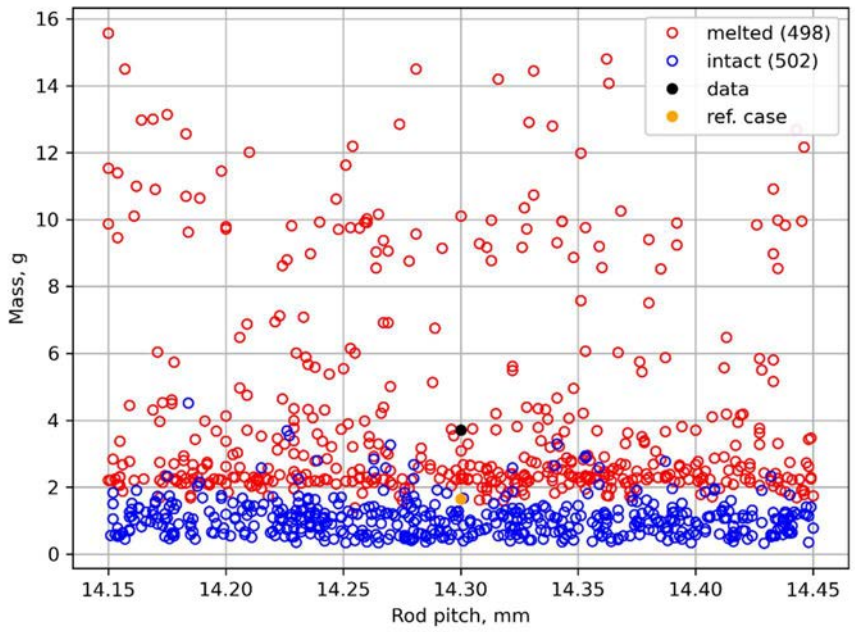

FIG. 85. Mass of accumulated H_2 at quenching (FOM #3) vs rod pitch (#1).

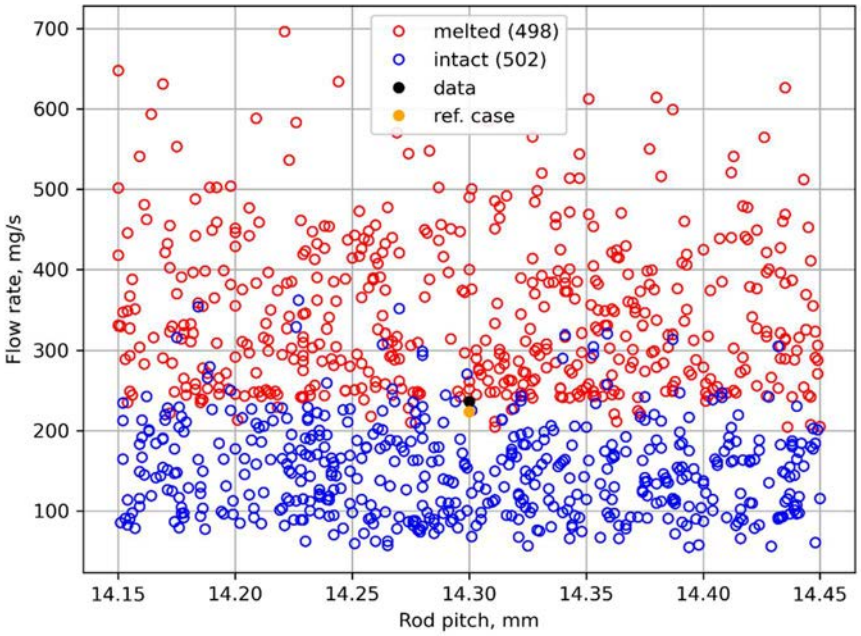

FIG. 86. Peak H_2 production rate (FOM #4) vs vs rod pitch (#1).

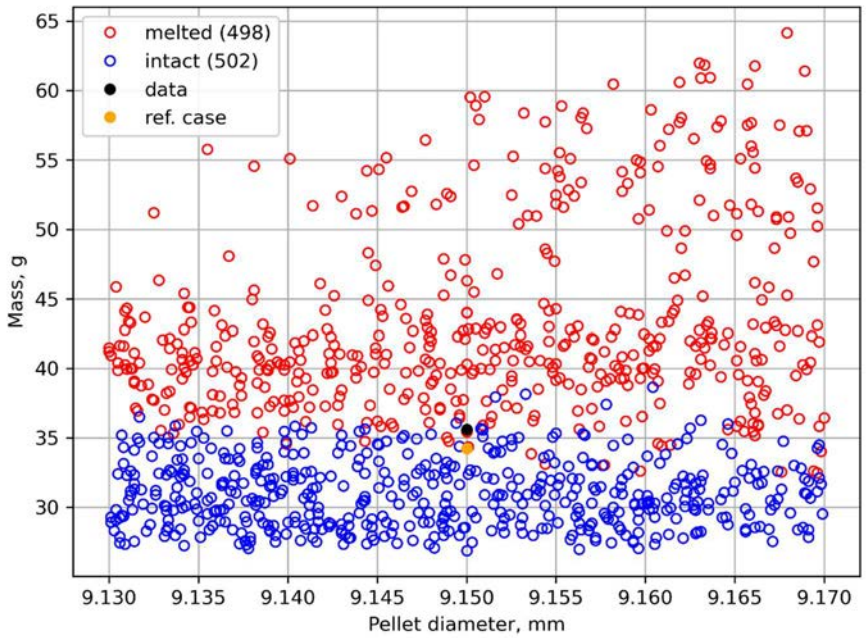

FIG. 87. Total mass of H_2 (FOM #1) vs pellet diameter (#2).

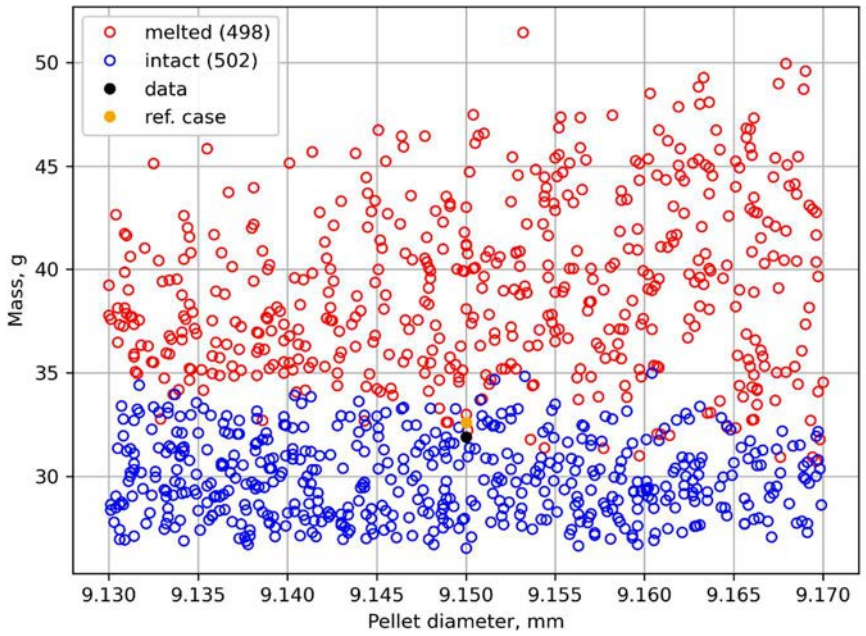

FIG. 88. Mass of H_2 accumulated by quenching (FOM #2) vs pellet diameter (#2).

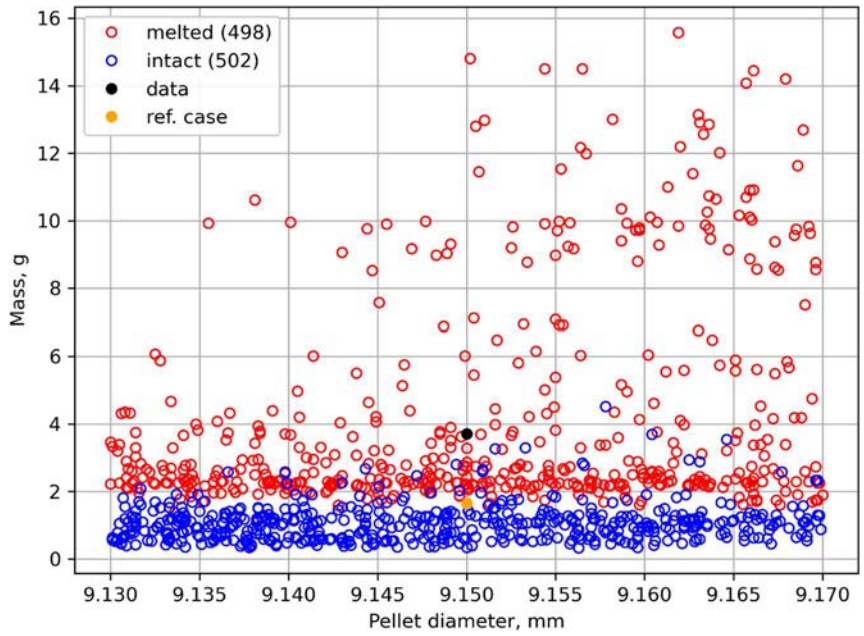

FIG. 89.. Mass of accumulated H_2 at quenching (FOM #3) vs pellet diameter (#2).

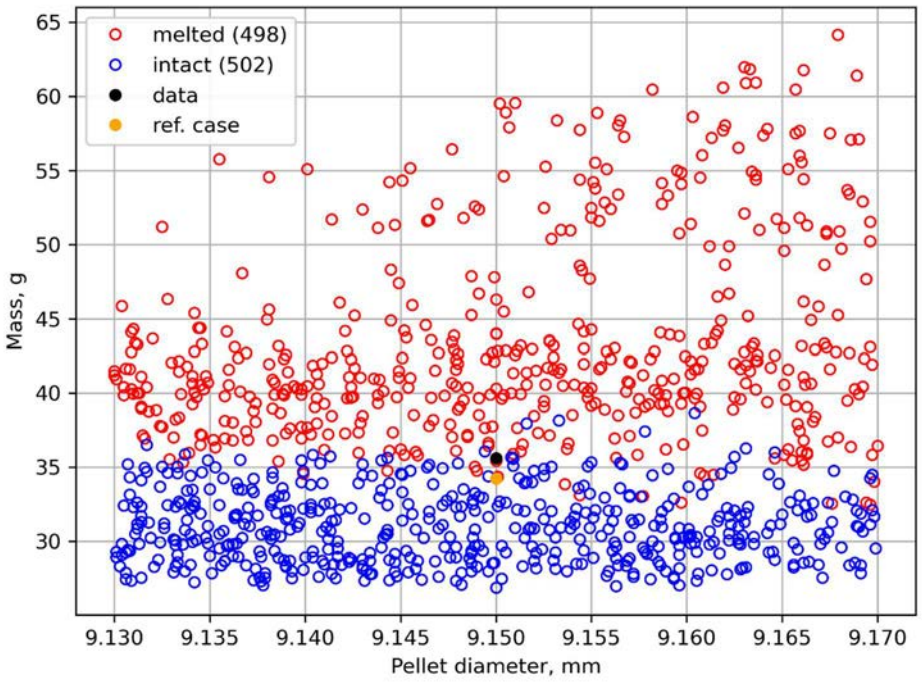

FIG. 90.. Peak H_2 production rate (FOM #4) vs pellet diameter (#2).

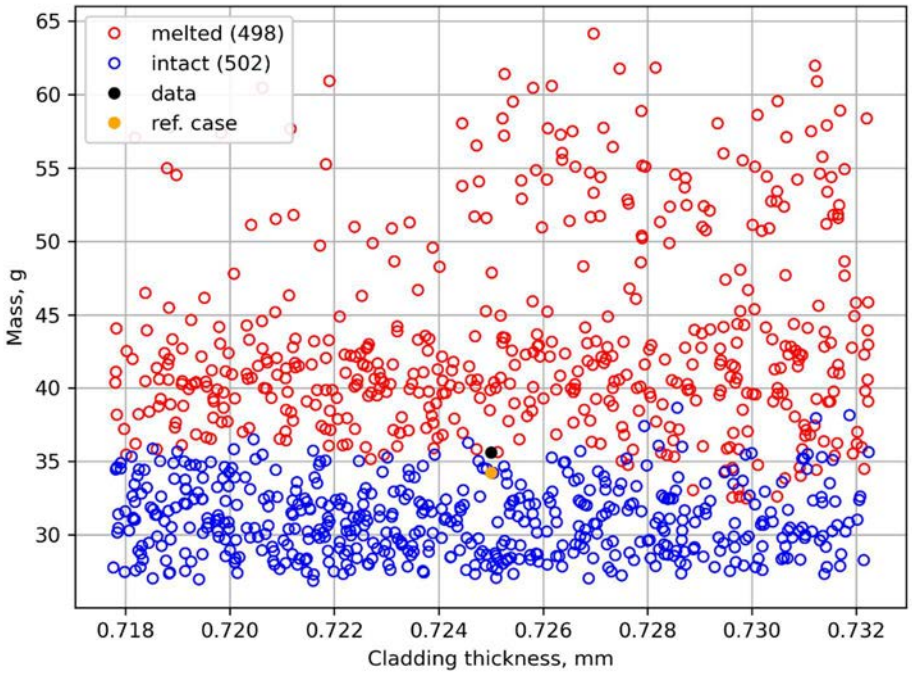

FIG. 91. Total mass of H_2 (FOM #1) vs cladding thickness (#3).

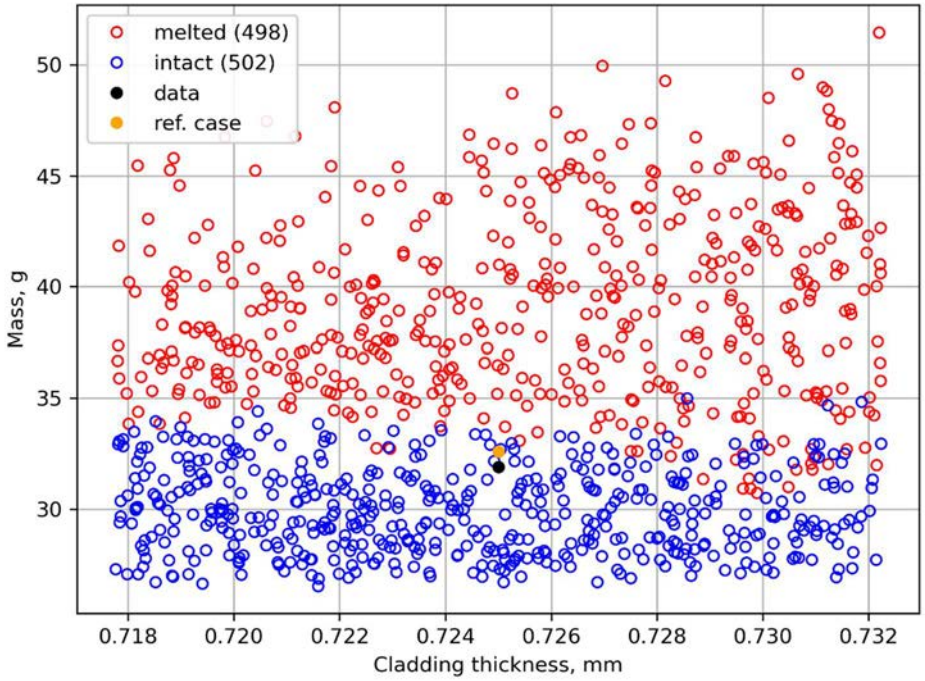

FIG. 92. Mass of H_2 accumulated by quenching (FOM #2) vs cladding thickness (#3).

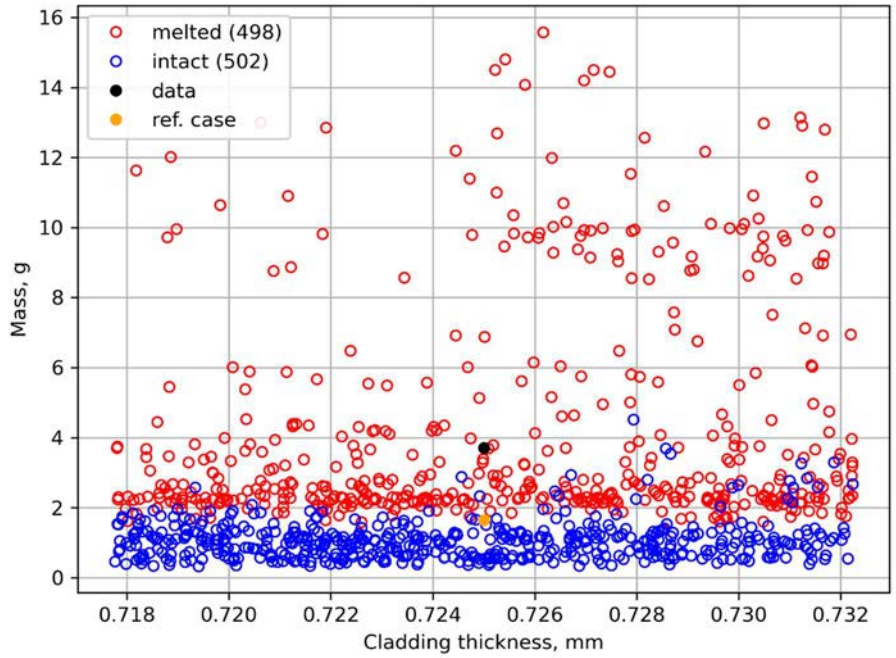

FIG. 93. Mass of H_2 accumulated at quenching (FOM #3) vs cladding thickness (#3).

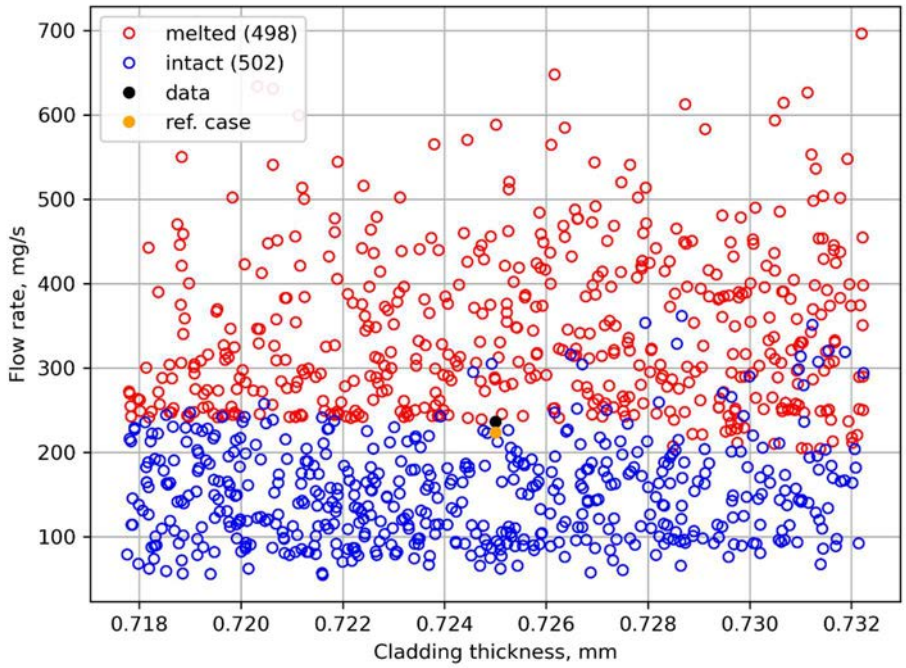

FIG. 94. Peak H_2 production rate (FOM #4) vs cladding thickness (#3).

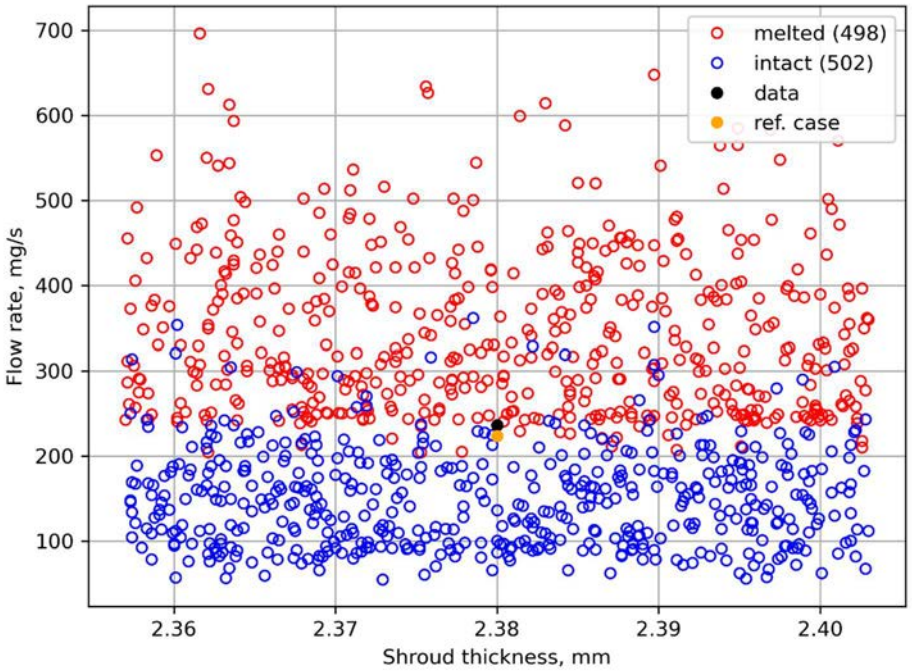

FIG. 95. Peak H_2 production rate (FOM #4) vs shroud thickness (#5).

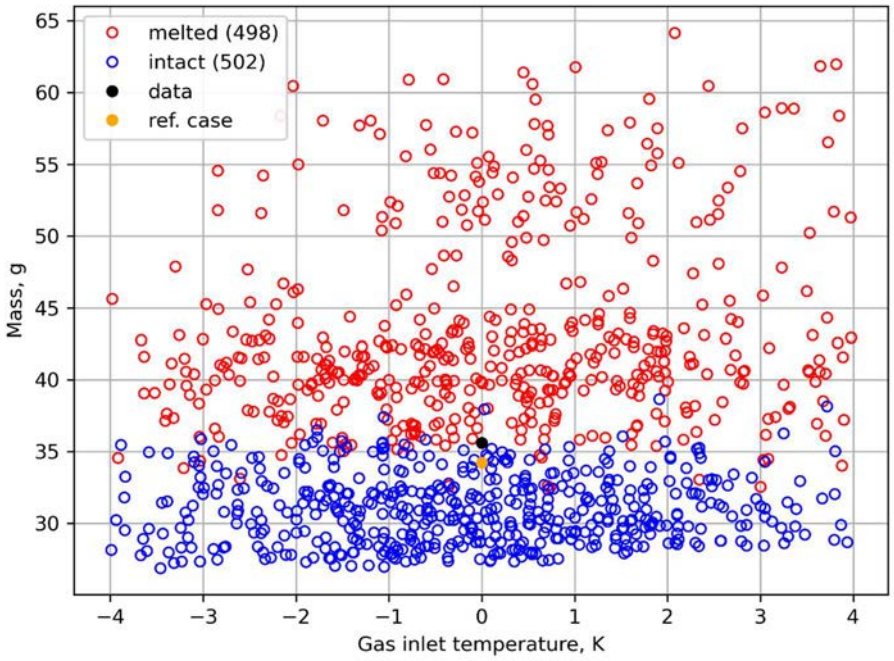

FIG. 96. Total mass of H_2 (FOM #1) vs gas inlet temperature (#7).

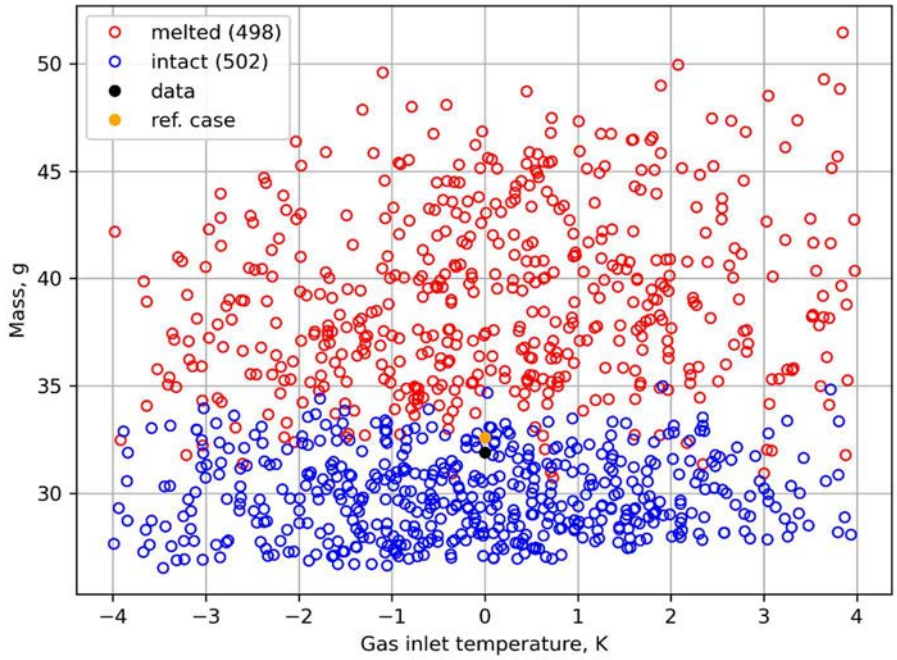

FIG. 97. Mass of H_2 accumulated by quenching (FOM #2) vs gas inlet temperature (#7).

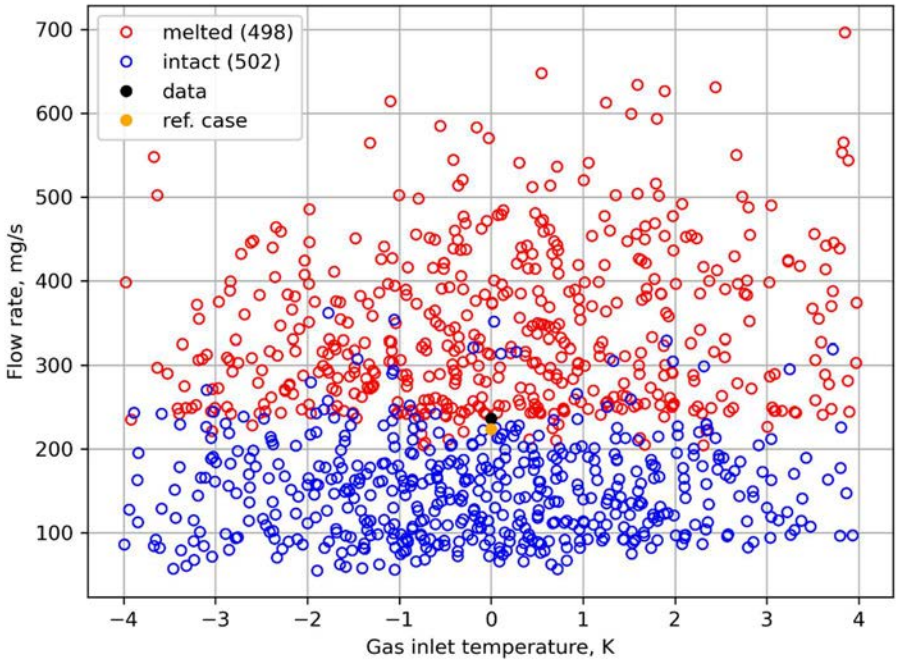

FIG. 98. Peak H_2 production rate (FOM #4) vs gas inlet temperature (#7).

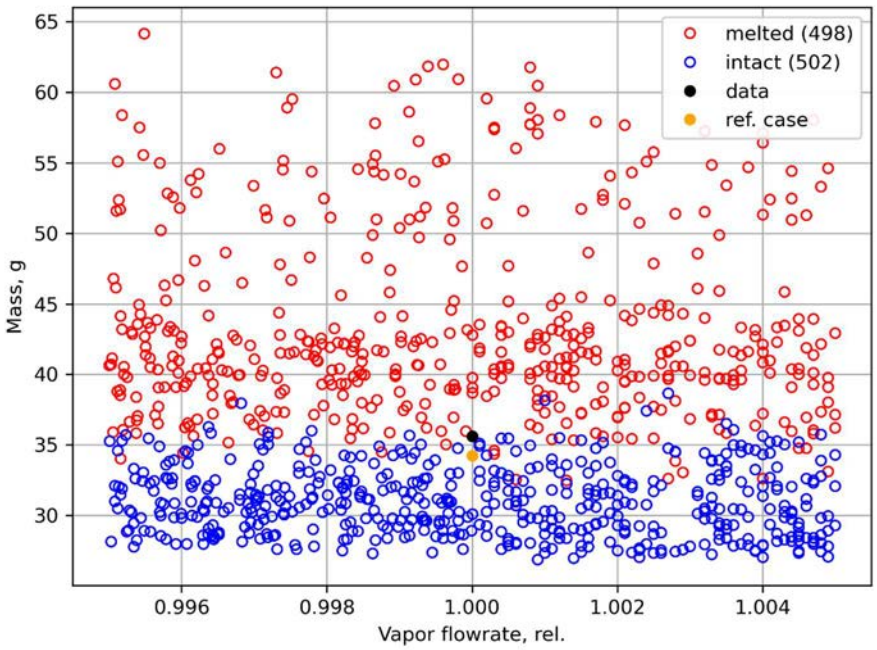

FIG. 99. Total mass of H_2 (FOM #1) vs vapor flow rate (#9).

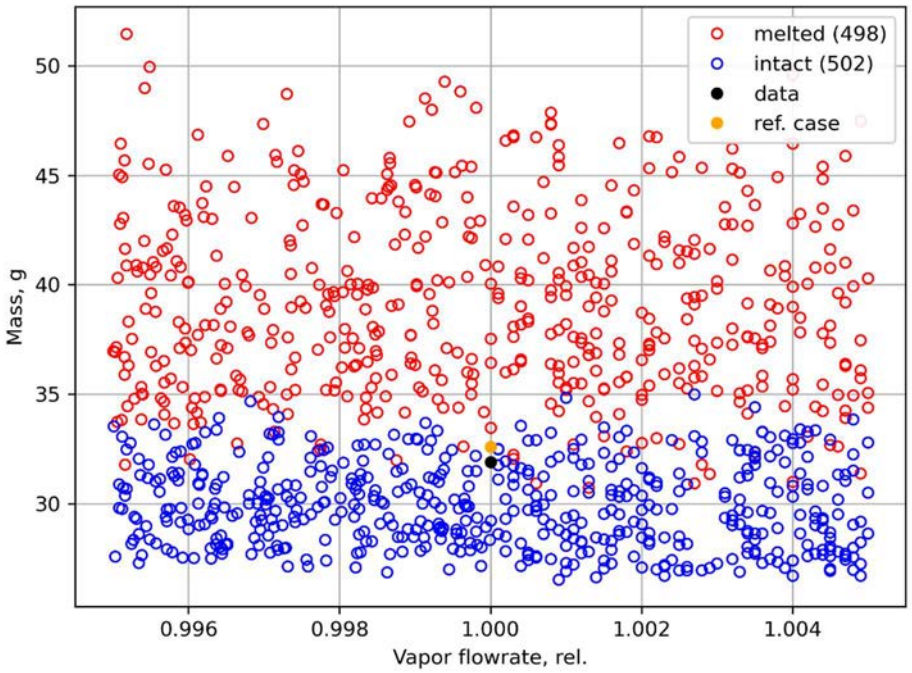

FIG. 100. Mass of H_2 accumulated by quenching (FOM #2) vs vapor flow rate (#9).

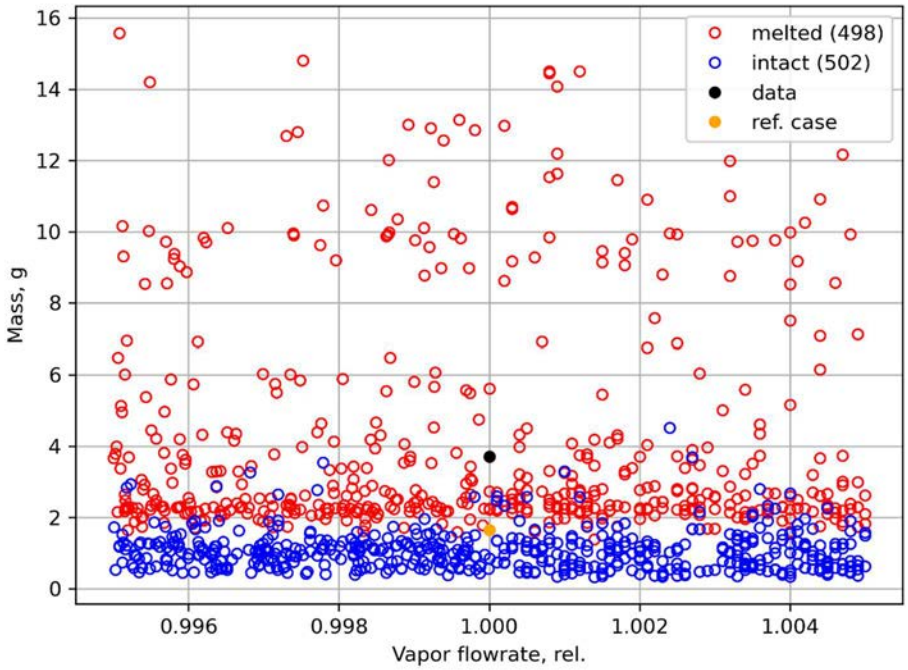

FIG. 101. Mass of accumulated H_2 at quenching (FOM #3) vs vapor flow rate (#9).

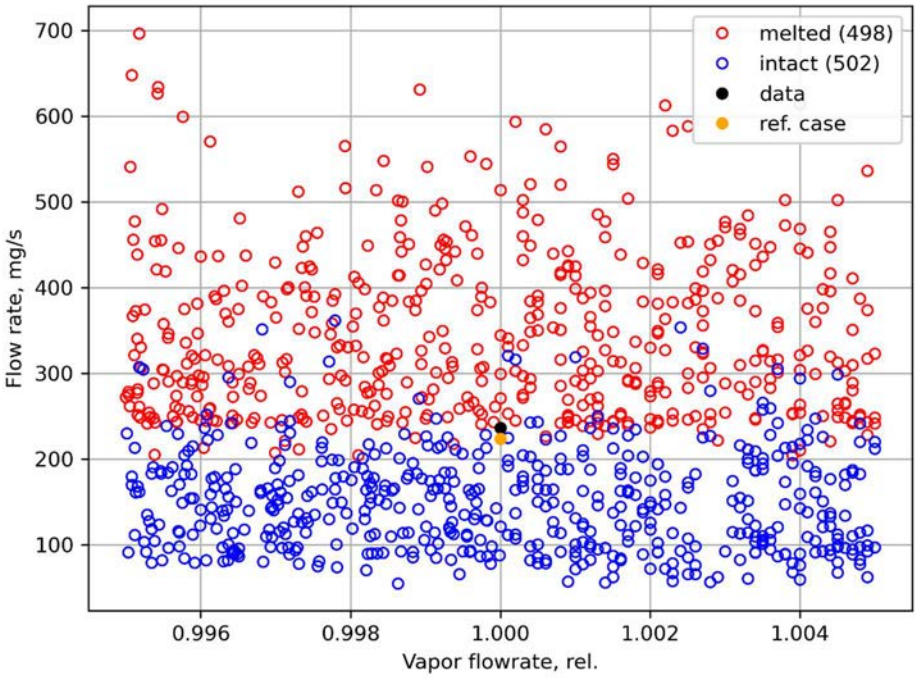

FIG. 102. Peak H_2 production rate (FOM #4) vs vapor flow rate (#9). The reference value and the measurement results are also shown in Figs. 103–106. The fact that a measurement result falls within the wide boundary area between two groups of the results confirms the conclusion of the experimenters that the assembly was close to melting and the results of post-test analysis, which revealed several small drops of melt on the surface of the claddings [1]. Visual analysis of scatter plots shown in Figs. 85–102 does not confirm the correlation for other parameters found in the correlation analysis. Next, let us consider those results where melt was pouring away on claddings surfaces. Correlation analysis of these

results shows that the total mass of H_2 (FOM #1), the mass of H_2 accumulated by quenching (FOM #2), and peak H_2 production rate (FOM #4) are positively correlated with the electrical power (parameter 11), gas inlet temperature (parameter 7), cladding thickness (parameter 3) and fuel pellet external diameter (parameter 2), Table 19.

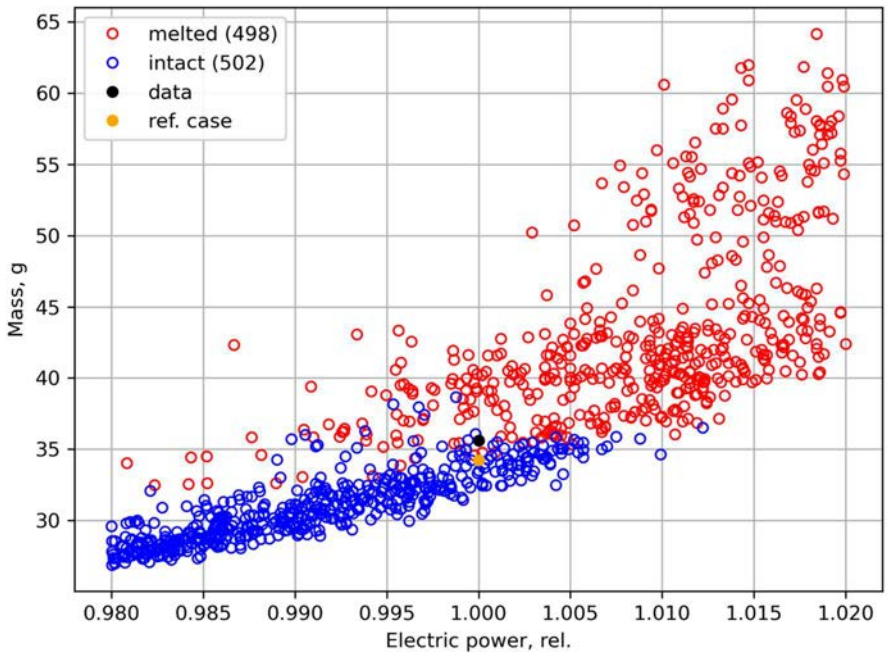

FIG. 103. Total mass of H_2 (FOM #1) vs electric power (#11).

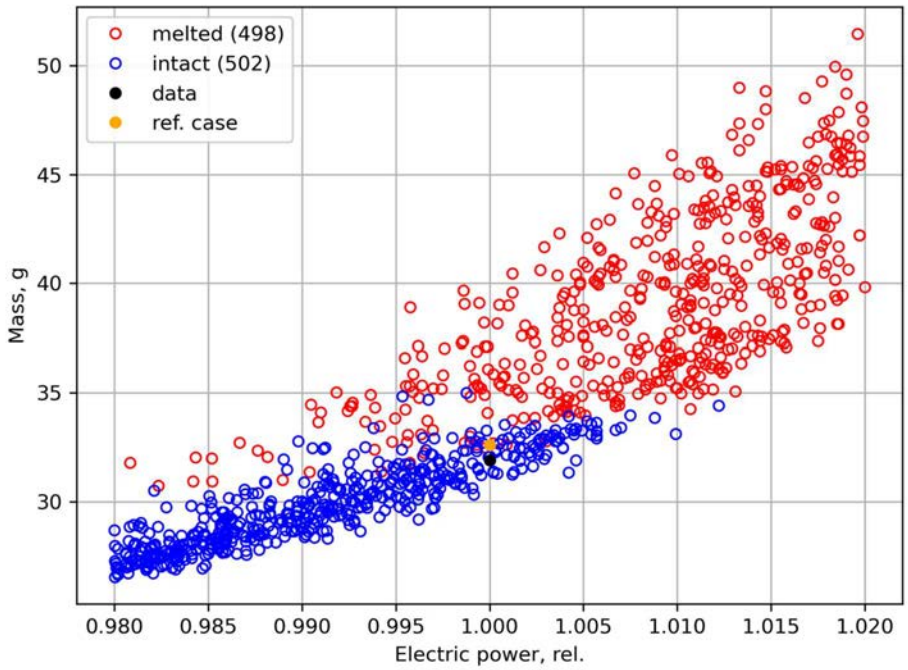

FIG. 104. Mass of H_2 accumulated by quenching (FOM #2) vs electric power (#11).

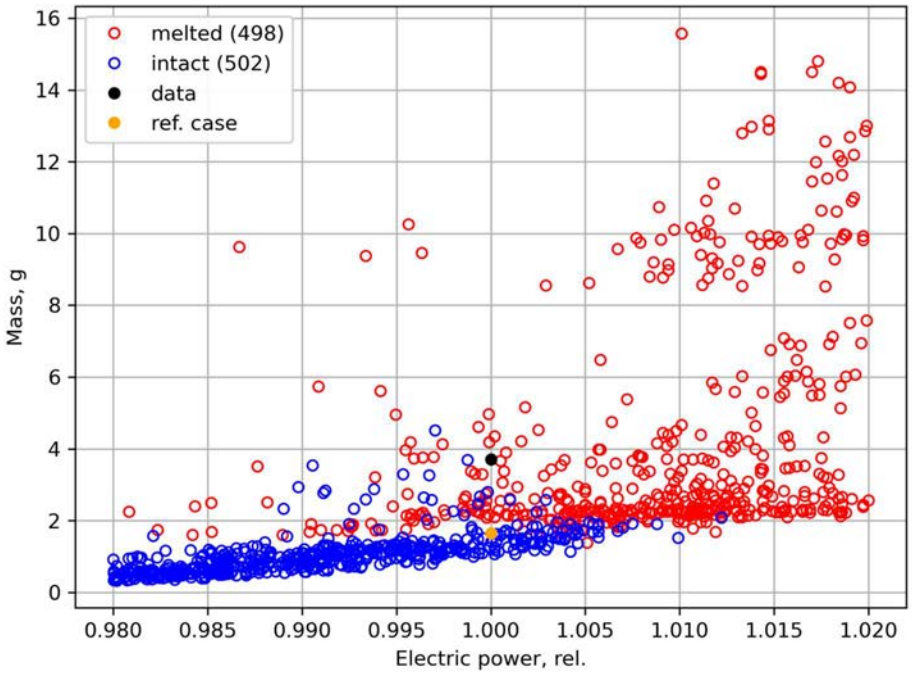

FIG. 105. Mass of H_2 accumulated at quenching (FOM #3) vs electric power (#11).

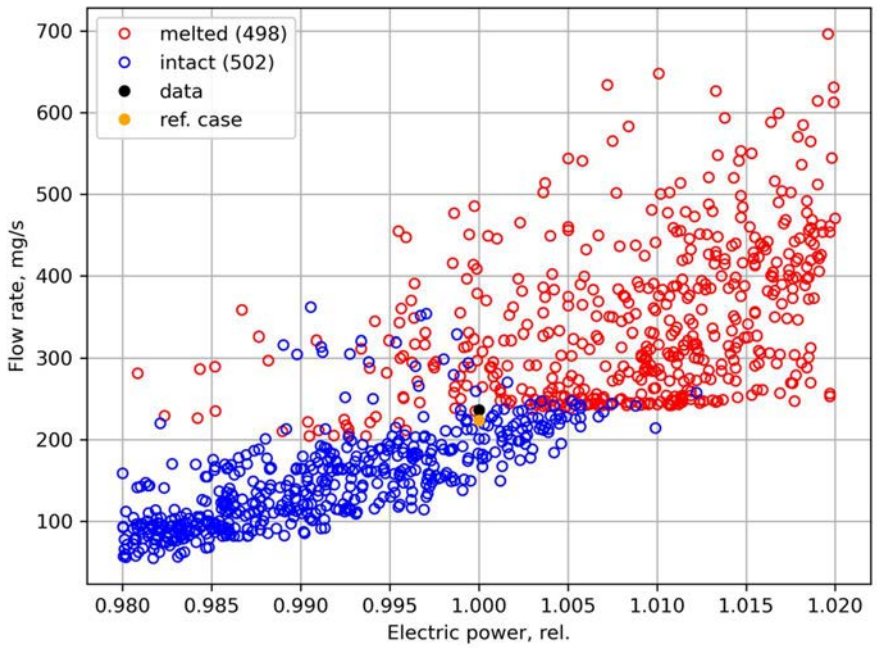

FIG. 106. Peak H_2 production rate (FOM #4) vs electric power (#11).

Positive correlations with power and fuel pellet external diameter were already discussed. An increase in gas inlet temperature leads to higher level of bundle temperatures which leads to higher H_2 production rate. This is valid for all FOMs except FOM #3 because according to experimental scenario, at quenching phase the injection of argon was switched from bundle inlet to bundle head. In the cladding thickness variation, the external diameter of the rod is kept unchanged meaning that an increase in cladding thickness leads to a decrease in gap thickness. Considerations for cladding thickness are the

same as for pellet external diameter. A negative correlation between the thickness of the shroud (parameter 5) and peak H_2 production (FOM #4) is caused by a higher heat sink for a thicker shroud since zirconium thermal conductivity is higher than that of the insulation material. Scatter plots shown in Figs. 103–106 confirm a strong positive correlation with total power, while visual analysis of scatter plots in Figs. 87–96 demonstrates a weak or absence of correlation with other parameters as discussed. To support the correlation analysis, Sobol' first order sensitivity coefficients S_i are additionally calculated. The calculation of Sobol' coefficients is carried out according to the algorithm proposed in [45]. In this analysis, all parameters were divided into two groups. The first group G1 includes all parameters except electrical power (parameter 11), and the second group G2 consists only of parameter 11. For an additional input parameters matrix 1000 Monte Carlo calculations are performed. Table 20 shows the resulting values of the coefficients. The magnitude of Sobol' first-order sensitivity coefficients S_i shows how much the variance of the calculation results decreases if the i-th parameter is fixed at any point of its multiple values. In other words, it estimates a fraction of variance $u^2_{\text{input}+D}$ that could be associated with a specific parameter. The obtained values of the coefficients confirm the conclusions that the uncertainty of the total electrical power determines the spread of the calculation results. The other input uncertain parameters do not lead to prominent deviation in considered FOMs.

TABLE 20. SOBOL'S FIRST ORDER SENSITIVITY COEFFICIENTS

Group	FOM #1	FOM #2	FOM #3	FOM #4
G1	0.298	0.187	0.115	0.347
G2	0.716	0.798	0.931	0.772

To estimate the coverage coefficient, it is necessary to attribute some analytical distribution function to the obtained samples. The histograms for FOMs in calculation series without melting and with melting are shown in Figs. 107–110. Histograms for calculations with melt release shown in Figs. 107 and 109 have two peaks. Thus, the PDFs can be related to joint distribution of two variables (for example, melt of one cell or melt of two cells).

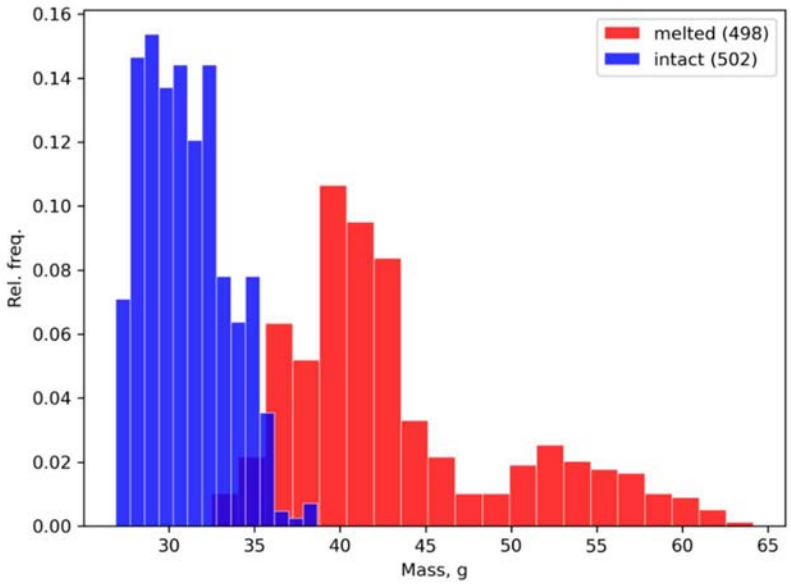

FIG. 107. Histogram of total H_2mass (FOM #1).

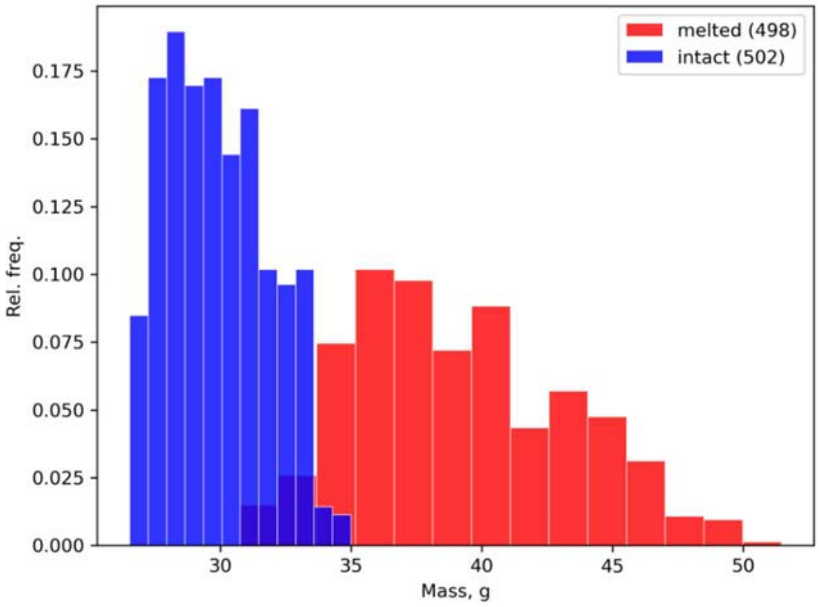

FIG. 108. Histogram of H_2 accumulated mass by quenching (FOM #2)

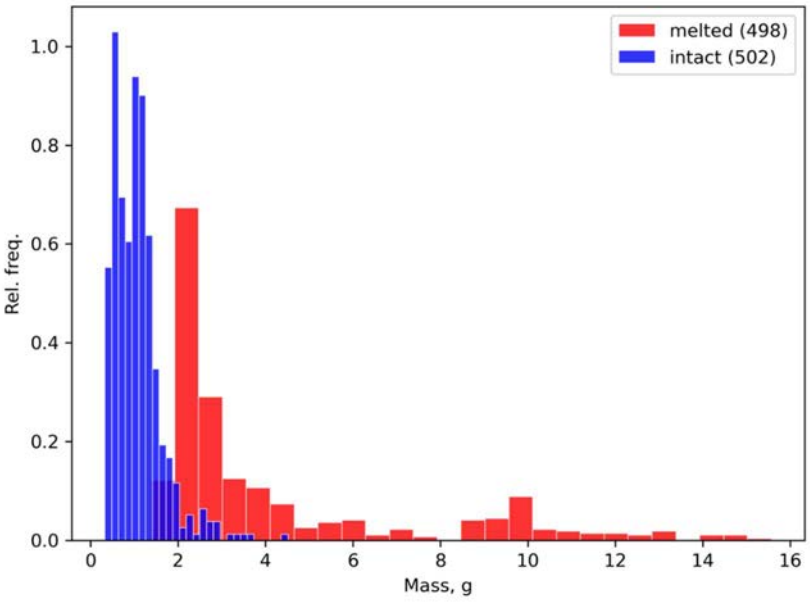

FIG. 109. Histogram of H_2 accumulated mass at quenching phase (FOM #3).

Two peaks are also observed in the histograms from calculations with intact geometry as shown in Figs. 109 and 110. Visually, it is difficult to attribute any analytical type of distribution to these histograms. Estimation of coverage coefficient can be an objective of further work.

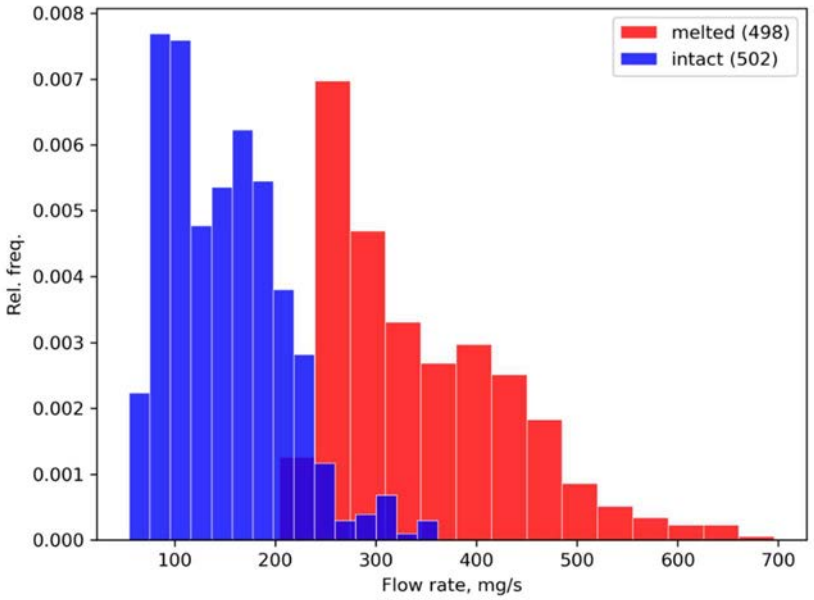

FIG. 110. Histogram of peak H_2 production rate (FOM #4).

4.6.CONCLUSIONS, LESSONS LEARNED, AND BEST PRACTISES

The Monte Carlo approach for propagating input uncertainties proves to be a valuable method for estimating validation uncertainty, especially when calculated and measured FOMs exhibit correlations. Adhering to the ASME V&V20 requirement that both experiment and calculation share the same regime is essential. However, it is observed that strict compliance with this requirement can lead to a biased estimation of the comparison error, particularly when the experiment is in proximity to a transition between regimes. Sensitivity analysis offers valuable insights into the physical behaviour of the experimental facility. It also has the potential to identify modelling errors when calculation results diverge from the expected understanding of a phenomenon. The Sobol' indices provide guidance for reducing data and simulation uncertainty. It is worth noting that estimating the coverage factor for a desired confidence level may not always be feasible. The present findings reveal the presence of asymmetric empirical PDFs, which may not be easily correlated with analytical PDFs. This underscores the complexity of accurately characterizing and quantifying uncertainty in certain scenarios.

5. INDIVIDUAL REPORT: KIT (GERMANY)

The ASTEC code described in Section 3.2 is used for the QUENCH-06 test exercise. Having this in mind, the QUENCH-06 ASTEC model described in Section 3.3 is then assessed [17].

5.1.RESULTS OF NOMINAL CASE

The ASTEC code is validated against the QUENCH-06 experiment [1] by employing the reference values as shown in Table 9 for the input parameters shown in Tables 3–8. In order to analyse the performance of the code, the ASTEC results concerning the axial temperature profiles in the fuel rod bundle and in the shroud at different instants during the test are compared with the corresponding experimental results. For such analysis, four instants are selected based on Fig. 4: end of the heat-up phase (1754 s), end of the pre-oxidation phase (6000 s), withdrawn of the corner rod (6620 s), and beginning of the quenching phase (7179 s). The calculated and experimental temperature profiles at such

instants are shown in Figs. 111–114. It can be observed that the ASTEC results show a very good agreement with the reference data.

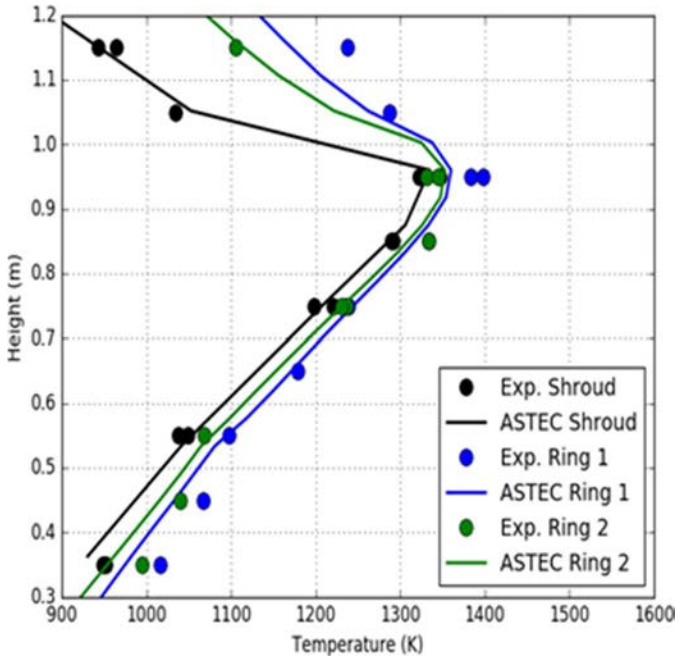

FIG. 111. ASTEC vs. Experiment: axial temperature profile of the heated rods and of the shroud at 1754 s.

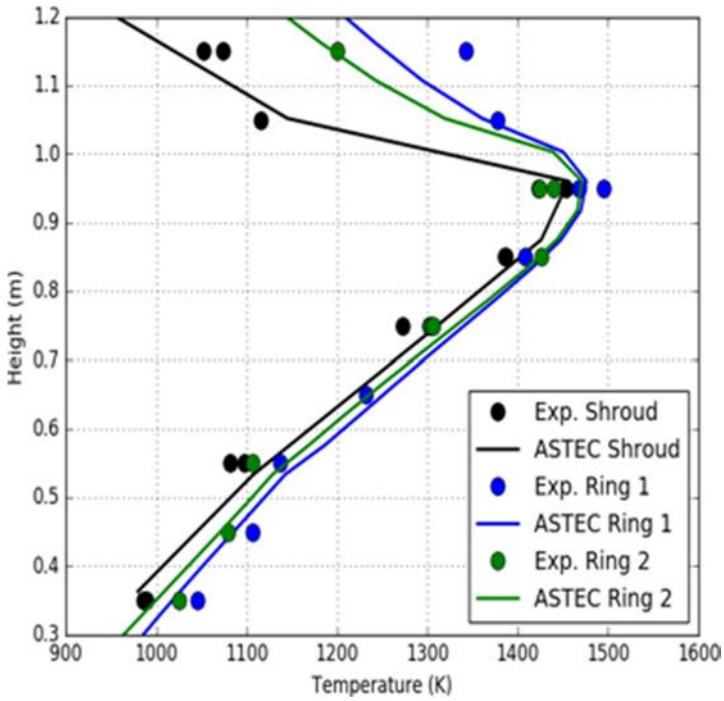

FIG. 112. ASTEC vs. experiment: axial temperature profile of the heated rods and of the shroud at 6000 s.

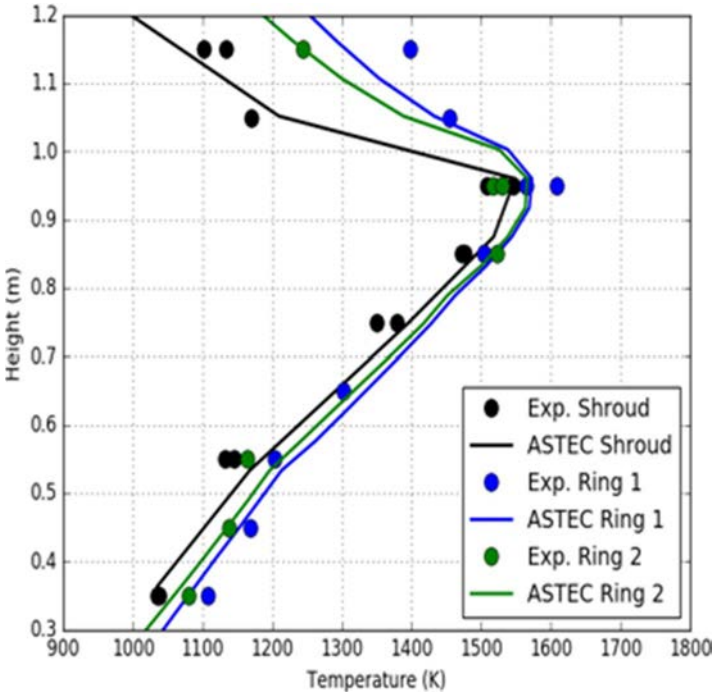

FIG. 113. ASTEC vs. Experiment: axial temperature profile of the heated rods and of the shroud at 6620 s.

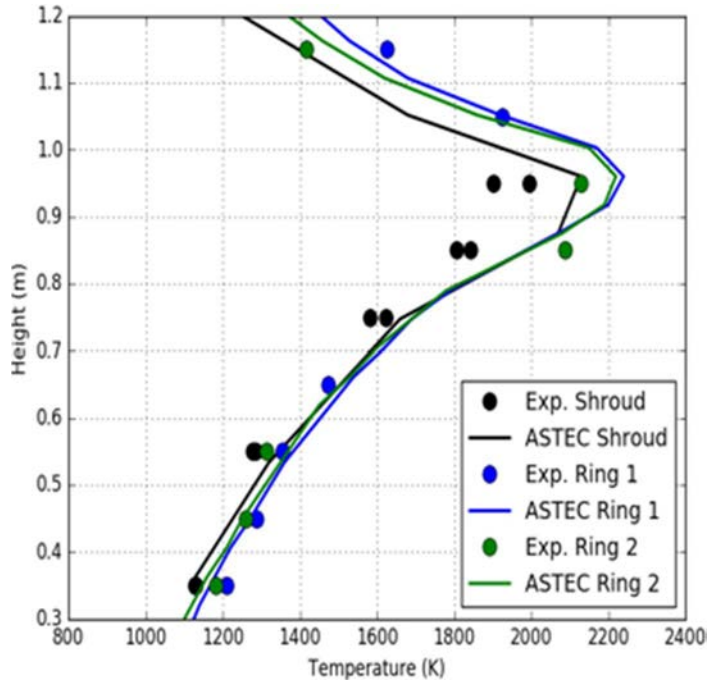

FIG. 114. ASTEC vs. Experiment: axial temperature profile of the heated rods and of the shroud at 7170 s.

The ASTEC predictions concerning the time dependent behaviour of the cladding and shroud temperature at 950 mm height are compared with the corresponding experimental results in Fig. 115. The results referring to the quenching phase are shown in Fig. 116.

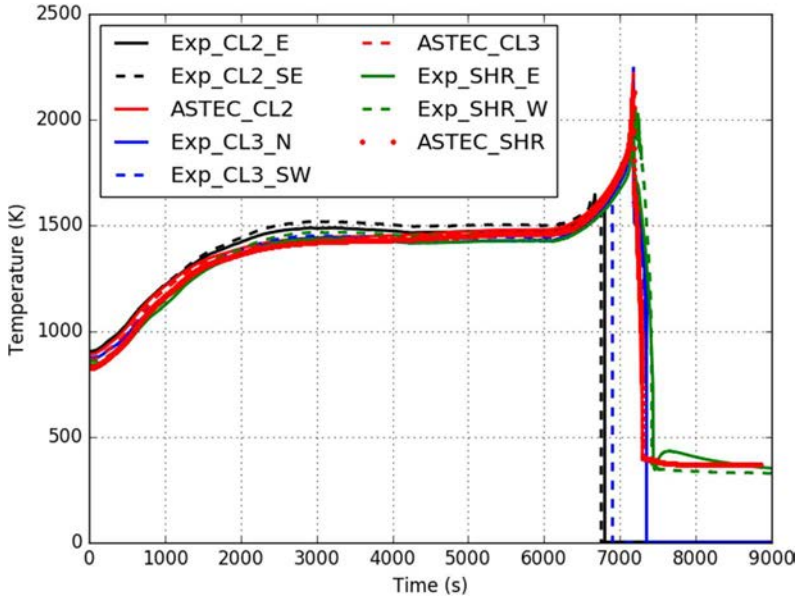

FIG. 115. ASTEC vs. experiment: time dependent temperature in the heated rods and in the shroud at 950 mm height.

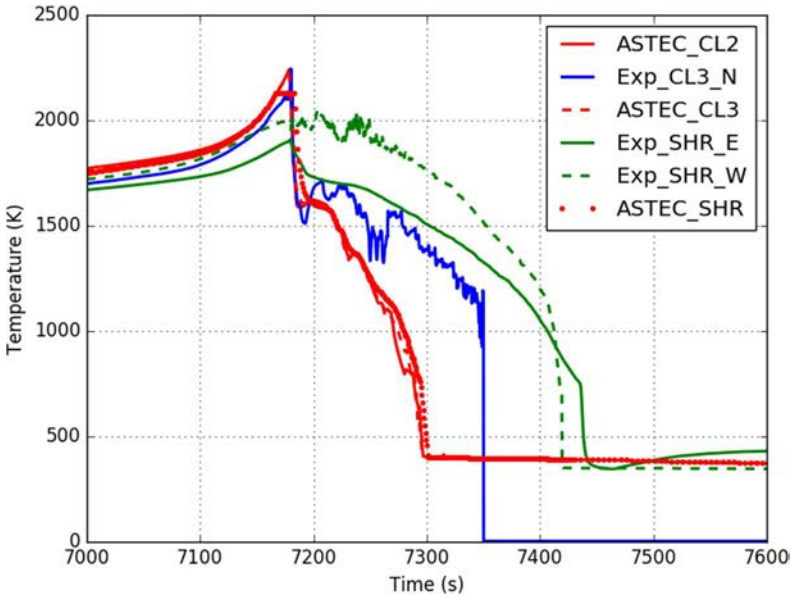

FIG. 116. ASTEC vs. experiment: time dependent temperature in the heated rods and in the shroud at 950 mm height after the water reflooding.

The labels ‘CLx’ refer to the cladding with x=1,2 being the ring number in the ASTEC model, and the label ‘SHR’ refers to the shroud region. In the experiment, the labels ‘E, SE, N, SW, W’ refer to the orientation. The ASTEC results show very good agreement with the reference data. The results after the quenching (Fig. 116) reveals that the code can reproduce the trend of the temperature after the quenching, but with a deviation in time of about 50–100s. The temperature behaviour of the cooling jacket at 950 mm height is shown in Fig. 117, the ASTEC results showing a very good agreement with the experimental data.

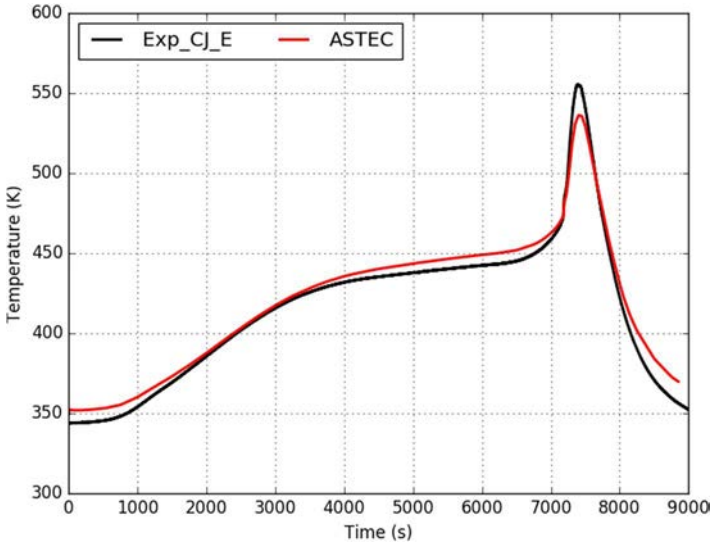

FIG. 117. ASTEC vs. experiment: temperature of the cooling jacket at 950 mm height.

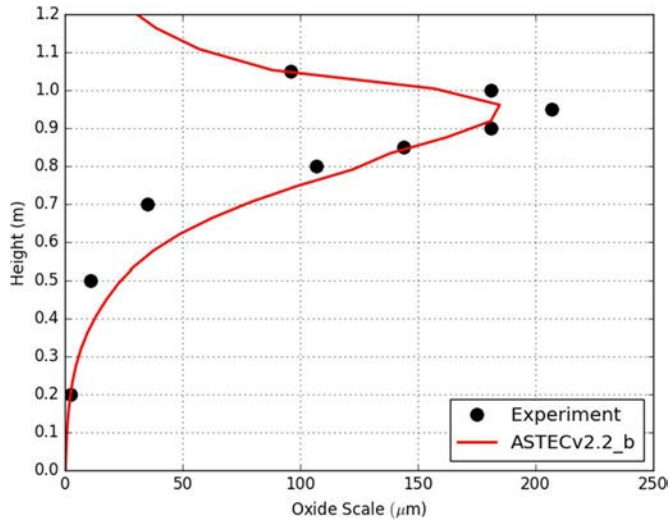

FIG. 118. ASTEC vs. experiment: oxide scale of the corner rod (B) at the withdrawn instant.

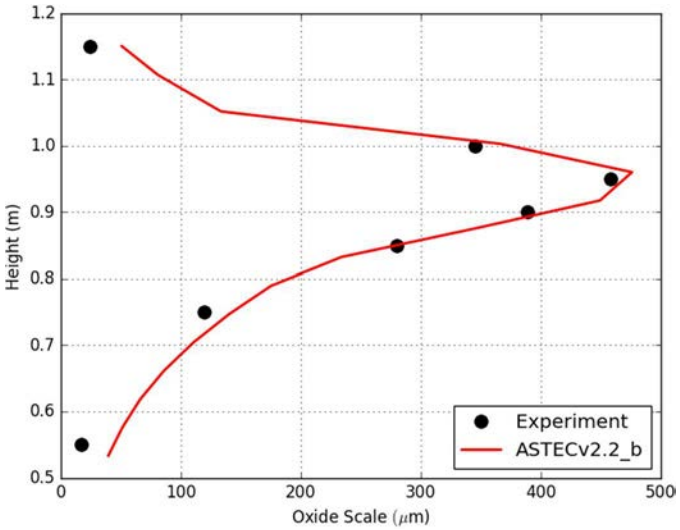

FIG. 119. ASTEC vs. experiment: oxide scale of the heated internal rod at the end of the transient.

The ASTEC predictions concerning the axial oxide scale of the corner rod at the withdrawn instant (6620 s) and at the end of the transient are shown in Figs. 118 and 119, respectively. Furthermore, the results concerning the oxide scale of the heated rods and of the shroud at the end of the transient are shown in Figs. 120 and 121, respectively. Concerning the corner rod, the ASTEC and reference results are compared at the instant when the rod is withdrawn and at the end of the test. The results show that ASTEC can reasonably well predict the experimental behaviour. for the oxide scale of the heated rods and the shroud, the ASTEC results show a general good agreement with the reference data, despite a discrepancy of about 200 μm is observed for the fuel rods at 950 mm height. The ASTEC results for the H_2 mass produced during the test are compared with the experiment in Fig. 122. It can be observed that ASTEC predictions rather well agree with the reference results. In particular, the H_2 production computed by ASTEC v2.2_b at the quenching (33.4 g) and at the end of the simulation (34.9 g) shows a very small deviation from the experimental results, being 34 g and 35.7 g, respectively. The H_2 production rate is shown in Fig. 123 indicating very good agreement between the ASTEC predictions and the reference data; It points to the conclusion that the code can reproduce properly the most important phenomena affecting H_2 production.

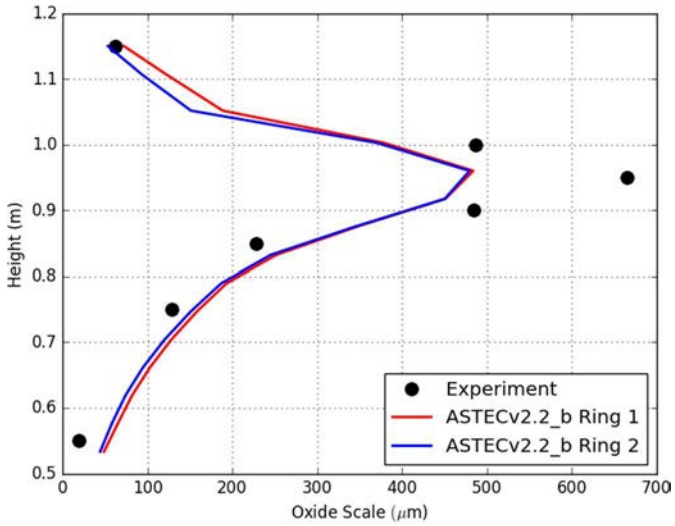

FIG. 120. ASTEC vs. experiment: oxide scale of the heated rods at the end of the transient.

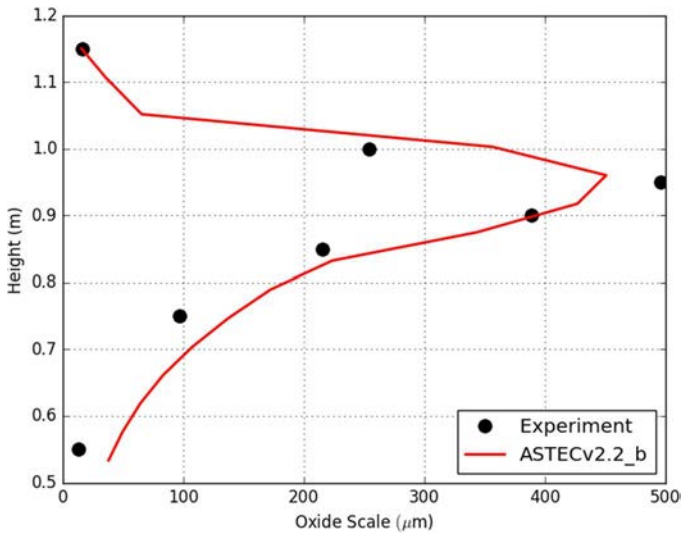

FIG. 121. ASTEC vs. experiment: oxide scale of the shroud at the end of the transient.

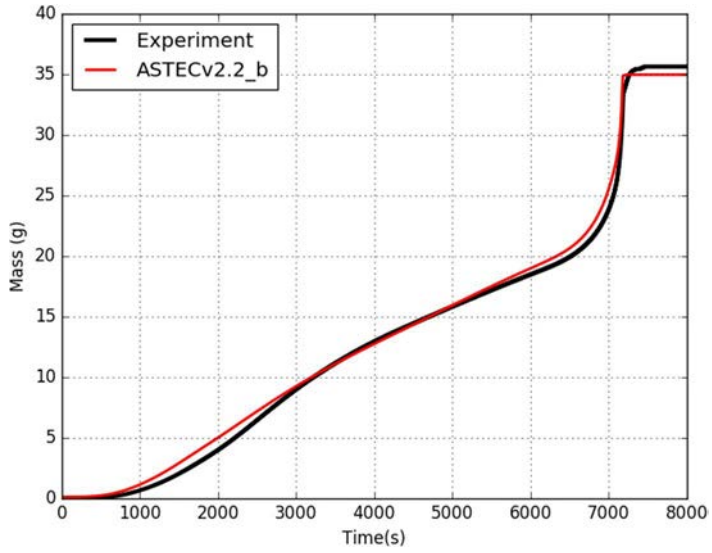

FIG. 122. ASTEC vs. experiment: total amount of H_2 produced.

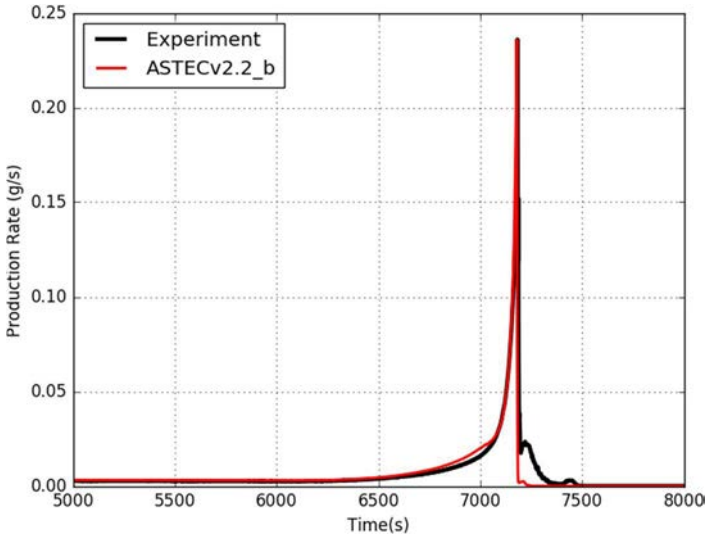

FIG. 123. ASTEC vs. experiment: H_2 production rate.

5.2.DESCRIPTION OF UNCERTAINTY AND SENSITIVITY TOOL

The uncertainty and sensitivity analysis of the QUENCH-06 test is performed by employing both the URANIE tool [46, 47], developed by CEA, and the Karlsruhe Tool for Uncertainty and Sensitivity Analysis (KATUSA), developed at KIT [12, 49]. The open source URANIE platform is developed within the ROOT analysis framework. The tool can perform the typical uncertainty and sensitivity studies as well as generating surrogate models generation and calibration, reliability analysis, optimization and construction of design-of-experiment. Details about the tool can be found in [48]. An interface based on C++ and Python scripts is developed at KIT to integrate the ASTEC results in the URANIE framework [46]. The flowchart of the ASTEC/URANIE platform is shown in Fig. 124.

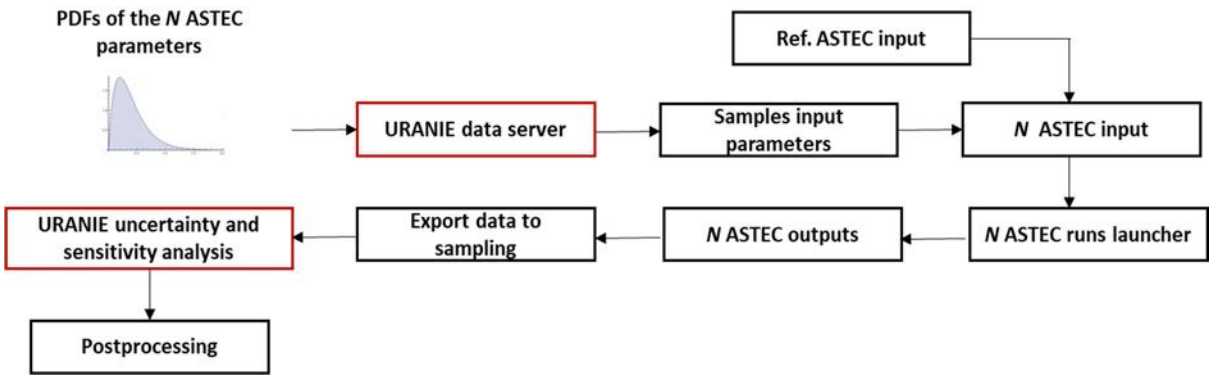

FIG. 124. Flowchart of the ASTEC/URANIE platform developed at KIT [50].

The interface performs three actions:

- Pre-processing: the information related to the PDFs of the uncertainties of the input parameters are loaded in an URANIE Data Server object; after having defined the *N* numbers of ASTEC runs to be performed, the random Monte Carlo sampling is employed to assess and run the corresponding *N* ASTEC inputs;
- Export of the ASTEC results to the URANIE sampling: the ASTEC results for the output variables of interest are collected in *.plt files; such data are reorganized in a unique file suitable to be employed by URANIE;
- Post-processing: the statistics is performed by URANIE; the results are sampled and provided as .txt or .csv files.

The KATUSA tool is extensively employed at KIT for performing uncertainty and sensitivity analysis analyses of the ASTEC results [12, 49]. The tool is coupled with the ASTEC code via Python based interface developed at KIT. The flowchart of the ASTEC/KATUSA platform is shown in Fig. 125.

The KATUSA tool consists of five different macro modules:

- Sampling module: the PDFs of the uncertainty of the input parameters is employed as basic information to generates random samples. The latin hypercube sampling and Monte Carlo methods are used for the random sampling;
- Running multiple simulations module: the ASTEC input decks are assessed by employing each sample and the simulation are performed in parallel;
- Collecting results module: the database of the results of the FOMs are collected and the tool checks that all the ASTEC runs successfully ended and, in case, identify which runs failed;
- Statistics and sensitivity analysis module perform simple statistics as well as sensitivity analyses are related post-processing. Currently, Pearson, Spearman, distance covariance [50], and maximal information coefficient [52] correlations are embedded in KATUSA;
- MOCABA module: the database is employed by the MOCABA data assimilation procedure [53], developed by Framatome, is embedded in KATUSA in order to perform prediction analyses [54].

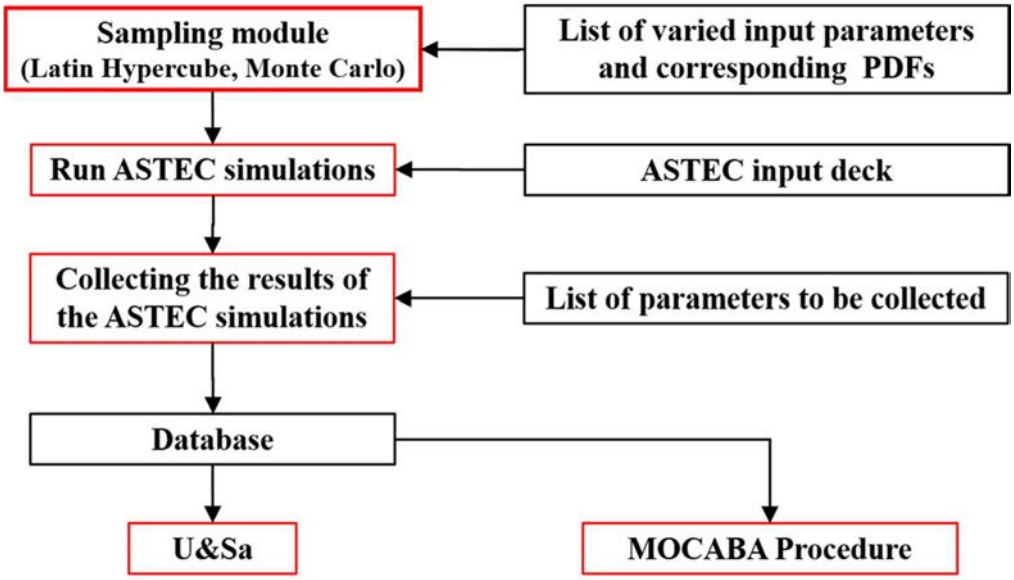

FIG. 125. Flowchart of the ASTEC/KATUSA Platform developed at KIT [49].

The employment of the Python language allows KATUSA to be employed on high performance computing systems. Furthermore, since the ASTEC's database management is also based on Python, the ASTEC/KATUSA coupling is much easier to be assessed.

5.3.RESULTS OF THE UNCERTAINTY AND SENSITIVITY ANALYSIS

The ASTEC/URANIE and the ASTEC/KATUSA analyses are performed by using the uncertainty parameters shown in Tables 3–8, the FOMs shown in Table 2 being considered. The database of the uncertainty and sensitivity analysis is composed by 300 ASTEC samples obtained by employing the Latin Hypercube Sampling method for propagating the uncertainty of the ASTEC input parameters. No ASTEC failures are encountered. The simple statistics for the FOM#1 (total mass of accumulated H_2, Table 2) is shown in Fig. 126. The results show that the mean value of the database is close to the experiment (see Fig. 122), as expected.

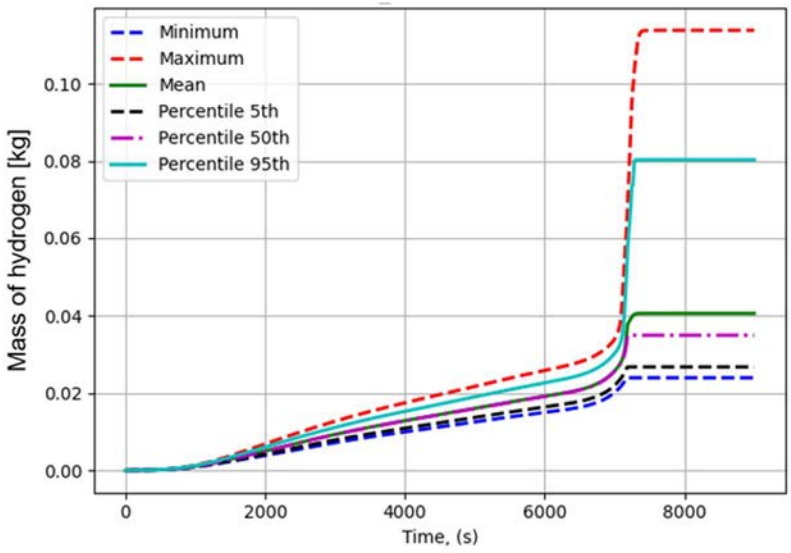

FIG. 126. Simple statistics of the FOM#1.

To illustrate the findings of the sensitivity analysis, the results pertaining to the uncertainty parameters that exhibit correlations exceeding 20% with each FOM are presented here. The uncertainty and sensitivity analysis conducted on the ASTEC results highlights those parameters 10 (steam mass flow rate at the bundle inlet) and 12 (Electrical power) exhibit the most substantial correlations with all FOMs. Time dependent Pearson correlation coefficients between parameters 10 and 12 and FOM#1, as computed by the ASTEC/URANIE and the ASTEC/KATUSA platforms, are depicted in Figs. 127 and 128, respectively. These correlations provide valuable insights into the relationships between specific input parameters and the computed FOMs, pointing at their impact and significance in the analysis. It can be observed that the results from the application of the ASTEC/URANIE and the ASTEC/KATUSA platforms show a very good agreement.

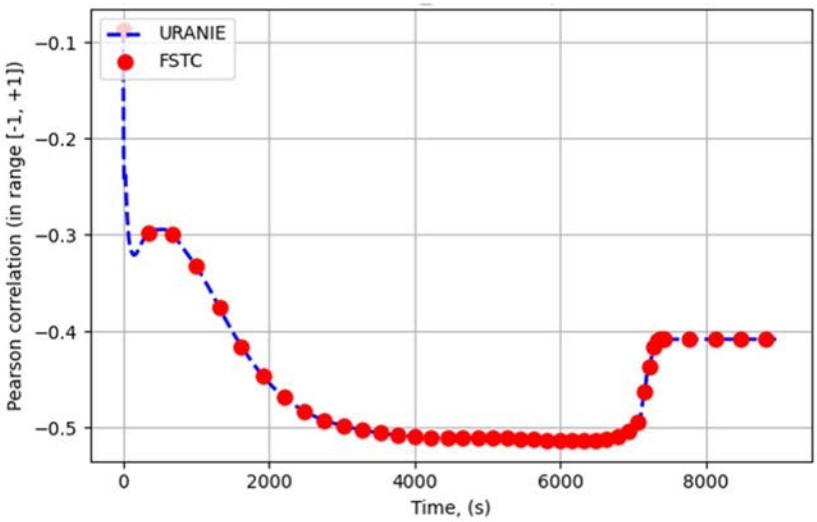

FIG. 127. Parameter 10 vs. FOM#1: time dependent Pearson coefficients computed by ASTEC/URANIE and ASTEC/KATUSA.

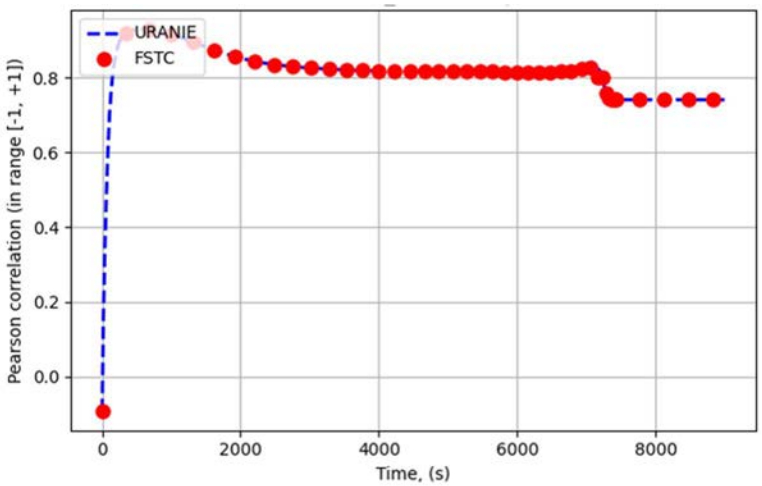

FIG. 128. Parameter 12 vs. FOM#1: time dependent Pearson coefficients computed by ASTEC/URANIE and ASTEC/KATUSA.

The Spearman correlations for the same parameters computed by ASTEC/KATUSA platform are shown in Figs. 129 and 130. Comparing the results in Figs. 127 and 128, it can be observed that the Spearman and the Pearson coefficients are quite close along the full transient. The results show a quite high

correlation between the electric power of the bundle (parameter 10) and the FOM#1 (about 0.8). Furthermore, a significant correlation exists between the steam flow rate (parameter 12) and the FOM#1, in the pre-heating phase (up to about 0.5).

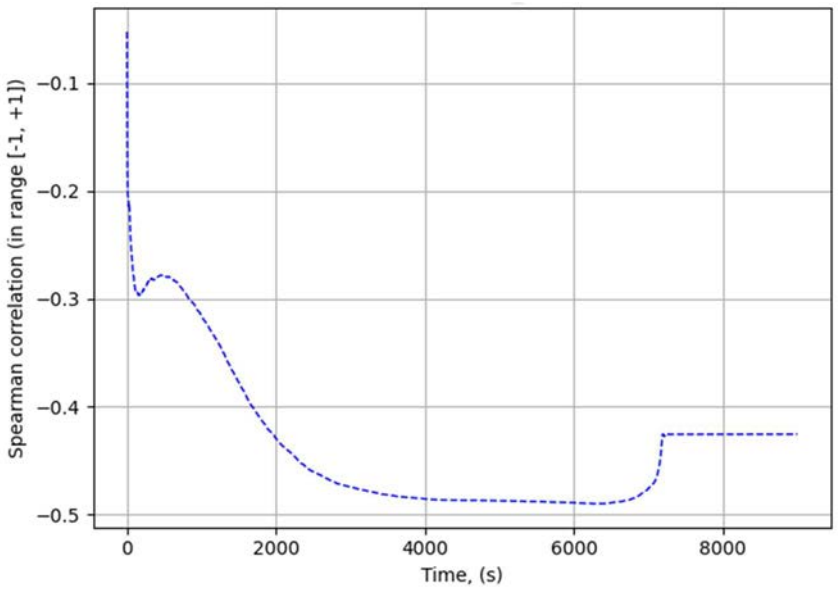

FIG. 129. Parameter 10 vs. FOM#1: time dependent Spearman coefficients computed by the ASTEC/KATUSA platform.

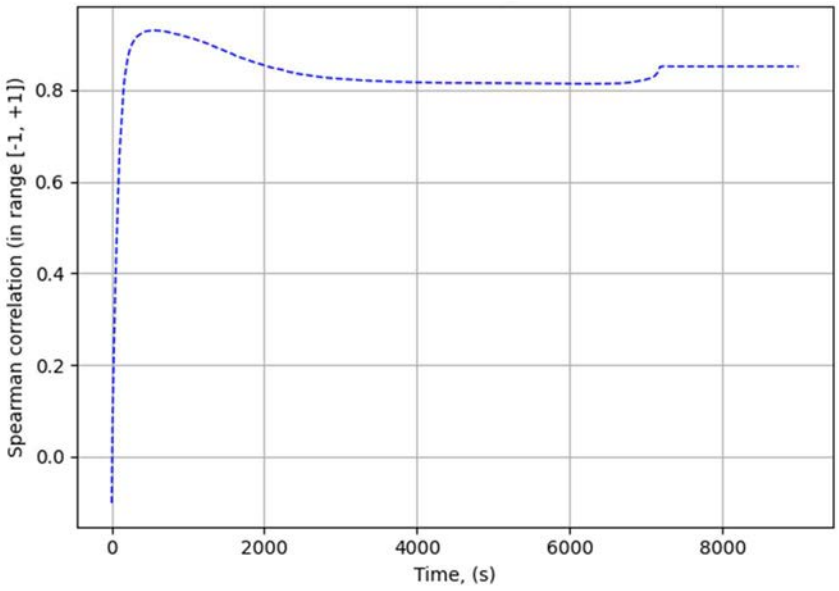

FIG. 130. Parameter 12 vs. FOM#1: time dependent Spearman coefficients computed by the ASTEC/KATUSA platform.

Regarding the FOM#2 (temperature of the central fuel rod simulator at elevation 950 mm, Table 2), the simple statistics of the time dependent profile of the temperature of the heated rods in the channels 2 and 3 (Fig. 6) at 950 mm height are shown in Figs. 131 and 132, respectively.

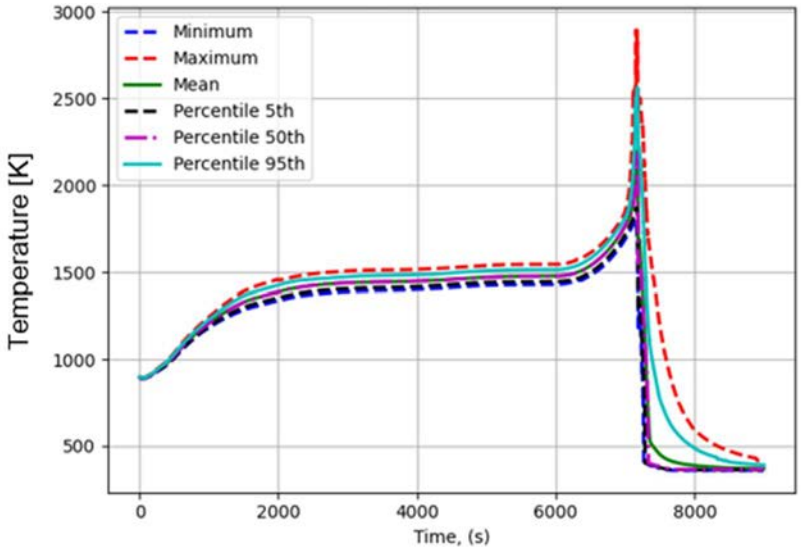

FIG. 131. Simple statistics of the time dependent profile of the temperature of the heated rods in the channel 2.

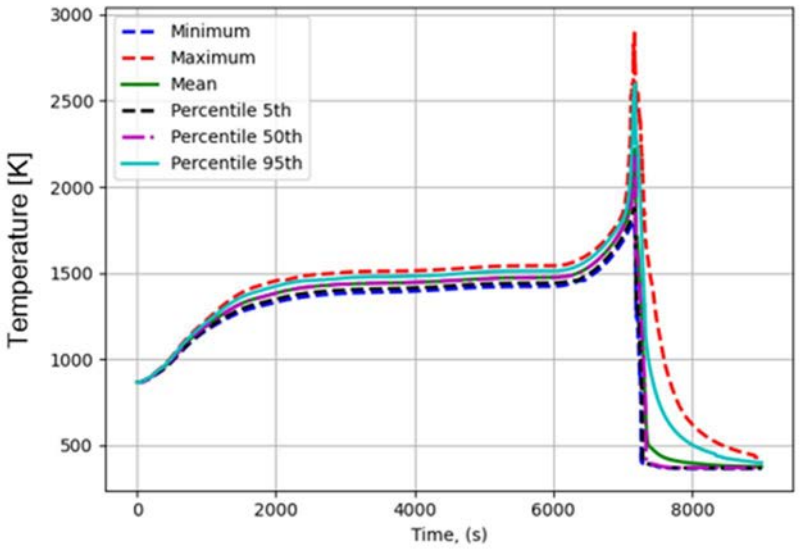

FIG. 132. Simple statistics of the time dependent profile of the temperature of the heated rods in the channel 3.

Other than the uncertainty parameters 10 and 12, the results of the sensitivity analysis show that the uncertainty parameters 7 (instant of the quench water injection) and 21 (threshold void fraction to allow exchange with liquid droplets) significantly affect such FOMs. The time dependent Pearson correlation coefficients between the parameters 10 and 12 and the temperature of the heated rods in the channel 2 at 950 mm height computed by the ASTEC/URANIE and the ASTEC/KATUSA platform are shown in Figs. 133 and 134, respectively. The results show a significant correlation (about −55%) between the parameter 10 and the FOM considered, in particular during the pre-oxidation phase of the test. At the same time a rather strong correlation (about 80%) is observed between the parameter 12 and the FOM.

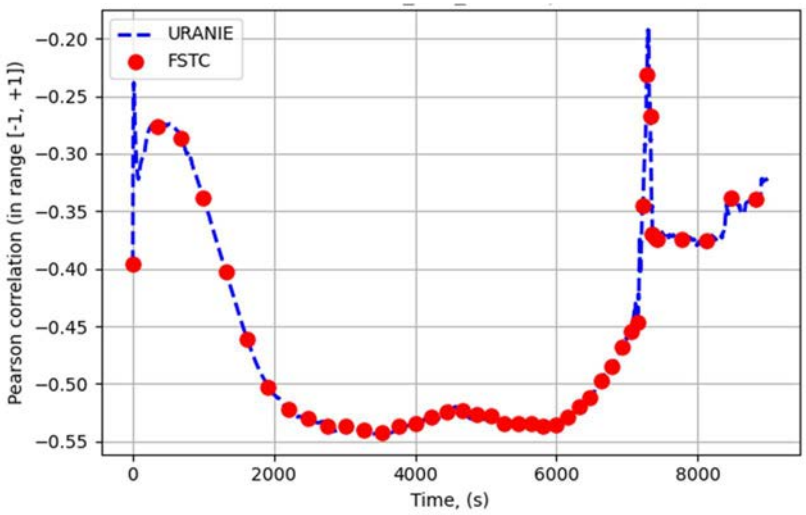

FIG. 133. Parameter 10 vs. temperature of the heated rods in the channel 2 at 950 mm height: time dependent Pearson coefficients computed by ASTEC/URANIE and ASTEC/KATUSA.

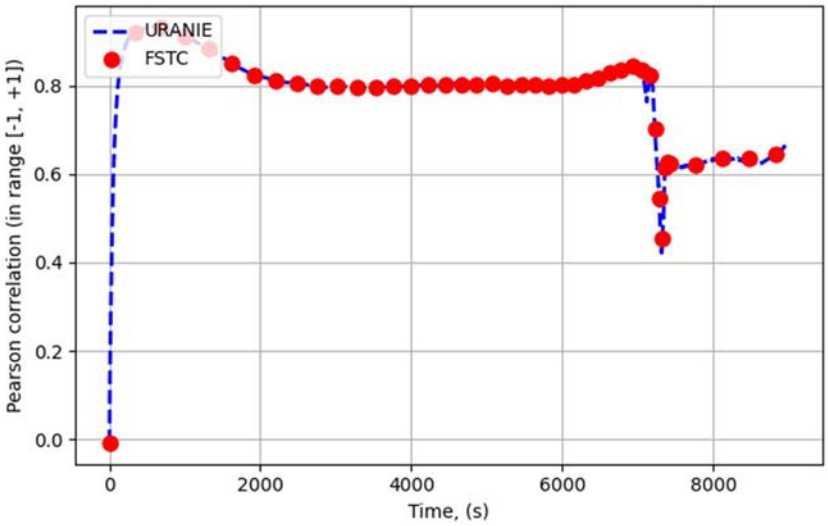

FIG. 134. Parameter 12 vs. temperature of the heated rods in the channel 2 at 950 mm height: time dependent Pearson coefficients computed by ASTEC/URANIE and ASTEC/KATUSA.

The time dependent Spearman correlation coefficients between the parameters 10 and 12 and the temperature of the heated rods in the channel 2 at 950 mm height computed by the ASTEC/KATUSA are shown in Figs. 135 and 136, respectively. The results show a quite good agreement between the Spearman and the Pearson correlations.

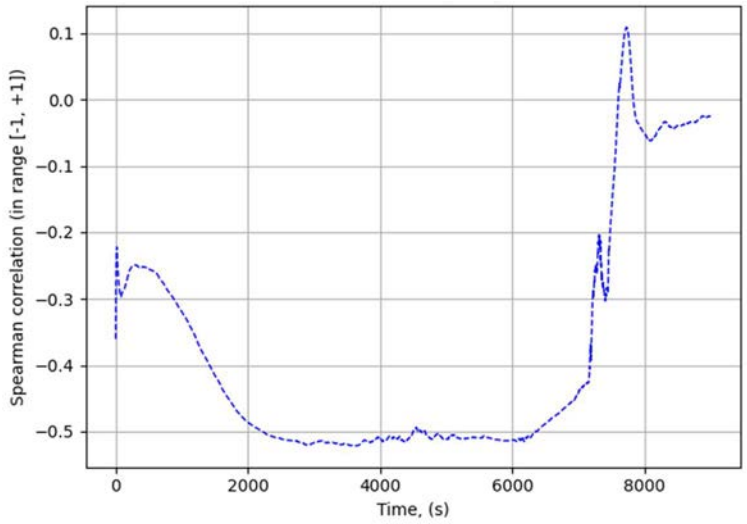

FIG. 135. Parameter 10 vs. temperature of the heated rods in the channel 2 at 950 mm height: time dependent Spearman coefficients computed by ASTEC/KATUSA.

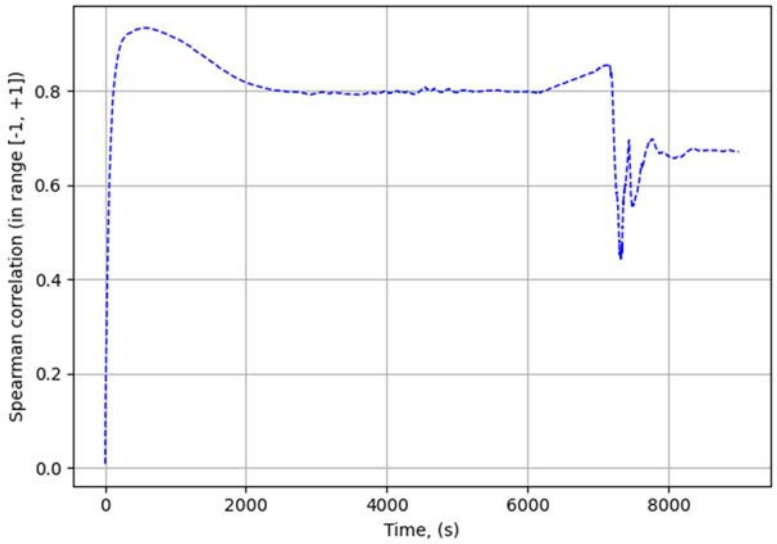

FIG. 136. Parameter 12 vs. temperature of the heated rods in the channel 2 at 950 mm height: time dependent Spearman coefficients computed by ASTEC/KATUSA.

The time dependent Pearson correlation coefficients between the parameters 10 and 12 and the temperature of the heated rods in the channel 3 at 950 mm height computed by the ASTEC/URANIE and the ASTEC/KATUSA platform are shown in Figs. 137 and 138, respectively. As for the heated rods in the channel 2, a rather strong correlation between the parameter 12 with the cladding temperature at 950 mm height may be observed (about 80%) and a lower, but still significant correlation between the parameter 10 and such a FOM.

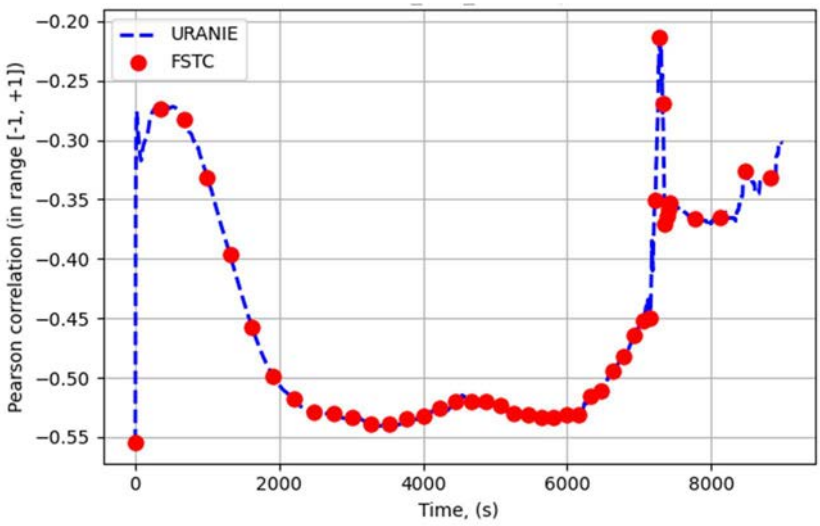

FIG. 137. Parameter 10 vs. temperature of the heated rods in the channel 3 at 950 mm height: time dependent Pearson coefficients computed by ASTEC/URANIE and ASTEC/KATUSA.

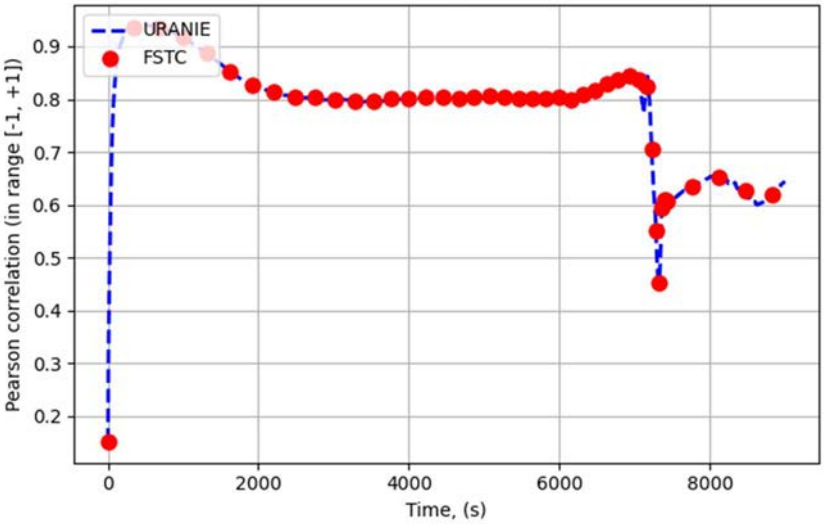

FIG. 138. Parameter 12 vs. temperature of the heated rods in the channel 3 at 950 mm height: time dependent Pearson coefficients computed by ASTEC/URANIE and ASTEC/KATUSA.

The time dependent Spearman correlation coefficients between the parameters 10 and 12 and the temperature of the heated rods in the channel 3 at 950 mm height computed by the ASTEC/KATUSA platform are shown in Figs. 139 and 140, respectively.

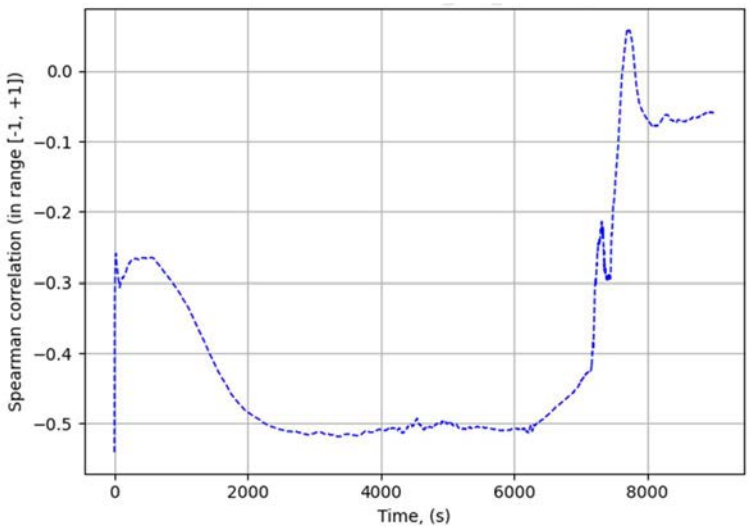

FIG. 139. Parameter 10 vs. temperature of the heated rods in the channel 3 at 950 mm height: time dependent Spearman coefficients computed by ASTEC/KATUSA.

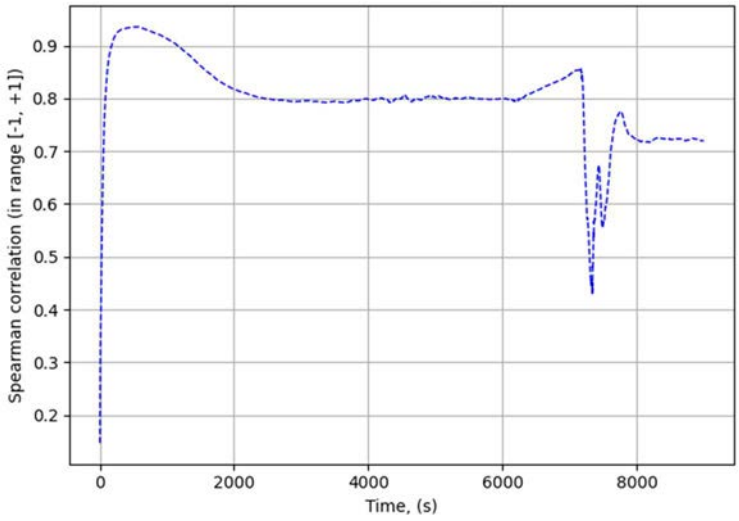

FIG. 140. Parameter 12 vs. temperature of the heated rods in the channel 3 at 950 mm height: time dependent Spearman coefficients computed by ASTEC/KATUSA.

The results show that the Pearson and Spearman correlations of the parameters 10 and 12 vs. the bundle temperature at 950 mm height looks rather similar. A deviation is observed after the instant of quenching (about 7215 s), where the Spearman coefficients are below −20% up to 0%, i.e. see Fig. 139 while the Pearson coefficients in the same time region approaches about −35%, i.e. see Fig. 137. Such a discrepancy, also shown in Figs. 55 and 57 for the FOM#2 (temperature of the central fuel rod simulator at elevation 950 mm, Table 2), may be explained by considering the larger spread of the data related to such FOMs during the cooling phase. The results therefore provide an indication of the need to consider different correlations to perform a reliable sensitivity analysis in the cases where the results from the integral codes are sparse, i.e., bifurcation. Such a behaviour is quite usual in severe accident analyses.

The time dependent Pearson correlation coefficients between the uncertainty parameters 7 and 21 and the temperature of the heated rods in the channel 2 at 950 mm height computed by the ASTEC/URANIE and the ASTEC/KATUSA platform are shown in Figs. 141 and 142, respectively. The corresponding

time dependent Spearman correlation coefficients are shown in Figs. 143 and 144. Similar results are obtained for the temperature of the heated rods in the channel 3 at 950 mm height. The results for the Pearson and the Spearman correlations show quite good agreement. The correlations of the parameter 7 against the FOM here considered reaches about 60% in correspondence of the water injection. Since a positive correlation exists, an increase of the delay in reflooding leads to an increase of the cladding temperature, as expected. On the contrary, a slight anti-correlation exists between the parameter 12 and the FOM, the correlations reaching about 35%. In particular, the decrease of the void fraction threshold above which the heat exchange with the water droplets begins lead to an increase of the cladding temperature. Such a phenomenon becomes significant at the instants following the water injection before a full quenching front is developed.

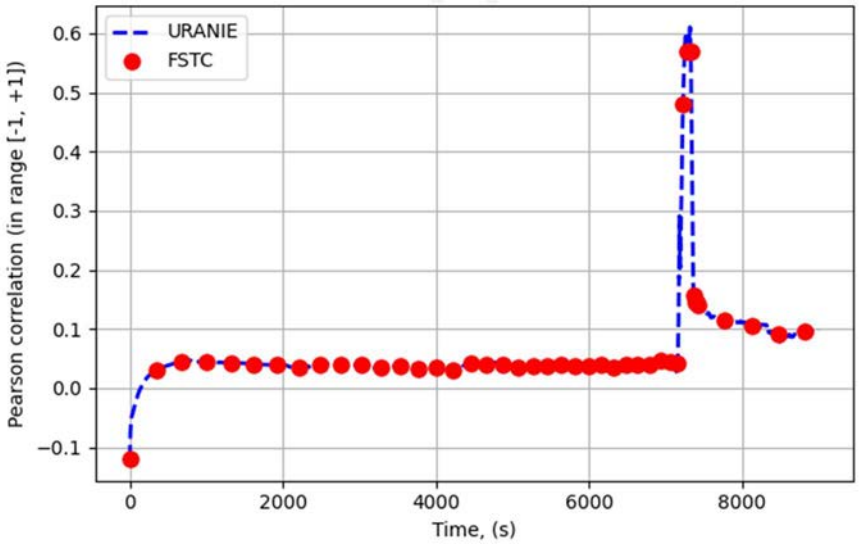

FIG. 141. Parameter 7 vs. temperature of the heated rods in the channel 2 at 950 mm height: time dependent Pearson coefficients computed by ASTEC/URANIE and ASTEC/KATUSA.

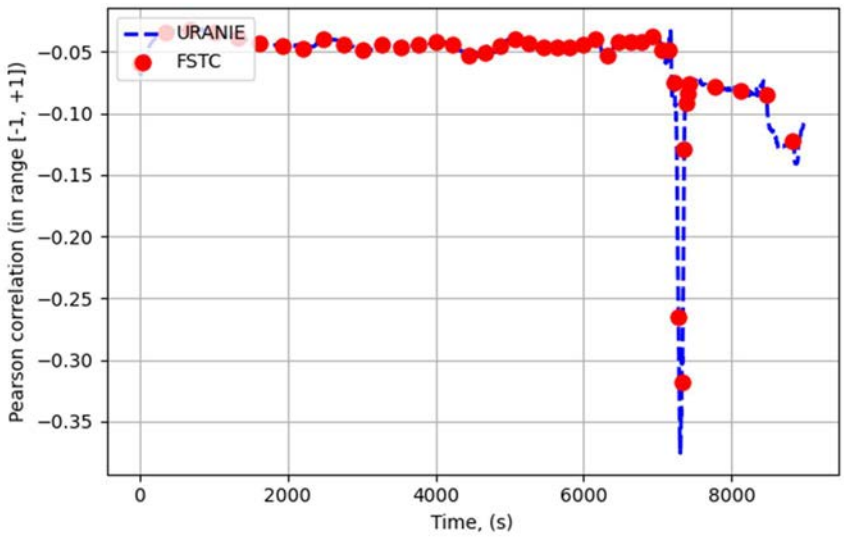

FIG. 142. Parameter 21 vs. temperature of the heated rods in the channel 2 at 950 mm height: time dependent Pearson coefficients computed by ASTEC/URANIE and ASTEC/KATUSA.

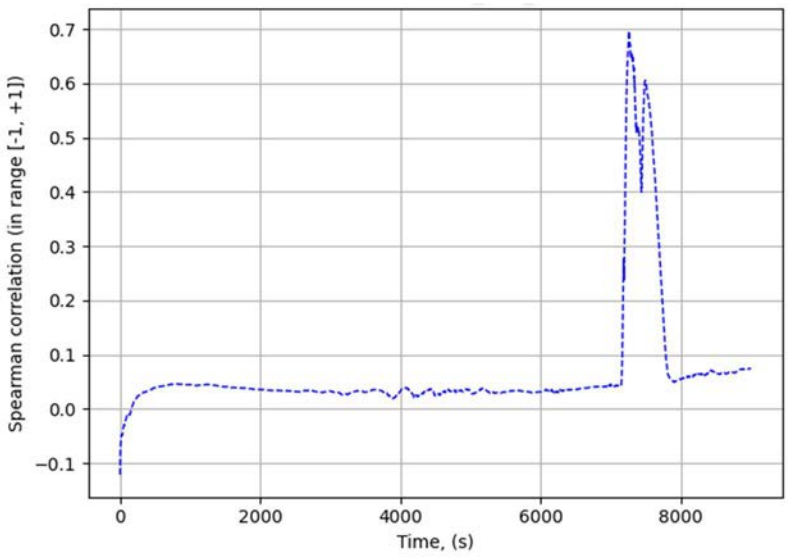

FIG. 143. Parameter 7 vs. temperature of the heated rods in the channel 2 at 950 mm height: time dependent Spearman coefficients computed by ASTEC/KATUSA.

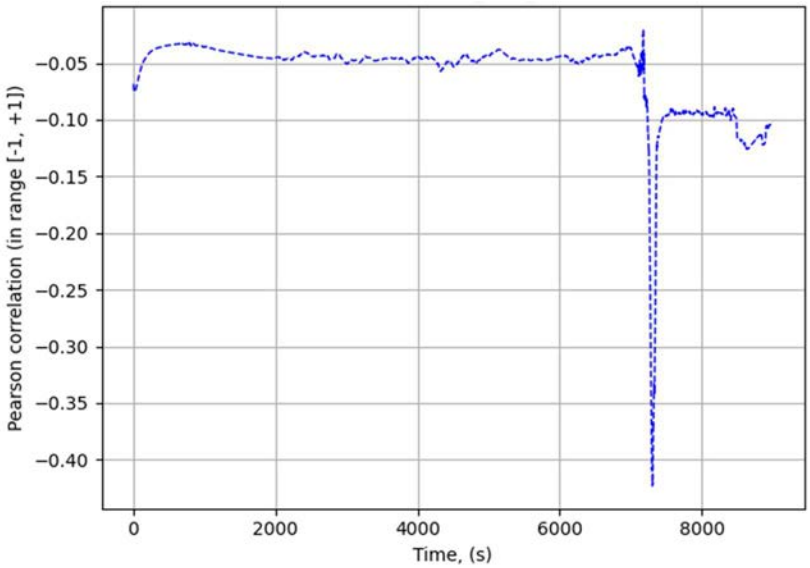

FIG. 144. Parameter 21 vs. temperature of the heated rods in the channel 2 at 950 mm height: time dependent Spearman coefficients computed by ASTEC/KATUSA.

The results of the simple statistics of the FOM#3 (H_2 generation rate, Table 2) are shown in Fig. 145. The ASTEC/URANIE and the ASTEC/KATUSA analyses show that the uncertainty parameters 10 and 12 mainly affect the FOM#3. The Pearson correlation results for such parameters are shown in Figs. 146 and 147, while the Spearman correlation results computed by employing the ASTEC/KATUSA platform only are shown in Figs. 148 and 149. As expected, the correlation coefficients look rather like the results for the FOM#1.

The correlation coefficients between the parameters 10 and 12 against the FOM#4 (axial profile of the oxide scale of the corner rod at 6620 s, Table 2) have been evaluated by means of the ASTEC/URANIE and the ASTEC/KATUSA platforms.

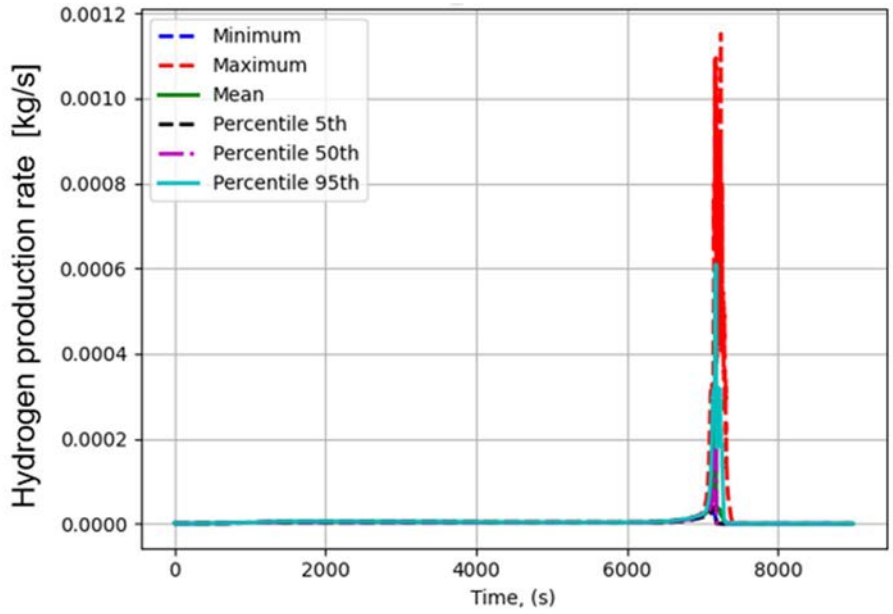

FIG. 145. Simple statistics of the H_2 generation rate.

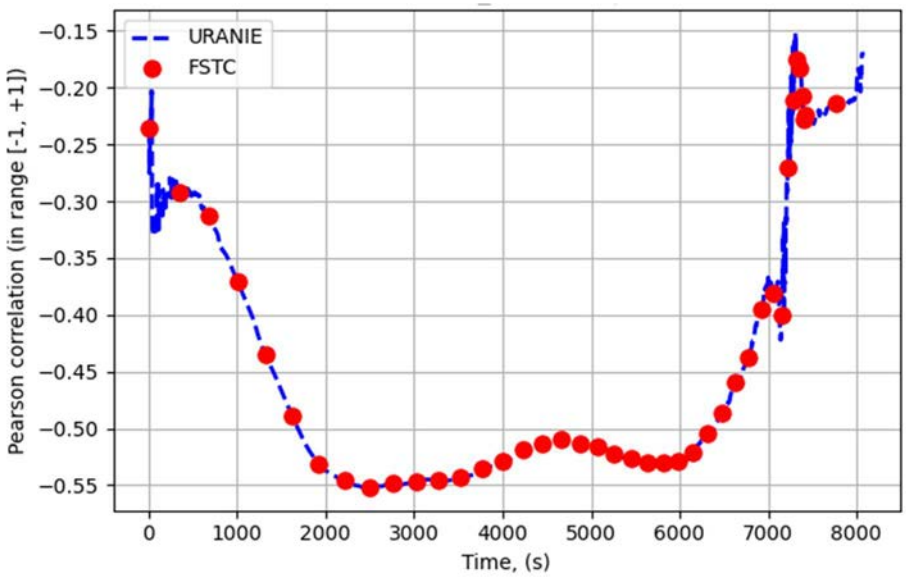

FIG. 146. Parameter 10 vs. the FOM#3: time dependent Pearson coefficients computed by ASTEC/URANIE and ASTEC/KATUSA.

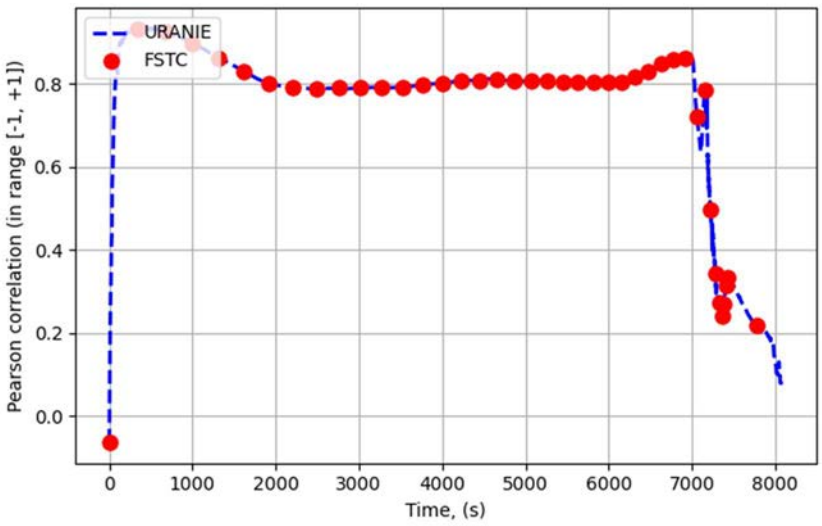

FIG. 147. Parameter 12 vs. the FOM#3: time dependent Pearson coefficients computed by ASTEC/URANIE and ASTEC/KATUSA.

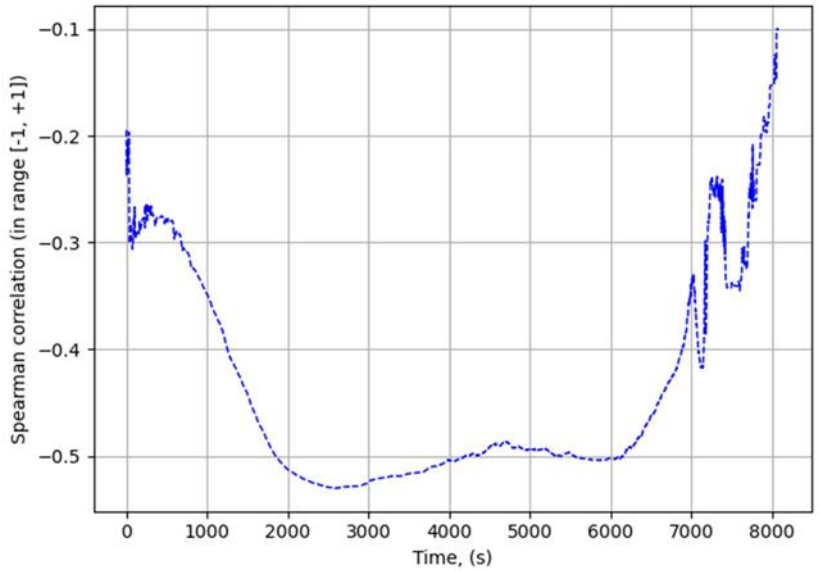

FIG. 148. Parameter 10 vs. the FOM#3: time dependent Spearman coefficients computed by ASTEC/KATUSA.

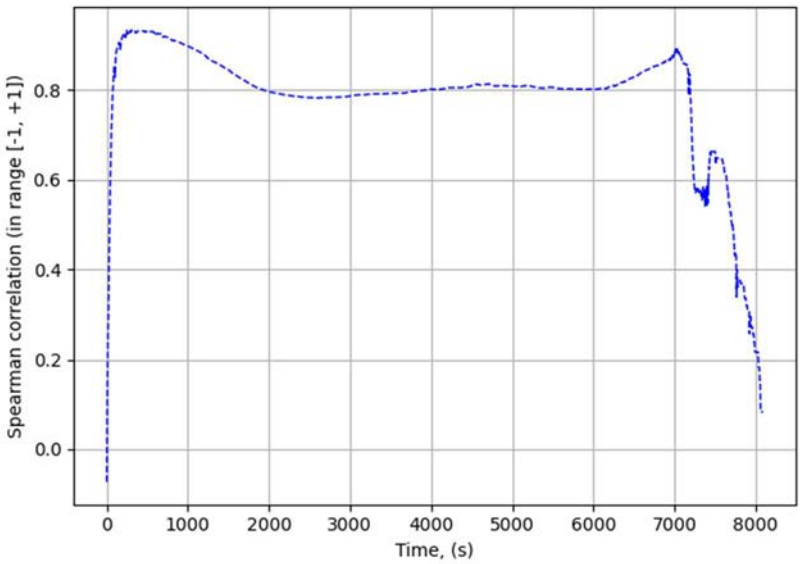

FIG. 149. Parameter 12 vs. the FOM#3: time dependent Spearman coefficients computed by ASTEC/KATUSA.

The Pearson coefficients shown in Fig. 150 indicate rather constant axial behaviour of the correlations. A relatively strong correlation with the parameter 12 (~80%) as well as a significant anti-correlation against the parameter 10 (about −50%) is observed. The Pearson correlations of the parameters 10 and 12 for the axial profile of the average oxide scale of the heated rods at the end of the scenario (FOM#5), are shown in Fig. 151. As expected, a similar behaviour as for the corner rod is observed.

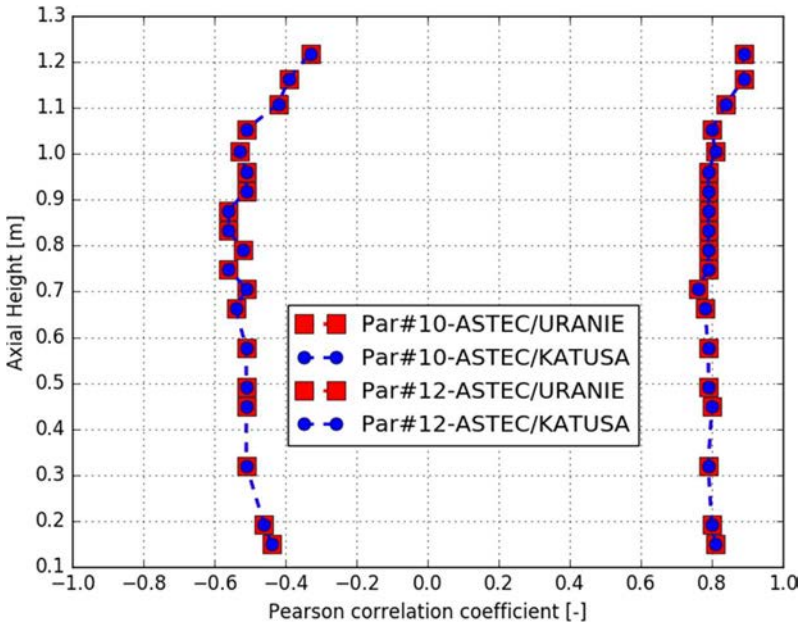

FIG. 150. Parameter 10 and 12 vs. the FOM#4: Pearson coefficients at different elevation computed by ASTEC/URANIE and ASTEC/KATUSA.

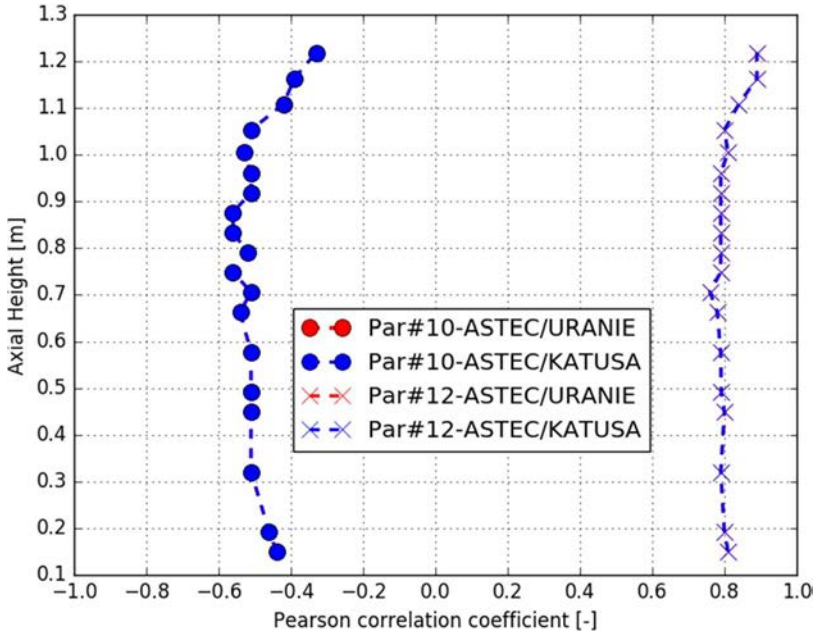

FIG. 151. Parameter 10 and 12 vs. axial oxide scale of the heated rods at the end of the scenario (FOM#5): Pearson coefficients at different elevation computed by ASTEC/URANIE and ASTEC/KATUSA.

5.4.CONCLUSIONS, LESSONS LEARNED, AND BEST PRACTISES

The best estimate case shows that the ASTEC code can reproduce the experimental data of the QUENCH-06 experiment (see Section 3.6 for more details). The ASTEC/URANIE and the ASTEC/KATUSA platforms demonstrated to be rather powerful tools for performing the uncertainty and sensitivity analysis of the QUENCH-06 experiment.

The QUENCH-06 test exercise showed to be a good example for testing the coupling between integral codes and uncertainty and sensitivity analysis tools as well as to train different uncertainty and sensitivity analysis methodologies and approaches. Since the wall clock time for the QUENCH-06 test simulation is rather short compared with the plant applications, many runs can be performed to have enough large databases and rather full matrices of data (uncertainty parameters vs. FOMs) to be analysed with an increased level of reliability with uncertainty and sensitivity analysis methods. Therefore, the possibility to access to a less sparse database allows to better evaluate the performance of different methodologies, i.e. correlation coefficients. The possibility to have access to the experimental data allows having a reference solution to the problem and the possibility of their employment in the uncertainty and sensitivity analysis methodologies themselves.

The analysis of the QUENCH-06 test also showed that:

- ASTEC code confirmed to be robust code, since no failures are observed during the assessment of database (300 samples employed). Such a behaviour is confirmed also when the ASTEC/KATUSA platform is applied at code nuclear plant level, as shown in [49, 54];
- FOMs selected for the test exercise are mainly affected by the steam mass flow rate at the bundle inlet and by the electric power;
- Using more than one single correlation, e.g. Pearson and Spearman, allows for better understanding the effects of uncertainty parameters for the selected FOMs. Such evidence is of relevance keeping in mind that different physical phenomena occur during the transients.

Therefore, the use of different correlations is suggested in view of the application of uncertainty and sensitivity analysis methods for simulations of NPPs with integral codes, which are characterized by the occurrence of several and non-linear phenomena when cliff-edge and bifurcation effects are expected;

— The selection of uncertainty parameters and the assessment of their associated PDFs are critical factors for effectively employing uncertainty and sensitivity analysis in integral code results. These analyses serve multiple purposes, such as identifying potential bottlenecks in integral codes and enhancing their performance. Additionally, they provide a reliable estimation of the impact of modelling physical phenomena during specific transient scenarios. In the context of the QUENCH-06 exercise, selecting parameters related to the test and the corresponding experimental uncertainties, determined by instrumentation performance, was relatively straightforward. However, the process became more challenging when identifying the most relevant uncertainty parameters for specific models, including aspects like molten material formation and movement, heat transfer involving water droplets, and defining their associated uncertainties. As outlined in Section 2.3, multiple sources of information are used to assess the list of uncertainty parameters. Nevertheless, in cases where data is limited, such as in the severe accident scenarios due to the sparse nature of experimental data, engineering judgments based on past uncertainty and sensitivity analyses become the primary approach. Given this recognized knowledge gap, particularly in severe accidents related research, it is advisable to make ongoing efforts to reduce and evaluate these uncertainties, enhancing the reliability and robustness of modelling and analysis.

6. INDIVIDUAL REPORT: LEI (LITHUANIA)

This section describes the severe accident code/s used for the analysis of QUENCH-06 experiment and discusses the obtained results.

6.1. DESCRIPTION OF SEVERE ACCIDENT CODE

Lithuanian Energy institute used the RELAP/SCDAPSIM severe accident code [52]. This code can describe the total thermal hydraulics response of the reactor coolant system (RELAP) and reactor core behaviour (SCDAP) during normal operation, transient or severe accident conditions. RELAP/SCDAPSIM integrates the US Nuclear Regulatory Commission's (NRC) publicly available RELAP/MOD3.3 [53] and SCDAP/RELAP5/MOD3.2 [54] models with proprietary advanced programming and numerical methods, user options, and models developed within the context of the International SCDAP Development and Training Program. Innovative Systems Software (Idaho Falls, USA) is the private, limited liability corporation that administers the SCDAP Development and Training Program, and it is the primary creator of particular models for the RELAP/SCDAPSIM.

The RELAP part of the code computes the thermal hydraulics response of the entire reactor coolant system (temperatures, pressure, velocity, etc.), the actions of the control system (adjusting the operating power settings, etc.), the reactor kinetics, and the actions of any unique reactor system components like valves and pumps.

The SCDAP part of the code determines how the core and vessel behave under normal, transient and accident conditions. Later phases of an accident are also modelled using SCDAP code, which include debris and molten pools formation, interactions between debris and the vessel, and structural

collapse (creep and rupture) of the vessel. As the damage to the core and vessel is progressed, the SCDAP models are invoked automatically.

The QUENCH experimental facility is modelled using RELAP/SCDAPSIM code version Mod4 [58]. RELAP/SCDAPSIM Mod4 version have integrated uncertainty package for the uncertainty analysis. The SUSA statistical tool is used for the uncertainty and sensitivity analysis.

6.2. DESCRIPTION OF RELAP/SCDAPSIM MODEL FOR THE QUENCH-06 TEST

QUENCH nodalization scheme is shown in Fig. 152. The pipe, time dependent volumes and junctions, single junctions, and branch, are used in the modelling of the QUENCH facility to simulate the space between the heated rods and the outside cooling loop.

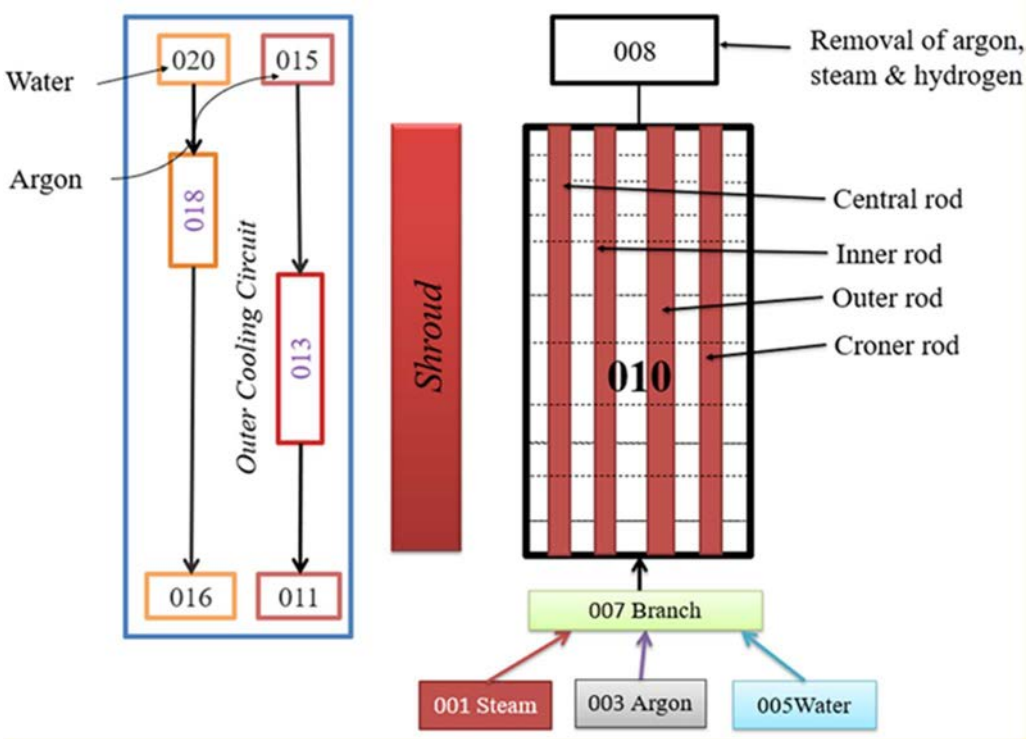

FIG. 152. Nodalization scheme of QUENCH test used in RELAP/SCDAPSIM.

Notations “001”, “003” and “005” shown in Fig. 152 represent the time dependent components, the steam, argon and water, respectively. Steam, argon, and water are injected in the branch component “007” using time dependent junctions according to the QUENCH-06 test phases. Branch component is connected to the pipe component “010” by single junction. Component “010” describes space between assembly. Component “010” is divided into 18 axial nodes with 0.1 m length. Component “010” is connected to the time dependent component “008” with single junction where the fluids flow through the bundle. The outer cooling circuit of the QUENCH bundle shroud is modelled using pipe components “013” and “018”. Components “011”, “015”, “016” and “020” are time dependent volumes which serving as fluid transfer (water and argon). To remove the heat from the shroud heat structure component is used which connects pipe component “010” and components “013” and “018”. Component “013” is divided into 13 axial nodes, and component “018” is divided into 5 axial nodes with 0.1 m length each.

The nodalization scheme of the SCDAP part of the QUENCH-06 test model is presented in Fig. 153. The SCDAP nodalization includes fuel," "cora," and "shroud" components. There are five components used for the SCDAP nodalization of the QUENCH-06 test model:

- Component 1: central rod (not heated), modelled as a "fuel" element composed of ZrO_2 pellets in the center, gas-filled gap, and Zircaloy cladding;
- Component 2: 8 heated rods around the central rod modelled using "cora" component which corresponds to the fuel rod imitators;
- Component 3: 12 heated rods, modelled using "cora" component, which correspond to the fuel rod imitators;
- Component 4: 4 unheated rods in the corners, modelled as fuel component;
- Component 5: shroud of the QUENCH-06 test bundle, modelled as "shroud" component, which consists of the inner Zr layer, an insulating layer of ZrO_2 and Inconel layer.

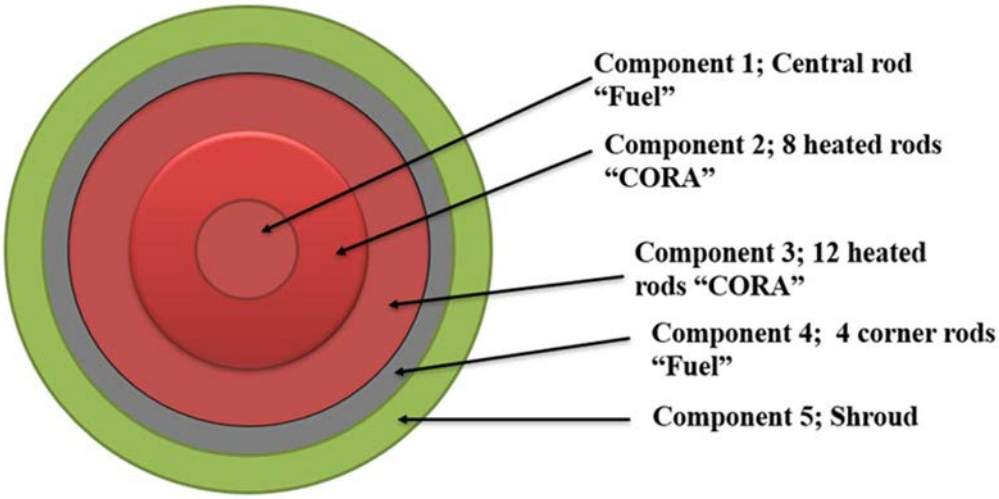

FIG. 153. SCDAP part scheme of QUENCH-06 test.

SCDAP components 1–4 are connected to the RELAP component "010" simulating the QUENCH-06 test assembly. According to the test, the total heated length is 1.0 m and according to the nodalization it is placed between 4^{th} and 13^{th} nodes. Shroud (component 5) has heat exchange between RELAP pipe components "013" and "018" which models the outer cooling circuit. The heat structure thickness is 0.012 m and it has radial nodes. The special component "cora" used in the SCDAP part models the electrically heated fuel rod imitators. This component models ZrO_2 pellets, gas filled gap, and Zircaloy cladding with specially developed mathematical model [56]. The total power input is specified by user, while the axial and temperature dependent thermal power release is calculated in the model.

The model computes heated area of the tungsten heater rod and includes the effects of contact resistance. The model first computes the electrical resistance of copper, molybdenum, and tungsten where the geometrical dimensions of the fuel rod imitators (copper, molybdenum, and tungsten) are built into the resistance equations [55] [60]. For the "cora" component, the user needs to define electrical power, tungsten heater parameters and contact resistance of sliding contacts. The electrical power for the model was given according to the measurement provided during the QUENCH-06 test. The radius of the tungsten heater rod is assumed to be 0.003 m. Contact resistance of sliding contacts is selected to be 3 mΩ.

Other basic geometrical parameters as well as some modelling parameters are chosen according to the data provided in Section 2.3. However, not all proposed parameters could be represented by RELAP/SCDAPSIM. Thus, Table 21 provides the list as used in this model.

TABLE 21. UNCERTAINTY PARAMETERS AND SELECTED CASES IN RELAP/SCDAPSIM MODEL

Uncertainty parameter	**Reference value and uncertainty range**	**Probability distribution**
P1 – Rod pitch, mm	14.3 ± 0.15	Uniform
P2 – Fuel pellet simulator (ZrO_2) external diameter, mm	9.15 ± 0.02	Uniform
P3 –Cladding thickness, mm	0.725 ± 0.00725	Uniform
P4 –Internal diameter Shroud, mm	80 ± 0.8	Uniform
P5 –Thickness of the Shroud, mm	2.38 ± 0.023	Uniform
P6 –Thickness of the Insulator, mm	37.0 ± 0.37	Uniform
P7 –Quench water injection it to test section, s	7215 ± 0.5%	Uniform
P8 –Quench water mass flow rate at the bundle inlet, kg/s	Ref. value ± 2%	Normal
P9 –Argon mass flow rate at the bundle inlet, kg/s	Ref. value ± 2%	Normal
P10 –Steam mass flow rate at the bundle inlet, kg/s	Ref. value ± 2%	Normal
P11 –Pressure at the bundle outlet, bar	2.0± 2%	Normal
P12 –Electrical power, W	Ref. value ± 2%	Normal
P13 –Quenching water temperature, K	Ref. value ± 2%	Normal
P14 –Fuel/clad internal pressure, bar	2.2± 2%	Normal
P15 –Fraction of oxidation of fuel rod cladding for stable oxide shell	Default value (0.6) ± 10%	Uniform
P16 –Failure temperature of the ZrO_2 layer, K	2374 ± 5%	Uniform
P19 –Fraction of surface area covered with drops that results in blockage that stops local oxidation	Default value (0.2) ± 5%	Uniform
P20 –Surface temperature for freezing of drops of liquefied/slumping fuel rod cladding, K	Default value (1750) ± 5%	Uniform
P21 –Velocity of drops of cladding material slumping down outside surface of fuel rod, m/s	Default value (0.5) ± 5%	Uniform

6.3.DESCRIPTION OF RELAP/SCDAPSIM MODEL FOR THE QUENCH-06 TEST

The main results of the calculation are chosen according to FOMs discussed in Section 2.3 and shown in Table 22. Additionally, the following parameters are analysed: temperature of the inner fuel ring simulator at elevation 750 and 950 mm, and the axial profile of the average oxide scale of the shroud at the end of the scenario. The calculation results and experimental data of the total H_2 generation and H_2 generation rate are shown in Figs. 154 and 155, respectively. It can be observed that at the quenching phase higher peak of the H_2 generation rate occurs in the QUENCH-06 test than it is calculated by RELAP/SCDAPSIM. The reason for this could be the oxidation model in the RELAP/SCDAPSIM Mod4.

TABLE 22. CHOSEN FIGURES OF MERITS

	FOM
1	Total mass of accumulated H_2
	Temperature of the central fuel rod simulator at elevation 950 mm
2	Temperature of the inner fuel ring simulator at elevation 950 mm
	Temperature of the inner fuel ring simulator at elevation 750 mm
3	H_2 generation rate
4	Axial profile of the oxide scale of the corner rod at 6620 s
5	Axial profile of the average oxide scale of the heated rods at the end of the scenario
	Axial profile of the average oxide scale of the shroud at the end of the scenario

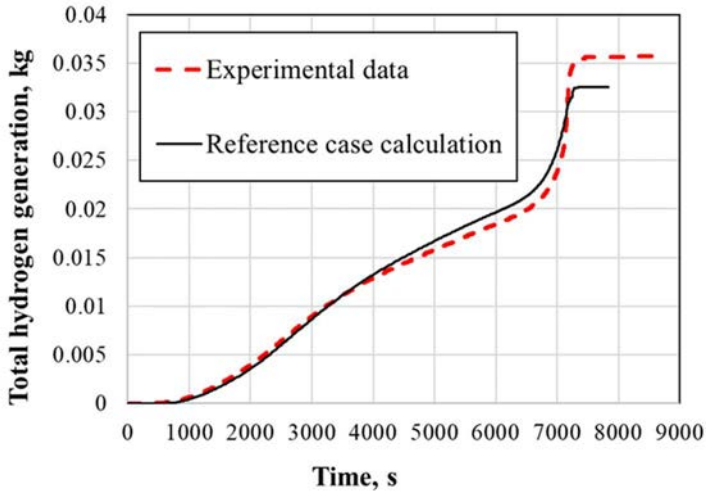

FIG. 154. Total H_2 generation.

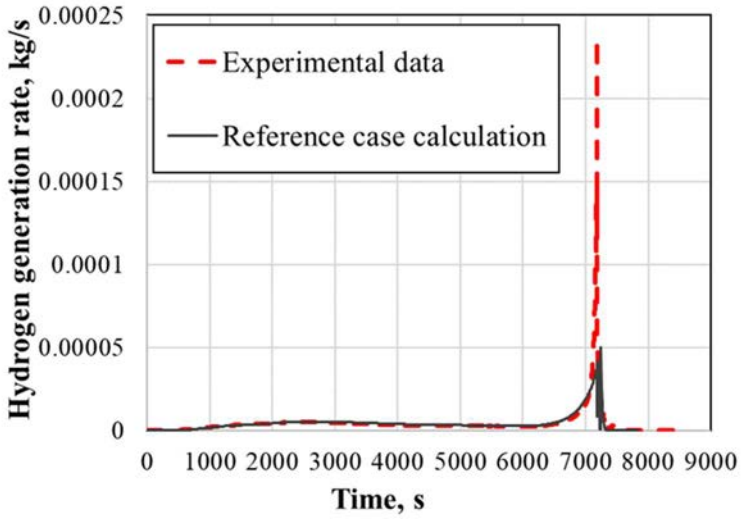

FIG. 155. Total H_2 generation rate.

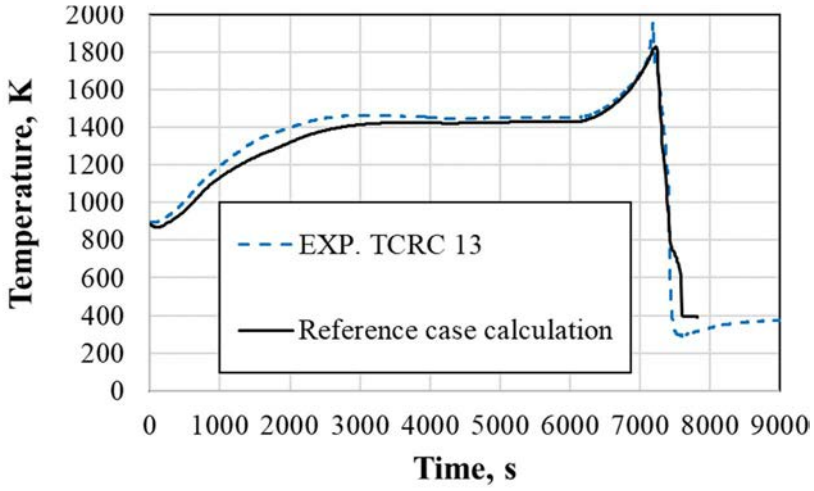

FIG. 156. Temperature of the unheated (central) rod at elevation 950 mm.

Comparison of calculated and measured temperatures of the unheated rod at 950 mm elevation is presented in Fig. 156 indicating good agreement between calculated and measured values. Comparison of the calculated and measured temperatures of the inner fuel imitators ring at elevation 950 and 750 mm are shown in Figs. 157 and 158. The calculated temperatures are lower than measured temperatures at the elevation 950 mm and higher at the elevation 750 mm. All calculated temperatures are higher when compared to measured values at elevation up to 750 mm and lower for the higher elevation.

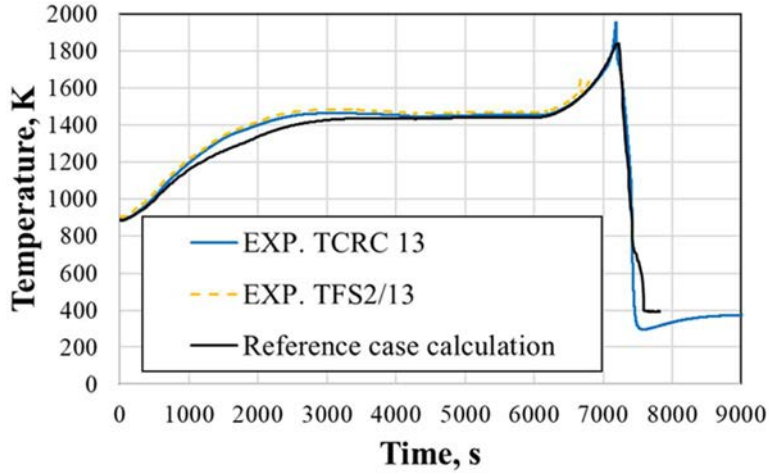

FIG. 157. Temperature of the inner fuel imitators ring at elevation 950 mm.

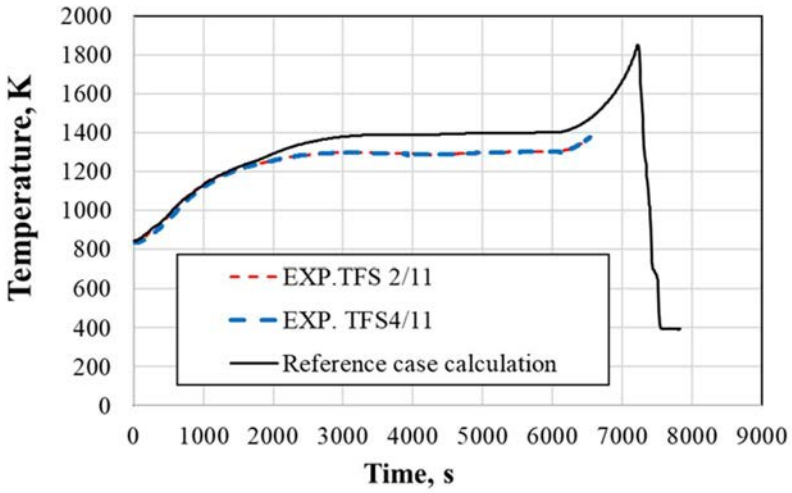

FIG. 158. Temperature of the inner fuel imitators ring at elevation 750 mm.

Axial profiles of the oxide scale of the corner rod and heated rod are shown in Figs. 159 and 160, respectively. The calculated oxide scale before the quenching phase (Fig. 159) is higher at the lower elevation of fuel imitators. Comparison of axial profile of the oxide scale of the heated rods at the end of the test (Fig. 160 shows that code did not predict such high oxidation scale at the elevation 950 mm compared to measured values. The calculated oxide scale is higher in the elevation from 600 mm to 850 mm. Similar results are observed for the axial profile of the average oxide scale of the shroud at the end of the test (Fig. 161).

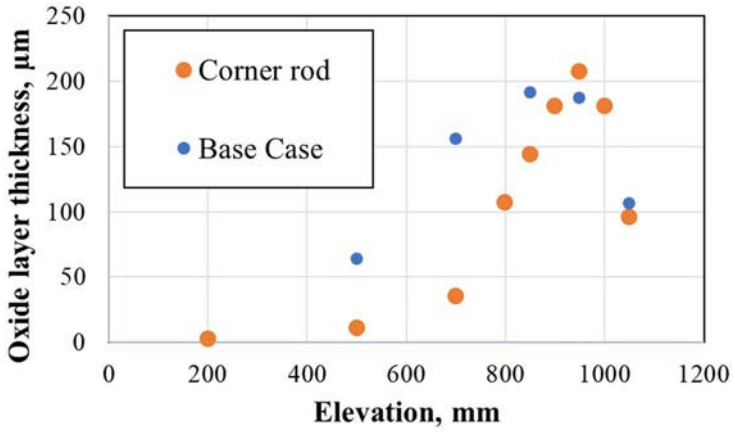

FIG. 159. Axial profile of the oxide scale of the corner rod at 6620 s.

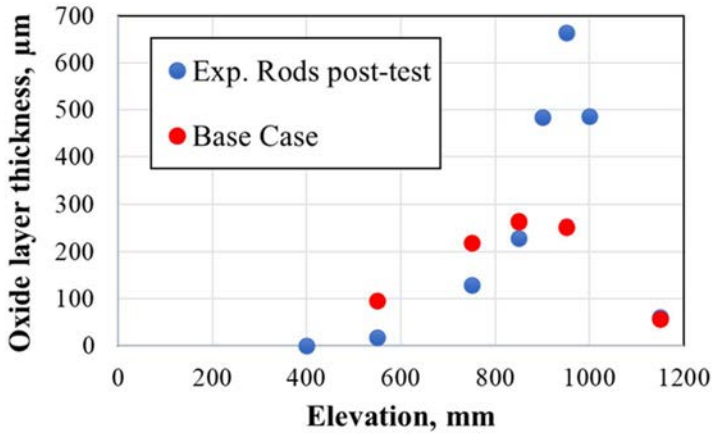

FIG. 160. Axial profile of the average oxide scale of the heated rods at the end of the test (calculation).

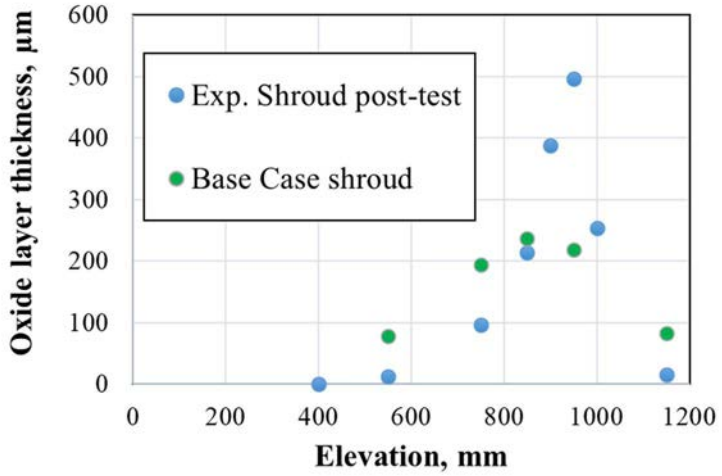

FIG. 161. Axial profile of the average oxide scale of the shroud at the end of the test (calculation).

6.4.DESCRIPTION OF THE UNCERTAINTY AND SENSITIVITY TOOL

The GRS methodology [58] is used for the uncertainty quantification of the QUENCH-06 modelling results. It allows to evaluate the impact of uncertainties in the input data on the results. The GRS methodology relies on a probabilistic quantification of the uncertainty of associated parameters and systematic identification of relevant physical processes. The uncertainty of the investigated parameters is described by their ranges and subjective probability distributions. Random uncertainty parameter values are created using Monte Carlo method. The key benefit of the GRS methodology is that the marginal number of calculations performed by numerical simulation tools are unaffected by the total number of selected uncertainty parameters. The number of code runs depends only on the desired probability content and the confidence level. For the analysis, the 95% probability content and 95% of confidence level using two sided tolerance limit are selected. According to [62], it is necessary to perform at least 93 runs. Thus, for the uncertainty analysis, 100 runs are generated, following the usual practice. The GRS methodology and statistical methods SUSA [63] are used for the sensitivity and uncertainty analysis of RELAP/SCDAPSIM calculation results.

6.4.1. Results of the uncertainty and sensitivity analysis

The dispersion of 100 RELAP/SCDAPSIM calculation results of a central rod temperature at 950 mm and upper and lower uncertainty limits comparison with experimental data, are shown in Fig. 162. The temperature difference between the lowest and the highest calculated temperature in the pre-oxidation phase is only ~50 K (~2.5% from the highest calculated temperature). A different situation exists for calculated total H_2 generation. The dispersion of the calculation results is presented in Fig. 163. At the end of the QUENCH test, the difference between the lowest and highest calculated values is 14.2%.

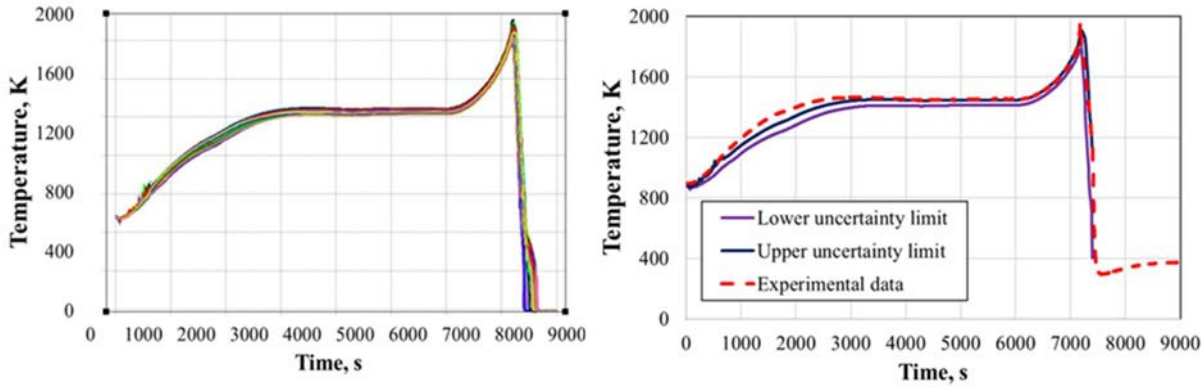

(a) *(b)*

FIG. 162. Temperature of the central rod at 950mm: (a) dispersion results, (b) upper and lower uncertainty limits.

Scalar uncertainty analysis for calculated oxide layer thickness is presented in Fig. 164. During the QUENCH-06 test, one of the corner rods was removed at 6620 s to investigate the thickness of the oxide layer before the quenching phase. In Fig. 164 (a) measurements of the oxide layer thickness at 6620 s is compared with upper and lower limits of RELAP/SCDAPSIM calculation results. It can be seen that the calculated values are slightly overestimated compared to the measurements. The best agreement is obtained for 950 mm elevation. In Fig. 164 (b) the oxide layer thickness measured after the QUENCH-06 test is compared with the upper and lower limits of the calculation results. Calculated values are overestimated in the lower elevation region (up to 850 mm), but in the elevation from

850 mm−1000 mm, the experimental values are much higher. This result shows that during the quench phase in the region 850 mm−1000 mm, zircaloy cladding oxidation was much more intensive compared to the results obtained by RELAP/SCDAPSIM code.

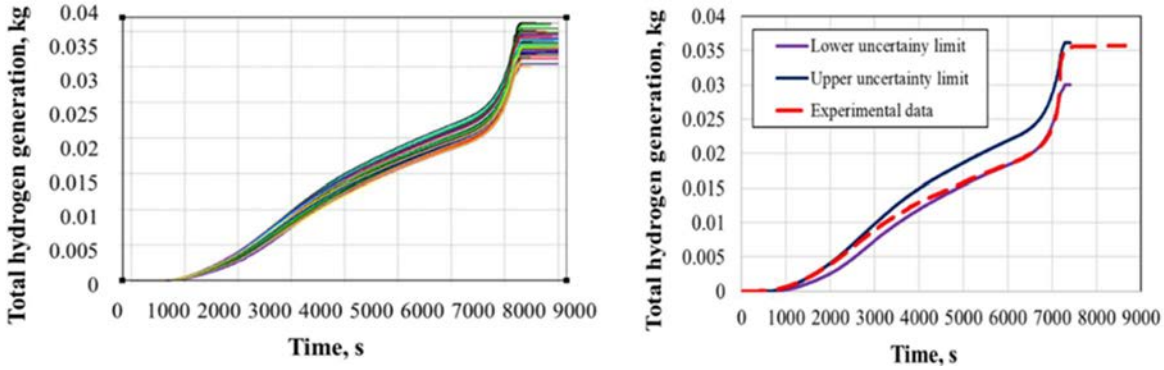

(a) *(b)*

FIG. 163. Total H_2 generation; a) dispersion results, b) upper and lower uncertainty limits.

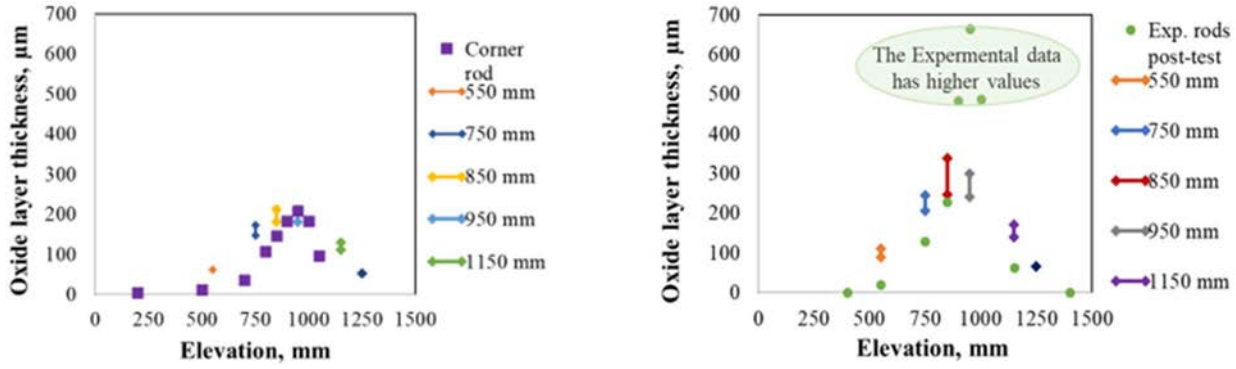

(a) *(b)*

FIG. 164. Results of the scalar uncertainty analysis of the oxide layer: (a) before the quenching phase (6620 s), (b) at the end of the QUENCH test.

It is important to check the determination coefficient (R^2) before analysing the results of the sensitivity analysis. Linear regression is one of the main requirements in the GRS methodology. Thus, R^2 is used to assess the quality of the correlation coefficient. The determination coefficient range is between 0 and +1. Common practice is, that if the value of $R^2 < 0.6$, the regression coefficient of the sensitivity parameters may be incorrect because of too many unexplained parameter variations. In that case, it is needed to use another method. In Fig. 165, R^2 of total H_2 generation and temperature of the central rod at 950 mm elevation are shown. The closer R^2 value is to 1, the better is the quality of the sensitivity analysis. For both results the determination coefficient is high, higher than 0.9, during all QUENCH-06 test, excluding the beginning of the heat-up phase

Spearman rank correlation coefficient is based on non-parametric methods. Spearman rank correlation coefficient range is [+1, −1]. The positive values indicate positive influence; an increase of the uncertain initial parameters increases the value of results. The negative influence has the opposite meaning. It is a common practice that if the influence of the uncertain parameter is less than 0.2, the parameter could be excluded from the analysis because the influence on the calculation results is too weak.

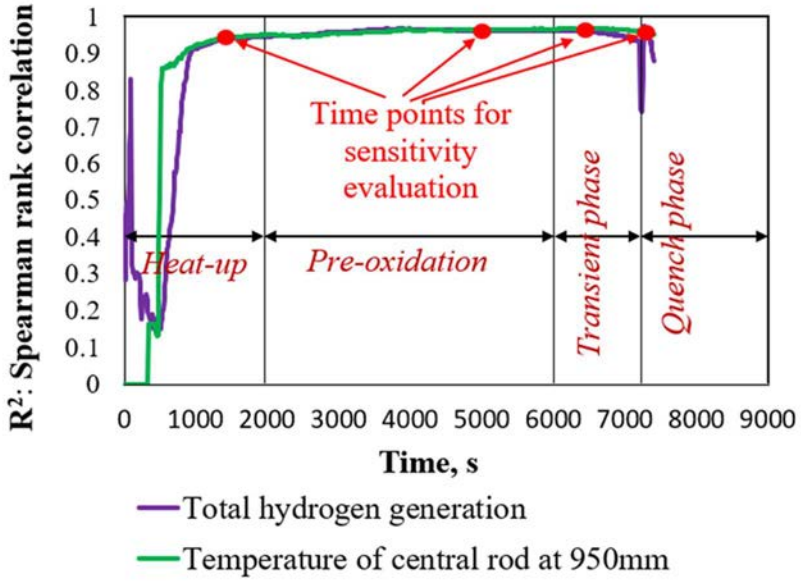

FIG. 165. Determination coefficient for total H_2 generation and temperature of central rod at 950 mm elevation.

The sensitivity analysis is provided for all periods of test. According to the Spearman rank correlation coefficient, the uncertain parameters influence is changing during the time as shown in Figs. 166 and 167. Thus, the representative time points were taken at each QUENCH-06 test phase to evaluate the influence of uncertain parameters. The influence of uncertain parameters for total H_2 generation and central tube temperature at 950 mm elevation at certain time points at different test phases are presented in Table 23. For total H_2 generation, the most influenced parameter is cladding thickness at the heat-up phase, however, electrical power is the most influenced uncertain parameter in all phases. Steam mass flow rate at the bundle inlet also has a significant influence in all test phases. Results of the sensitivity analysis for the central rod temperature at 950 mm elevation shows that the most influenced parameter is electrical power in heat-up, peroxidation and transient phases. However, the most influenced parameter in the quench phase is the quenched water injection time.

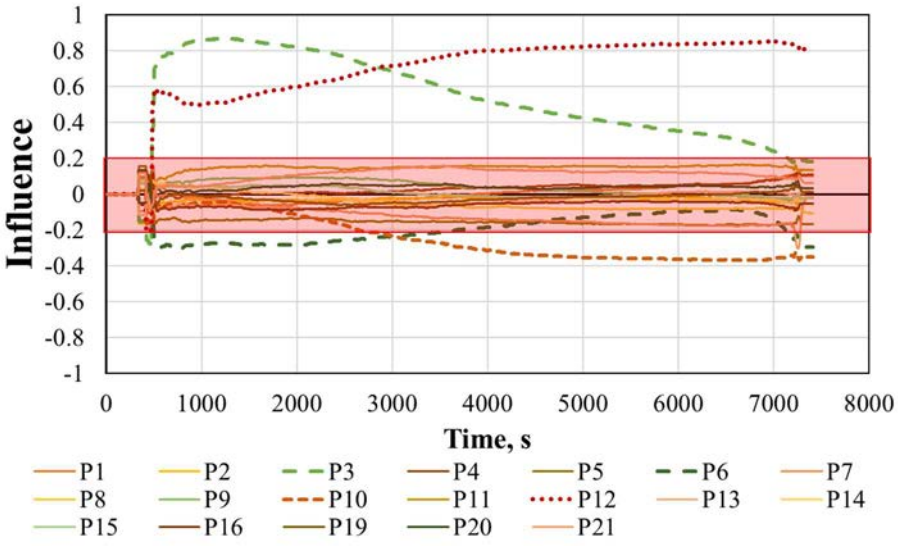

FIG. 166. Influence of uncertain parameters for total H_2 generation.

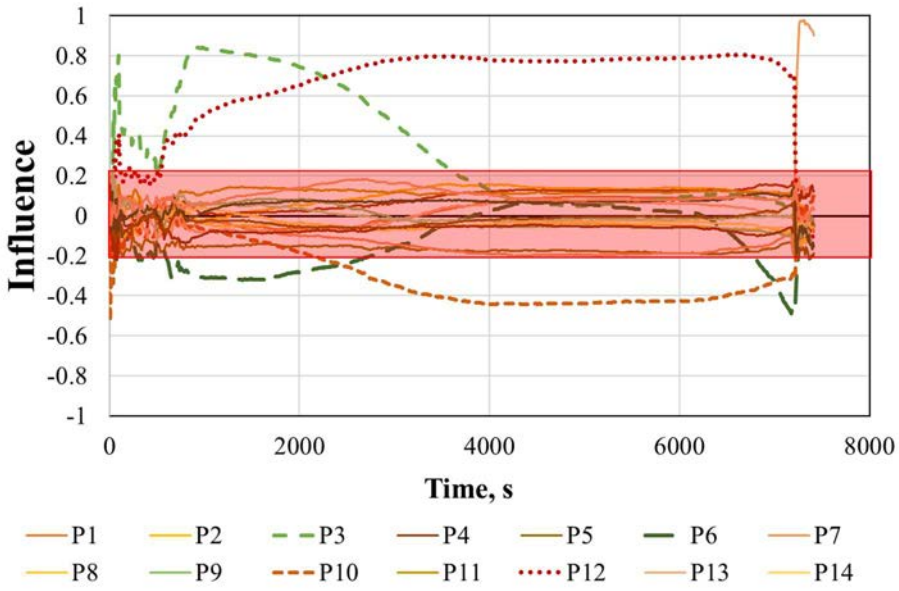

FIG. 167. Influence of uncertain parameters of temperature of central rod.

TABLE 23. INFLUENCE OF UNCERTAINTY PARAMETERS FOR TOTAL HYDROGEN GENERATION AND TEMPERATURE OF CENTRAL ROD AT 950 MM ELEVATION

Phase	**Total H_2 generation Parameter (influence on calculation results)**	**Temperature at 950mm Parameter (influence on calculation results)**
Heat up(1500s)	Cladding thickness (+0.85) Electrical power (+0.55) Thickness of the insulator (–0.27)	Cladding thickness (+0.8) Electrical power (+0.58)
Pre-oxidation (5000s)	Electrical power (+0.82) Cladding thickness (+0.43) Steam mass flow rate at the bundle inlet (–0.35)	Electrical power (+0.78) Steam mass flow rate at the bundle inlet (–0.43)
Transient (6500s)	Electrical power (+0.85) Steam mass flow rate at the bundle inlet (–0.36) Cladding thickness (+0.32)	Electrical power (+0.81) Steam mass flow rate at the bundle inlet (–0.39)
Quench (7350s)	Electrical power (+0.81) Steam mass flow rate at the bundle inlet (–0.35) Thickness of the insulator (–0.29)	Quench water injection to test section (+0.97)

To evaluate the sensitivity of the initial parameters to oxide layer thickness, the scalar sensitivity analysis for each analysed bundle elevation is provided. Analysed elevations are 550 mm, 750 mm, 850 mm, 950 mm, 1150 mm, and 1250 mm. Sensitivity results for these elevations at time 6620 s are shown in Fig. 168 while for the end of calculations in Fig. 169.

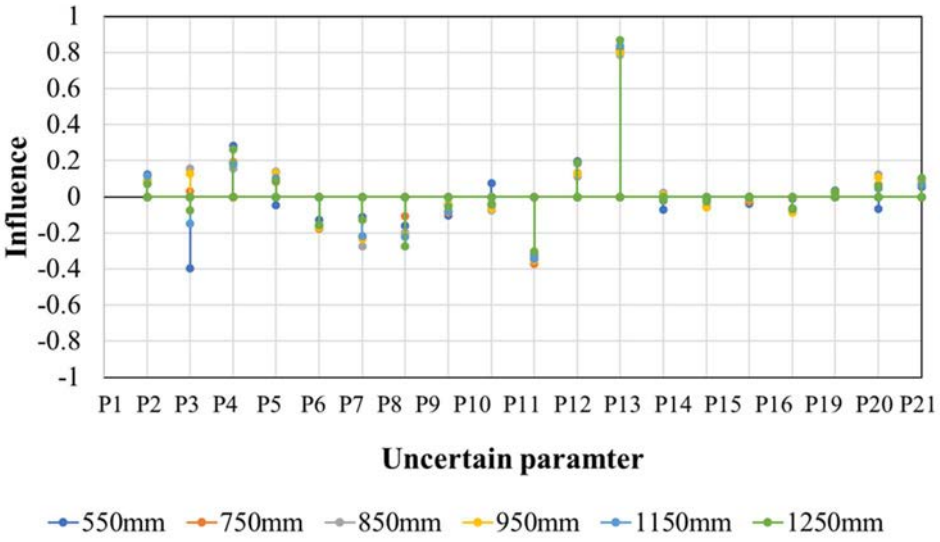

FIG. 168. Results of sensitivity scalar analysis of the oxide thickness at 6620 s (before transient phase).

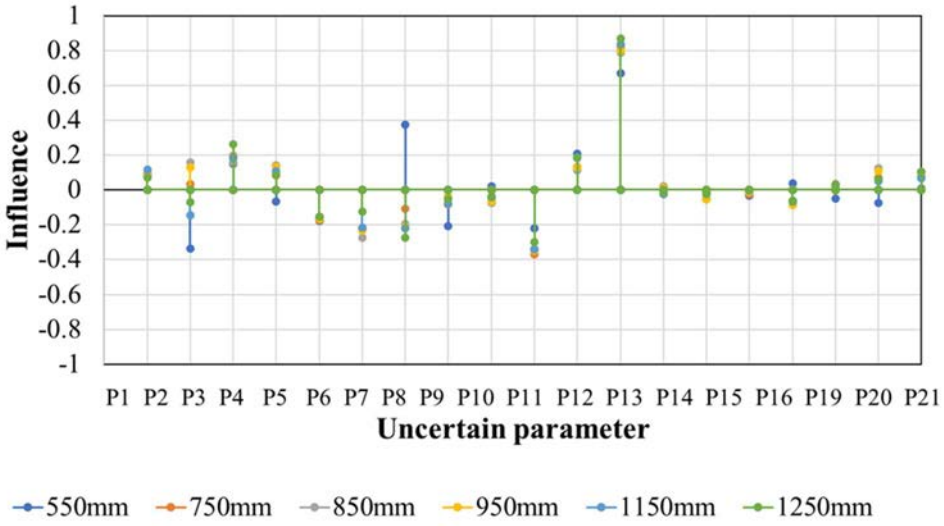

FIG. 169. Results of sensitivity scalar analysis of the oxide thickness at the end of the calculation.

The most influenced uncertain parameter on calculation results at 6620 s and at the end of calculations is found to be P12 (electrical power) with a positive influence (+0.8) and P10 (steam mass flow rate) with negative influence (–0.4) at 550 mm, 750 mm, 850 mm, 950 mm, 1150 mm, and 1250 mm elevations. However, P7 (cladding thickness) has a positive influence (+0.4) on calculation results at the end of calculations at 550 mm elevation and has a negative influence at other elevations.

The most influenced parameters on calculations results are shown in Tables 24 and 25. Detailed discussion is presented in the following section.

TABLE 24. INFLUENCE OF UNCERTAINTY PARAMETERS FOR OXIDE THICKNESS

Phenomenon	Parameter (influence to result)
Oxide thickness before transient phase (6620 s)	Electrical power (+0.8)
	Steam mass flow rate at the bundle inlet (–0.4)
	Cladding thickness (+0.35)
Oxide thickness at the end of the calculation	Electrical power (+0.8)

6.4.2. Calculation cases

It is a good practice to generate calculations with parameters' values at the end of the uncertainty region to examine if RELAP/SCDAPSIM code is capable to calculate the most extreme cases without running into calculation failures. Prior to the uncertainty and sensitivity analysis, two calculation cases are developed:

- **Case 1**: upper and lower uncertainty parameters are selected from the uncertainty ranges (Table 25) to achieve the highest calculation result for total mass of accumulated H_2 and temperatures;
- **Case 2**: upper and lower uncertainty parameters are selected from the uncertainty ranges (Table 25) to achieve the lowest calculation result for total mass of accumulated H_2 and temperatures.

TABLE 25. UNCERTAINTY RANGE FOR CASE 1 AND CASE 2

Parameter name	Case 1	Case 2	Maximum	Minimum
P1	Ref. value -0.15 mm	Ref. value +0.15 mm	Ref. value +0.15 mm	Ref. value –0.15 mm
P2	Ref. value +0.02 mm	Ref. value –0.02 mm	Ref. value –0.02 mm	Ref. value +0.02 mm
P3	Ref. value –0.00725 mm	Ref. value +0.00725 mm	Ref. value +0.00725 mm	Ref. value –0.00725 mm
P4	Ref. value –0.8 mm	Ref. value +0.8 mm	Ref. value +0.8 mm	Ref. value –0.8 mm
P5	Ref. value +0.023 mm	Ref. value –0.023 mm	Ref. value –0.023 mm	Ref. value +0.023 mm
P6	Ref. value +0.37 mm	Ref. value –0.37 mm	Ref. value –0.37 mm	Ref. value +0.37 mm
P7	Ref. value +0.5%	Ref. value –0.5%	Ref. value –0.5%	Ref. value +0.5%
P8	Ref. value –2%	Ref. value +2%	Ref. value +2%	Ref. value –2%
P9	Ref. value –2%	Ref. value +2%	Ref. value +2%	Ref. value –2%
P10	Ref. value –2%	Ref. value +2%	Ref. value -2%	Ref. value +2%
P11	Ref. value –2%	Ref. value +2%	Ref. value +2%	Ref. value –2%
P12	Ref. value +2%	Ref. value –2%	Ref. value +2%	Ref. value –2%
P13	Ref. value +2%	Ref. value –2%	Ref. value +2%	Ref. value -2%
P14	Ref. value +2%	Ref. value -2%	Ref. value -2%	Ref. value +2%
P15	Ref. value –10%	Ref. value +10%	Ref. value -10%	Ref. value +10%
P16	Ref. value –5%	Ref. value +5%	Ref. value –5%	Ref. value +5%
P19	Ref. value +5%	Ref. value –5%	Ref. value +5%	Ref. value –5%
P20	Ref. value +5%	Ref. value –5%	Ref. value +5%	Ref. value –5%
P21	Ref. value –5%	Ref. value +5%	Ref. value +5%	Ref. value –5%

The assumptions for Case 1 and Case 2 are made based on the engineering judgment and experience from the modelling of other QUENCH tests. These assumptions need to be revised after uncertainty and sensitivity analysis are complete. Case 1 and Case 2 calculations are successful, without calculation failures or errors. Results are reasonable and full uncertainty and sensitivity analysis are discussed in Section 6.4.1. Depending on FOM i selected for the analysis, influence of uncertainty parameters could be different and need to be considered. According to negative or positive influence on the calculation

result, the lower or upper values from the parameter uncertainty ranges are selected for calculation of the selected FOM (temperature of the unheated (central) rod at elevation 950 mm). These values are presented in Table 25.

Only one third (7 out of 19 parameters) of all selected uncertainty parameter values has coincided with the sensitivity results. However, the values of the uncertainty parameters which have the highest influence on calculation results for Case 1 and Case 2 are selected to be the same as for the maximum and minimum cases. As it is presented in Figs. 166 and 167, the parameter influence is changing during different QUENCH-06 phases. For some parameters, the influence changes from positive to negative or vice versa. In analysing the results of sensitivity analysis, it is needed to consider the nature of the parameters and to understand at which test phase it could influence the calculation results. Analysed 19 parameters were grouped as follows:

- P1, P6 and P14 initial parameters, which have the highest influence at the beginning of the calculation, but its influence needs to be evaluated;
- P7, P8 and P13, quenching water parameters that only affect after the start of quenching phase;
- P9, P12 boundary conditions that have similar behaviour to initial parameters, noting that steam flow is actual only until the start of quenching phase;
- P15, P21 SCDAP parameters that belong to oxidation processes and fuel degradation processes. The biggest effect of these parameters could be in transient and quench phases.

Considering these groups and their influences on the calculation results for different phases, the lower and upper values were selected for corresponding maximum and minimum calculation cases. Cladding temperature of the unheated (central) rod at 750 mm and 950 mm elevation for these cases is presented in Figs. 170 and 171. Comparison of the calculation results shows that minimum case and Case 2 are very close as well as are the maximum case and Case 1. Comparison of the calculation results of total H_2 generation is shown in Fig. 172. Upper and lower uncertainty limits are bounded by maximum and minimum cases, and Case1 and Case2. Some difference is observed for maximum case and Case1 for H_2 generation values at the end of the quenching phase where Case1 shows the higher values.

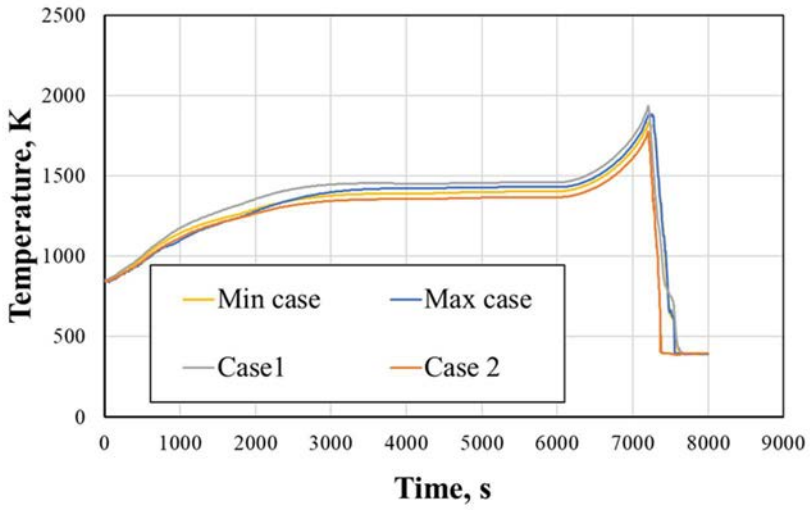

FIG. 170. Cladding temperature of the unheated (central) rod at 750 mm elevation. Results of maximum and minimum cases compared to Case 1 and Case 2

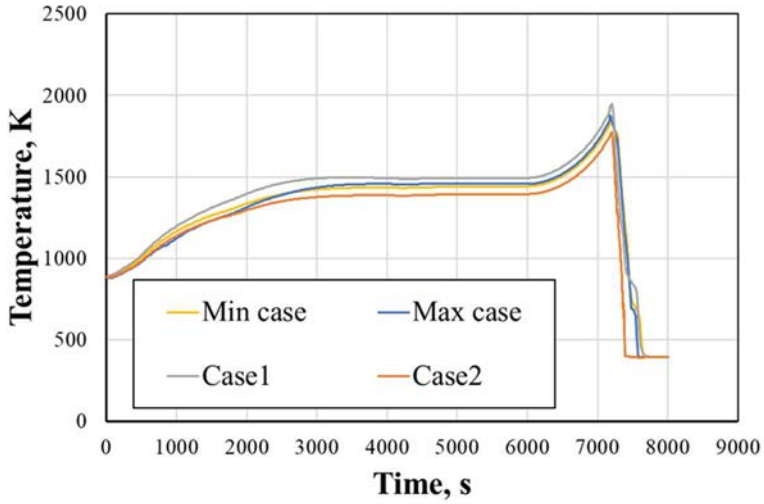

FIG. 171. Cladding temperature of the unheated (central) rod at 950 mm elevation. Results of maximum and minimum cases compared to Case 1 and Case 2.

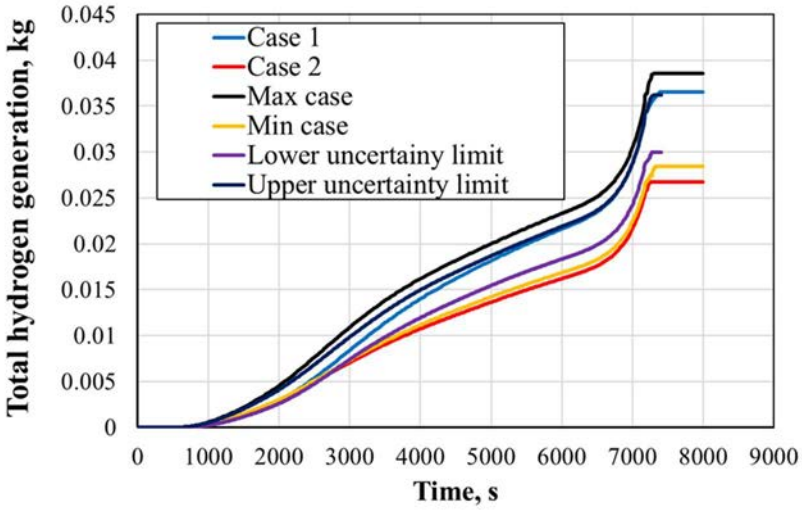

FIG. 172. Total H_2 generation. Results of maximum and minimum cases compared to Case 1 and Case 2.

6.5.CONCLUSIONS, LESSONS LEARNED, AND BEST PRACTICES

The QUENCH-06 calculations are based on RELAP/SCDAPSIM code version Mod4. The results of the reference calculations are compared to experimental data for all FOMs. It is observed that the experimental values are higher for total H_2 generation rate and oxide layer thickness at the elevation from 600 mm to 850 mm during the oxidation phase. The reference calculation is in a good agreement with experimental values for the central rod temperature and inner heated rod at elevations 750 mm and 950 mm.

The GRS methodology and SUSA statistical tool are used for the uncertainty quantification of the calculation results. In total, 19 uncertainty parameters are investigated. Uncertainty calculations are provided for all FOMs, except for the H_2 generation rate. Results of uncertainty analysis shows that upper and lower uncertainty limits of total H_2 generation enclose the experimental data. The same is observed for the temperature of the central rod at 950 mm elevation. However, during the quench phase

at the elevations 850−1000 mm, the zircaloy cladding oxidation is much higher compared to the results of the uncertainty analysis.

Spearman rank correlation coefficient is used in sensitivity analysis with the results showing that influence of the investigated uncertainty parameters varies with test phases. The most influencing parameters on results for total H_2 generation and temperature are electrical power and steam mass flow rate at the bundle inlet in all phases. Quench water injection has significant influence on the calculations. The uncertainty parameters, which have a significant influence on calculation results for the oxide layer before quenching are electrical power, steam mass flow rate at the bundle inlet, and cladding thickness. For oxide layer at the end of calculation is electrical power and steam mass flow rate at the bundle inlet.

7. CONCLUSIONS

Severe accidents in NPPs are rare events that can result in the release of radioactive materials into the environment in thus posing a significant risk to human health and the environment. These accidents can occur due to a variety of causes, such as equipment failures, operator errors, or natural disasters. The severe accidents in NPPs to date were: Three Mile Island (1979) with partial meltdown of the reactor core occurred due to a cooling system failure, Chernobyl (1986) with an explosion and fire that resulted in a complete meltdown of the reactor core and significant release of radioactive materials to the environment, and Fukushima Daiichi (2011) caused by massive earthquake and tsunami that led to a series of reactor meltdowns and releases of radioactive materials to the environment.

The QUENCH-06 experiment performed at KIT in 2000 is selected as a test exercise with the main goal to test the advanced calculation codes based on currently available severe accident codes and relevant uncertainty tools for uncertainty and sensitivity analysis. During the experiment, a single fuel rod is heated until it has failed, and then cooled with water to simulate the injection of coolant. The test aimed to investigate the behaviour of fuel rod during the quenching process, as well as to examine the potential for fuel fragmentation and the release of fission products.

Four organizations contributed to this analysis: ENEA (Italy), IBRAE (Russian Federation), KIT (Germany) and LEI (Lithuania). In view of the uncertainty and sensitivity analysis, 23 uncertainty parameters with the corresponding PDFs and five FOMs are analysed.

The exercise consisted of the following steps:

- Assessment of the severe accident code model for the QUENCH-06 experiment;
- Reference case simulation to validate the facility model against the experiment;
- Uncertainty and sensitivity analysis of the QUENCH-06 test; the uncertainty of the selected FOMs is characterized by both, the tolerance limits and standard deviation. The main method of sensitivity analysis is to evaluate the correlation coefficients between the uncertainty input parameters and selected FOMs. Pearson, Spearman, and Sobol' correlations are used;
- Lessons learned from the application of uncertainty and sensitivity analysis methodologies to severe accident analyses.

The severe accident codes and the uncertainty and sensitivity analysis tool used in the presented analysis are:

— ENEA: ASTEC/RAVEN;
— KIT: ASTEC/URANIE and ASTEC/KATUSA);
— IBRAE: SOCRAT/ELENA;
— LEI: RELAP-SCDAPSIM/SUSA.

The results show that the severe accident codes can predict the behaviour of the selected FOMs. Additionally, the severe accident codes/uncertainty tools are well characterized by high performance in terms of wall-clock time and accuracy. The results of the sensitivity analyses show that the uncertainties of the electric power and steam flow rates have the highest correlation with the FOMs.

The exercise also points out that:

— Efforts need to be focused at properly selecting the uncertainty parameters and assessment of the corresponding PDFs;
— Attention needs to be paid to the evaluation of the minimum number of samples in case of bifurcation of the output domain of a FOM;
— Number of code calculations need to be much larger than the number of uncertainty parameters to limit the impact of random code failures and then to guarantee reliable sensitivity results;
— Using different correlations provides better and clearer picture of physical behaviour of the transients, particular in the case of occurrence of cliff edge and bifurcation effects; the sensitivity analysis has the potential to ease finding errors in the modelling if the calculation results contradict the common understanding of a phenomenon.

The QUENCH-06 test exercise demonstrated to be a good example for testing the couplings in between integral codes and uncertainty and sensitivity analysis tools. The wall clock time for the severe accident code simulations is rather short, compared to the full plant calculations, allowing the assessment of a very large database for the application of the uncertainty and sensitivity analysis methodologies.

REFERENCES

[1] SEPOLD, L., et al., Experimental and Computational Results of the QUENCH-06 Test (OECD ISP-45). Report FZKA-6664. Karlsruhe, Germany (2004).

[2] MASCARI F; et.al., "Overview of IAEA CRP I31033 "Advancing the State-of-Practice in Uncertainty and Sensitivity Methodologies for Severe Accident Analysis in Water Cooled Reactors", Proc. of the 10th European Review Meeting on Severe Accidents Research (ERMSAR2022): Severe Accident Research Eleven Years after the Fukushima Accident, Karlsruhe, May 16–19, DOI: 10.5445/IR/1000151444.

[3] HERING, W., HOMANN, C., LAMY, J.-S., MIASSOEDOV, A., SCHANZ, G., SEPOLD, L., STEINBRÜCK, M., "Comparison and Interpretation report of the OECD International Standard Problem no.45 Exercise (QUENCH-06)"; Report FZKA-6722, Forschungszentrum Karlsruhe (2002).

[4] STUCKERT, J., STEINBRÜCK, M., GROßE, M., "Experimental Program QUENCH at KIT on Core Degradation During Reflooding Under LOCA Conditions and in the Early Phase of a Severe Accident", Proc. of Modelling of Water Cooled Fuel Including Design Basis and Severe Accidents, Chengdu, China, October 28 – November 1, 2013.

[5] SCHANZ, G., HAGEN, S., HOFMANN, P., SCHUMACHER, G., SEPOLD, L., 1992. "Information on the evolution of severe LWR fuel element damage obtained in the CORA program", J. Nucl. Mater. **188** pp. 131–145 (1992).

[6] CHATELARD; P., REINKE; N., ARNDT; S., et al., "ASTEC V2 severe accident integral code main features, current V2.0 modelling status, perspectives", Nucl. Eng. and Des. **272** pp. 119–135 (2014).

[7] GAUNTT, R. O., "MELCOR Computer Code Manuals, Vol. 1: Primer and Users' Guide", Sandia National Laboratories Albuquerque, NM 87185–0739, NUREG/CR-6119 (2005).

[8] STUCKERT, J., BIRCHLEY, J., GROßE, M., HASTE, T., SEPOLD, L., 2009. "Experimental and post-test calculation results of the integral reflood test QUENCH-12 with a VVER-type bundle", Annals of Nuclear Energy **36** pp. 183–192 (2009)

[9] HOFMANN, C., HERING, W., MIASSOEDOV, A., SEPOLD, L., "Detailed Investigation of Thermal-Hydraulics Aspects during the Reflood Phase in QUENCH Experiments", Proc. of ICONE12, Arlington, Virginia USA, April 25–29 (2004).

[10] KOBZAR, V., et al., "Uncertainty and Sensitivity Analysis of CORA-W2 Test Using ICARE2/SUNSET Tool", NSI RRC KI 2127, Moscow, Russia (1997).

[11] GABRIELLI, F., SANCHEZ-ESPINOZA, V.H.; "Uncertainty and Sensitivity Analysis by means of ASTEC/URANIE Platform of the QUENCH-08 Experiment", Proceedings of the 24th International QUENCH Workshop, Karlsruhe, Germany, pp. 354–375, (2018).

[12] STAKHANOVA, A., GABRIELLI, F., SANCHEZ-ESPINOZA, V.H., HÖFER, A., PAULI, E., "Uncertainty and sensitivity analysis of the QUENCH-08 experiment using the FSTC tool", Annals of Nuclear Energy **169** (2022), ISSN 0306-4549, https://doi.org/10.1016/j.anucene.2022.108968.

[13] DE LUZE, O., BARRACHIN, M., REPETTO, G., 2013; "Early phase fuel degradation in Phébus FP: Initiating phenomena of degradation in fuel bundle tests", Annals of Nuclear Energy **61** pp. 23–35 (2013).

[14] CHATELARD, P., et al., "Main modelling features of the ASTEC V2.1 major version", Annals of Nuclear Energy **93** pp. 83–93 (2016)

[15] PIAR, L., "CESAR physical and numerical modelling", IRSN Report n° PSN-RES/SAG/2015-00332, (2015).

[16] COINDREAU, O., “ASTEC V2.1: Physical modelling of the ICARE module”, IRSN Rapport n° PSN-RES/SAG/2016-00422, (2016).
[17] GABRIELLI, F., SANCHEZ-ESPINOZA, V.H., STUCKERT; J., GOMEZ-GARCIA-TORANO, I., 2019, “Validation of the ASTEC Integral Code using the QUENCH-06 and QUENCH-08 Experiments”, Proc. of the 9TH European Review Meeting on Severe Accident Research (ERMSAR2019), Prague, Czech Republic, March 18–20 (2019).
[18] D'AURIA, F. S., et al., “Best Estimate Safety Analysis for Nuclear Power Plants: Uncertainty Evaluation”, IAEA Safety Report Series., Vol. 52, (2008).
[19] BERSANO, A., et al., “Ingress of Coolant Event simulation with TRACE code with accuracy evaluation and coupled DAKOTA Uncertainty Analysis”, Fusion Engineering and Design **159** (2020) 111944.
[20] WILKS, S.S., “Determination of sample sizes for setting tolerance limits”, Annals of Mathematical Statistic, 12(1), pp. 91–96 (1941).
[21] WILKS; S.S., “Statistical prediction with special reference to the problem of tolerance limits”, Annals of Mathematical Statistic, 13(4), pp. 400–409 (1942).
[22] GUBA, A., et al., “Statistical aspects of best estimate method—I”, Reliability engineering & system safety **80** pp. 217–232 (2003).
[23] HORST, G., “GRS method for uncertainty and sensitivity evaluation of code results and applications”, Science and Technology of Nuclear Installations vol. 2008 (2008).
[24] ALFONSI, A., et al., “RAVEN Theory Manual”, INL/EXT-16-38178, Idaho National Laboratory (INL), (2020).
[25] ALFONSI, C., et al., “RAVEN User Guide, INL/EXT-18-44465”, Idaho National Laboratory (INL), (2020).
[26] ROSSUM, V., “Python reference manual”, Centrum voor Wiskunde en Informatica, Amsterdam, (1995).
[27] MACCARI, P., et. al., “ASTEC-RAVEN coupling for uncertainty analysis of an ingress of coolant event in fusion plants”, Fusion Engineering and Design **169** pp. 112–442 (2021).
[28] AMBROSINI, W., et. al., “Evaluation of accuracy of thermal hydraulic code calculation”, Energia Nucleare **7**(2) pp. 5–16 (1990).
[29] PROŠEK, A., et. al., “Quantitative assessment with improved fast Fourier”, Nucl. Eng. and Des. **238** pp. 2668–2677 (2008).
[30] PROŠEK, A., et. al., “Use of FFTBM by signal mirroring for sensitivity study”, Annals of Nuclear Energy **76** pp. 253–262 (2015).
[31] PROŠEK, A., “JSI FFTBM Add-In 2007 User’s Manual”, IJS-DP-9752, (2007).
[32] PROŠEK, A., et. al., “Review of quantitative accuracy assessments with fast Fourier transform based method (FFTBM)”, Nucl. Eng. and Des. **217**(1–2) pp. 179–206 (2002).
[33] PROŠEK A., et. al., “Application of FFTBM to Severe Accidents”, Proceedings of Nuclear Energy for New Europe, Bled, Slovenia, (2005).
[34] D'AURIA, F. S, FROGHERI, M., GIANNOTTI, W., RELAP/MOD3.2 Post Test Analysis and Accuracy Quantification of SPES Test SP-SB-04, NUREG/IA-0155 (1999).
[35] PEREZ, M., et. al., “Uncertainty and sensitivity analysis of a LBLOCA in a PWR Nuclear Power Plant: Results of the Phase V of the BEMUSE programme”, Nucl. Eng. and Des. **241**(10) pp. 4206–4222 (2011).
[36] “Status and Evaluation of Severe Accident Simulation Codes for Water Cooled Reactors”, IAEA-TECDOC-1872, IAEA, Vienna (2019).
[37] BOLSHOV L. et al., “Results of SOCRAT code development, validation and applications for NPP safety assessment under severe accidents”, Nucl. Eng. and Des. **341** pp. 326–345 (2019).

[38] STUCKERT J., at al., “Results of the QUENCH-12 Experiment on Reflood of a VVER-type Bundle”, FZKA, Karlsruhe (2008).
[39] PELETSKY V. E., BELSKAYA E. A., “Electrical resistance of refractory metals (handbook)”, Energoizdat, Moscow (1981) (in Russian).
[40] ASME, “Standard for verification and validation in computational fluid dynamics and heat transfer”, ASME V&V20–2009, New York. (2009).
[41] “International vocabulary of metrology – Basic and general concepts and associated terms (VIM)”, 3-rd edition, JCGM 200:2012.
[42] SILVIU GUIASU and ABE SHENITZER, “The principal of Maximum Entropy”, The Mathematical Intelligencer **7** 1 pp. 42–48 (1985).
[43] WILLIAM L., OBERKAMPF, CHRISTOPHER J. ROY, “Verification and Validation in Scientific Computing”, Cambridge University Press (2010).
[44] SALTELLI A., at al., “Global Sensitivity Analysis. The Primer”, John Wiley &Sons Ltd (2008).
[45] SALTELLI A., at al., “Variance based sensitivity analysis of model output. Design and estimator for the total sensitivity index”, Computer Physics Communications **181**, pp. 259–270 (2010).
[46] BLANCHARD, J.-B., DAMBLIN, G., MARTINEZ, J.M., ARNAUD, G., GAUDIER, F., “The Uranie platform: an open-source software for optimisation, meta-modelling and uncertainty analysis”, EPJ Nucl. Sci. Technology **5** pp. 4 (2019).
[47] GAUDIER, F., “URANIE: The CEA/DEN Uncertainty and Sensitivity platform”, Procedia Social and Behavioral Sciences **2** pp. 760–766 (2010).
[48] ROCQUIGNY, E. D., “Quantifying uncertainty in an industrial approach: an emerging consensus in an old epistemological debate,” Surveys and Perspectives Integrating Environment and Society **2** (2009).
[49] STAKHANOVA, A., GABRIELLI, F., SANCHEZ-ESPINOZA, V.H., HÖFER, A., PAULI, E., “Uncertainty and Sensitivity Analysis of the ASTEC Simulations Results of a MBLOCA Scenario in a Generic KONVOI Plant using the FSTC Tool”, Proc. of the 10th European Review Meeting on Severe Accidents Research (ERMSAR2022): Severe Accident Research Eleven Years after the Fukushima Accident, Karlsruhe, May 16-19, DOI: 10.5445/IR/1000151444 (2022).
[50] GABRIELLI, F., SANCHEZ-ESPINOZA, V.H., “Uncertainty and Sensitivity Analysis by Means of ASTEC/URANIE Platform of the QUENCH-08 Experiment”, Proceedings of the 24th International Quench Workshop, Karlsruhe, November 13−15 (2018).
[51] SZÉKELY, G. J., RIZZO, M. L., "Brownian distance covariance", Ann. Appl. Stat. **3** (4) pp. 1236−1265, https://doi.org/10.1214/09-AOAS312. (2009)
[52] RESHEF, D.N., RESHEF, Y. A., FINUCANE, H.K., et al., GROSSMAN, S.R., MCVEAN, G., TURNBAUGH, P.J., LANDER, E.S., MITZENMACHER, M., SABETI, P.C., “Detecting novel associations in large data sets“, Science 2011 Dec 16;334(6062):1518-24. doi: 10.1126/science.1205438. PMID: 22174245; PMCID: PMC3325791.
[53] HÖFER, A, BUSS, O., HENNEBACH, M., et al., "MOCABA: A general Monte Carlo-Bayes procedure for improved predictions of integral functions of nuclear data", Annals of Nuclear Energy **77** pp. 514–521 (2015).
[54] PAULI, E.-M., HÖFER, A., GABRIELLI, F., STAKHANOVA, A:, SANCHEZ-ESPINOZA, V.H., “Prediction of the radiological consequences of a severe accident scenario in a generic KONVOI nuclear power plant”, Proc. of the 10th European Review Meeting on Severe Accidents Research (ERMSAR2022): Severe Accident Research Eleven Years after the Fukushima Accident, Karlsruhe, May 16-19, DOI: 10.5445/IR/1000151444 (2022).
[55] ALLISON, C. M., WAGNER, R. J., “RELAP5/SCDAPSIM/MOD3.2(am+) Input Manual Supplemental,” Innovative Systems Software”, LLC, http://www.relap.com/ (2020).

[56] RELAP5 Code Development Team, “RELAP5/MOD3.3 Code Manual. Vol 1–8”, NUREG/CR-5535/Rev1 (2001).
[57] SCDAP/RELAP5 Development Team, “SCDAP/RELAP5/MOD3.2 Code Manual, Vol. 1–5”, NUREG/CR-6150, INEL-96/0422 (1981).
[58] RATTANADECHO, N., RASSAME, S., SILVA, K., ALLISON, C.M., HOHORST, J., “Assessment of RELAP/SCDAPSIM/MOD3.4 Prediction Capability with Severe Fuel Damage Scoping Test”, Science and Technology of Nuclear Installations, Vol. 2017, https://doi.org/10.1155/2017/7456380. (2017)
[59] KALIATKA, T., KALIATKA, A., VILEINIŠKIS, V., UŠPURAS, E., “Modelling of QUENCH-03 and QUENCH-06 Experiments Using RELAP/SCDAPSIM and ASTEC Codes”, Science and Technology of Nuclear Installations Vol. 2014 Article ID 849480. (2014)
[60] SADEK, S., SPALJ, S., GRGIC, D., “RELAP5/SCDAPSIM analysis of the QUENCH-06 experiment”, FER-ZVNE/SA/DA-IR01/03-0 (2003).
[61] KLOOS, M., HOFER, E., “SUSA Version 3.5, User’s Guide and Tutorial”, Gesellschaft fur Anlagen und REaktorsicherheit (GRS) mbH, Germany (2002).
[62] WILKS, S.S., “Statistical prediction with special reference to the problem of tolerance limits”, Ann. Math. Stat. **13** pp. 400–409 (1942)
[63] KLOOS, M., BERNER, N., “SUSA, Software for Uncertainty and Sensitivity Analyses Classical Methods”, Gesellschaft fur Anlagen und Reaktorsicherheit (GRS) mbH, GRS – 631, ISBN 978-3-949088-20-9, Germany (2021).

LIST OF ABBREVATIONS

ASTEC:	Accident Source Term Evaluation Code
CIEMAT:	Centre for Energy, Environmental and Technological Research (Spain)
CNEA:	National Atomic Energy Commission (Argentina)
CNL:	Canadian National Laboratories (Canada)
CNSNS:	National Nuclear Safety and Safeguards Commission (Mexico)
ENEA:	Italian National Agency for New Technologies, Energy and Sustainable Economic Development (Italy)
ENERGOATOM:	National Nuclear Power Company State Enterprise (Ukraine)
ENNRA:	Egyptian Nuclear and Radiological Regulatory (Egypt)
ENSO:	Engineering Solutions for Energy Systems (Spain)
FFTBM:	Fast Fourier Transform Based Method
FOM:	Figure of Merit
GAEC:	Ghana Atomic Energy Commission (Ghana)
GIDROPRESS:	OKB Gidropress Rosatom (Russian Federation)
HYU:	Hanyang University (Republic of Korea)
IBRAE:	Nuclear Safety Institute (Russian Federation)
ININ:	National Institute for Nuclear Research (Mexico)
ISS:	Innovative Systems Software, LLC. (USA)
KAERI:	Korea Atomic Energy Research Institute (Republic of Korea)
KIT:	Karlsruhe Institute of Technology (Germany)
LEI:	Lithuanian Energy Institute (Lithuania)
MNA:	Malaysian Nuclear Agency
PAEC:	Pakistan Atomic Energy Commission (Pakistan)
RAVEN:	Risk Analysis and Virtual Environment
SJTU:	Shanghai Jiao Tong University (China)
SNL:	Sandia National Laboratory (USA)
STD:	Standard Deviation
UPB:	Politehnica University of Bucharest (Romania)
U. Sharjah:	University of Sharjah (UAE)

CONTRIBUTORS TO DRAFTING AND REVIEW

Agnello, G.	University of Palermo (UNIPA)
Bersano, A.	National Agency for New Technologies, Energy and Sustainable Economic Development (ENEA)
Chalyy, R.V.	Nuclear Safety Institute of the Russian Academy of Sciences (IBRAE)
Ederli, S.	National Agency for New Technologies, Energy and Sustainable Economic Development (ENEA)
Elsalamouny, N.	Lithuanian Energy Institute (LEI)
Gabrielli, F.	Karlsruhe Institute of Technology (Germany)
Jevremovic, T.	International Atomic Energy Agency
Kaliatka, T.	Lithuanian Energy Institute (LEI)
Maccari, P.	National Agency for New Technologies, Energy and Sustainable Economic Development (ENEA)
Mascari, F.	National Agency for New Technologies, Energy and Sustainable Economic Development (ENEA)
Massone, M.	National Agency for New Technologies, Energy and Sustainable Economic Development (ENEA)
Rehman, H. ur	International Atomic Energy Agency
Ryzhov, N.I.	Nuclear Safety Institute of the Russian Academy of Sciences (IBRAE)
Semenov, V. N.	Nuclear Safety Institute of the Russian Academy of Sciences (IBRAE)

Research Coordination Meetings (RCMs)

1st RCM, EVT1803724, IAEA Headquarters, Vienna, Austria, 14–17 October, 2019.

2nd RCM, EVT1903891, IAEA Headquarters, Vienna, Austria, 20–22 October, 2020.

3rd RCM, EVT2004045, IAEA Headquarters, Vienna, Austria, 8–10 November, 2021.

4th RCM, EVT2103131, IAEA Headquarters, Vienna, Austria, 7–10 November, 2022.

IAEA
International Atomic Energy Agency

No. 26

ORDERING LOCALLY

IAEA priced publications may be purchased from the sources listed below or from major local booksellers.

Orders for unpriced publications should be made directly to the IAEA. The contact details are given at the end of this list.

NORTH AMERICA

Bernan / Rowman & Littlefield

15250 NBN Way, Blue Ridge Summit, PA 17214, USA
Telephone: +1 800 462 6420 • Fax: +1 800 338 4550

Email: orders@rowman.com • Web site: www.rowman.com/bernan

REST OF WORLD

Please contact your preferred local supplier, or our lead distributor:

Eurospan Group

Gray's Inn House
127 Clerkenwell Road
London EC1R 5DB
United Kingdom

Trade orders and enquiries:

Telephone: +44 (0)176 760 4972 • Fax: +44 (0)176 760 1640
Email: eurospan@turpin-distribution.com

Individual orders:

www.eurospanbookstore.com/iaea

For further information:

Telephone: +44 (0)207 240 0856 • Fax: +44 (0)207 379 0609
Email: info@eurospangroup.com • Web site: www.eurospangroup.com

Orders for both priced and unpriced publications may be addressed directly to:

Marketing and Sales Unit
International Atomic Energy Agency
Vienna International Centre, PO Box 100, 1400 Vienna, Austria
Telephone: +43 1 2600 22529 or 22530 • Fax: +43 1 26007 22529
Email: sales.publications@iaea.org • Web site: www.iaea.org/publications

24-00637E

International Atomic Energy Agency
Vienna